

UNIVERSITÀ DEGLI STUDI DI PISA



FACOLTÀ DI SCIENZE M.F.N.

**Measurement of branching fraction
ratios and CP asymmetries in
 $B \rightarrow D_{CP}^0 K$ decays with the *BABAR*
detector**

Dissertazione di Dottorato in Fisica

Candidato:

Dr. Giovanni Marchiori

Relatore:

Prof. Giovanni Batignani

Coordinatore:

Prof. Kenichi Konishi

Controrelatori:

Prof. Jacques Chauveau

Prof. Flavio Costantini

Prof. Nello Paver

XVII Ciclo

23 Giugno 2005

Work supported in part by US Department of Energy contract DE-AC02-76SF00515.

SLAC National Accelerator Laboratory, Menlo Park, CA 94025

To my beloved family

Contents

Introduction	7
Goal of the analysis	7
Status of the measurement of $\mathcal{B}(B \rightarrow D_{(CP\pm)}^0 K)$ and $A_{CP}(B \rightarrow D_{(CP\pm)}^0 K)$	10
Outline of the manuscript	13
1 Theoretical review	15
1.1 Why B physics?	15
1.2 CP violation in the Standard Model. The CKM matrix and the Unitarity Triangle	15
1.3 The system of $B_{u,d}$ mesons	19
1.4 CP violation in B decays	21
1.4.1 CP violation in decay	21
1.4.2 CP violation in mixing	22
1.4.3 CP violation in the interference between decay and mixing	23
1.5 Measurement of the angle β	24
1.6 Measurement of the angle α	25
1.7 Measurement of the angle γ	27
1.7.1 The Gronau-London-Wyler method	29
1.7.2 The Atwood-Dunietz-Soni method	30
1.7.3 The Giri-Grossmann-Soffer-Zupan method	32
1.7.4 Measuring $\sin(2\beta + \gamma)$ in time-dependent $B^0 \rightarrow D^{(*)}\pi$	33
1.7.5 Current results on γ from model-independent measurements	35
1.7.6 Model-dependent methods for extracting γ	37
1.8 Conclusion	39
2 Experimental Apparatus	41
2.1 The PEP-II B Factory	41
2.1.1 PEP-II layout	41
2.1.2 PEP-II performances	44
2.2 Overview of the <i>BABAR</i> detector	46
2.3 The Silicon Vertex Tracker	50
2.3.1 Detector layout	50
2.3.2 Detector performance	51
2.4 The Drift Chamber	54
2.4.1 Detector layout	54
2.4.2 Detector performance	55
2.5 The Cherenkov light detector	56
2.5.1 Detector layout	57
2.5.2 Detector performance	59

2.6	The Electromagnetic Calorimeter	62
2.6.1	Detector layout	62
2.6.2	Detector performance	62
2.7	The Instrumented Flux Return	65
2.7.1	Detector layout	66
2.7.2	Detector performance	66
2.8	The <i>BABAR</i> Trigger	68
2.9	Conclusion	68
3	$B \rightarrow D_{(CP)}^0 K$ and $B \rightarrow D_{(CP)}^0 \pi$ selection	71
3.1	D^0 decay modes that have been studied and overall $B \rightarrow D^0 h$ branching fractions	72
3.2	Data and Monte Carlo sample	73
3.3	Reconstruction of charged and neutral particles in the final state	74
3.3.1	Charged tracks selection	75
3.3.2	Charged particle identification	75
3.3.3	Photon selection	79
3.4	“Composite” candidates reconstruction	80
3.4.1	π^0 reconstruction	80
3.4.2	K_s^0 reconstruction	80
3.4.3	ϕ reconstruction	81
3.4.4	ω reconstruction	82
3.4.5	D^0 reconstruction	83
3.5	B reconstruction	85
3.5.1	Additional selection criteria	90
3.6	Continuum background suppression through event-shape variables	90
3.7	Arbitration of multiple candidates	95
3.8	Summary of the selection criteria	97
3.9	Data-MC comparison	97
3.10	Expected signal yields	98
4	Measurement of the $B^\pm \rightarrow D_{(CP)}^0 h^\pm$ yields and of the GLW observables	105
4.1	Background characterization	106
4.2	Fit procedure	111
4.3	Particle ID probability density functions	112
4.4	ΔE probability density function	114
4.4.1	Signal ΔE parameterization	114
4.4.2	$q\bar{q}$ background ΔE parameterization	114
4.4.3	$B\bar{B}$ background ΔE parameterization	118
4.5	Fit validation with Monte Carlo studies	119
4.6	Fit to generic Monte Carlo	125
4.7	Fit results on data	133
4.7.1	$K^- \pi^+$	133
4.7.2	$K^+ K^-$	136
4.7.3	$\pi^+ \pi^-$	138
4.7.4	$K_s^0 \pi^0$	140
4.7.5	$K_s^0 \phi$	142
4.7.6	$K_s^0 \omega$	144
4.8	Fit on background-only data samples	146
4.9	Systematic errors evaluation	147
4.9.1	Parameterization of the $\Delta E B\bar{B}$ and $q\bar{q}$ distribution	147
4.9.2	Parameterization of $\text{PDF}(\theta_C)$	147
4.9.3	Evaluation of the peaking backgrounds	147

4.9.4	Detector charge asymmetry	147
4.9.5	S-wave Pollution in $B \rightarrow D^0 K, D^0 \rightarrow K_s^0 \phi$ and $B \rightarrow D^0 K, D^0 \rightarrow K_s^0 \omega$	148
4.10	Measurement of the direct CP asymmetry	154
4.11	Measurement of the ratio R_{\pm}	155
4.12	Constraints on the CKM angle γ	156
4.13	Conclusions	159
A	γ and charged $B^{\pm} \rightarrow D^{0(-)} K^{\pm}$ decays	161
	Bibliography	165

Introduction

The primary goals of the *BABAR* experiment are the detection of *CP* violation (CPV) in the *B* meson system, the precise measurement of some of the elements of the CKM matrix and the measurement of the rates of rare *B* meson decays. At present, *BABAR* has achieved major successes:

- the discovery, in neutral *B* decays, of *direct* and *mixing-induced CP* violation
- accurate measurements of the magnitudes of the CKM matrix elements $|V_{cb}|$ and $|V_{ub}|$
- a precise measurement of the CKM parameter $\beta \equiv \arg \left[-\frac{V_{cd}V_{cb}^*}{V_{td}V_{tb}^*} \right]$
- a first measurement of the CKM parameters $\alpha \equiv \arg \left[-\frac{V_{td}V_{tb}^*}{V_{ud}V_{ub}^*} \right]$, $\gamma \equiv \arg \left[-\frac{V_{ud}V_{ub}^*}{V_{cd}V_{cb}^*} \right]$
- the observation of several rare *B* decays and the discovery of new particles (in the charmed and charmonium mesons spectroscopy)

However, the physics program of *BABAR* is not yet complete. Two of the key elements of this program that still need to be achieved are

- the observation of direct *CP* violation in charged *B* decays, which would constitute the first evidence of direct CPV in a charged meson decay
- the precise measurement of α and γ , which are necessary ingredients for a stringent test of the Standard Model predictions in the quark electroweak sector.

A possibility for the discovery of direct *CP* violation in charged *B* decays would be the observation of a non-vanishing rate asymmetry in the Cabibbo-suppressed decay $B^- \rightarrow D^0 K^-$,¹ with the D^0 decaying to either a *CP*-even or a *CP*-odd eigenstate. This class of decays can also provide theoretically-clean information on γ .

Goal of the analysis

The subject of the work presented in this thesis is the reconstruction, in a data sample of $(231.8 \pm 2.6) \times 10^6$ charged *B* meson decays collected by the *BABAR* experiment during the years 1999-2004, of the Cabibbo-suppressed $B^- \rightarrow D^0 K^-$ decays, along with the Cabibbo-allowed $B^- \rightarrow D^0 \pi^-$ decays, with the D^0 decaying to *CP*-even ($K^+ K^-$, $\pi^+ \pi^-$), *CP*-odd ($K_S^0 \pi^0$, $K_S^0 \phi$, $K_S^0 \omega$)² and non-*CP* flavor ($K^- \pi^+$) eigenstates. The goal is the measurement of the two direct *CP* asymmetries

$$A_{CP\pm} \equiv \frac{\mathcal{B}(B^- \rightarrow D_{CP\pm}^0 K^-) - \mathcal{B}(B^+ \rightarrow D_{CP\pm}^0 K^+)}{\mathcal{B}(B^- \rightarrow D_{CP\pm}^0 K^-) + \mathcal{B}(B^+ \rightarrow D_{CP\pm}^0 K^+)} \quad (1)$$

and the two ratios of charge averaged branching fractions

$$R_{\pm} \equiv \frac{\frac{\mathcal{B}(B^- \rightarrow D_{CP\pm}^0 K^-) + \mathcal{B}(B^+ \rightarrow D_{CP\pm}^0 K^+)}{\mathcal{B}(B^- \rightarrow D_{CP\pm}^0 \pi^-) + \mathcal{B}(B^+ \rightarrow D_{CP\pm}^0 \pi^+)}}{\frac{\mathcal{B}(B^- \rightarrow D^0 K^-) + \mathcal{B}(B^+ \rightarrow \bar{D}^0 K^+)}{\mathcal{B}(B^- \rightarrow D^0 \pi^-) + \mathcal{B}(B^+ \rightarrow \bar{D}^0 \pi^+)}} \quad (2)$$

¹Charge conjugation is implied here and throughout the text unless otherwise stated

² K_S^0 , π^0 , ϕ and ω mesons are reconstructed through the decays $K_S^0 \rightarrow \pi^+ \pi^-$, $\pi^0 \rightarrow \gamma \gamma$, $\phi \rightarrow K^+ K^-$, $\omega \rightarrow \pi^+ \pi^- \pi^0$

where $D_{CP\pm}^0 = \frac{D^0 \pm \bar{D}^0}{\sqrt{2}}$ are (neglecting the tiny $D^0 - \bar{D}^0$ mixing) the two CP -eigenstates of the neutral D^0 meson system. A significant deviation of either A_{CP+} or A_{CP-} from zero would provide evidence for direct CP violation in the corresponding $B \rightarrow D_{CP}^0 K$ decay, since $B^+ \rightarrow D_{CP}^0 K^+$ is the CP -conjugate of the $B^- \rightarrow D_{CP}^0 K^-$ process. Moreover, an accurate measurement of the four observables $\{R_{\pm}, A_{CP\pm}\}$ would allow – in the Standard Model framework – to extract γ in a theoretically clean way, together with two hadronic unknowns r_B and δ_B (respectively the magnitude of the ratio of the $B^- \rightarrow \bar{D}^0 K^-$ and $B^- \rightarrow D^0 K^-$ amplitudes and their strong phase difference). In fact the observables $\{R_{\pm}, A_{CP\pm}\}$ are expressed in terms of $\{\gamma, r_B, \delta_B\}$ through the relations:

$$R_{\pm} \approx R_{CP\pm} = 1 + r_B^2 \pm 2r_B \cos \delta_B \cos \gamma \quad (3)$$

$$A_{CP\pm} = \frac{\pm 2r_B \sin \delta_B \sin \gamma}{1 + r_B^2 \pm 2r_B \cos \delta_B \cos \gamma}. \quad (4)$$

where we have defined the branching fraction ratio:

$$R_{CP\pm} \equiv \frac{\mathcal{B}(B^- \rightarrow D_{CP\pm}^0 K^-) + \mathcal{B}(B^+ \rightarrow D_{CP\pm}^0 K^+)}{\mathcal{B}(B^- \rightarrow D^0 K^-) + \mathcal{B}(B^+ \rightarrow \bar{D}^0 K^+)} \quad (5)$$

and the approximate equality $R_{CP\pm} \approx R_{\pm}$ follows from the exact cancellation of $D^0 \pi$ phase-space factors in the double ratio R_{\pm} and from the approximation $A(B^+ \rightarrow D_{CP\pm}^0 \pi^+) \approx A(B^- \rightarrow D_{CP\pm}^0 \pi^-) \approx \frac{1}{\sqrt{2}} A(B^- \rightarrow D^0 \pi^-)$, where a term $r_B \times |V_{us} V_{cd} / V_{ud} V_{cs}|$ is neglected. The ratio r_B – which involves the ratio of CKM factors $|V_{ub} V_{cs} / V_{cb} V_{us}| \approx 0.4 - 0.5$ and a probably comparable color-suppression factor [1] – is expected from theory to be $r_B \approx 0.1 - 0.2$ [1]. This (crude) estimation is confirmed by recent experimental determinations from the *BABAR* and *Belle* experiments:

$$r_B = 0.12 \pm 0.09 \text{ BABAR [2]}$$

$$r_B = 0.21 \pm 0.09 \text{ Belle [3]},$$

and suggests that the approximation $R_{\pm} \approx R_{CP\pm}$ is valid to order $r_B \times \tan^2 \theta_C \approx 0.5 - 1.0\%$, where θ_C is the Cabibbo angle ($\tan \theta_C \approx 0.22$). The phase δ_B ($0 \leq \delta_B < 360^\circ$) is unknown from the theory, and recent experimental determinations from *BABAR* and *Belle* favor a value (modulo 180°) between 90° and 180° :

$$\delta_B \text{ mod } 180^\circ = 114^\circ \pm 55^\circ \text{ BABAR [2]}$$

$$\delta_B \text{ mod } 180^\circ = 157^\circ \pm 30^\circ \text{ Belle [3]}.$$

In the analysis presented in this thesis $B^- \rightarrow D^0 K^-$ decays are reconstructed together with the Cabibbo-allowed $B^- \rightarrow D^0 \pi^-$ decays with the same D^0 final states. While $B^- \rightarrow D_{(CP\pm)}^0 \pi^-$ decays are not very interesting by themselves, since the expected CP asymmetries in these channels are at most at the 1% level and γ could be extracted from only the $B^- \rightarrow D_{(CP\pm)}^0 K^-$ branching fractions and CP asymmetries, their reconstruction is useful for four reasons:

- it provides a way to estimate possible charge asymmetries in the detector (the CP asymmetry is expected to be zero in this channel) which could potentially bias the measurement of $A_{CP\pm}$;
- since the kinematics of $B^- \rightarrow D_{CP\pm}^0 \pi^-$ and $B^- \rightarrow D_{CP\pm}^0 K^-$ decays are very similar, the former – with a branching fraction ≈ 12 times larger than the latter – are an abundant and excellent control sample;
- for the reasons explained above, the process $B^- \rightarrow D_{CP\pm}^0 \pi^-$ gives a significant contribution to the background for the process $B^- \rightarrow D_{CP\pm}^0 K^-$ and must therefore be well understood;

- normalizing the branching fraction of $B \rightarrow D_{(CP\pm)}^0 K$ to that of $B \rightarrow D_{(CP\pm)}^0 \pi$ and measuring R_{\pm} instead of $R_{CP\pm}$ leads to a cancellation of many systematic uncertainties (like, for instance, the ones connected to the number of B mesons in the original data sample and to the branching fractions of the D^0 and its instable daughters) and therefore can be useful to obtain more precise results.

The separate measurement of the $B^- \rightarrow D^0 K^-$ and $B^- \rightarrow D^0 \pi^-$ rates and asymmetries is performed through a maximum likelihood fit that exploits the particle identification (PID) information of the prompt particle provided by *BABAR*'s excellent PID system, along with a few kinematical variables which characterize the decay of the B meson and are reconstructed by means of *BABAR* charged particle tracking system and its electromagnetic calorimeter.

Status of the measurement of $\mathcal{B}(B \rightarrow D_{(CP\pm)}^0 K)$ and $A_{CP}(B \rightarrow D_{(CP\pm)}^0 K)$

At present, three experiments, CLEO, Belle and *BABAR*, have detected the Cabibbo-suppressed decay $B^- \rightarrow D^0 K^-$ with D^0 decaying to Cabibbo-allowed non- CP flavor eigenstates. In all three experiments, B mesons are originated in the decays $\Upsilon(4S) \rightarrow B\bar{B}$ of the vector resonance $\Upsilon(4S) = (b\bar{b})$ produced in e^+e^- collisions at a center-of-mass (CM) energy $\sqrt{s} = m(\Upsilon(4S))c^2 = 10.58$ GeV. In CLEO, installed at the Cornell Electron Storage Ring (CESR), electrons and positrons have the same energy in the laboratory frame; in Belle (at the KEKB facility) and *BABAR* (at the SLAC PEP-II e^+e^- storage ring), $B\bar{B}$ pairs are produced in collisions where electrons are ≈ 3 times more energetic than positrons. The total number of B^\pm mesons collected by CLEO, in the years 1999-2001, is 15.4×10^6 ; the number of B^\pm collected by *BABAR* and Belle until the end of year 2004 is 15–20 times larger, and should reach about one billion by 2008. For this reason KEKB and PEP-II are usually referred to as “ B -factories”. The measured branching fraction ratio between the $B^- \rightarrow D^0 K^-$ and the $B^- \rightarrow D^0 \pi^-$ processes is:

$$\begin{aligned} \mathcal{B}(B^- \rightarrow D^0 K^-)/\mathcal{B}(B^- \rightarrow D^0 \pi^-) &= (9.9^{+1.4+0.7}_{-1.2-0.6}) \times 10^{-2} \text{ CLEO [4]} \\ \mathcal{B}(B^- \rightarrow D^0 K^-)/\mathcal{B}(B^- \rightarrow D^0 \pi^-) &= (7.7 \pm 0.5 \pm 0.6) \times 10^{-2} \text{ Belle [5]} \\ \mathcal{B}(B^- \rightarrow D^0 K^-)/\mathcal{B}(B^- \rightarrow D^0 \pi^-) &= (8.31 \pm 0.35 \pm 0.20) \times 10^{-2} \text{ BABAR [6]} \end{aligned}$$

The weighted average of the *BABAR*, Belle and CLEO measurements is:

$$\mathcal{B}(B^- \rightarrow D^0 K^-)/\mathcal{B}(B^- \rightarrow D^0 \pi^-) = (8.19 \pm 0.28)\%$$

The CLEO measurement is based on the whole CLEO data sample (15.4 million B^\pm mesons collected in the years 1990-2001); the D^0 candidates are reconstructed in the decay modes $K^-\pi^+$, $K^-\pi^+\pi^+\pi^-$, $K^-\pi^+\pi^0$. The Belle result is based on a sample of 85.4 million B^\pm mesons collected in the years 1999-2002; the D^0 candidates are reconstructed in the $K^-\pi^+$ decay mode. The *BABAR* measurement is based on a sample of 88.8 million B^\pm mesons collected in the years 1999-2002; the D^0 candidates are reconstructed in the decay modes $K^-\pi^+$, $K^-\pi^+\pi^+\pi^-$, $K^-\pi^+\pi^0$.

In the case of D^0 decaying to CP eigenstates, the expected branching fraction ratios and CP asymmetries depend – as anticipated in the Introduction – on the value of three quantities γ , r_B and δ_B through the relations

$$\begin{aligned} \frac{\mathcal{B}(B^- \rightarrow D_{CP\pm}^0 K^-)}{\mathcal{B}(B^- \rightarrow D_{CP\pm}^0 \pi^-)} &\approx R_{CP\pm} \frac{\mathcal{B}(B^- \rightarrow D^0 K^-)}{\mathcal{B}(B^- \rightarrow D^0 \pi^-)} \\ &= (1 + r_B^2 \pm 2r_B \cos \delta_B \cos \gamma) \frac{\mathcal{B}(B^- \rightarrow D^0 K^-)}{\mathcal{B}(B^- \rightarrow D^0 \pi^-)} \\ A_{CP\pm} &= \frac{\pm 2r_B \sin \delta_B \sin \gamma}{1 + r_B^2 \pm 2r_B \cos \delta_B \cos \gamma} \end{aligned}$$

where in principle γ and δ_B are angles which lie in the range $[0, 360]^\circ$, and r_B is a positive quantity. Theoretical estimates [1] and recent experimental determinations [2, 3] for r_B are in the range 0.1 – 0.2, and γ is expected to be, from indirect constraints and if the Standard Model is correct, around 60° [7, 8]. In Figure 1 are shown the expected values of $R_{CP\pm}$ and $A_{CP\pm}$ as a function of δ for $\gamma = 60^\circ$ and for different values of r_B in the range 0.05-0.20. In the $r_B = 0.15$ case $R_{CP\pm}$ varies between 0.87 and 1.17 depending on the value of δ_B , and CP asymmetries are expected to be at most $\pm 24\%$.

Since D^0 decays to CP eigenstates are Cabibbo suppressed, with branching fractions of the order of 10^{-3} , and reconstruction efficiencies are typically between 10 and 30%,

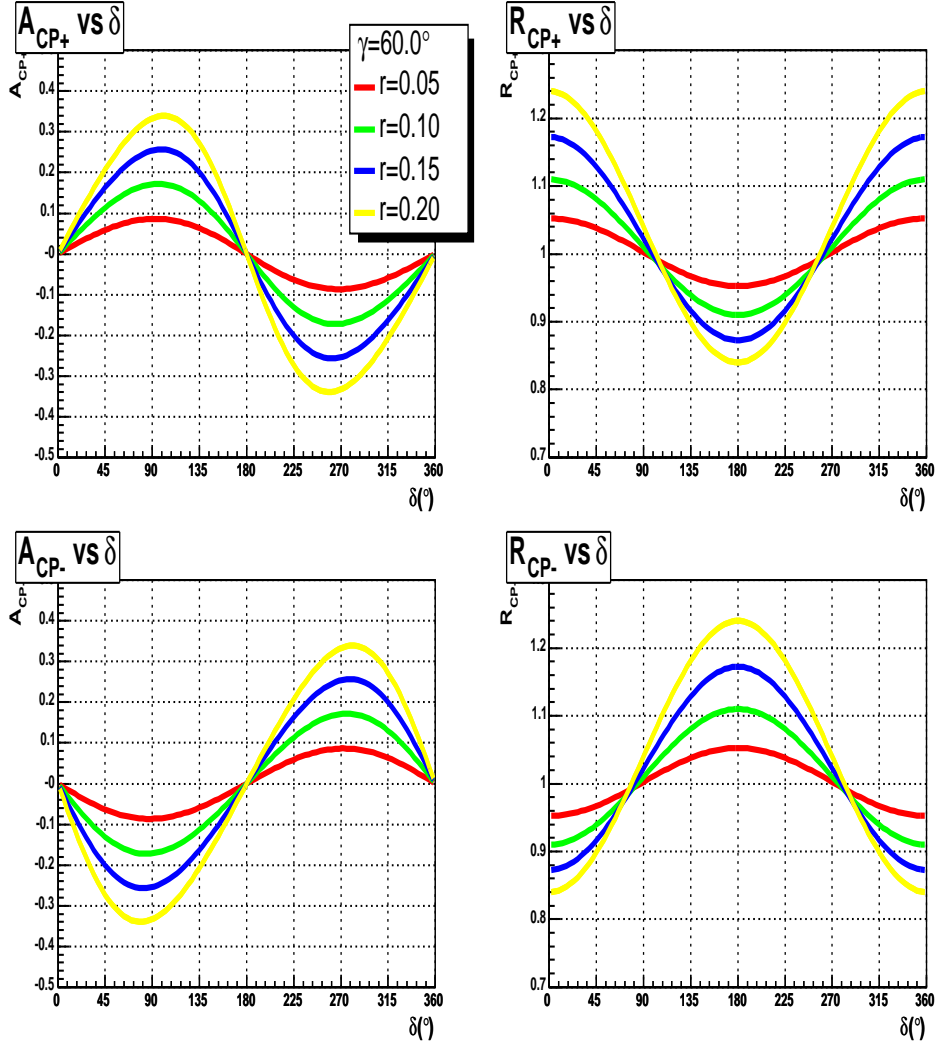


Figure 1: Expected values of $R_{CP\pm}$ and $A_{CP\pm}$ as a function of δ for $\gamma = 60^\circ$ and different values of r_B .

to measure $R_{CP\pm}$ and $A_{CP\pm}$ a huge number of charged B mesons must be collected. Therefore the measurement of $R_{CP\pm}$ and $A_{CP\pm}$ is precluded to the CLEO experiment, while it is possible with the large data sample accumulated up to now by the B factories, and will be refined in the next three years as long as this data sample will be increased by a factor ≈ 4 . Prior to the analysis presented in this thesis, a measurement of R_{CP+} and A_{CP+} , with D_{CP+}^0 decaying to the CP -even eigenstates K^-K^+ and $\pi^-\pi^+$, has been performed both by Belle and BABAR:

$$\begin{aligned} R_{CP+} &= 1.21 \pm 0.25 \pm 0.14 \\ A_{CP+} &= 0.06 \pm 0.19 \pm 0.04 \text{ Belle [5]} \end{aligned}$$

$$\begin{aligned} R_{CP+} &= 1.06 \pm 0.20 \pm 0.06 \\ A_{CP+} &= 0.07 \pm 0.17 \pm 0.06 \text{ BABAR [6]} \end{aligned}$$

while $B \rightarrow D_{CP-}^0 K$ decays have been reconstructed only by Belle:

$$\begin{aligned} R_{CP-} &= 1.41 \pm 0.27 \pm 0.15 \\ A_{CP-} &= -0.19 \pm 0.17 \pm 0.06 \text{ Belle [5]} \end{aligned}$$

The data sample used for these analyses are the same as those used to measure the ratio $\mathcal{B}(B^- \rightarrow D^0 K^-)/\mathcal{B}(B^- \rightarrow D^0 \pi^-)$. *BABAR* finds, on a sample of 88.8 million B^\pm , $44.3 \pm 9.0 \pm 3.3$ $B \rightarrow D_{CP+}^0 [K^+ K^-] K$ candidates and $24.2 \pm 7.2_{-2.5}^{+1.6}$ $B \rightarrow D_{CP+}^0 [\pi^+ \pi^-] K$ candidates. Belle reconstructs the D_{CP-}^0 in the CP -odd channels $K_s^0 \pi^0$, $K_s^0 \phi$, $K_s^0 \omega$, $K_s^0 \eta$, $K_s^0 \eta'$, with $K_s^0 \rightarrow \pi^+ \pi^-$, $\pi^0 \rightarrow \gamma \gamma$, $\phi \rightarrow K^+ K^-$, $\omega \rightarrow \pi^+ \pi^- \pi^0$, $\eta \rightarrow \gamma \gamma$, $\eta' \rightarrow \eta \pi^+ \pi^-$. They find, on a sample of 85.4 million B^\pm mesons, 52 $B \rightarrow D_{CP-}^0 K^\pm$ candidates. The yields are not quoted separately for the various decay modes of the D_{CP-}^0 , but – taking into account the branching fractions of the decay processes that are involved – the $K_s^0 \eta$ and $K_s^0 \eta'$ modes are expected to give a negligible contribution to the total signal yield.

An updated measurement has been presented by the Belle Collaboration at ICHEP'04, based on a sample of 274 million $B\bar{B}$ events; the preliminary results are [9]:

$$\begin{aligned} R_{CP+} &= 0.98 \pm 0.18 \pm 0.10 \\ A_{CP+} &= 0.07 \pm 0.14 \pm 0.06 \\ R_{CP-} &= 1.29 \pm 0.16 \pm 0.08 \\ A_{CP-} &= -0.11 \pm 0.14 \pm 0.05 \end{aligned}$$

No evidence for direct CP violation is found from the measured values of $A_{CP\pm}$.

Outline of the manuscript

In Chapter 1 an overview on CP violation, in general and in B meson decays, is presented. In particular, direct CP violation is described in Section 1.4.1. The main, most promising methods for the extraction of γ are reviewed, together with the current experimental information that we have (Section 1.7).

The general structure of the *BABAR* detector and the performances of its subsystems are described in Chapter 2.

In Chapter 3 the selection of the $B^- \rightarrow D^0 h^-$ ($h = K, \pi$) candidates is discussed in details.

In Chapter 4 the fit technique used to extract the signal yields of $B^- \rightarrow D^0 K^-$ and $B^- \rightarrow D^0 \pi^-$ and the quantities $R_{CP\pm}$ and $A_{CP\pm}$ is presented. In the same Chapter the results are detailed, with the inclusion of the systematic uncertainties.

Chapter 1

Theoretical review

1.1 Why B physics?

The Standard Model (SM) of strong and electroweak interactions of quark and leptons [10] has so far been able to accommodate, in a simple and elegant way, the experimental data collected in the past years. It must be noted, however, that whereas the gauge sector of the electroweak interactions has been tested to a very high precision in the 1990s, the study of flavor-changing and CP -violating transitions has not reached the same level of accuracy.

In the Standard Model with three quark generations, flavor changing transitions and in particular CP violation (CPV) can in principle be accommodated with the well-known CKM mechanism [11], just requiring that CP is not imposed as a symmetry of the Lagrangian. Several stringent tests of the flavor and CP sector of the SM can be obtained from the measurement of B mesons decays, where a multitude of CP -odd effects are expected, with non negligible size and – in some cases – with very clean and accurate predictions by the theory.

In the last decade two experiments, *BABAR* [12] and *Belle* [13], have been built at the so-called “ B Factories” to extensively study B ($= B_{u,d}$) meson decays and make enough independent CP violation measurements to overconstrain the theory:¹ eventually either those measurements will be consistent with the Standard Model, where all CP violation effects in nature are described in terms of a single phase parameter, or – in the most exciting case – there will not be any set of CKM parameters consistent with all measurements, thus opening the way for a new physics theory beyond the SM.

1.2 CP violation in the Standard Model. The CKM matrix and the Unitarity Triangle

In quantum field theories CP violation is directly connected with the presence, in the Lagrangian, of one or more complex coupling constants whose phases cannot be removed by means of a suitable phase redefinition of the fields in the theory. [15]

In the Standard Model based on $SU(2)_L \times U(1)$ gauge symmetry, CP violation in weak processes arises from a single irremovable complex phase in the mixing matrix for quarks, which governs the charged W gauge boson interaction with the quarks: this is called the Cabibbo-Kobayashi-Maskawa (CKM) mechanism [11]. Such charged current

¹An extensive description of B physics and of the wide experimental program of the B -factories is contained in [14]

weak interaction can be written as:²

$$\mathcal{L}_W = -\frac{g}{\sqrt{2}} (\bar{u} \quad \bar{c} \quad \bar{t})_L \gamma^\mu V \begin{pmatrix} d \\ s \\ b \end{pmatrix}_L W_\mu^+ + \text{h.c.}, \quad (1.1)$$

where g is the $SU(2)_L$ coupling constant,³ W_μ is the W boson field operator, and $\{u, c, t\}_L$ and $\{d, s, b\}_L$ are the left-handed quark field flavor eigenstates, with charges $Q = 2/3$ and $Q = -1/3$ respectively. The matrix of the couplings, called *Cabibbo-Kobayashi-Maskawa* (CKM) *matrix*,

$$V = \begin{pmatrix} V_{ud} & V_{us} & V_{ub} \\ V_{cd} & V_{cs} & V_{cb} \\ V_{td} & V_{ts} & V_{tb} \end{pmatrix}, \quad (1.2)$$

is in principle a unitary, 3×3 matrix, thus depending on nine parameters, three real angles and six phases. The number of phases can be reduced to one by a redefinition of the phases of the quark fields.⁴ An explicit parameterization in terms of three mixing angles θ_{12} , θ_{13} , θ_{23} and a phase δ , with a particular quark fields phase convention, is the so-called ‘‘standard parameterization’’ [16]:

$$V = \begin{pmatrix} c_{12}c_{13} & s_{12}c_{13} & s_{13}e^{-i\delta} \\ -s_{12}c_{23} - c_{12}s_{23}s_{13}e^{i\delta} & c_{12}c_{23} - s_{12}s_{23}s_{13}e^{i\delta} & s_{23}c_{13} \\ s_{12}s_{23} - c_{12}c_{23}s_{13}e^{i\delta} & -c_{12}s_{23} - s_{12}c_{23}s_{13}e^{i\delta} & c_{23}c_{13} \end{pmatrix}, \quad (1.3)$$

where $c_{ij} \equiv \cos \theta_{ij}$ and $s_{ij} \equiv \sin \theta_{ij}$, $0 \leq \theta_{ij} \leq \pi/2$, and $0 \leq \delta \leq 2\pi$.

Experimentally one can gain information on the magnitudes of the CKM matrix elements from several tree-level constraints.⁵ When taking into account these measurements and the constraints from unitarity in a global fit, one can determine confidence intervals for the moduli of each of the nine CKM elements.⁶ The 1σ (68%) confidence limits from such a global fit are [7]:

$$|V_{ij}| = \begin{pmatrix} 0.97399^{+0.00046}_{-0.00046} & 0.2265^{+0.0020}_{-0.0020} & 0.00379^{+0.00025}_{-0.00023} \\ 0.2264^{+0.0020}_{-0.0020} & 0.97316^{+0.00046}_{-0.00047} & 0.0411^{+0.0013}_{-0.0006} \\ 0.00807^{+0.00045}_{-0.00035} & 0.0405^{+0.0013}_{-0.0006} & 0.999147^{+0.000024}_{-0.000057} \end{pmatrix} \quad (1.4)$$

and a well-defined hierarchy in the mixing angles appears:

$$\begin{cases} s_{12} = 0.2265^{+0.0020}_{-0.0020} \\ s_{23} = 0.0411^{+0.0013}_{-0.0006} \\ s_{13} = 0.00379^{+0.00025}_{-0.00023} \end{cases} \implies \theta_{13} \ll \theta_{23} \ll \theta_{12} \quad (1.5)$$

This corresponds to a hierarchy in the strengths of the charged-current quark-level processes, and is exploited in the so-called ‘‘Wolfenstein parameterization’’ of the CKM matrix [17]. This is an approximation of the standard parameterization in terms of four real

²Summation over quark colors is not explicitly indicated.

³ g is connected to the Fermi constant G_F and the mass M_W of the W boson through the relation $G_F = \frac{g^2}{8M_W^2}$.

⁴In the general case of N quark generations, the mixing matrix would consist of $(N-1)^2$ physical parameters, $N(N-1)/2$ angles and $(N-1)(N-2)/2$ complex phases. $N=3$ is therefore the minimum number of quark generations that is necessary in the Standard Model to accommodate CP violation.

⁵For a review see for instance chapter 11 (‘‘The Cabibbo-Kobayashi-Maskawa quark-mixing matrix’’) of [16].

⁶Different fitting methods exist in the literature which differ in the statistical methods used to deal with theoretical errors: the CKMfitter group [7] advocates a frequentist approach, while the UTfit collaboration [8] chooses a bayesian approach. However, the different fitting methods, if they use the same input parameters, give essentially the same result.

quantities, $(\lambda, A, \bar{\rho}, \bar{\eta})$, with $\lambda = \sin \theta_C = |V_{us}| = (0.2265 \pm 0.0020)$ playing the rôle of the expansion parameter. These parameters are related to those of (1.3) through:

$$s_{12} \equiv \lambda, \quad s_{23} \equiv A\lambda^2, \quad s_{13}e^{-i\delta} \equiv \frac{A\lambda^3}{1 - \lambda^2/2}(\bar{\rho} - i\bar{\eta}). \quad (1.6)$$

From these relations the Wolfenstein representation of V is easily derived:

$$V = \begin{pmatrix} 1 - \frac{\lambda^2}{2} + \mathcal{O}(\lambda^4) & \lambda + \mathcal{O}(\lambda^7) & A\lambda^3(1 + \frac{\lambda^2}{2})(\bar{\rho} - i\bar{\eta}) + \mathcal{O}(\lambda^7) \\ -\lambda + \mathcal{O}(\lambda^5) & 1 - \frac{\lambda^2}{2} + \mathcal{O}(\lambda^4) & A\lambda^2 + \mathcal{O}(\lambda^8) \\ A\lambda^3(1 - \bar{\rho} - i\bar{\eta}) + \mathcal{O}(\lambda^7) & -A\lambda^2[1 - \frac{\lambda^2}{2} + \lambda^2(\bar{\rho} + i\bar{\eta})] + \mathcal{O}(\lambda^6) & 1 + \mathcal{O}(\lambda^4) \end{pmatrix} \quad (1.7)$$

Since V is a 3×3 unitary matrix ($VV^\dagger = V^\dagger V = 1$), a set of 12 equations hold, 6 expressing the normalization conditions of the rows and columns, and 6 expressing the fact that the hermitian product of each pair of different columns or rows must vanish. Of particular relevance is the relation:

$$V_{ud}V_{ub}^* + V_{cd}V_{cb}^* + V_{td}V_{tb}^* = 0, \quad (1.8)$$

which can be rewritten – after dividing by $V_{cd}V_{cb}^*$ – in the following way, which is independent of the phase convention chosen for the quark fields:

$$\frac{V_{ud}V_{ub}^*}{V_{cd}V_{cb}^*} + 1 + \frac{V_{td}V_{tb}^*}{V_{cd}V_{cb}^*} = 0. \quad (1.9)$$

This relation requires that the sum of three complex quantities vanishes and can therefore be represented in the complex plane as a triangle, called “Unitarity Triangle”. Its sides are all of comparable magnitude, $\mathcal{O}(1)$.⁷ As shown in Figure 1.1, two vertices have coordinates $(0,0)$ e $(1,0)$ and the coordinates of the third vertex (apex) in terms of the Wolfenstein parameters are – if we neglect terms of order λ^4 – simply given by $(\bar{\rho}, \bar{\eta})$. The lengths of

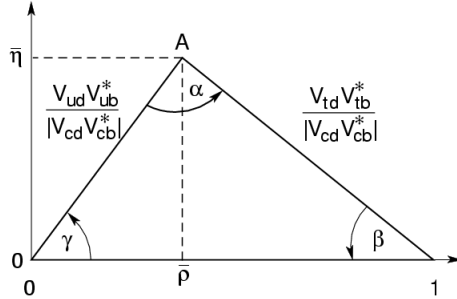


Figure 1.1: The (rescaled) Unitarity Triangle.

the two complex sides are

$$R_b \equiv \left| \frac{V_{ud}V_{ub}}{V_{cd}V_{cb}} \right| = \sqrt{\bar{\rho}^2 + \bar{\eta}^2} = \frac{1 - \lambda^2/2 + \mathcal{O}(\lambda^4)}{\lambda} \left| \frac{V_{ub}}{V_{cb}} \right|, \quad (1.10)$$

$$R_t \equiv \left| \frac{V_{td}V_{tb}}{V_{cd}V_{cb}} \right| = \sqrt{(1 - \bar{\rho})^2 + \bar{\eta}^2} = \frac{1 + \mathcal{O}(\lambda^4)}{\lambda} \left| \frac{V_{td}}{V_{cb}} \right|. \quad (1.11)$$

⁷There exist five other “unitarity triangles”, corresponding to the remaining unitarity relations between the columns or the rows of the CKM matrix. However, one is, to order λ^3 , identical to the Unitarity Triangle, while in the other four one side is a factor $\mathcal{O}(\lambda^2)$ or $\mathcal{O}(\lambda^4)$ shorter than the other two and therefore measurements related to these triangles are experimentally very challenging.

The three angles, denoted by α , β and γ , are

$$\alpha \equiv \arg \left[-\frac{V_{td}V_{tb}^*}{V_{ud}V_{ub}^*} \right], \quad \beta \equiv \arg \left[-\frac{V_{cd}V_{cb}^*}{V_{td}V_{tb}^*} \right], \quad \gamma \equiv \arg \left[-\frac{V_{ud}V_{ub}^*}{V_{cd}V_{cb}^*} \right] \quad (1.12)$$

The special relevance of the Unitarity Triangle is due to the fact that there are a certain number of $B_{u,d}$ meson decays which are expected to have rates and CP -violating effects that can be measured at the B factories experiments, and from which we can gain redundant information on the angles and sides of the triangle, thus allowing us to perform a stringent test of the CKM sector of the Standard Model. Information on the lengths of the sides comes from:

- the values of $|V_{ub}|$ and $|V_{cb}|$, measured in inclusive or exclusive semileptonic $B \rightarrow X_{u,c}l\nu_l$ decays ($l = e, \mu$), which constrain $R_b \equiv \sqrt{\bar{\rho}^2 + \bar{\eta}^2}$ ($R_b \propto |V_{ub}|/|V_{cb}|$). This corresponds in the $(\bar{\rho}, \bar{\eta})$ plane to a circle centered in $(0,0)$ with radius R_b .
- the value of ΔM_d , the mass difference of the two mass eigenstates of the neutral B_d meson system, measured in $B^0-\bar{B}^0$ oscillations, which constrain $R_t \equiv \sqrt{(1-\bar{\rho})^2 + \bar{\eta}^2}$. This corresponds in the $(\bar{\rho}, \bar{\eta})$ plane to a circle centered in $(1,0)$ with radius R_t .

Information on the angles α , β and γ can be obtained from the measurement of CP -violating B_u and B_d decays as described in Sections 1.5, 1.6 and 1.7. Additional constraints on the sides of the Unitarity Triangle are provided by non B -factory experiments, and consist of the measured value of the indirect CP violation parameter ε_K of the neutral Kaon system, and the quantity ΔM_s , analogous of ΔM_d for the neutral B_s system, measured by LEP and CDF in neutral B_s oscillations. The former constrains the quantity $\bar{\eta}[(1-\bar{\rho})+P]$, where P is a constant which depends on A , λ , and the ratios m_c/m_W and m_t/m_W between the masses of the charm and top quarks and that of the W boson. This constraint corresponds to a hyperbola in the $(\bar{\rho}, \bar{\eta})$ plane. The latter provides an additional constraint on R_t .

A few comments are in order:

- to relate the experimental observables to the CKM parameters, or equivalently to $\bar{\rho}$ and $\bar{\eta}$, one needs some theoretical input. Typically hadronic matrix elements of the weak interaction Hamiltonian, originally expressed in terms of quark fields, need to be evaluated, thus introducing a theoretical uncertainty.
- the experimental quantities themselves have a limited precision due to the finite statistics and the systematic uncertainties that affect the measurements. Therefore, the constraints have a finite precision, that improves in time as soon as updated measurements and more refined theoretical estimates are available.

In Figure 1.2 one can see the constraints, in the $(\bar{\rho}, \bar{\eta})$ plane, from the current measurements of $|V_{ub}|/|V_{cb}|$, ΔM_d and ΔM_s , ε , and the angles α , β and γ , together with the 3σ allowed region for the apex of the Unitarity Triangle obtained from a combined fit to these constraints [7]. With the present experimental and theoretical information the Standard Model is therefore consistent with data, and the following predictions (at 95% C.L.) can be made (in the context of the SM)[7]:

$$A = 0.801_{-0.035}^{+0.060} \quad (1.13)$$

$$\bar{\rho} = 0.204_{-0.093}^{+0.120} \quad (1.14)$$

$$\bar{\eta} = 0.340_{-0.055}^{+0.056} \quad (1.15)$$

$$\alpha = (93.1_{-18.5}^{+22.4})^\circ \quad (1.16)$$

$$\beta = (23.1_{-2.6}^{+3.1})^\circ \quad (1.17)$$

$$\gamma = (58.2_{-20.3}^{+15.6})^\circ \quad (1.18)$$

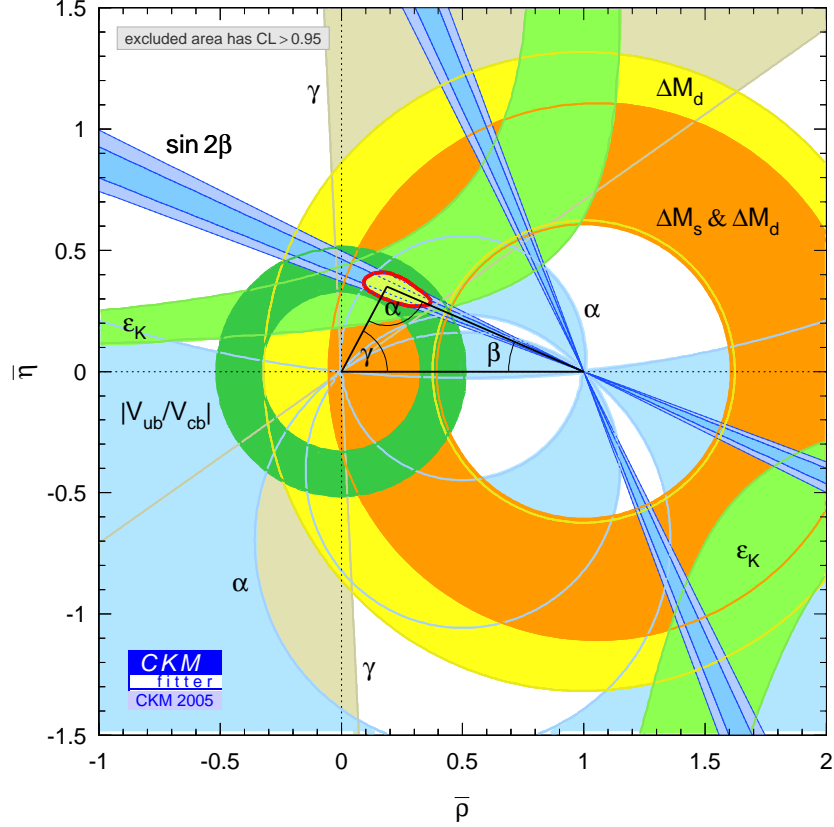


Figure 1.2: Constraints (at 68% and 95% C.L.) on the position of the apex of the Unitarity Triangle in the $(\bar{\rho}, \bar{\eta})$ plane from the measured values of $|V_{cb}|$, $|V_{ub}|$, ΔM_d , ΔM_s , ε_K , $\sin 2\beta$. The combined 3σ allowed contour is also shown.

1.3 The system of $B_{u,d}$ mesons

The light $B \equiv B_{u,d}$ mesons consist of four states with the following valence quark content:

$$B^+ = u\bar{b}, \quad B^0 = d\bar{b}, \quad (1.19)$$

$$B^- = \bar{u}b, \quad \bar{B}^0 = \bar{d}b \quad (1.20)$$

They are pseudoscalar 0^- mesons, with masses around $5279 \text{ MeV}/c^2$ ($m_{B^+} = 5279.0 \pm 0.5 \text{ MeV}/c^2$, $m_{B^0} = 5279.4 \pm 0.5 \text{ MeV}/c^2$) and mean lives of the order of 1.6 ps ($\tau_{B^+} = 1.671 \pm 0.018 \text{ ps}$, $\tau_{B^0} = 1.536 \pm 0.014 \text{ ps}$). B mesons are copiously produced in present B -factory experiments from decays of the vector resonance $\Upsilon(4S) = b\bar{b}$ produced in e^+e^- collisions: in fact, the $\Upsilon(4S)$, whose mass m and width Γ are $m = (10.5800 \pm 0.0035) \text{ GeV}/c^2$, $\Gamma = (20 \pm 4) \text{ MeV}$, is just above threshold for $B\bar{B}$ production and decays with the same probability $> 48\%$ into B^+B^- and $B^0\bar{B}^0$. The neutral B system, like the neutral K system, exhibits some peculiar features which we summarize here [14].

Due to the presence of flavor-non-conserving weak processes that can connect B^0 and \bar{B}^0 states, the effective Hamiltonian of the $B^0\bar{B}^0$ system⁸ is not diagonal in the $\{B^0, \bar{B}^0\}$ base:

$$H_{\text{eff}} = \begin{pmatrix} H_0 & H_{12} \\ H_{21} & H_0 \end{pmatrix} = M - \frac{i}{2}\Gamma = \begin{pmatrix} M_0 & M_{12} \\ M_{12}^* & M_0 \end{pmatrix} - \frac{i}{2} \begin{pmatrix} \Gamma_0 & \Gamma_{12} \\ \Gamma_{12}^* & \Gamma_0 \end{pmatrix} \quad (1.21)$$

⁸Here and throughout the text we assume CPT conservation, that implies $H_{11} = H_{22}$

Therefore the flavor eigenstates are not the same as the mass eigenstates and can undergo particle-antiparticle mixing. The mass and lifetime eigenstates are:

$$B_L = \frac{pB^0 + q\bar{B}^0}{\sqrt{|p|^2 + |q|^2}}, \quad B_H = \frac{pB^0 - q\bar{B}^0}{\sqrt{|p|^2 + |q|^2}}, \quad (1.22)$$

with p and q complex parameters. We denote their masses with $m_{L,H}$ and their widths $\Gamma_{L,H}$, where we assume B_L to be the lightest of the two. We have:

$$M_d \equiv (m_H + m_L)/2 = M_0, \quad \Gamma_d \equiv (\Gamma_H + \Gamma_L)/2 = \Gamma_0 \quad (1.23)$$

The evaluation of the Standard Model amplitudes for the $|\Delta B| = 2$ process $B^0 \leftrightarrow \bar{B}^0$, determined at quark level by box $(b\bar{d}) \leftrightarrow (\bar{b}d)$ diagrams, leads to [19]:

$$\Delta M_d \equiv \frac{m_H - m_L}{2} \approx 2|M_{12}| \quad (1.24)$$

$$\Delta\Gamma_d \equiv \frac{\Gamma_H - \Gamma_L}{2} \approx -2|\Gamma_{12}| \quad (1.25)$$

$$\left| \frac{\Gamma_{12}}{M_{12}} \right| = \mathcal{O}\left(\frac{m_b^2}{m_t^2}\right) \ll 1 \quad (1.26)$$

$$\frac{q}{p} \approx e^{-2i\beta} \quad (1.27)$$

where in the last line the same quark field phase convention adopted for the standard parameterization of the CKM matrix has been used, and we have also made the phase choice $CP(B^0) = \bar{B}^0$. We see that:

- $\Delta\Gamma_d < 0$, therefore the heaviest mass eigenstate has longer lifetime than that of the light state;
- $|\Delta\Gamma_d|/\Delta M_d = \mathcal{O}(10^{-2}) \ll 1$. Since $\Delta M_d/\Gamma_d$ has been measured to be (0.771 ± 0.012) , then $|\Delta\Gamma_d|/\Gamma_d = \mathcal{O}(10^{-2}) \ll 1$.
- $\frac{q}{p} \approx e^{-2i\beta}$ is almost a pure phase. The expected deviation of $|q/p|$ from 1 is $\left|\frac{q}{p}\right| - 1 \approx 5 \times 10^{-4}$ [19].

Since the B^0 and \bar{B}^0 are not the eigenstates of the hamiltonian (1.21), then a state which, at (proper) time $t = 0$, is a pure B^0 , evolves at time t into a state $B^0(t)$ which is a linear superposition of B^0 and \bar{B}^0 , and similarly a state which is a pure \bar{B}^0 at $t = 0$ evolves at time t into a mixed state $\bar{B}^0(t)$:

$$B^0(t) = g_+(t)B^0 + \frac{q}{p}g_-(t)\bar{B}^0 \quad (1.28)$$

$$\bar{B}^0(t) = g_+(t)\bar{B}^0 + \frac{p}{q}g_-(t)B^0 \quad (1.29)$$

where the functions $g_+(t)$ and $g_-(t)$, if we neglect $\Delta\Gamma_d/\Gamma_d$, are:

$$g_+(t) = e^{-iM_d t} e^{-\Gamma_d t/2} \cos\left(\frac{\Delta M_d t}{2}\right) \quad (1.30)$$

$$g_-(t) = e^{-iM_d t} e^{-\Gamma_d t/2} i \sin\left(\frac{\Delta M_d t}{2}\right) \quad (1.31)$$

A peculiarity of the B factories is that the $B^0\bar{B}^0$ pair originated from the $e^+e^- \rightarrow \Upsilon(4S) \rightarrow B^0\bar{B}^0$ process is produced in a coherent $L = 1$ state

$$S(t=0) = \frac{B^0\bar{B}^0 - \bar{B}^0B^0}{\sqrt{2}} \quad (1.32)$$

The time evolution of the two B mesons is then such that at any time, until one particle decays, there is exactly one B^0 and one \bar{B}^0 :

$$S(t) = e^{-2iM_{at}} e^{-\Gamma_{at}} \frac{B^0 \bar{B}^0 - \bar{B}^0 B^0}{\sqrt{2}} \quad (1.33)$$

As soon as one of the two B mesons decays to a final state that is accessible only to \bar{B}^0 or B^0 , for instance a semileptonic decay into $Xl\nu$ (for example, $D^*l\nu$),⁹ the other follows a time evolution given by Eqs. (1.28) or (1.29), where t is now the difference between its proper time and the decay instant of the former B .

1.4 CP violation in B decays

It is possible to distinguish – in a manner which does not depend on a specific theory – three ways in which CP violation can show up in B (as well as K) meson decays:

- CP violation in decay, also called *direct CP violation*;
- CP violation in mixing, also referred to as *indirect CP violation*;
- CP violation in the interference between decays with and without mixing, sometimes abbreviated to *CP violation in the interference between mixing and decay*.

1.4.1 CP violation in decay

CP violation in decay, or direct CPV, takes place when the amplitude $A_f = \langle f|H|B\rangle$ for a decay $B \rightarrow f$ and the amplitude $\bar{A}_{\bar{f}} = \langle \bar{f}|H|\bar{B}\rangle$ for its CP conjugate $\bar{B} \rightarrow \bar{f}$ have different magnitudes:

$$\left| \frac{\bar{A}_{\bar{f}}}{A_f} \right| \neq 1. \quad (1.34)$$

Indeed, if we write $\bar{B} = e^{i\phi_{CP}(B)} CP(B)$ and $\bar{f} = e^{i\phi_{CP}(f)} CP(f)$, then we have:

$$\langle \bar{f}|H|\bar{B}\rangle = e^{i(\phi_{CP}(B) - \phi_{CP}(f))} \langle f|(CP)H(CP)|B\rangle \quad (1.35)$$

and CP invariance implies that the Hamiltonian commutes with the CP operator, thus leading to $\langle \bar{f}|H|\bar{B}\rangle = e^{i(\phi_{CP}(B) - \phi_{CP}(f))} \langle f|H|B\rangle$.

For direct CP violation to take place in a process $B \rightarrow f$ an essential condition is that at least two interfering amplitudes, with different weak (CP violating) and strong (CP conserving) phases, contribute to it. In that case in fact:

$$A_f = \sum_i |A_i| e^{i(\delta_i + \phi_i)}, \quad (1.36)$$

where ϕ_i are the weak phases and δ_i are the strong ones. Thus:

$$\bar{A}_{\bar{f}} = e^{i(\phi_{CP}(B) - \phi_{CP}(f))} \sum_i |A_i| e^{i(\delta_i - \phi_i)} \quad (1.37)$$

and

$$|A_f|^2 - |\bar{A}_{\bar{f}}|^2 = -2 \sum_{i,j} |A_i| |A_j| \sin(\phi_i - \phi_j) \sin(\delta_i - \delta_j), \quad (1.38)$$

⁹In this case the charge of the lepton uniquely identifies the flavor of the B at the instant t_1 when it decayed (such a decay is called “flavor-tagging” as it allows to identify the flavor of the B). Suppose for instance that a $D^{*+}l^-\bar{\nu}$ final state is observed: in this eventuality the decaying B is a \bar{B}^0 . Due to the coherence of the $B^0\bar{B}^0$ pair, therefore, at the same instant t_1 the other B must have opposite flavor: it is a B^0 .

which is different from zero if at least two amplitudes A_i and A_j have $\phi_i \neq \phi_j$ as well as $\delta_i \neq \delta_j$, modulo π . In the simplest case of two amplitudes A_1 and A_2 , then $|A_f|^2 - |\bar{A}_{\bar{f}}|^2 = -4|A_1||A_2|\sin(\phi_1 - \phi_2)\sin(\delta_1 - \delta_2)$ and it is straightforward to compute the partial widths asymmetry:

$$\frac{|\bar{A}_{\bar{f}}|^2 - |A_f|^2}{|\bar{A}_{\bar{f}}|^2 + |A_f|^2} = \frac{2|A_1||A_2|\sin(\phi_1 - \phi_2)\sin(\delta_1 - \delta_2)}{|A_1|^2 + |A_2|^2 + 2|A_1||A_2|\cos(\phi_1 - \phi_2)\cos(\delta_1 - \delta_2)} \quad (1.39)$$

The asymmetry is larger the more the two interfering amplitudes A_1 , A_2 are comparable in magnitude.

Any rate asymmetry in charged B decays of the form:

$$A_{CP}^{\text{dir}} = \frac{\Gamma(B^- \rightarrow f) - \Gamma(B^+ \rightarrow \bar{f})}{\Gamma(B^- \rightarrow f) + \Gamma(B^+ \rightarrow \bar{f})} \neq 0, \quad (1.40)$$

would be a clear signature of direct CP violation, since:

$$A_{CP}^{\text{dir}} = \frac{|\bar{A}_{\bar{f}}/A_f|^2 - 1}{|\bar{A}_{\bar{f}}/A_f|^2 + 1} \quad (1.41)$$

At present, all rate asymmetries measured in several different charged B (and K) decays have been found consistent with zero.

In neutral B decays direct CPV can be searched in rate asymmetries of decays to final states f that are self-tagging, i.e. are only accessible to either B^0 or \bar{B}^0 but not to both.¹⁰ Following this method *BABAR* has observed, for the first time, direct CP violation in the B meson system, measuring the rate asymmetry for the $B^0 \rightarrow K^+\pi^-$ decay [22]:

$$\frac{\Gamma(\bar{B}^0 \rightarrow K^-\pi^+) - \Gamma(B^0 \rightarrow K^+\pi^-)}{\Gamma(\bar{B}^0 \rightarrow K^-\pi^+) + \Gamma(B^0 \rightarrow K^+\pi^-)} = -0.133 \pm 0.030(\text{stat}) \pm 0.009(\text{syst}) \quad (1.42)$$

Another way to measure direct CPV in neutral B decays, as discussed in Section 1.4.3, is from the time-dependent rates of the processes $B^0(t) \rightarrow f$, $B^0(t) \rightarrow \bar{f}$, $\bar{B}^0(t) \rightarrow f$ and $\bar{B}^0(t) \rightarrow \bar{f}$, where f and \bar{f} are final states accessible both to B^0 and \bar{B}^0 (typically, $f = \pm \bar{f}$ is a CP eigenstate) and for which the amplitudes $A(B^0 \rightarrow f)$ and $A(\bar{B}^0 \rightarrow f)$ have comparable magnitudes.

1.4.2 CP violation in mixing

CP violation in mixing can only take place in the neutral system and occurs when the mass eigenstates $B_{L,H}$ are not CP eigenstates. This is equivalent to require that q/p is not a pure phase:

$$\left| \frac{q}{p} \right| \neq 1. \quad (1.43)$$

Since the SM predicts $|q/p| - 1 \approx 5 \times 10^{-4}$, CP violation effects in neutral B mixing are expected to be very small. A clear indication of CP violation in B^0 - \bar{B}^0 mixing would be a non-zero time-dependent asymmetry, for instance in semileptonic decays, of the form:

$$A_{\text{sl}}(t) = \frac{\Gamma(\bar{B}^0(t) \rightarrow \ell^+\nu X) - \Gamma(B^0(t) \rightarrow \ell^-\nu X)}{\Gamma(\bar{B}^0(t) \rightarrow \ell^+\nu X) + \Gamma(B^0(t) \rightarrow \ell^-\nu X)} = \frac{1 - |q/p|^4}{1 + |q/p|^4}. \quad (1.44)$$

However, this asymmetry is expected to be of the order of 10^{-3} and therefore tiny: if $(|q/p| - 1) \equiv h \approx 5 \times 10^{-4}$, then

$$\frac{1 - |q/p|^4}{1 + |q/p|^4} \approx \frac{1 - (1 + 4h)}{2} = -2h \approx -10^{-3} \quad (1.45)$$

¹⁰The observed asymmetries must be significantly greater than $\approx 10^{-3}$, otherwise they could arise purely from CP violation in mixing.

The current experimental constraints from the B -factories are below the 10^{-2} level:

$$|q/p| = 0.998 \pm 0.006(\text{stat}) \pm 0.007(\text{syst}) \text{ (BABAR [23])} \quad (1.46)$$

$$|q/p| = 1.0006 \pm 0.0030(\text{stat}) \pm 0.0028(\text{syst}) \text{ (Belle [24])} \quad (1.47)$$

The world average, from measurements at LEP, CLEO, BABAR and Belle, is

$$|q/p| = 1.0013 \pm 0.0034 \text{ [18]} \quad (1.48)$$

1.4.3 CP violation in the interference between decay and mixing

CP violation in the interference between decay and mixing can arise in decays of neutral B mesons to final states f and \bar{f} which are accessible to both B^0 and \bar{B}^0 , due to the interference between the “unmixed” $B^0 \rightarrow f$ and the “two-step” $B^0 \rightarrow \bar{B}^0 \rightarrow f$ processes. It shows up as a difference between the time-dependent probabilities $P(B^0(t) \rightarrow f)$ and $P(\bar{B}^0(t) \rightarrow \bar{f})$.

At the B -factories this can be studied by exploiting the coherence of the $B^0\bar{B}^0$ system: a neutral B , which we denote by B_{reco} , is reconstructed in the f or \bar{f} final state of interest (let us denote with t_{reco} the proper time of the B_{reco} when it decays), while the other neutral B (which we call B_{tag}) is reconstructed (typically only partially) in a final state f_{tag} which unambiguously identifies the flavor of B_{tag} at the instant t_{tag} of its decay. Due to $B^0\bar{B}^0$ coherence, the flavor of the B_{reco} at time t_{tag} is therefore also identified, it is opposite to the B_{tag} flavor: if $B_{\text{tag}} = \bar{B}^0$ then $B_{\text{reco}}(t_{\text{tag}}) = B^0$ and the time-dependent rate $N_f(t \equiv t_{\text{rec}} - t_{\text{tag}}) \equiv N(B_{\text{reco}}(t) \rightarrow f, B_{\text{tag}} = \bar{B}^0)$ is proportional to the probability $P(B^0(t) \rightarrow f)$. If, on the other hand, $B_{\text{tag}} = B^0$ then $B_{\text{reco}}(t_{\text{tag}}) = \bar{B}^0$ and the time-dependent rate $N_{\bar{f}}(t \equiv N(B_{\text{reco}}(t) \rightarrow \bar{f}, B_{\text{tag}} = B^0)$ is proportional to the probability $P(\bar{B}^0(t) \rightarrow \bar{f})$.

The simplest case is when f is a CP eigenstate, $\bar{f} = CP f = \pm f \equiv \eta_f^{CP} f$. In this case, let us define the quantity:

$$\lambda_f \equiv \frac{q}{p} \frac{\bar{A}_f}{A_f} = \eta_f^{CP} \frac{q}{p} \frac{\bar{A}_f}{A_f} \quad (1.49)$$

where $A_f \equiv A(B^0 \rightarrow f)$ and $\bar{A}_f \equiv A(\bar{B}^0 \rightarrow f)$ are the amplitudes for the decays of B^0 and \bar{B}^0 into the final state f . The time-dependent CP asymmetry, defined as:

$$A_{CP}^f(t) \equiv \frac{\Gamma(\bar{B}^0(t) \rightarrow f) - \Gamma(B^0(t) \rightarrow f)}{\Gamma(\bar{B}^0(t) \rightarrow f) + \Gamma(B^0(t) \rightarrow f)} \quad (1.50)$$

is given by:

$$A_{CP}^f(t) = -C_f \cos(\Delta M_d t) + S_f \sin(\Delta M_d t) \quad (1.51)$$

with

$$C_f \equiv \frac{1 - |\lambda_f|^2}{1 + |\lambda_f|^2} \approx \frac{|A_f|^2 - |\bar{A}_f|^2}{|A_f|^2 + |\bar{A}_f|^2} \quad (1.52)$$

and

$$S_f \equiv \frac{2\text{Im}\lambda_f}{|\lambda_f|^2 + 1} \quad (1.53)$$

The observable C_f measures (neglecting CPV in mixing, i.e. assuming $|q/p| = 1$), direct CP violation in the decay $B^0 \rightarrow f$. However, also in the case when CP is not violated in decay or in mixing, the time-dependent CP asymmetry can still be different from zero due to the presence of the $S_f \sin(\Delta M_d t)$ term: this term gives the so-called CP violation in interference between decay with and without mixing, also known as “mixing-induced CP violation”. The (phase-convention independent) condition for CPV to occur in interference is:

$$\text{Im}\lambda_f \neq 0 \quad (1.54)$$

1.5 Measurement of the angle β

The angle β of the Unitarity Triangle can be accurately measured from the time-dependent CP asymmetry (1.50) in the “golden modes” $f = (c\bar{c})K^0$, such as $J/\psi K_S^0$, $\psi(2S)K_S^0$, $\chi_{c1}K_S^0$, $\eta_c K_S^0$ (CP -odd) and $J/\psi K_L^0$ (CP -even). These decays, as shown in Figure 1.3,

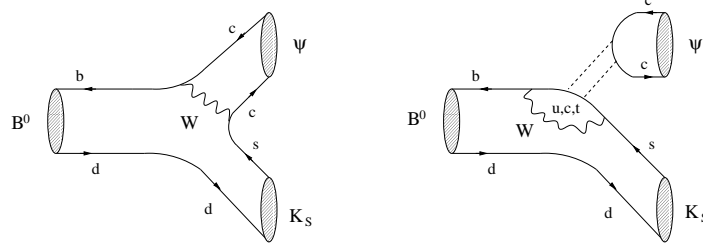


Figure 1.3: Feynman diagrams contributing to the $B^0 \rightarrow J/\psi K_S$ decay amplitude. The dashed lines in the penguin topology (on the right) represent a colour-singlet exchange.

originate from $\bar{b} \rightarrow \bar{c}c\bar{s}$ quark-level decays and receive contribution from tree and penguin topologies. The total $B^0 \rightarrow (c\bar{c})K^0$ amplitude is therefore

$$A_f = TV_{cb}^*V_{cs} + P_u V_{ub}^*V_{us} + P_c V_{cb}^*V_{cs} + P_t V_{tb}^*V_{ts} \quad (1.55)$$

where we have explicitly written the CKM elements relevant to the tree (T) and the u, c, t -mediated penguin ($P_{u,c,t}$) amplitudes. Taking into account the relation $V_{tb}^*V_{ts} = -V_{cb}^*V_{cs} - V_{ub}^*V_{us}$ which follows from the unitarity of the CKM matrix, grouping together terms with the same weak phase, and using the definition of γ in (1.12), the amplitude becomes:

$$A_f = (T + P_c - P_t)V_{cb}^*V_{cs} \left[1 + \frac{P_u - P_t}{T + P_c - P_t} \frac{V_{ub}^*V_{us}}{V_{cb}^*V_{cs}} \right] \quad (1.56)$$

$$\approx (T + P_c - P_t)V_{cb}^*V_{cs} [1 + \lambda^2 a e^{i\delta} e^{i\gamma}] \quad (1.57)$$

where

$$a e^{i\delta} \equiv R_b \frac{P_u - P_t}{T + P_c - P_t} \quad (1.58)$$

is a hadronic parameter which measures the relative strength of the penguin and tree contributions. The \bar{B}^0 amplitude is:

$$\bar{A}_f = \eta_f^{CP} \bar{A}_{\bar{f}} \approx \eta_f^{CP} (T + P_c - P_t) V_{cb} V_{cs}^* [1 + \lambda^2 a e^{i\delta} e^{-i\gamma}] \quad (1.59)$$

and the parameter λ_f defined in (1.49) is:

$$\lambda_f \approx \eta_f^{CP} e^{-2i\beta} \frac{1 + \lambda^2 a e^{i\delta} e^{i\gamma}}{1 + \lambda^2 a e^{i\delta} e^{-i\gamma}} \quad (1.60)$$

The quantity $a e^{i\delta}$ can only be estimated with large hadronic uncertainties; however, it enters the amplitude in a doubly Cabibbo-suppressed way, $\lambda^2 = 0.0513 \pm 0.0005$, therefore its impact on the CP -violating observables is negligible. Hence,

$$\lambda_f \simeq \eta_f^{CP} e^{-2i\beta} \quad (1.61)$$

$$A_{CP}^f(t) \simeq -\eta_f^{CP} \sin(2\beta) \sin(\Delta M_d t) \quad (1.62)$$

and β can be cleanly extracted, up to a four-fold ambiguity ($\beta \leftrightarrow \pi/2 - \beta$, $\beta \leftrightarrow \beta + \pi$), from the coefficient of the $\sin(\Delta M_d t)$ term in the time-dependent CP asymmetry.

With this method *BABAR* and *Belle* find:

$$\sin 2\beta = 0.722 \pm 0.040(\text{stat}) \pm 0.023(\text{syst}) \quad (\text{BABAR [20]}) \quad (1.63)$$

$$\sin 2\beta = 0.728 \pm 0.056(\text{stat}) \pm 0.023(\text{syst}) \quad (\text{Belle [21]}) \quad (1.64)$$

and the world average is:

$$\sin 2\beta = 0.726 \pm 0.037 \quad [18] \quad (1.65)$$

One of the four solutions for β , $\beta \approx 23^\circ$, is in excellent agreement with the value predicted from the CKM fits to the Unitarity Triangle constraints, unlike the other three. The two solutions with $\cos 2\beta < 0$ are excluded by *BABAR* at 86% C.L. from the study of the time- and angular-dependent distribution of neutral B decays to the mixed- CP $J/\psi K^{*0}(K^{*0} \rightarrow K_S^0 \pi^0)$ final state [25]. Therefore, at 86% C.L., the two allowed solutions for β are $\beta \approx 23^\circ$ and $\beta \approx 203^\circ$.

1.6 Measurement of the angle α

The angle α can be measured from the study of charmless B decays such as $\pi\pi$, $\rho\pi$ and $\rho\rho$. At present the decays $B \rightarrow \rho\rho$ provide the most accurate information on α .

Originally it was believed that α could be extracted, in a straightforward way analogous to that used for β , from the time-dependent evolution of neutral B decays to the CP -even eigenstate $f = \pi^+\pi^-$. These decays, as shown in Figure 1.4, originate from $\bar{b} \rightarrow \bar{u}u\bar{d}$ quark-level decays and receive contributions from tree (T) and penguin (P) amplitudes. The total amplitudes for the $B^0 \rightarrow \pi^+\pi^-$ and $\bar{B}^0 \rightarrow \pi^+\pi^-$ processes are

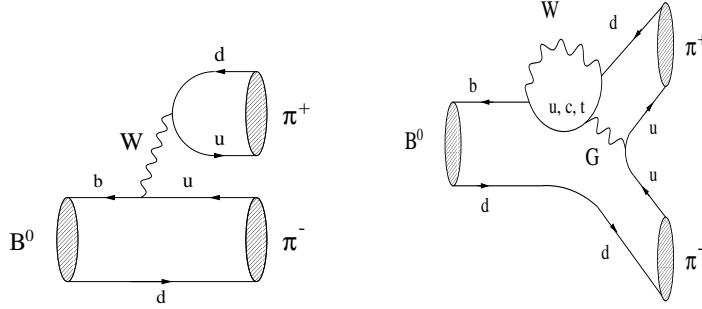


Figure 1.4: Feynman diagrams contributing to $B^0 \rightarrow \pi^+\pi^-$.

respectively, taking into account the unitarity of the CKM matrix and the Wolfenstein parameterization,

$$A_{\pi^+\pi^-} \approx (T + P_u - P_t)V_{ub}^*V_{ud} [1 - ae^{i\delta}e^{-i\gamma}] \quad (1.66)$$

$$\bar{A}_{\pi^+\pi^-} \approx (T + P_u - P_t)V_{ub}V_{ud}^* [1 - ae^{i\delta}e^{i\gamma}] \quad (1.67)$$

where the hadronic parameter measuring the relative strength of the penguin and tree contributions is now

$$ae^{i\delta} \equiv \frac{1}{R_b} \frac{P_c - P_t}{T + P_u - P_t}. \quad (1.68)$$

The parameter λ_f , taking into account that $\eta_{\pi^+\pi^-}^{CP} = 1$, is therefore

$$\lambda_{\pi^+\pi^-} \approx e^{-2i\beta} e^{-2i\gamma} \frac{1 - ae^{i\delta}e^{i\gamma}}{1 - ae^{i\delta}e^{-i\gamma}} = e^{2i\alpha} \frac{1 - ae^{i\delta}e^{i\gamma}}{1 - ae^{i\delta}e^{-i\gamma}} \quad (1.69)$$

where in the last equality we have used $\alpha = \pi - \beta - \gamma$. At the beginning of the B -factories era, penguin amplitudes were expected to play a minor role in this decay, therefore $a \ll 1$ and $\lambda_{\pi^+\pi^-} \approx e^{2i\alpha}$, which would imply that $\sin 2\alpha$ could be determined from the time-dependent CP asymmetry $A_{CP}^{\pi^+\pi^-}(t) \approx \sin(2\alpha) \sin(\Delta M_d t)$.

However, branching fraction measurements of B decays to $\pi\pi$ and $K\pi$ final states indicate that the penguin contribution is not negligible in the $\pi^+\pi^-$ channel. The time-dependent CP asymmetry is therefore:

$$A_{CP}^{\pi^+\pi^-}(t) = -C_{\pi^+\pi^-} \cos(\Delta M_d t) + S_{\pi^+\pi^-} \sin(\Delta M_d t) \quad (1.70)$$

where:

$$C_{\pi^+\pi^-} \equiv \frac{1 - |\lambda_{\pi^+\pi^-}|^2}{1 + |\lambda_{\pi^+\pi^-}|^2} = -\frac{2a \sin \delta \sin \gamma}{1 - 2a \cos \delta \cos \gamma + a^2} \quad (1.71)$$

$$S_{\pi^+\pi^-} \equiv \frac{2\text{Im}\lambda_{\pi^+\pi^-}}{|\lambda_{\pi^+\pi^-}|^2 + 1} = \frac{\sin 2\alpha - 2a \cos \delta \sin(2\alpha + \gamma) + a^2 \sin(2\alpha + 2\gamma)}{1 - 2a \cos \delta \cos \gamma + a^2} \quad (1.72)$$

$$= \sqrt{1 - C_{\pi^+\pi^-}^2} \sin \alpha_{\text{eff}}^{\pi\pi}. \quad (1.73)$$

Here, $\alpha_{\text{eff}}^{\pi\pi}$ is defined by

$$\sin 2\alpha_{\text{eff}}^{\pi\pi} \equiv \frac{\text{Im}\lambda_{\pi^+\pi^-}}{|\lambda_{\pi^+\pi^-}|} \quad (1.74)$$

and is the experimental quantity that can be measured, up to a four-fold ambiguity ($\alpha_{\text{eff}} \leftrightarrow \pi/2 - \alpha_{\text{eff}}$, $\alpha_{\text{eff}} \leftrightarrow \alpha_{\text{eff}} + \pi$), from the $\sin \Delta M_d t$ term of the time-dependent CP asymmetry. To extract α from α_{eff} one needs to know a and δ , whose theoretical estimates are affected by hadronic uncertainties. A way out – neglecting electroweak penguins, which are expected to be at most at the few percent level in this channel – would be an isospin analysis of the six amplitudes [26]:

$$A_{+-} \equiv A(B^0 \rightarrow \pi^+\pi^-) \quad \bar{A}_{+-} \equiv A(\bar{B}^0 \rightarrow \pi^+\pi^-) \quad (1.75)$$

$$A_{+0} \equiv A(B^+ \rightarrow \pi^+\pi^0) \quad \bar{A}_{-0} \equiv A(B^- \rightarrow \pi^-\pi^0) \quad (1.76)$$

$$A_{00} \equiv A(B^0 \rightarrow \pi^0\pi^0) \quad \bar{A}_{00} \equiv A(\bar{B}^0 \rightarrow \pi^0\pi^0) \quad (1.77)$$

which would allow, through the isospin triangular relations

$$(1/\sqrt{2})A_{+-} + A_{00} = A_{+0}, \quad (1.78)$$

$$(1/\sqrt{2})\bar{A}_{+-} + \bar{A}_{00} = \bar{A}_{-0}, \quad (1.79)$$

to eliminate a and δ and to extract α . Unfortunately, for this method to be applied one needs to separately measure the amplitudes $A(B^0 \rightarrow \pi^0\pi^0)$ and $A(\bar{B}^0 \rightarrow \pi^0\pi^0)$, and the following experimental difficulties are met:

- the branching fraction $\mathcal{B}(\pi^0\pi^0)$ (measured for the first time by the *BABAR* experiment [27]) is quite small:

$$\frac{\mathcal{B}(B^0 \rightarrow \pi^0\pi^0) + \mathcal{B}(\bar{B}^0 \rightarrow \pi^0\pi^0)}{2} = (1.51 \pm 0.28) \times 10^{-6}$$

and, due to the presence of two neutral pions in the final state, the background level is rather high and the reconstruction efficiency is correspondingly low, about 15-20%. This implies that, in a dataset of ≈ 250 million $B\bar{B}$ pairs produced in four years of running of a B factory, only ≈ 65 $\pi^0\pi^0$ events are reconstructed

- to separate A_{00} and \bar{A}_{00} a time-dependent analysis must be performed, therefore the number of reconstructed $\pi^0\pi^0$ decays must be significantly larger.

Grossman and Quinn have shown [28] that even without performing the full isospin analysis, some information on α can be obtained by using the following bound on $|\alpha - \alpha_{\text{eff}}^{\pi\pi}|$:

$$\sin^2(\alpha - \alpha_{\text{eff}}^{\pi\pi}) \leq \frac{\mathcal{B}(B^0 \rightarrow \pi^0\pi^0) + \mathcal{B}(\bar{B}^0 \rightarrow \pi^0\pi^0)}{\mathcal{B}(B^+ \rightarrow \pi^+\pi^0) + \mathcal{B}(B^- \rightarrow \pi^-\pi^0)} \quad (1.80)$$

Unfortunately, the branching fraction for the $\pi^0\pi^0$ decay is too small to perform the full isospin analysis with the present B factories data, but at the same time is not small enough to give a stringent bound on $|\alpha - \alpha_{\text{eff}}^{\pi\pi}|$. The current limit is in fact quite weak, $|\alpha - \alpha_{\text{eff}}^{\pi^+\pi^-}| < 30^\circ$ at 68% C.L. (35° at 90% C.L.)

The situation is better when one considers, instead of $\pi^+\pi^-$, the $\rho^+\rho^-$ final state. In principle, since the ρ meson is a vector particle, the final state is not a CP eigenstate, due to presence of both CP -even ($L=0,2$) and CP -odd ($L=1$) final states. However, it turns out experimentally that the two ρ mesons produced in $B^0 \rightarrow \rho^+\rho^-$ decays are almost 100% longitudinally polarized and therefore the final state is purely CP -even. A time-dependent analysis of the decays into $\rho^+\rho^-$ therefore allows, in analogy to the $\pi^+\pi^-$ case, to extract the quantities $C_{\rho^+\rho^-}$ and $S_{\rho^+\rho^-}$ and the angle $\alpha_{\text{eff}}^{\rho^+\rho^-}$. The difference with the $\pi^+\pi^-$ case is that the bound on $|\alpha - \alpha_{\text{eff}}|$ in the $\rho\rho$ channel is significantly tighter, since:

$$\begin{aligned} \frac{\mathcal{B}(B^0 \rightarrow \rho^0\rho^0) + \mathcal{B}(\bar{B}^0 \rightarrow \rho^0\rho^0)}{2} &< 1.1 \times 10^{-6} \text{ (90\% C.L.)} \\ \frac{\mathcal{B}(B^+ \rightarrow \rho^+\rho^0) + \mathcal{B}(B^- \rightarrow \rho^-\rho^0)}{2} &= (26.4_{-6.4}^{+6.1}) \times 10^{-6} \\ f_L^{+0} &= (0.97 \pm 0.07 \pm 0.04) \end{aligned}$$

imply

$$\sin^2(\alpha - \alpha_{\text{eff}}^{\rho\rho}) \leq \frac{f_L^{00} \times \frac{\mathcal{B}(B^0 \rightarrow \rho^0\rho^0) + \mathcal{B}(\bar{B}^0 \rightarrow \rho^0\rho^0)}{2}}{f_L^{+0} \times \frac{\mathcal{B}(B^+ \rightarrow \rho^+\rho^0) + \mathcal{B}(B^- \rightarrow \rho^-\rho^0)}{2}}$$

from which

$$|\alpha - \alpha_{\text{eff}}^{\rho\rho}| \leq 11^\circ \text{ (68\% C.L.)} \quad (1.81)$$

Here, f_L^{+0} is the measured ρ polarization in $B^+ \rightarrow \rho^+\rho^0$ decays and the most conservative limit on $|\alpha - \alpha_{\text{eff}}^{\rho\rho}|$ has been obtained by assuming $f_L^{00} = 1$. With this bound and the measured value of $\alpha_{\text{eff}}^{\rho\rho}$ from the time-dependent analysis of $B \rightarrow \rho^+\rho^-$ decays, one of the four solutions for α is

$$\alpha = (96 \pm 10(\text{stat}) \pm 4(\text{syst}) \pm 11(\text{peng}))^\circ$$

where the last error comes from the limit on $|\alpha - \alpha_{\text{eff}}^{\rho\rho}|$. Like β , α is determined up to a four-fold ambiguity ($\alpha \leftrightarrow \pi/2 - \alpha$, $\alpha \leftrightarrow \alpha + \pi$). Combining this result with those from $B^0 \rightarrow \pi^+\pi^-$ and $B^0 \rightarrow \rho\pi$ decays allows to break the two-fold ambiguity $\alpha \leftrightarrow \pi/2 - \alpha$ and improves the sensitivity to α : the combined constraint [18] is

$$\alpha \bmod 180^\circ = (101_{-9}^{+16})^\circ \quad (1.82)$$

The solution $\alpha \approx 101^\circ$ is in good agreement with the value predicted from the CKM fits to the Unitarity Triangle constraints.

1.7 Measurement of the angle γ

The angle γ is considered to be the most difficult to measure of the three angles of the Unitarity Triangle, since

- the branching fractions and the reconstruction efficiencies of the B decays that are useful to extract γ are typically lower than in the charmonium or charmless B decays used to measure β and α
- in the modes with higher branching fractions, the two amplitudes that give rise to the interference term which provides sensitivity to γ usually have quite different magnitudes. Hence, the interference term is small and the sensitivity to γ is reduced.

Several methods have been proposed in the past for the measurement of γ ; the strategy pursued at the B factories is to reconstruct as many as possible γ -related observables and to combine the information from all of them, to improve the overall accuracy. In this Section we summarize the various methods that have been proposed so far for measuring γ , and describe in some detail the ones that look more promising for the extraction of γ at the present B factory experiments.

In general, we can classify these methods in two classes:

- model-independent techniques, which extract γ from B decays that proceed through tree diagrams only and for which exact relations¹¹ involving γ can be found between the measured branching fractions and CP asymmetries of some related channels. Since no penguin amplitudes are involved, these approaches are unaffected by a large class of possible new-physics effects that, presumably, can be expected to show up in this kind of decay mechanism.
- model-dependent methods, where some theoretical assumptions are made for the extraction of γ . Typically the observables that are needed as input for these approaches are easier to measure than those relevant to the model-independent methods, however the final derivation of γ is affected by a significant model-dependent theoretical uncertainty, which sometimes can also be quite difficult to assess.

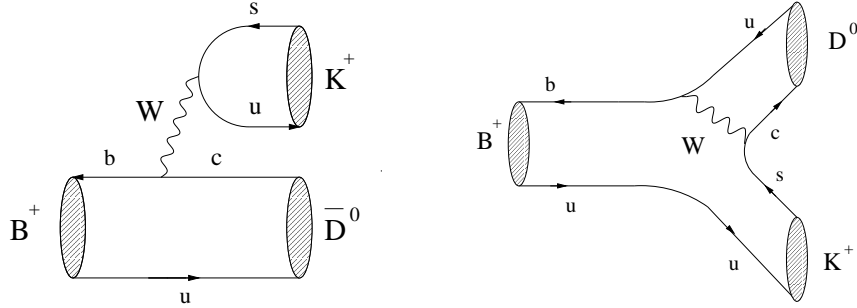


Figure 1.5: Feynman diagrams contributing to $B^+ \rightarrow \bar{D}^0 K^+$ and $B^+ \rightarrow D^0 K^+$.

The model-independent techniques extract γ by exploiting the interference between the tree processes $b \rightarrow c\bar{u}q$ ($q = s, d$), whose amplitude is proportional to $V_{cb}V_{uq}^*$, and $b \rightarrow u\bar{c}q$, whose amplitude is proportional to $V_{ub}V_{cq}^*$. An example of such processes is shown in Figure 1.5. γ is the relative weak phase between the two diagrams, and in principle can be probed by measuring CP -violating effects in B decays where the two amplitudes interfere. In the case $q = s$, this can happen either in

- charged $B^- \rightarrow D^{(*)0} K^{(*)-}$ and $B^- \rightarrow \bar{D}^{(*)0} K^{(*)-}$ decays, where the $D^{*0}(\bar{D}^{*0})$ eventually undergoes $D^{*0} \rightarrow D^0\pi^0$ ($\bar{D}^{*0} \rightarrow \bar{D}^0\pi^0$) or $D^{*0} \rightarrow D^0\gamma$ ($\bar{D}^{*0} \rightarrow \bar{D}^0\gamma$) and

¹¹Actually in methods based on charged $B \rightarrow D^{(*)0}K$ decays the approximation of neglecting $D^0-\bar{D}^0$ mixing and CP -violation in D^0 decays is used. However, the induced bias in the measurement of γ is expected to be of the order of 1° in the so-called ‘‘ADS’’ method of Subsection 1.7.2 and of the order of 0.1° in the other approaches described in the text. [29]

the D^0 and \bar{D}^0 mesons are reconstructed through a decay in a common final state. This can be either:

1. a singly Cabibbo-suppressed CP eigenstate, like $D^0 \rightarrow K^+K^-$ (Gronau-London-Wyler method [30, 31])
 2. a doubly Cabibbo-suppressed flavor eigenstate, like $D^0 \rightarrow K^+\pi^-$ (Atwood-Dunietz-Soni method [32])
 3. a Cabibbo-allowed self-conjugate multi-body state, like $D^0 \rightarrow K_s^0\pi^+\pi^-$ (Giri-Grossman-Soffer-Zupan method [33])
- neutral B to $D^{(*)0}K_s^0$ and $\bar{D}^{(*)0}K_s^0$ decays [34], where interference between the $B^0 \rightarrow D^{(*)0}K_s^0$ and $\bar{B}^0 \rightarrow D^{(*)0}K_s^0$ amplitudes (and similarly for the $\bar{D}^{(*)0}K_s^0$ case) arises via $B^0-\bar{B}^0$ mixing. In this case time-dependent CP asymmetries must be measured, which allow to extract the sum $2\beta + \gamma$, where 2β is carried in by the mixing parameter $q/p = e^{-2i\beta}$.

Variations of these methods consider color-allowed 3-body B decays to $DK\pi$ final states [35]. In the case $q = d$, one can either look at charged $B^- \rightarrow D^{(*)0}\pi^-$ decays with the same $D^{(*)0}$ final states as before, or neutral B decays to $D^{(*)\pm}\pi^\mp$ [36]. More complex techniques involve final states with vector mesons (ρ, a_1) replacing the pions [36, 37]. With respect to the $q = s$ case, the advantage is that the branching fractions are at least an order of magnitude higher, but the interfering amplitudes $b \rightarrow c\bar{u}d \propto V_{cb}V_{ud}^* \approx A\lambda^2$ and $b \rightarrow u\bar{c}d \propto V_{ub}V_{cd}^* \approx R_b A\lambda^4 e^{-i\gamma}$ have magnitudes which differ by a factor $\approx \mathcal{O}(R_b\lambda^2) \approx 0.02$ and therefore the interference, and therefore the sensitivity to γ , is small.

The most promising model-independent methods, at the moment, seem to be those based on charged $B \rightarrow D^0K$ or neutral $B \rightarrow D^{(*)\pm}\pi^\mp$ decays, which will be described in the following sections.

1.7.1 The Gronau-London-Wyler method

The Gronau-London-Wyler (GLW) method [30, 31] is based on the reconstruction of charged B decays to D^0K where the D^0 and \bar{D}^0 decay to CP -even (like K^+K^-) and CP -odd (like $K_s^0\pi^0$) eigenstates $f_{CP\pm}$. The CKM angle γ can be extracted from the measurement of the four quantities (see Introduction and Appendix A):

$$\begin{aligned} R_{CP\pm} &\equiv \frac{\mathcal{B}(B \rightarrow D_{CP}^0 K)}{\mathcal{B}(B \rightarrow D^0 K)} \\ &\equiv \frac{\mathcal{B}(B^- \rightarrow D_{CP\pm}^0 K^-) + \mathcal{B}(B^+ \rightarrow D_{CP\pm}^0 K^+)}{\mathcal{B}(B^- \rightarrow D^0 K^-) + \mathcal{B}(B^+ \rightarrow \bar{D}^0 K^+)} \end{aligned} \quad (1.83)$$

$$= 1 + r_B^2 \pm 2r_B \cos \gamma \cos \delta_B \quad (1.84)$$

$$A_{CP\pm} \equiv \frac{\mathcal{B}(B^- \rightarrow D_{CP\pm}^0 K^-) - \mathcal{B}(B^+ \rightarrow D_{CP\pm}^0 K^+)}{\mathcal{B}(B^- \rightarrow D_{CP\pm}^0 K^-) + \mathcal{B}(B^+ \rightarrow D_{CP\pm}^0 K^+)} \quad (1.85)$$

$$= \pm 2r_B \sin \gamma \sin \delta_B / R_{CP\pm} \quad (1.86)$$

where r_B is the magnitude of the ratio of the color suppressed $B^- \rightarrow \bar{D}^0 K^-$ amplitude and the color allowed $B^- \rightarrow D^0 K^-$ amplitude and δ_B is their relative strong phase:

$$r_B e^{i\delta_B} e^{-i\gamma} \equiv \frac{A(B^- \rightarrow \bar{D}^0 K^-)}{A(B^- \rightarrow D^0 K^-)} \quad (1.87)$$

The value of γ obtained with this method is known up to 8 discrete ambiguities, due to the impossibility to distinguish the solutions

$$(\gamma, \delta_B) \leftrightarrow (-\gamma, -\delta_B) \quad (1.88)$$

$$(\gamma, \delta_B) \leftrightarrow (\gamma + \pi, \delta_B + \pi) \quad (1.89)$$

$$(\gamma, \delta_B) \leftrightarrow (\delta_B, \gamma) \quad (1.90)$$

The main limitations of this method are two:

- the low overall branching fractions of the relevant decays. The branching fraction of the $B^- \rightarrow D^0 K^-$ process is in fact $\approx 4 \times 10^{-4}$ and the branching fractions (including eventual secondary decays for instance $K_s^0 \rightarrow \pi^+ \pi^-$) for D^0 decays to CP eigenstates are at the level of a few parts in 10^3 , with final reconstruction efficiencies varying between $\approx 5\%$ and 35% based on the number of charged tracks and neutral pions in the B decay and on the background level. It is therefore necessary to reconstruct as many as possible $f_{CP\pm}$ final states to increase the statistics. With the same purpose, the method can also be applied to $B \rightarrow D_{CP}^{*0} K$, $B \rightarrow D_{CP}^0 K^*$ and $B \rightarrow D_{CP}^{*0} K^*$ decays, having different values for r_B and δ_B but the same functional dependence on γ : this has the effect of increasing the sensitivity to γ and to break the twofold ambiguity $\gamma \leftrightarrow \delta_B$, thus reducing the number of discrete ambiguities to four. In the case of final states containing vector D^{*0} mesons, it must be noted [39] that there is an effective strong phase difference of 180° whenever the D^{*0} is reconstructed as $D^0 \pi^0$ or $D^0 \gamma$, or equivalently that $D_{CP\pm}^{*0} \rightarrow D_{CP\pm}^0 \pi^0$ while $D_{CP\pm}^{*0} \rightarrow D_{CP\mp}^0 \gamma$.
- however large the data sample, the sensitivity to γ is essentially proportional to the value of r_B and is therefore limited by the small value of r_B , which can be expressed as [31]:

$$r_B \approx \left| \frac{V_{ub} V_{cs}^*}{V_{cb} V_{us}^*} \right| \frac{a_2}{a_1} \quad (1.91)$$

where $a_2/a_1 \approx 0.26 - 0.44$ is a color suppression factor estimated from the measured branching fractions of color-suppressed B decays [31], and $\left| \frac{V_{ub} V_{cs}^*}{V_{cb} V_{us}^*} \right| \approx 0.4$, from which r_B is expected to be around $0.1 - 0.2$.

Depending on the value of δ_B , if $\gamma \approx 60^\circ$ and $r_B \approx 0.15$, CP asymmetries up to 25% may be possible. It should be noted, however, that even if δ_B vanished and the CP asymmetries were zero, the analysis could still be performed to yield γ : in that case the unknowns would reduce to two, r_B and γ , which could be extracted from the two observables $R_{CP\pm} = 1 + r_B^2 \pm 2r_B \cos \gamma$, through the relations

$$\frac{R_{CP+} + R_{CP-}}{2} - 1 = r_B^2 \quad (1.92)$$

$$\frac{R_{CP+} - R_{CP-}}{4} = r_B \cos \gamma \quad (1.93)$$

1.7.2 The Atwood-Dunietz-Soni method

The Atwood-Dunietz-Soni (ADS) method [32] is based on the reconstruction of charged B decays to $D^0 K$ where the D^0 decays to a doubly-Cabibbo-suppressed (DCS) final state f , like for instance $f = K^+ \pi^-$. In this case a large interference is expected between the $B^- \rightarrow D^0 K^-$, $D^0 \rightarrow K^+ \pi^-$ amplitude, which proceeds through the color-allowed $b \rightarrow c$ transition followed by the DCS D^0 decay, and the $B^- \rightarrow \bar{D}^0 K^-$, $\bar{D}^0 \rightarrow K^+ \pi^-$ amplitude, where the color-suppressed $b \rightarrow u$ transition is followed by a Cabibbo-allowed (CA) \bar{D}^0 decay:

$$|A(B^- \rightarrow D^0 K, D^0 \rightarrow K^+ \pi^-)| = \underbrace{|A(B^- \rightarrow D^0 K)|}_{\propto |V_{cb} V_{us}^*|} \times \underbrace{|A(D^0 \rightarrow K^+ \pi^-)|}_{\propto |V_{cd}^* V_{us}|}$$

$$\begin{aligned}
|A(B^- \rightarrow \bar{D}^0 K, \bar{D}^0 \rightarrow K^+ \pi^-)| &= \underbrace{|A(B^- \rightarrow \bar{D}^0 K)|}_{\propto |V_{ub} V_{cs}^*| a_2/a_1} \times \underbrace{|A(\bar{D}^0 \rightarrow K^+ \pi^-)|}_{\propto |V_{cs} V_{ud}^*|} \\
&= r_B |A(\bar{D}^0 \rightarrow K^+ \pi^-)|.
\end{aligned}$$

Here r_B is the ratio of the magnitudes of the $B^- \rightarrow \bar{D}^0 K^-$ and $B^- \rightarrow D^0 K^-$ defined in (1.87), therefore:

$$\frac{|A(B^- \rightarrow \bar{D}^0 K, \bar{D}^0 \rightarrow K^+ \pi^-)|}{|A(B^- \rightarrow D^0 K, D^0 \rightarrow K^+ \pi^-)|} = r_B \left| \frac{V_{cs} V_{ud}}{V_{us} V_{cd}} \right| \approx r_B \lambda^{-2} \approx 2 - 3 \quad (1.94)$$

Accordingly, the (direct) CP asymmetries are potentially large in these decays, up to 40%, and the sensitivity to γ , which – like in the previous method – is proportional to the interference term, should be enhanced. Unfortunately, on the other hand, considering doubly-Cabibbo-suppressed D^0 decays instead of singly-Cabibbo-suppressed decays to CP eigenstates reduces the overall branching fractions by a factor $\approx \lambda^2$ and a significantly larger statistics is needed to perform the measurement. Within the same data sample, the sensitivities of this and the previous methods are probably comparable.

To extract γ from these decays one needs to measure their branching fractions and CP asymmetries, which are related to γ through the relations (see Appendix A):

$$\begin{aligned}
R_{\text{ADS}}(f) &\equiv \frac{\mathcal{B}(B^- \rightarrow [f]_{D^0} K^-) + \mathcal{B}(B^+ \rightarrow [f]_{D^0} K^+)}{\mathcal{B}(B^- \rightarrow [\bar{f}]_{D^0} K^-) + \mathcal{B}(B^+ \rightarrow [\bar{f}]_{D^0} K^+)} \\
&= r_D^f{}^2 + r_B^2 + 2r_D^f r_B \cos \gamma \cos(\delta_B + \delta_D^f) \quad (1.95)
\end{aligned}$$

$$\begin{aligned}
A_{\text{ADS}}(f) &\equiv \frac{\mathcal{B}(B^- \rightarrow [f]_{D^0} K^-) - \mathcal{B}(B^+ \rightarrow [f]_{D^0} K^+)}{\mathcal{B}(B^- \rightarrow [\bar{f}]_{D^0} K^-) + \mathcal{B}(B^+ \rightarrow [\bar{f}]_{D^0} K^+)} \\
&= 2r_D^f r_B \sin \gamma \sin(\delta_B + \delta_D^f) / R_{\text{ADS}}(f). \quad (1.96)
\end{aligned}$$

Here, \bar{f} (CP conjugate of f) is the Cabibbo-allowed D^0 decay. The notation $[f]_{D^0}$ means that the reconstructed final state f must have been produced in a D^0 or \bar{D}^0 decay, δ_B is the strong phase difference between the $B^- \rightarrow \bar{D}^0 K^-$ and $B^- \rightarrow D^0 K^-$ amplitudes, and r_D^f and δ_D^f are the magnitude ratio and the strong phase difference of the doubly-Cabibbo-suppressed and the Cabibbo-allowed D^0 amplitudes:

$$r_D^f e^{i\delta_D^f} \equiv \frac{A(D^0 \rightarrow f)}{A(D^0 \rightarrow \bar{f})} \quad (1.97)$$

Since there are now four unknowns (γ , r_B , r_D^f and $\delta_B + \delta_D^f$) and two observables, measuring γ is not possible with this method if we just reconstruct one D^0 decay. If we added n more D^0 channels, the number of observables would increase by $2n$ (R_{ADS} and A_{ADS} for each channel) and the number of unknowns would increase by the same number (r_D^f and $\delta_B + \delta_D^f$ for each channel), therefore the system would remain unconstrained. We therefore need some additional experimental input to extract γ . In particular, the quantities r_D^f can be measured from D^0 decays (for instance, for the $K^+ \pi^-$ decay $r_D^{K^+ \pi^-} = 0.060 \pm 0.003$ [38]), thus reducing the number of unknowns to $2+n$. Since the observables are $2n$, the minimum number of D^0 channels that is needed to measure γ is therefore $n = 2$. Moreover, unless the strong phases δ_D^f are all the same, which is unlikely, reconstructing more than one channel breaks the 2-fold ambiguity $\gamma \leftrightarrow \delta_B + \delta_D^f$ contained in equations (1.95) and (1.96) and reduces the number of discrete ambiguities on γ to four:

$$(\gamma, \delta_B, \delta_D^f) \leftrightarrow (-\gamma, -\delta_B, -\delta_D^f) \quad (1.98)$$

$$(\gamma, \delta_B, \delta_D^f) \leftrightarrow (\gamma + \pi, \delta_B + \pi, \delta_D^f + \pi) \quad (1.99)$$

Like the previous one, also this method can be generalized to $B \rightarrow D^{*0}K$, $B \rightarrow D^0K^*$ and $B \rightarrow D^{*0}K^*$ decays. Again, when reconstructing D^{*0} in $D^0\pi^0$ or $D^0\gamma$, one needs to take into account the effective strong phase difference of 180° between the $B \rightarrow [D^0\pi^0]_{D^{*0}}K$ and the $B \rightarrow [D^0\gamma]_{D^{*0}}K$ amplitudes [39], which leads to

$$R_{\text{ADS}}^{D^0\pi^0}(f) = r_D^f{}^2 + r_B^{*2} + 2r_D^f r_B^* \cos\gamma \cos(\delta_B^* + \delta_D^f) \quad (1.100)$$

$$R_{\text{ADS}}^{D^0\gamma}(f) = r_D^f{}^2 + r_B^{*2} - 2r_D^f r_B^* \cos\gamma \cos(\delta_B^* + \delta_D^f) \quad (1.101)$$

$$A_{\text{ADS}}^{D^0\pi^0}(f) = +2r_D^f r_B^* \sin\gamma \sin(\delta_B^* + \delta_D^f) / R_{\text{ADS}}^{D^0\pi^0}(f) \quad (1.102)$$

$$A_{\text{ADS}}^{D^0\gamma}(f) = -2r_D^f r_B^* \sin\gamma \sin(\delta_B^* + \delta_D^f) / R_{\text{ADS}}^{D^0\gamma}(f) \quad (1.103)$$

where r_B^* and δ_B^* are the analogous of r_B and δ_B for the $B \rightarrow D^{*0}K$ decay. Therefore, the measurement of the four observables $R_{\text{ADS}}^{D^0\pi^0}(f)$, $A_{\text{ADS}}^{D^0\pi^0}(f)$, $R_{\text{ADS}}^{D^0\gamma}(f)$, $A_{\text{ADS}}^{D^0\gamma}(f)$ (only 3 are independent, since $R_{\text{ADS}}^{D^0\pi^0} A_{\text{ADS}}^{D^0\pi^0} = -R_{\text{ADS}}^{D^0\gamma} A_{\text{ADS}}^{D^0\gamma}$) for $B \rightarrow D^{*0}K$, with $D^{*0} \rightarrow D^0\pi^0$ and $D^{*0} \rightarrow D^0\gamma$, and $D^0 \rightarrow f$, would be enough to extract the three unknowns γ , r_B^* and $\delta_B^* + \delta_D^f$, through the relations:

$$\frac{R_{\text{ADS}}^{D^0\pi^0}(f) + R_{\text{ADS}}^{D^0\gamma}(f)}{2} - r_D^f{}^2 = r_B^{*2} \quad (1.104)$$

$$\frac{R_{\text{ADS}}^{D^0\pi^0}(f) - R_{\text{ADS}}^{D^0\gamma}(f)}{4r_D^f} = r_B^* \cos\gamma \cos(\delta_B^* + \delta_D^f) \quad (1.105)$$

$$\frac{A_{\text{ADS}}^{D^0\pi^0}(f) R_{\text{ADS}}^{D^0\pi^0}(f) - A_{\text{ADS}}^{D^0\gamma}(f) R_{\text{ADS}}^{D^0\gamma}(f)}{4r_D^f} = r_B^* \sin\gamma \sin(\delta_B^* + \delta_D^f) \quad (1.106)$$

1.7.3 The Giri-Grossmann-Soffer-Zupan method

The Giri-Grossmann-Soffer-Zupan (GGSZ) method [33] is based on the reconstruction of $B \rightarrow D^0K$ and $B \rightarrow \bar{D}^0K$ decays with the D^0 and \bar{D}^0 reconstructed into three-body (or multi-body) self-conjugate final states. We consider here, as an example, the decay $D^0 \rightarrow K_s^0\pi^+\pi^-$.

Let us denote with m_-^2 and m_+^2 the squared invariant masses of the $K_s^0\pi^-$ and $K_s^0\pi^+$ combinations respectively, and

$$A(D^0 \rightarrow K_s^0\pi^+\pi^-) = f(m_-^2, m_+^2) = |f(m_-^2, m_+^2)| e^{i\Delta(m_-^2, m_+^2)}$$

the amplitude of the $D^0 \rightarrow K_s^0\pi^-\pi^+$ decay to the point (m_-^2, m_+^2) of the Dalitz plot. Neglecting CP violation in D^0 decays, the amplitude $A(\bar{D}^0 \rightarrow K_s^0\pi^+\pi^-)$ to the same point of the Dalitz plot is

$$A(\bar{D}^0 \rightarrow K_s^0\pi^+\pi^-) = f(m_+^2, m_-^2) = |f(m_+^2, m_-^2)| e^{i\Delta(m_+^2, m_-^2)}.$$

The total B^- and B^+ amplitudes for the process $B \rightarrow [K_s^0\pi^-\pi^+]_{D^0}K$, denoted with A_- and A_+ , are:

$$\begin{aligned} A_-(m_-^2, m_+^2) &= A(B^- \rightarrow D^0K^-) \left[f(m_-^2, m_+^2) + r_B e^{i(\delta_B - \gamma)} f(m_+^2, m_-^2) \right] \\ A_+(m_-^2, m_+^2) &= A(B^+ \rightarrow \bar{D}^0K^+) \left[f(m_+^2, m_-^2) + r_B e^{i(\delta_B + \gamma)} f(m_-^2, m_+^2) \right] \end{aligned}$$

The resulting bi-dimensional Dalitz (m_-^2, m_+^2) distributions for negative and positive B candidates, modulo reconstruction efficiency variations, are proportional to

$$|A_-(m_-^2, m_+^2)|^2 = |A|^2 \times \left[|f(m_-^2, m_+^2)|^2 + r_B^2 |f(m_+^2, m_-^2)|^2 + \right.$$

$$2r_B|f(m_-^2, m_+^2)||f(m_+^2, m_-^2)|\cos(\delta_B - \gamma + \delta_D(m_+^2, m_-^2))\Big] \quad (1.107)$$

and

$$\begin{aligned} |A_+(m_-^2, m_+^2)|^2 &= |A|^2 \times \left[|f(m_+^2, m_-^2)|^2 + r_B^2 |f(m_-^2, m_+^2)|^2 + \right. \\ &\quad \left. 2r_B|f(m_+^2, m_-^2)||f(m_-^2, m_+^2)|\cos(\delta_B + \gamma - \delta_D(m_+^2, m_-^2)) \right] \end{aligned} \quad (1.108)$$

where $|A| \equiv |A(B^- \rightarrow D^0 K^-)| = |A(B^+ \rightarrow \bar{D}^0 K^+)|$ and

$$\delta_D(m_-^2, m_+^2) \equiv \bar{\Delta}(m_-^2, m_+^2) - \Delta(m_-^2, m_+^2) = \Delta(m_+^2, m_-^2) - \Delta(m_-^2, m_+^2) \quad (1.109)$$

is the strong phase difference between the \bar{D}^0 and D^0 amplitudes at the point (m_-^2, m_+^2) of the $K_s^0 \pi^+ \pi^-$ Dalitz plot. It is easy to see that these formulae are just the generalization of the equations (A.19) and (A.20) for the two-body D^0 decays, when the dependence of the amplitude on the Mandelstam variables for the 3-body decay is introduced.

If the Dalitz structure of the $D^0 \rightarrow K_s^0 \pi^+ \pi^-$ decay is known, i.e. $f(m_-^2, m_+^2)$ is known (for instance from charm factories), then the Dalitz distribution of the $K_s^0 \pi^+ \pi^-$ candidates originating from B^+ and B^- decays to $D^0 K$ can be fitted to extract r_B , δ_B and γ . Like in the ADS case, the presence of a non-trivial ($\neq 0, \pi$) D^0 strong-phase δ_D which is different in different regions of the Dalitz plot breaks the exchange ambiguity $\gamma \leftrightarrow \delta_B + \delta_D$. Moreover, since δ_D is known (assuming $f(m_-^2, m_+^2)$ to be fully known), also the sign ambiguity $\gamma \leftrightarrow -\gamma$ is broken, since the relative sign between γ and δ_D is different in the B^- and B^+ Dalitz distributions in (1.107) and (1.108), respectively. Therefore, the discrete ambiguity on γ of this method is only twofold:

$$(\gamma, \delta_B) \leftrightarrow (\gamma + \pi, \delta_B + \pi) \quad (1.110)$$

The main advantages of this method are that

- the D^0 decays that are considered are Cabibbo-allowed, therefore the branching fractions are about one order of magnitudes higher than in the GLW case (and even higher with respect to the ADS case)
- the full sub-resonance structure of the three-body (or multi-body) D^0 decay is considered, including interferences that could be used for the GLW (like $K_s^0 \rho^0$) and ADS methods (like $K^{*+} \pi^-$), which allows to reduce the number of discrete ambiguities and to improve the overall γ sensitivity.

On the other hand, the Dalitz plot (m_-^2, m_+^2) of the selected B candidates must be sufficiently populated to perform the fit, which requires a significant number of $B \rightarrow [K_s^0 \pi^+ \pi^-]_{D^0} K$ decays to be reconstructed, and the $D^0 \rightarrow K_s^0 \pi^+ \pi^-$ amplitude $f(m_-^2, m_+^2)$ must be known. The imprecise knowledge of f can thus lead to a systematic uncertainty on the measured value of γ .

Like in the previous cases, the method can be generalized to $B \rightarrow D^{*0} K$, $B \rightarrow D^0 K^*$ and $B \rightarrow D^{*0} K^*$ decays.

1.7.4 Measuring $\sin(2\beta + \gamma)$ in time-dependent $B^0 \rightarrow D^{(*)} \pi$

A different approach for the measurement of γ in a clean model-independent way is based on the study of the time-dependent evolution of neutral B decays to $D^{(*)\pm} \pi^\mp$ final states [36]. γ is extracted by exploiting the interference between the ‘‘unmixed’’, $\bar{b} \rightarrow \bar{u}$ mediated $B^0 \rightarrow D^+ \pi^-$ amplitude and the ‘‘mixed’’, $\bar{b} \rightarrow \bar{c}$ mediated $B^0 \rightarrow \bar{B}^0 \rightarrow D^+ \pi^-$

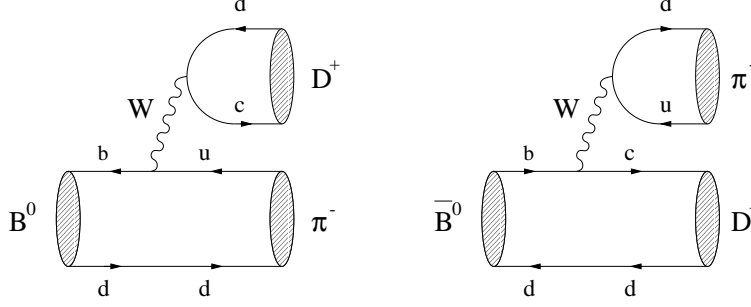


Figure 1.6: Feynman diagrams contributing to $B^0 \rightarrow D^+\pi^-$ and $\bar{B}^0 \rightarrow D^+\pi^-$.

amplitude, the former carrying - with respect to the latter - the weak phase $2\beta + \gamma$. 2β comes from $B^0-\bar{B}^0$ mixing and $\gamma = \arg \frac{V_{ub}^* V_{cd}}{V_{cb}^* V_{ud}}$, see (1.12), is the relative weak phase between the $\bar{B}^0 \rightarrow D^+\pi^-$ and $B^0 \rightarrow D^+\pi^-$ diagrams, which are shown in Figure 1.6. Since β is accurately known from the time-dependent CP asymmetries of B decays to charmonium, measuring $2\beta + \gamma$ from the time evolution of the $D^{(*)\pm}\pi^\mp$ decays implies a determination of γ .

The probabilities for the decays $\bar{B}^0(t) \rightarrow D^\pm\pi^\mp$ and $B^0(t) \rightarrow D^\pm\pi^\mp$ are:

$$\begin{aligned}
 P(\bar{B}^0(t) \rightarrow D^\pm\pi^\mp) \propto 1 & \pm \frac{1-r^2}{1+r^2} \cos(\Delta M_d t) \\
 & - \frac{2r}{1+r^2} \sin(2\beta + \gamma \mp \delta) \sin(\Delta M_d t) \quad (1.111)
 \end{aligned}$$

$$\begin{aligned}
 P(B^0(t) \rightarrow D^\pm\pi^\mp) \propto 1 & \mp \frac{1-r^2}{1+r^2} \cos(\Delta M_d t) \\
 & + \frac{2r}{1+r^2} \sin(2\beta + \gamma \pm \delta) \sin(\Delta M_d t) \quad (1.112)
 \end{aligned}$$

where $r \equiv |A(B^0 \rightarrow D^+\pi^-)/A(\bar{B}^0 \rightarrow D^+\pi^-)|$ and $\delta \equiv (\Delta - \bar{\Delta})$ is the relative strong phase between the doubly CKM-suppressed $B^0 \rightarrow D^+\pi^+$ amplitude ($\propto |V_{ub}V_{cd}| \approx A\lambda^4 R_b$) and the CKM-allowed $\bar{B}^0 \rightarrow D^+\pi^-$ amplitude ($\propto |V_{cb}V_{ud}| \approx A\lambda^2$):

$$r \approx R_b \lambda^2 \approx 0.4 \times 0.05 = 0.02 \quad (1.113)$$

Analogous relations hold for the $D^*\pi$ case, with $(r, \delta) \rightarrow (r^*, \delta^* + \pi)$.

In principle, one could therefore measure the time-dependent evolution of these decays and, from the coefficients of the sine and cosine terms, extract $2\beta + \gamma$, along with the unknown hadronic parameters r and δ . However, since $r \approx 0.02$ is very small, and the sensitivity to r comes from the $\cos(\Delta M_d t)$ terms, where r enters quadratically, it is impossible - at present B factory experiments - to determine r in this way. The time-dependent probabilities therefore, neglecting $\mathcal{O}(r^2)$ terms, take the simpler form

$$P(\bar{B}^0(t) \rightarrow D^\pm\pi^\mp) \propto 1 \pm \cos(\Delta M_d t) - 2r \sin(2\beta + \gamma \mp \delta) \sin(\Delta M_d t) \quad (1.114)$$

$$(1.115)$$

$$P(B^0(t) \rightarrow D^\pm\pi^\mp) \propto 1 \mp \cos(\Delta M_d t) + 2r \sin(2\beta + \gamma \pm \delta) \sin(\Delta M_d t) \quad (1.116)$$

$$(1.117)$$

and to extract $2\beta + \gamma$ and δ from the measured coefficients of the $\sin(\Delta M_d t)$ terms alternative methods to fix r are required. A possible approach consists in estimating r

(and r^*) from the $SU(3)$ symmetry relation (neglecting annihilation contributions)

$$r^{(*)} = \lambda \sqrt{\frac{\mathcal{B}(B^0 \rightarrow D_s^{(*)+} \pi^-)}{\mathcal{B}(B^0 \rightarrow D^{(*)+} \pi^-)} \frac{f_{D^{(*)}}}{f_{D_s^{(*)}}}} \quad (1.118)$$

where $\lambda = 0.2250 \pm 0.0027$, and the decay constant ratios $f_{D_s}/f_D = 1.11 \pm 0.01$ and $f_{D_s^*}/f_{D^*} = 1.10 \pm 0.02$ [40] take into account factorizable $SU(3)$ breaking effects. An additional, guessed error (typically of the order of 30%) is attributed on $r^{(*)}$ to take into account possible non-factorizable $SU(3)$ breaking effects and the unknown size of annihilation contributions.

Other drawbacks of this method are that:

- a time-dependent analysis must be performed, which is intrinsically more complicated than a time-integrated measurement, and which requires a high signal yield to give accurate results
- to do a time-dependent analysis, the flavor of the other B at the moment of its decay must be unambiguously determined (tagged). This is done by looking for a high p_t lepton (from $B \rightarrow X l \bar{\nu}_l$ decays) or a kaon in the event. This requirement reduces the overall selection efficiency, since only about 30% of the neutral B decays are tagged.
- when the flavor of the other B is tagged through hadronic decays, CP violation on the tag side may alter, through the coherent evolution of the $B^0-\bar{B}^0$ pair, the time evolution of $P(B^0(t) \rightarrow D^\pm \pi^\mp)$ and $P(\bar{B}^0(t) \rightarrow D^\pm \pi^\mp)$ as shown in [41]. Additional terms of unknown size are introduced in the expression of the time-dependent probabilities; the measurement of $2\beta + \gamma$ however is not spoiled and can still be performed, but at the price of using only part of the information contained in the selected data, thus reducing the sensitivity of the method
- since the ratio of the interfering amplitudes is $r \approx 0.02$, the interference and therefore the sensitivity to $2\beta + \gamma$ are rather small

On the other hand, the main advantage of this method over the previous ones is that the favored B decay amplitude is Cabibbo-allowed, and so are the D and D^* secondary decays that are reconstructed, therefore the number of selected $D^{(*)}\pi$ events in a certain dataset is, ultimately, at least about two orders of magnitude higher than the number of $D^0 K$ events selected for the previous methods. Moreover, in the $D^*\pi$ case, a partial reconstruction technique may be used, where the $B^0 \rightarrow D^*\pi$ is not fully reconstructed, but only the pion from the B and the soft pion from the $D^* \rightarrow D^0\pi$ decay are detected. In that case signal events are selected by requiring that the invariant mass of the unreconstructed D^0 , obtained by applying kinematic constraints consistent with the decay mode, peak at the nominal D^0 mass. The partial reconstruction technique allows a significant improvement in the number of reconstructed signal events (by a factor 8 – 10), at the cost of an increased background and a poorer B vertex resolution (the B vertex position is necessary to measure the proper time difference t between the decays of the two B mesons). The requirement of a B meson on the tag side helps, in this case, to reduce the background level.

1.7.5 Current results on γ from model-independent measurements

Several results have been presented at the ICHEP conference in Summer 2004 in the channels related to the model-independent extraction of γ . Some results have been updated recently. These results finally offer the first direct constraints on γ .

B decay mode	R_{CP+}	A_{CP+}	R_{CP-}	A_{CP-}
$D^0 K$	0.87 ± 0.15	0.40 ± 0.17	0.80 ± 0.16	0.21 ± 0.18
$D^{*0} K$	1.06 ± 0.28	-0.10 ± 0.23		
$D^0 K^*$	1.96 ± 0.41	-0.08 ± 0.21	0.65 ± 0.27	-0.26 ± 0.42

Table 1.1: Measured branching fraction ratios and CP asymmetries in $B \rightarrow D_{(CP\pm)}^{(*)0} K^{(*)}$ decays (*BABAR*).

B decay mode	R_{CP+}	A_{CP+}	R_{CP-}	A_{CP-}
$D^0 K$	0.98 ± 0.21	0.07 ± 0.15	1.29 ± 0.18	-0.11 ± 0.15
$D^{*0} K$	1.43 ± 0.29	-0.27 ± 0.25	0.94 ± 0.29	0.26 ± 0.26

Table 1.2: Measured branching fraction ratios and CP asymmetries in $B \rightarrow D_{(CP\pm)}^{(*)0} K$ decays (*Belle*).

Both the *BABAR* and *Belle* experiments have presented measurements of the $B \rightarrow D_{CP}^{(*)0} K^{(*)}$ decays, which are summarized in Tables 1.1 and 1.2.

The two experiments have also investigated the mode $B^- \rightarrow [K^+\pi^-]_{D^0} K^-$; *BABAR* has also performed the search in the $D^{*0} K$ ($D^{*0} \rightarrow D^0 \pi^0$ and $D^{*0} \rightarrow D^0 \gamma$) channel [43]. No signal is found in their current data samples, and an upper limit on the hadronic parameters r_B and r_B^* is obtained:

$$\begin{aligned}
r_B &< 0.23(90\% \text{C.L.}) \text{ BABAR} \\
r_B &< 0.28(90\% \text{C.L.}) \text{ Belle} \\
r_B^* &< 0.16(90\% \text{C.L.}) \text{ BABAR}
\end{aligned}$$

The two experiments have also performed a measurement of γ and the hadronic parameters $r_B^{(*)}$ and $\delta_B^{(*)}$ by studying the Dalitz distributions of $B \rightarrow D^{(*)0} K$ decays with $D^0 \rightarrow K_s^0 \pi^+ \pi^-$, $D^{*0} \rightarrow D^0 \pi^0$ and $D^{*0} \rightarrow D^0 \gamma$ [44]. The amplitude for the decay $D^0 \rightarrow K_s^0 \pi^+ \pi^-$ is described as the sum of a non-resonant term and two-body (Breit-Wigner) amplitudes, whose magnitudes and phases are determined on a clean, high-statistics sample of tagged D^0 mesons originating in $D^0 \pi$ decays of D^* mesons produced in $e^+ e^- \rightarrow c \bar{c}$ collisions. Their results are summarized in Table 1.3.

Parameter	<i>BABAR</i>	<i>Belle</i>
γ	$(70 \pm 31_{-10-11}^{+12+14})^\circ$	$(68 \pm 15 \pm 13 \pm 11)^\circ$
r_B	$0.118 \pm 0.079 \pm 0.034_{-0.034}^{+0.036}$	$0.21 \pm 0.08 \pm 0.03 \pm 0.04$
δ_B	$(104 \pm 45_{-21-24}^{+17+16})^\circ$	$(157 \pm 19 \pm 11 \pm 21)^\circ$
r_B^*	$0.169 \pm 0.096_{-0.028-0.026}^{+0.030+0.029}$	$0.12_{-0.11}^{+0.16} \pm 0.02 \pm 0.04$
δ_B^*	$(296 \pm 41_{-12}^{+14} \pm 15)^\circ$	$(321 \pm 57 \pm 11 \pm 21)^\circ$

Table 1.3: Measured values for the angle γ and the hadronic parameters $r_B^{(*)}$ and $\delta_B^{(*)}$. γ and $\delta_B^{(*)}$ are measured up to a discrete ambiguity of 180° .

When combining all the information coming from the GLW, ADS and GGSZ measurements of the two experiments, the 68% confidence interval for γ is [8]:

$$\gamma = (64 \pm 18)^\circ \text{ or } \gamma = (244 \pm 18)^\circ \tag{1.119}$$

The 95% C.L. allowed region is:

$$\gamma \in [30, 100]^\circ \text{ or } \gamma \in [210, 280]^\circ \quad (1.120)$$

The error is still quite large and needs a significant increase in statistics or in the number of decay modes that are reconstructed to be significantly improved. The results are significantly driven by the value of γ measured with $B \rightarrow D^{(*)0}K, D^0 \rightarrow K_s^0\pi^+\pi^-$ decays, which at the moment provide the best sensitivity. It must be noted however that the error on γ of each method is largely correlated with the value or r_B and r_B^* , and the current GGSZ measurements tend to favor a higher value for $r_B^{(*)}$ with respect to the GLW measurements.

The B -factory experiments have also measured the time-dependent evolution of neutral B decays to $D\pi, D^*\pi$ and $D\rho$ decays [45]. At present, a combined interpretation of the measured coefficients of the time-dependent probabilities given in (1.111) and (1.112) is not yet ready. *BABAR* sets, using only the sample of $D^*\pi$ partially reconstructed, the following lower limit on $2\beta + \gamma$:

$$|\sin(2\beta + \gamma)| > 0.75 \text{ (68\% C.L.)} \quad (1.121)$$

$$|\sin(2\beta + \gamma)| > 0.58 \text{ (90\% C.L.)} \quad (1.122)$$

1.7.6 Model-dependent methods for extracting γ

Model-dependent techniques try to extract γ , together with some hadronic parameters that are hard to estimate from the theory, through approximate relations between different B decay amplitudes containing the weak phase $e^{\pm i\gamma}$. These relations are typically obtained by making some dynamical assumptions and requiring that strong interaction are invariant under some flavor symmetries (isospin, $SU(3)$). Factorizable flavor-symmetry breaking terms are also included, while non-factorizable corrections are neglected. Two methods representative of this category are the following:

- the first approach is based on charmless $B \rightarrow \pi\pi, K\pi$ decays [46]. As we have seen in Section 1.6, eqs (1.71) and (1.72), the coefficients of the time evolution of neutral B decays to charged pion pairs $\pi^+\pi^-$ are a function of γ, β and two hadronic parameters a and δ defined in (1.68):

$$C_{\pi^+\pi^-} = \text{fct}(a, \delta, \gamma) \quad (1.123)$$

$$S_{\pi^+\pi^-} = \text{fct}(a, \delta, \gamma, \beta) \quad (1.124)$$

If we now consider also $B^0 \rightarrow \pi^\pm K^\mp$ decays, neglect some amplitudes that are expected to be suppressed (electroweak penguins, penguin annihilation and exchange topologies), and use the $SU(3)$ isospin symmetry, we arrive to the following relation:

$$\frac{1}{\epsilon} \left(\frac{f_K}{f_\pi} \right)^2 \left[\frac{\mathcal{B}(B^0 \rightarrow \pi^+\pi^-)}{\mathcal{B}(B^0 \rightarrow \pi^\mp K^\pm)} \right] \equiv \zeta \approx \text{fct}(a, \delta, \gamma) = \frac{1 - 2a \cos \delta \cos \gamma + a^2}{\epsilon^2 + 2\epsilon a \cos \delta \cos \gamma + a^2} \quad (1.125)$$

where $\epsilon \equiv \frac{\lambda^2}{1-\lambda^2} = 0.053$, and the factor f_K/f_π , involving the kaon and pion decay constants, takes into account factorizable $SU(3)$ breaking corrections. If we fix β to the value measured in time-dependent CP asymmetries to $(c\bar{c})K^0$, the previous equalities provide three relations between the three unknowns a, δ and γ , which can therefore be determined simultaneously. Additional information is provided by the direct CP asymmetry in $B^0 \rightarrow K^\pm \pi^\mp$, which – with the same theoretical assumptions – is given by

$$A_{CP}^{\text{dir}}(B^0 \rightarrow K^\pm \pi^\mp) = \frac{2\epsilon a \sin \delta \sin \gamma}{\epsilon^2 + 2\epsilon a \cos \delta \cos \gamma + a^2} \quad (1.126)$$

and, since the decay constant ratio cancel, is expected to be affected to a smaller extent – with respect to ζ – by $SU(3)$ -breaking corrections. It is also possible to consider charged B decays to $\pi^\pm\pi^0$ and $\pi^\pm K^0$, where again electroweak penguin are expected to play a minor role. Within the same theoretical framework as before one can find:

$$\sqrt{2} \left| \frac{V_{us}}{V_{ud}} \right| \frac{f_K}{f_\pi} \sqrt{\frac{\mathcal{B}(B^\pm \rightarrow \pi^\pm\pi^0)}{\mathcal{B}(B^\pm \rightarrow \pi^\pm K^0)}} = \frac{\epsilon}{a} \sqrt{[1 - 2a \cos \delta \cos \gamma + a^2] R_{+-}^{\pi\pi}} \quad (1.127)$$

where

$$R_{+-}^{\pi\pi} \equiv 2 \left[\frac{\mathcal{B}(B^+ \rightarrow \pi^+\pi^0) + \mathcal{B}(B^- \rightarrow \pi^-\pi^0)}{\mathcal{B}(B^0 \rightarrow \pi^+\pi^-) + \mathcal{B}(\bar{B}^0 \rightarrow \pi^+\pi^-)} \right] \frac{\tau_B^0}{\tau_B^+} \quad (1.128)$$

With the present measurements of the relevant branching fractions (which are of the order of 10^{-5}) and CP asymmetries, the authors of [46] find, at 68% C.L, the value $\gamma = (65 \pm 7)^\circ$ or $\gamma = (245 \pm 7)^\circ$, in excellent agreement with the indirect measurements from the CKM fits. However, the uncertainty to be assigned to γ due to the theoretical assumptions is not included and the quoted error on γ is likely to be underestimated. Moreover, the likelihood function around the best-fit solution is significantly non-gaussian, and the 95% C.L. interval for γ is quite worse, $34^\circ \lesssim \gamma \lesssim 77^\circ$.

- an alternative model-dependent method for measuring γ has been proposed very recently [47] and is based on $B^0 \rightarrow D_{(s)}^{(*)+} D^{(*)-}$ decays. The technique is quite straightforward in the DD case: the total amplitude, receiving contribution from several processes, tree (T), exchange (E), QCD penguins (P) and color-suppressed electroweak penguins (P_{EW}^C), is

$$\begin{aligned} A(B^0 \rightarrow D^+ D^-) &= (T + E + P_c - P_t - P_{EW}^C) V_{cb}^* V_{cd} + (P_u - P_t - P_{EW}^C) V_{ub}^* V_{ud} \\ &\equiv A_{ct} e^{i\delta_{ct}} + A_{ut} e^{i\gamma} e^{i\delta_{ut}}, \end{aligned} \quad (1.129)$$

and from a time-dependent measurement three observables can be obtained:

1. the branching fraction:

$$B \propto \frac{1}{2} (|A|^2 + |\bar{A}|^2) = A_{ct}^2 + A_{ut}^2 + 2A_{ct}A_{ut} \cos(\delta_{ut} - \delta_{ct}) \cos \gamma \quad (1.130)$$

2. the direct CP asymmetry:

$$A_{CP}^{\text{dir}} \propto \frac{1}{2} (|\bar{A}|^2 - |A|^2) = 2A_{ct}A_{ut} \sin(\delta_{ut} - \delta_{ct}) \sin \gamma \quad (1.131)$$

3. the CP asymmetry due to interference:

$$\begin{aligned} A_{CP}^{\text{interf}} \propto \text{Im}(e^{-2i\beta} \bar{A}A) &= -A_{ct}^2 \sin 2\beta - A_{ut}^2 \sin(2\beta + 2\gamma) \\ &\quad - 2A_{ct}A_{ut} \cos(\delta_{ut} - \delta_{ct}) \sin(2\beta + \gamma). \end{aligned} \quad (1.132)$$

The idea is to extract γ from these three observables; however, even after fixing β to the value measured in time-dependent $B^0 \rightarrow (c\bar{c})K^0$ decays, there remain four unknowns, γ and the three hadronic parameters A_{ct} , A_{ut} and $\delta_{ut} - \delta_{ct}$. A theoretical

input is therefore needed, and comes from the $B^0 \rightarrow D_s^+ D^-$ decay, whose amplitude is

$$\begin{aligned} A(B^0 \rightarrow D_s^+ D^-) &= (T' + E' + P'_c - P'_t - P'_{EW})V_{cb}^*V_{cs} + (P'_u - P'_t - P'_{EW})V_{ub}^*V_{us} \\ &\approx A'_{ct}e^{i\delta'_{ct}} \end{aligned} \quad (1.133)$$

where we have neglected the terms proportional to $V_{ub}^*V_{us}$ since $|V_{ub}^*V_{us}|/|V_{cb}^*V_{cs}| \approx 2\%$. From the branching fraction of $B^0 \rightarrow D_s^+ D^-$ one can therefore measure A'_{ct} , which yields A_{ct} neglecting there exchange contributions and assuming flavor $SU(3)$ invariance of the strong interactions. The number of unknowns is therefore reduced to three and γ can be extracted (up to a π ambiguity) from the three observables in $B^0 \rightarrow D^+ D^-$. The method can be applied, with some additional complexity (and additional theoretical assumptions), also to the $D^{*+} D^-$ and $D^{*+} D^{*-}$ decays. Factorizable $SU(3)$ breaking terms are taken into account through the decay constant ratios $f_{D_s^{(*)}}/f_{D^{(*)}}$.

Like in the $\pi\pi/K\pi$ case, also in this approach the uncertainty on γ due to some of the theoretical assumptions is not precisely quantified. Moreover, with the current experimental results, γ (modulo π) is measured only at 68% C.L. ($\gamma = (50 \pm 31)^\circ$ or $\gamma = (133.5 \pm 13.5)^\circ$ or $\gamma = (167 \pm 7)^\circ$), while the 95% C.L. for γ is the whole range $[0^\circ, 360^\circ]$.

1.8 Conclusion

B physics offers an excellent field where to look for CP violation and to test the Standard Model predictions in the CP and flavor sector. In particular, the B -Factory experiments like $BABAR$ can overconstrain the so-called ‘‘Unitarity Triangle’’, which is related to one of the off-diagonal unitarity relations of the CKM matrix V . The most difficult to measure of the angles of this triangle is $\gamma \equiv \arg \left[-\frac{V_{ud}V_{ub}^*}{V_{cd}V_{cb}^*} \right]$, due to either small branching fractions or small interference effects in the B decays that provide sensitivity to it. To improve the accuracy on γ it is necessary to measure as many as possible γ -related observables in $B \rightarrow D^{(*)}K^{(*)}$ and $B \rightarrow D^{(*)}\pi/\rho$ decays, following the several methods that have been proposed in the past years and summarized in Section 1.7. One of the most promising methods is based on the reconstruction of $B \rightarrow D^0 K$ decays with D^0 decaying to CP -eigenstates (Subsection 1.7.1), which is the subject of the work presented in this thesis. In the next Chapter we shall see why the $BABAR$ experiment is well-suited to perform B -physics studies and in particular the measurement presented in this work.

Chapter 2

Experimental Apparatus

BABAR is a high energy physics experiment installed at the Stanford Linear Accelerator Center (SLAC), California. It was designed and built by a large international team of scientists and engineers in the 90s, with a comprehensive physics program consisting in the systematic measurement of CP violation in the B meson system, precision measurements of decays of bottom and charm mesons and of the τ lepton, and search for rare processes. The experiment consists of a detector (*BABAR* [48]) built around the interaction region of a high luminosity e^+e^- asymmetric collider (PEP-II [49]). In this chapter the main features of the final designs and the performances of PEP-II and the *BABAR* detector are described.

2.1 The PEP-II B Factory

The PEP-II B Factory is an asymmetric-energy e^+e^- collider designed to operate at a center-of-mass energy of 10.58 GeV, corresponding to the mass of the $\Upsilon(4S) = b\bar{b}$ vector meson resonance (see Figure 2.1). The effective cross section¹ for the production of the $\Upsilon(4S)$ at $\sqrt{s} = 10.58$ GeV is about 1.1 nb, and the $\Upsilon(4S)$ decays almost exclusively into $B^0\bar{B}^0$ or B^+B^- pairs. The design peak luminosity was foreseen to be $\mathcal{L} = 3 \times 10^{33}$ cm⁻²s⁻¹, but during year 2004 – thanks to higher beam currents, improved beam orbits and focusing – PEP-II has achieved a stable $\mathcal{L} = 9 \times 10^{33}$ cm⁻²s⁻¹, thus producing B meson pairs at a rate of about 10 Hz, which translates to about 100 million $B\bar{B}$ pairs in one year of continuous running, and providing an ideal laboratory for the study of B mesons.

The cross sections of the main physics processes in PEP-II are listed in Table 2.1 [14]. At the peak of the $\Upsilon(4S)$ there is a non-negligible amount of continuum $e^+e^- \rightarrow q\bar{q}$ ($q=u,d,s,c$) and $e^+e^- \rightarrow \ell^+\ell^-$ ($\ell = e, \mu, \tau$) events. To study the background events due to these processes, part of the data is collected at a CM energy 40 MeV below the $\Upsilon(4S)$ peak, where $B\bar{B}$ production is not allowed. This data sample corresponds to about 1/10 of the sample taken at the $\Upsilon(4S)$ peak.

2.1.1 PEP-II layout

In PEP-II, the electron beam of 9.0 GeV collides head-on with the positron beam of 3.1 GeV resulting in a boost to the $\Upsilon(4S)$ resonance of $\beta\gamma \approx 0.56$ in the laboratory frame. This boost makes it possible to reconstruct the decay vertices of the two B mesons and to determine their relative decay times, since the average separation between the two

¹This effective cross section is lower (about one third) than the peak cross section (3.6 nb) due to the energy spread (3-6 MeV) of the beams and to initial state radiation.

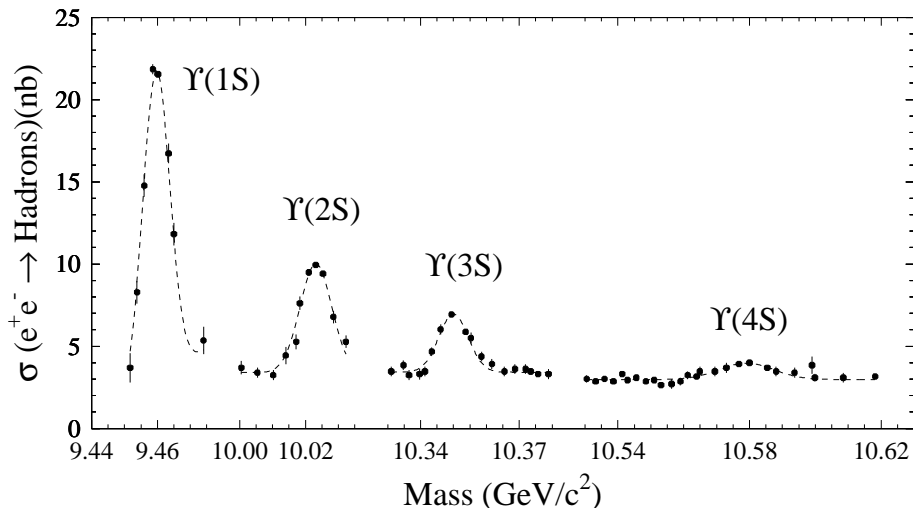


Figure 2.1: The first four S -wave Υ resonances shown with the hadronic cross section versus center-of-mass energy/ c^2 in the Υ mass region. The $\Upsilon(4S)$ is the third radial excitation of the ground state. Its larger width corresponds to the fact that the $\Upsilon(4S)$ is just above threshold for strongly decaying to $B^0\bar{B}^0$ and B^+B^- pairs.

Event	Cross section (nb)
$b\bar{b}$	1.10 (effective) - 3.6 (peak)
$c\bar{c}$	1.30
$s\bar{s}$	0.35
$u\bar{u}$	1.39
$d\bar{d}$	0.35
e^+e^-	~ 53
$\mu^+\mu^-$	1.16
$\tau^+\tau^-$	0.94

Table 2.1: Cross sections of the main physics processes at the $\Upsilon(4S)$. The cross section for e^+e^- is referred to the volume of the *BABAR* electromagnetic calorimeter, which is used to trigger these events.

B vertices is $\beta\gamma c\tau \approx 250\mu\text{m}$. One can therefore measure the time dependent decay rates and CP -asymmetries.

The unequal beam energies require a two rings configuration, as shown in Figure 2.2. The parameters of PEP-II rings are summarized in Table 2.2. Electrons and positrons are accelerated from the 3 km long SLAC linac and accumulated into two 2.2 km long storage rings, called HER (high-energy ring) and LER (low-energy ring) respectively. A fraction of electrons instead of being delivered to the HER is further accelerated to an energy of 30 GeV and sent to a target where positrons are produced. In proximity of the interaction region the beams are focused by a series of offset quadrupoles (Q1, Q2, Q4, Q5 in Figure 2.5) and bent by means of a pair of samarium-cobalt dipole magnets (B1), which allow the bunches to collide head-on. The tapered B1 dipoles, located at ± 21 cm

Parameters	Units	Design	June 2004
Energy (E) HER/LER	GeV	9.0/3.1	9.0/3.1
Current (I) HER/LER	A	0.75/2.15	1.55/2.45
β_y^*	mm	15-25	10.5
ξ_y HER/LER		0.03/0.03	0.046/0.0064
σ_x	μm	110	85
σ_y	μm	3.3	3.6
σ_z	mm	11	13
Peak luminosity	$\text{cm}^{-2}\text{s}^{-1}$	3.0	9.1
Integrated luminosity	$\text{fb}^{-1}/\text{month}$	3.3	16.0

Table 2.2: PEP-II beam parameters; both design values and values achieved in colliding beam operation during year 2004 are given. HER and LER refer to the high energy e^- and low energy e^+ ring, respectively. σ_x , σ_y and σ_z refer to the horizontal, vertical, and longitudinal r.m.s. size of the luminous region. The peak luminosity is proportional to $E I \xi_y / \beta_y^*$

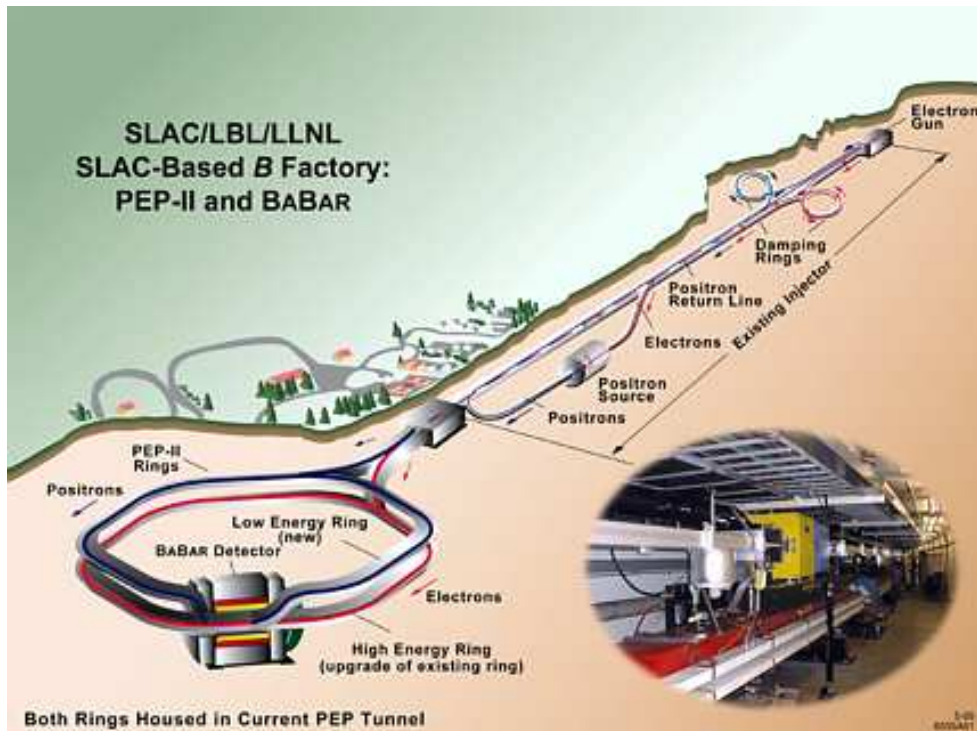


Figure 2.2: PEP-II overview.

on each side of the interaction point (IP), and the Q1 quadrupoles operate inside the field of the *BABAR* superconducting solenoid, while Q2, Q4, and Q5, are located outside or in the fringe field of the solenoid.

The interaction region is enclosed in a water-cooled beam pipe consisting of two thin layers of beryllium (0.83 mm and 0.53 mm) with a 1.48-mm water channel in between. To attenuate synchrotron radiation, the inner surface of the pipe is gold-plated (approximately 4 μm). The total thickness of the central beam pipe section at normal incidence

corresponds to 1.06 % of a radiation length. The beam pipe, the permanent magnets and the Silicon Vertex Tracker (SVT) are assembled and aligned and then enclosed in a 4.4-m long support tube. This rigid structure is inserted into the *BABAR* detector, spanning the IP.

2.1.2 PEP-II performances

Collisions in PEP-II started at the end of 1999, and since then *BABAR* has recorded 21 million $\Upsilon(4S)$ decays in RUN1 (Oct 1999 - Oct 2000), 66 million in RUN2 (Feb 2001 - Jun 2002), 34 million in RUN3 (Dec 2002 - Jun 2003) and 110 million in RUN4 (Sep 2003 - Jul 2004), for a total of 231 million $B\bar{B}$ pairs. The corresponding integrated luminosity is about 211 fb^{-1} , while the luminosity integrated off-peak in the first four runs is 21 fb^{-1} . The actual *BABAR* recorded luminosity is shown in Figure 2.3.

2005/04/04 10.10

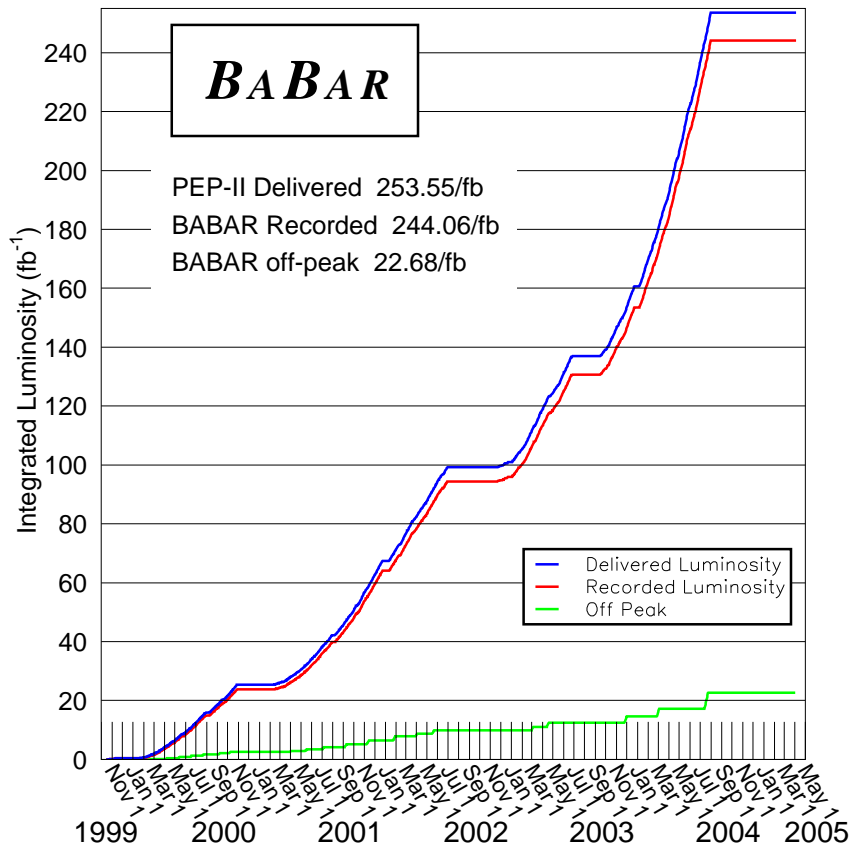


Figure 2.3: PEP-II delivered and *BABAR*-recorded integrated luminosity in RUN1 to RUN4 (from october 1999 to July 2004).

As shown in Table 2.2 [49, 50], PEP-II has already surpassed its design performances, both in terms of the instantaneous luminosity (by a factor 3) and the monthly integrated luminosity (by a factor 5), with fewer bunches than anticipated. Future upgrades that are currently being studied are expected to push the peak luminosity up to about $2.2 \times 10^{34} \text{ cm}^{-2}\text{s}^{-1}$ and will eventually allow the experiment to collect about 1 billion $B\bar{B}$ pairs

by 2008. With this huge dataset the desired sensitivity for many exciting measurements of CP -violating and rare B decays will be reached. The progresses in the instantaneous luminosity are mainly due to the increase of the beam currents and improved focusing and beam orbits. A significant improvement to the integrated luminosity has been achieved between December 2003 and March 2004 with the implementation of a novel mode of operation of PEP-II, called “trickle injection”, which increases the production of $B\bar{B}$ pairs by up to 50 percent (Figure 2.4). Until the end of 2003, PEP-II typically operated in a series of 40 minute fills during which the colliding beams coasted: at the end of each fill, it took about three to five minutes to replenish the beams for the next fill, and during this period the $BABAR$ data acquisition system had to be turned off for safety and dead-time reasons. With the new technique, the $BABAR$ detector can keep taking data virtually uninterrupted while the linac continuously injects electron and positron bunches (at a rate up to 10 Hz) into the two PEP-II storage rings to replace those that are lost in collisions in the $BABAR$ interaction region. After more than a year of testing, trickle injection was introduced first in the low energy ring in December 2003, bringing the B Factory a 30% increase in output. In March 2004 also trickle injection for the high energy ring has been implemented, thus providing an additional 15% increase. The advantages of this novel mode of operation go beyond just the increase in luminosity: continuous injection makes the storage of particles more stable, so that PEP-II rings are easier to operate and beam losses are far less frequent than with the previous operational mode. This result is very important since, after a loss of the stored beams, it takes approximately 15 minutes to refill the two beams.

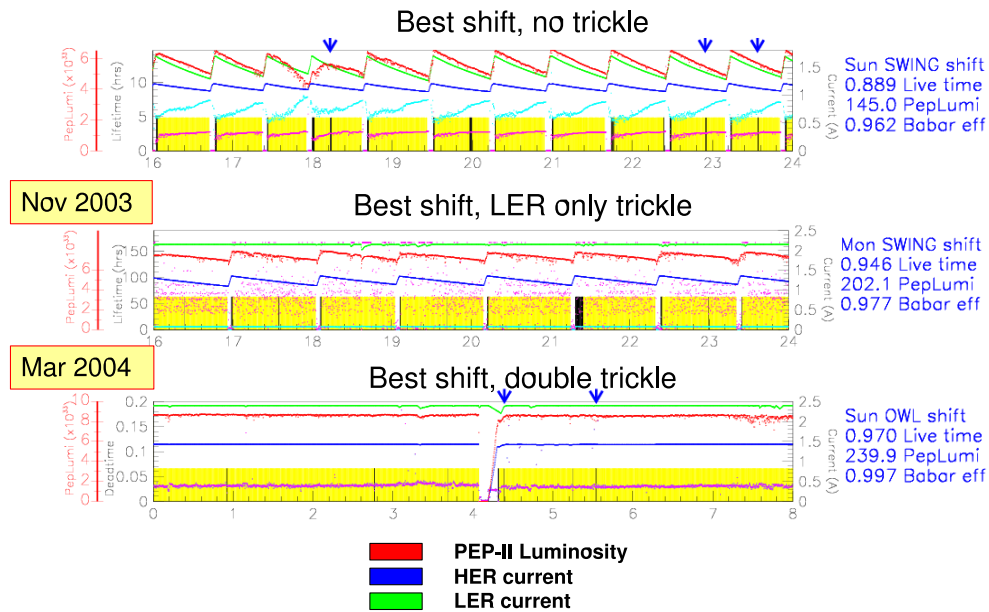


Figure 2.4: Comparison of the best 8-hour periods of data taking for three different mode of operation of PEP-II: no trickle injection (top), trickle injection of the low energy ring only (middle), and trickle injection of both beams (bottom).

2.2 Overview of the *BABAR* detector

To achieve the goal of performing accurate CP violation measurements there are many requirements:

- a large and uniform acceptance, in particular down to small polar angles relative to the boost direction, to avoid particle losses;
- excellent detection efficiency for charged particles down to 60 MeV/ c and for photons down to 25 MeV;
- high momentum resolution to separate small signals from background;
- excellent energy and angular resolution for the detection of photons from π^0 and radiative B decays in the range from 25 MeV to 4 GeV;
- very good vertex resolution, both transverse and parallel to the beam;
- identification of electrons and muons over a range of momentum, primarily for the detection of semi-leptonic decays used to tag the B flavor and for the study of semi-leptonic and rare decays;
- identification of hadrons over a wide range of momentum for B flavor tagging as well as for the separation of pions from kaons in decay modes like $B^0 \rightarrow K^\pm \pi^\mp$ and $B^0 \rightarrow \pi^+ \pi^-$ as well as in charm meson and τ decays;
- a highly efficient, selective trigger system with redundancy so as to avoid significant signal losses and systematic uncertainties.

The *BABAR* detector (Figure 2.5), designed and fabricated by a collaboration of 600 physicists of 75 institutions from 9 countries, meets all these requirements, as will be shown in the next sections of this chapter.

An overview of the polar angle (θ) coverage, the segmentation and performance of the *BABAR* detector systems is summarized in Table 2.3. The *BABAR* superconducting solenoid, which produces a 1.5 T axial magnetic field, contains a set of nested detectors, which are – going from inside to outside – a five layers Silicon Vertex Tracker (SVT), a central Drift Chamber (DCH) for charged particles detection and momentum measurement, a fused-silica Cherenkov radiation detector (DIRC) for particle identification, and a CsI(Tl) crystal electromagnetic calorimeter for detection of photons and electrons. The calorimeter has a barrel and an endcap which extends it asymmetrically into the forward direction (e^- beam direction), where many of the collision products emerge. All the detectors located inside the magnet have full acceptance in azimuth (ϕ). The flux return outside the cryostat is composed of 18 layers of steel, which increase in thickness outwards, and are instrumented (IFR) with 19 layers of planar resistive plate chambers (RPCs) or limited streamer tubes (LSTs) in the barrel and 18 in the end-caps. The IFR allows the separation of muons and charged hadrons, and also detect penetrating neutral hadrons. As indicated in Figure 2.5, the right-handed coordinate system is anchored to the main tracking system, the drift chamber, with the z -axis coinciding with its principal axis. This axis is offset relative to the beam axis by about 20 mrad in the horizontal plane. The positive y -axis points upward and the positive x -axis points away from the center of the PEP-II storage rings.

Since the average momentum of charged particles produced in B meson decay is below 1 GeV/ c , the errors on the measured track parameters are dominated by multiple Coulomb scattering, rather than the intrinsic spatial resolution of the detectors. Similarly, the detection efficiency and energy resolution of low energy photons are severely impacted by material in front of the calorimeter. Thus, special care has been given to keep the material

Table 2.3: Overview of the coverage, segmentation, and performance of the *BABAR* detector systems. The notation (C), (F), and (B) refers to the central barrel, forward and backward components of the system, respectively. Performance numbers are quoted for 1 GeV/ c particles, except where noted.

System	Polar angle coverage	Channels	Layers	Segmentation	Performance
SVT	[20.1,150.2] $^\circ$	150K	5	50-100 μm $r - \phi$ 100-200 μm z	$\sigma_{d_0} = 55 \mu\text{m}$ $\sigma_{z_0} = 65 \mu\text{m}$
DCH	[17.2,152.6] $^\circ$	7,104	40	6-8 mm drift distance	$\sigma_\phi = 1 \text{ mrad}$ $\sigma_{\tan \lambda} = 0.001$ $\sigma_{p_T}/p_T = 0.47\%$ $\sigma(dE/dx) = 7.5\%$
DIRC	[25.5,141.4] $^\circ$	10,752	1	$35 \times 17 \text{ mm}^2$ ($r\Delta\phi \times \Delta r$) 144 bars	$\sigma_{\theta_C} = 2.5 \text{ mrad}$ per track
EMC(C)	[27.1,140.8] $^\circ$	2×5760	1	$47 \times 47 \text{ mm}^2$ 5760 crystals	$\sigma_E/E = 3.0\%$ $\sigma_\phi = 3.9 \text{ mrad}$
EMC(F)	[15.8,27.1] $^\circ$	2×820		820 crystals	$\sigma_\theta = 3.9 \text{ mrad}$
IFR(C)	[47,123] $^\circ$	22K+2K	19+2	20-38 mm	90% μ^\pm eff. 6-8% π^\pm mis-id
IFR(F)	[20,47] $^\circ$	14.5K	18	28-38 mm	(loose selection, 1.5–3.0 GeV/ c)
IFR(B)	[123,154] $^\circ$	14.5K	18	28-38 mm	

in the active volume of the detector to a minimum. Figure 2.6 shows the distribution of material in the various detector systems in units of radiation lengths. Specifically, each curve indicates the material a particle traverses before it reaches the first active element of a specific detector system.

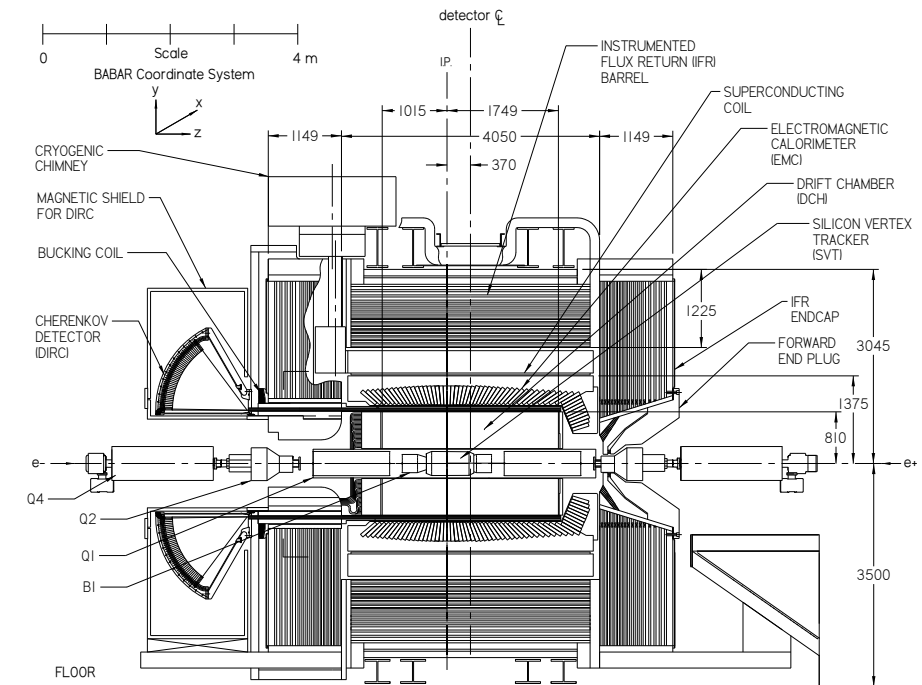
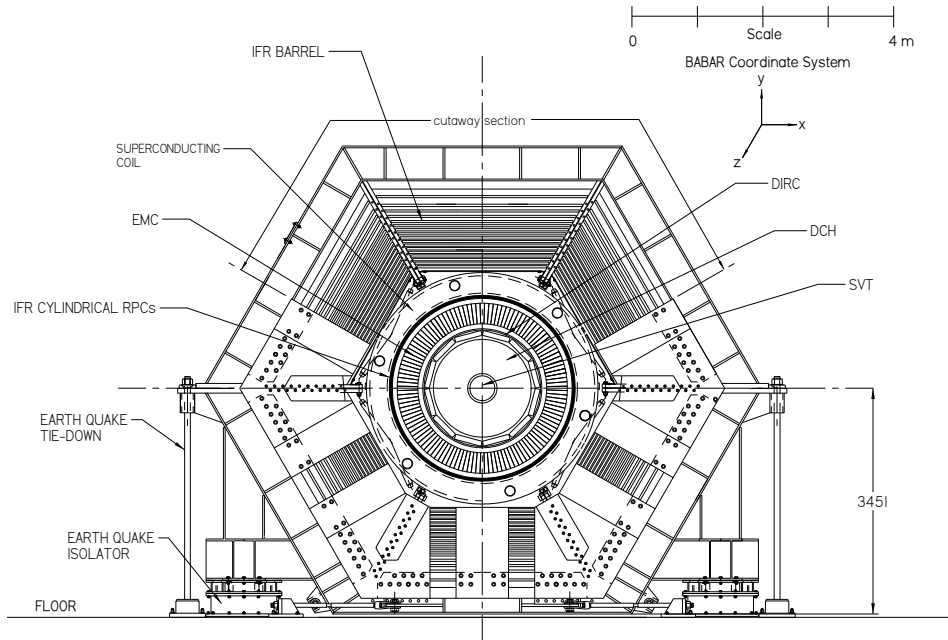


Figure 2.5: *BABAR* detector front view (top) and side view (bottom).

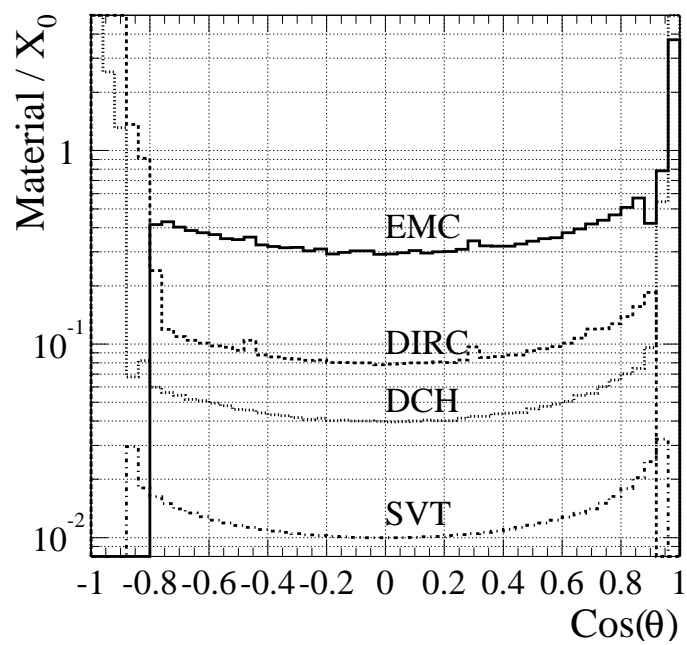


Figure 2.6: Amount of material (in units of radiation lengths) which a high energy particle, originating from the center of the coordinate system at a polar angle θ , traverses before it reaches the first active element of a specific detector system.

2.3 The Silicon Vertex Tracker

The Silicon Vertex Tracker (SVT) provides a precise measurement of the decay vertices and of the charged particle trajectories near the interaction region. The mean vertex resolution along the z -axis for a fully reconstructed B decay must be better than $80 \mu\text{m}$ in order to avoid a significant impact on the time-dependent CP asymmetry measurement precision; a $100 \mu\text{m}$ resolution in the $x - y$ transverse plane is necessary in reconstructing decays of bottom and charm mesons, as well as τ leptons.

The SVT also provides standalone tracking for particles with transverse momentum too low to reach the outer tracker, like soft pions from D^* decays and many charged particles produced in multi-body B meson decays. The choice of a vertex tracker made of five layers of double-sided silicon strip sensors allows a complete track reconstruction even in the absence of the drift chamber information.

Finally, the SVT supplies particle identification (PID) information both for low and high momentum tracks. For low momentum tracks the SVT dE/dx measurement is the only PID information available, for high momentum tracks the SVT provides the best measurement of the track angles, required to achieve the design resolution on the Cherenkov angle measured by the DIRC.

2.3.1 Detector layout

The Silicon Vertex Tracker is composed of five layers of $300 \mu\text{m}$ thick, double-sided microstrip detectors [51]. The total active silicon area is 0.96 m^2 and the material traversed by particles at normal incidence is $4\% X_0$. The geometrical acceptance is 90% of the solid angle in the c.m. system.

The silicon detectors and the associated readout electronics are assembled into mechanical units called *modules*. The inner three layers are barrel-shaped and are composed by six modules each. They are placed next to the interaction region, at radii 3.3, 4.0 and 5.9 cm from the beam axis (Figures 2.7 and 2.8), and provide an accurate measurement of the track impact parameters along z and in the $x - y$ plane. The outer two layers, composed by 16 and 18 modules (Figure 2.8), have a peculiar arch structure to reduce the incident angles of particles going in the forward and backward direction; their barrel parts are placed at radii between 12.7 and 14.6 cm from the beam axis. They permit an accurate polar angle measurement and, along with the inner three layers, enable standalone tracking for particles with low transverse momentum p_T . Full azimuthal coverage is obtained by partially overlapping adjacent modules, either by tilting them in ϕ by 5° (inner layers) or by staggering them (outer layers); this overlap is also advantageous for alignment. The polar angle coverage is $20.1^\circ < \theta_{\text{lab}} < 150.2^\circ$.

Each silicon detector consists of a high-resistivity n^- bulk on which are implanted p^+ strips on one side and orthogonally-oriented n^+ strips on the other side. The strips are AC-coupled to the electronics via integrated decoupling capacitor. The detectors are operated in reverse mode at full depletion, with bias voltage V_{bias} typically 10 V higher than the depletion voltage V_{depl} (which lies in the range 25 V – 35 V). The strips are biased through polysilicon resistors (4-20 $\text{M}\Omega$) and the detector active area is surrounded by an implanted guard ring that collects the edge currents and shapes the electric field in the active region. The n^+ strips insulation is provided by surrounding each n^+ strip with a p implant called *p-stop*, so as to achieve an inter-strip resistance greater than 100 $\text{M}\Omega$ at the operating bias voltage. The strip readout pitch varies with the layer (1..5) and the side of the sensors (z, ϕ) from a minimum of $50 \mu\text{m}$ to a maximum of $210 \mu\text{m}$.

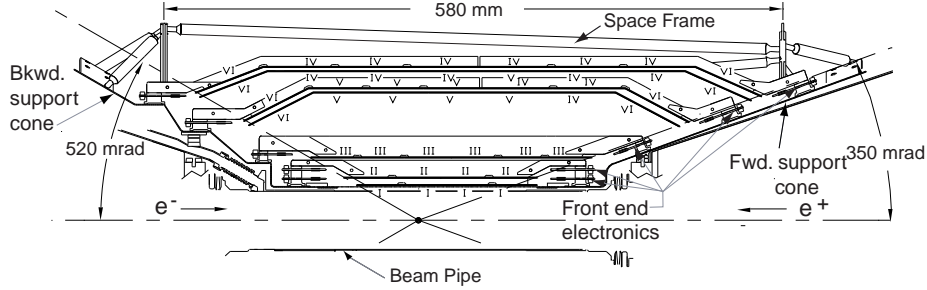


Figure 2.7: Schematic view of the SVT: longitudinal section.

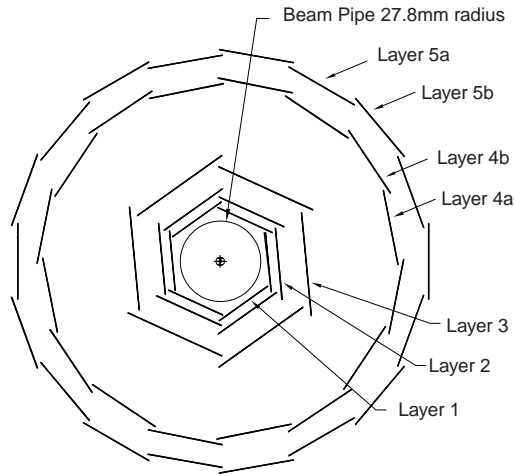


Figure 2.8: Schematic view of SVT: transverse section.

2.3.2 Detector performance

B decay vertex resolution

Figure 2.9 [52] shows the estimated error in the measurement of the difference along the z -axis between the vertices of two neutral B mesons, one of them being fully reconstructed and the other one only partially for flavor-tagging purposes. The RMS width of the distribution, equal to $190 \mu\text{m}$, meets the design expectation. It is dominated by the reconstruction of the tagging B vertex, the RMS vertex resolution for fully reconstructed B mesons being only $70 \mu\text{m}$.

Tracking efficiency and track parameter resolution

A comparison of the detected slow pion spectrum with the Monte Carlo prediction is presented in Figure 2.10 [48]. Based on this very good agreement the detection efficiency is estimated to be 20% for particles with transverse momenta of $50 \text{ MeV}/c$, rapidly increasing to over 80% at $70 \text{ MeV}/c$.

For the purpose of most physics analyses, charged tracks are defined by five parameters

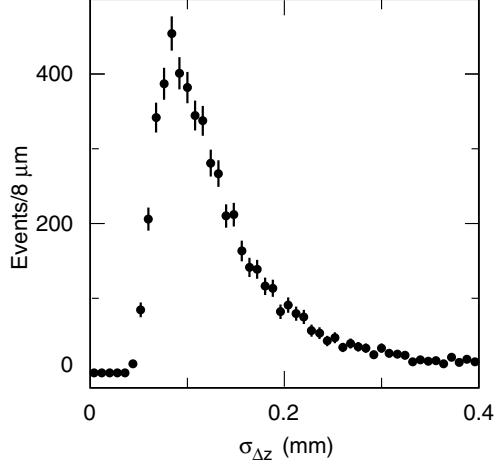


Figure 2.9: Distribution of the error on the difference Δz between two neutral B meson vertices for a sample of events in which one B^0 is fully reconstructed.

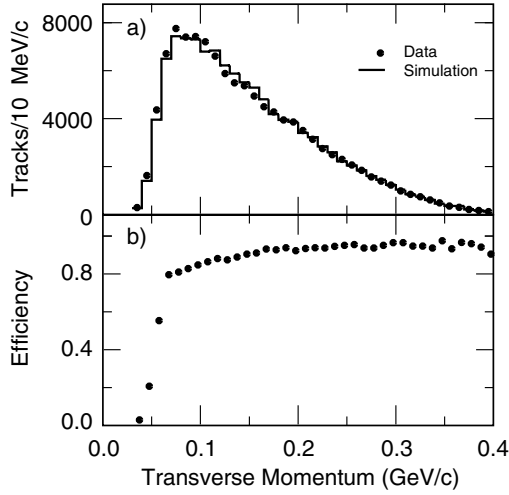


Figure 2.10: Monte Carlo studies of low momentum tracks in the SVT: (a) comparison between data and simulation of the transverse momentum spectrum of soft pions in $D^{*+} \rightarrow D^0 \pi^+$, and (b) efficiency for slow pions detection estimated from simulated events.

$(d_0, \phi_0, \omega, z_0, \tan \lambda)$ at the track's point of closest approach (POCA) to the z axis, and the associated error matrix. d_0 and z_0 are the distances from the origin to this POCA in the transverse (x, y) plane and along the z axis respectively. ϕ_0 is the angle between the transverse component of the track tangent vector at this POCA and the x axis. λ is the angle between the transverse plane and the track tangent vector at this POCA (the so called "dip" angle). ω is the curvature of the track. The charge of the track is incorporated in the signing convention for ω while the sign of d_0 is determined from the angular momentum of the track w.r.t. the x axis. d_0, ϕ_0, z_0 and $\tan \lambda$ resolutions are dominated by the resolution of the SVT, while ω (and therefore p_T) resolution is dominated by the drift chamber. Track parameter resolution is monitored online in promptly reconstructed Bhabha and $\mu^+ \mu^-$ events, and is further investigated offline, after the data is fully recon-

structed, on tracks in hadronic events or in dedicated cosmic ray runs. Figure 2.11 shows the d_0 , z_0 , ϕ_0 and $\tan \lambda$ resolutions determined from cosmic ray muons with transverse momenta above 3 GeV/c: they are measured to be

$$\begin{aligned}\sigma_{d_0} &= 23 \mu\text{m}, & \sigma_{\phi_0} &= 0.43 \text{ mrad} \\ \sigma_{z_0} &= 29 \mu\text{m}, & \sigma_{\tan \lambda} &= 0.53 \cdot 10^{-3}\end{aligned}$$

Figure 2.12 [52] shows the d_0 and z_0 resolutions as a function of p_T as determined from tracks in hadronic events. The d_0 and z_0 resolutions so measured are about 25 and 40 μm respectively at $p_T = 3 \text{ GeV}/c$, in good agreement with resolutions measured in cosmic ray studies.

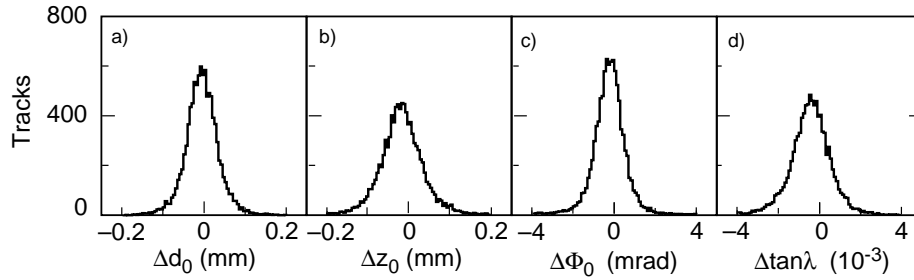


Figure 2.11: Distributions of the differences between the fitted track parameters of the two halves of cosmic ray muons, with transverse momenta above 3 GeV/c.

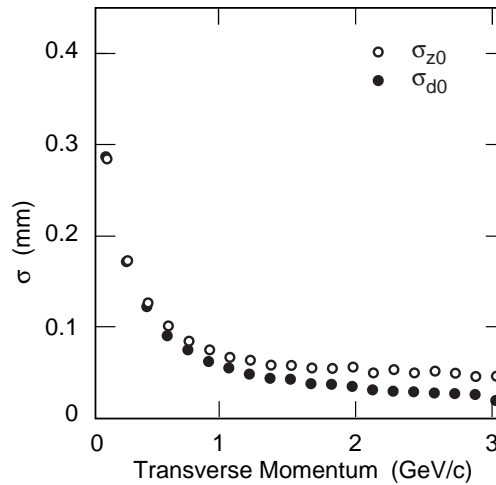


Figure 2.12: Impact parameter resolution of tracks reconstructed in multi-hadron events in the xy plane and along z for tracks in multi-hadron events as a function of transverse momentum.

dE/dx resolution

Limited particle ID information for low momentum particles that do not reach the drift chamber and the Cherenkov detector is provided by the SVT through the measurement of the specific ionization loss, dE/dx , as derived from the total charge deposited in each

silicon layer. It is computed as a truncated mean from the lowest 60% of the individual dE/dx measurements for tracks with at least 4 associated SVT hits. The resulting SVT dE/dx distribution as a function of momentum is shown in Figure 2.13 [53]. The superimposed Bethe-Bloch curves for the individual particle species have been determined using various particle control samples. The resolution achieved to date is typically about 14% for minimum ionizing particles, and a 2σ separation between kaons and pions can be achieved up to momenta of 500 MeV/ c .

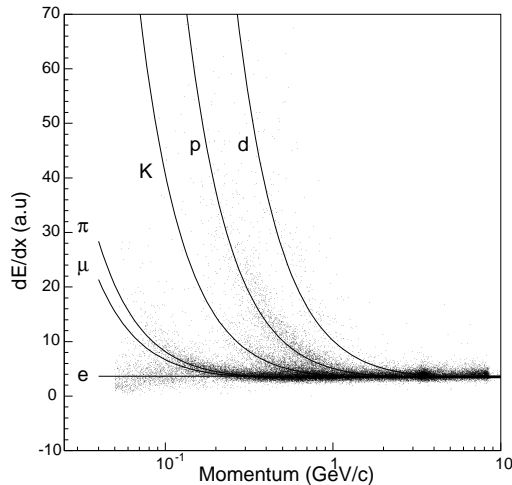


Figure 2.13: Energy loss per unit length (dE/dx) as measured in the SVT as a function of momentum. The enhancement of protons is due to beam-gas interactions. The vertical scale is arbitrary.

2.4 The Drift Chamber

The Drift Chamber (DCH) is the main tracking device for charged particles with transverse momenta p_T above ≈ 120 MeV/ c , providing the measurement of p_T from the curvature of the particle's trajectory inside the 1.5 T solenoidal magnetic field.

The DCH also allows the reconstruction of secondary vertices located outside the silicon detector volume, such as those from $K_s^0 \rightarrow \pi^+\pi^-$ decays. For this purpose, the chamber is able to measure not only the transverse coordinate, but also the longitudinal (z) position of tracks with good (~ 1 mm) resolution. Good z resolution also aids in matching DCH and SVT tracks, and in projecting tracks to the DIRC and the calorimeter.

For low momentum particles the DCH provides particle identification by measurement of ionization loss (dE/dx), thus allowing for K/π separation up to ≈ 700 MeV/ c . This capability is complementary to that of the DIRC in the barrel region, while it is the only mean to discriminate between different particle hypotheses in the extreme backward and forward directions which fall outside of the geometric acceptance of the DIRC.

Finally, the DCH provides real-time information to the charged particle trigger.

2.4.1 Detector layout

The final design adopted for the Drift Chamber, illustrated in Figure 2.14, consists of a 280 cm-long cylinder located within the volume inside the DIRC and outside the PEP-II support tube [54]. The inner radius is 23.6 cm and the outer radius is 80.9 cm. To

take into account PEP's asymmetric boost, the center of the chamber is displaced in the forward direction with respect to the IP by 36.7 cm, thus increasing the acceptance for forward-going tracks. The active volume provides charged particle tracking over the polar angle range $17.2^\circ < \theta_{\text{lab}} < 152.6^\circ$.

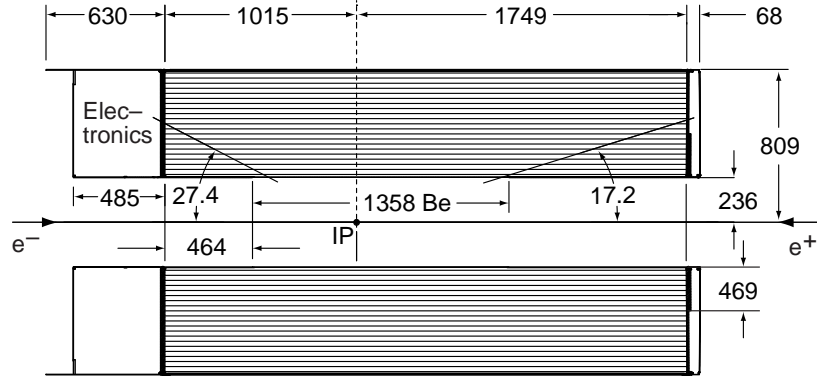


Figure 2.14: *BABAR* Drift Chamber side view. Lengths are in mm, angles in degrees.

The drift system consists of 7104 hexagonal cells, approximately 1.8 cm wide by 1.2 cm high, arranged in 40 concentric layers providing up to 40 spatial and ionization loss measurements for charged particles with p_T greater than 180 MeV/ c . The main properties of the gas system are listed in Table 2.4. In order to reduce the impact of multiple scattering on p_T resolution, material within the chamber volume has been minimised (0.2% X_0) using low-mass aluminum field-wires and a helium-based gas mixture. The inner wall has been kept thin (0.28% X_0) to improve the contribution of the high-precision measurement in the outer layer of the SVT to the p_T resolution, and minimize backgrounds due to photon conversions in the chamber wall. Material in the outer wall has also been minimised (0.6% X_0) so as not to degrade the DIRC and the EMC performances.

Table 2.4: Properties of helium-isobutane gas mixture at atmospheric pressure and 20°C (in *BABAR* the gas is operated at a small over pressure of 4 mbar). The drift velocity is given for operation without magnetic field, while the Lorentz angle is stated for a 1.5 T magnetic field. The anode-cathode operating potential difference is 1960 V.

Parameter	Values
Mixture He : C ₄ H ₁₀	80:20
Radiation Length	807 m
Primary Ions (m.i.p.)	21.2/cm
Drift Velocity	22 $\mu\text{m}/\text{ns}$
Avalanche gain	5×10^4
Lorentz Angle	32°
dE/dx Resolution	6.9%

2.4.2 Detector performance

Tracking efficiency and resolution

The drift chamber reconstruction efficiency has been measured on data in selected samples of multi-track events by exploiting the fact that tracks can be reconstructed independently

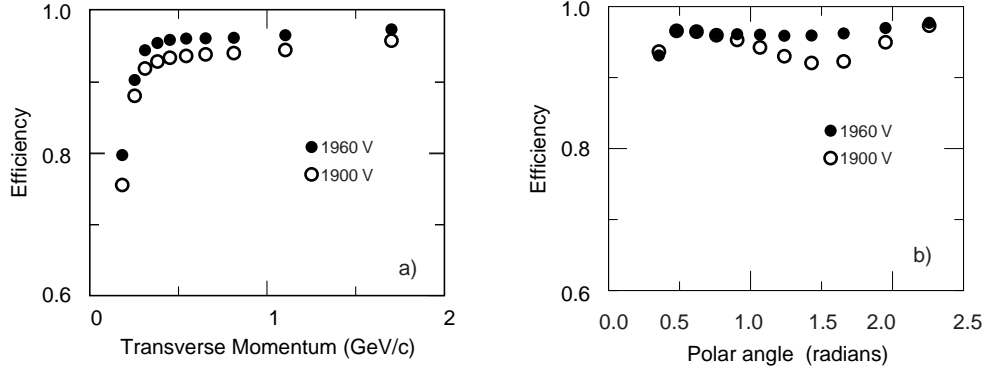


Figure 2.15: Track reconstruction efficiency in the drift chamber at operating voltages of 1900 V and 1960 V, as a function of transverse momentum (a) and polar angle (b).

in the SVT and the DCH. The absolute drift chamber tracking efficiency is determined as the fraction of all tracks detected in the SVT which are also reconstructed by the DCH when they fall within its acceptance. Its dependency on the transverse momentum and polar angle is shown in Figure 2.15 [48]. At the design voltage of 1960V the reconstruction efficiency of the drift chamber averages $98 \pm 1\%$ for tracks above 200 MeV/c and polar angle $\theta > 500$ mrad (29°). At the typical operating voltage of 1930V it decreases by about 2%.

The p_T resolution, directly related to the curvature (ω) resolution, is measured as a function of p_T in cosmic ray studies (see Figure 2.16 [55]). The data are well represented by a linear function:

$$\frac{\sigma_{p_T}}{p_T} = (0.13 \pm 0.01)\% \cdot p_T + (0.45 \pm 0.03)\%, \quad (2.1)$$

where p_T is measured in GeV/c. The first contribution, dominating at high p_T , comes from the curvature error due to finite spatial measurement resolution; the second contribution, dominating at low momenta, is due to multiple Coulomb scattering.

dE/dx Resolution

The specific ionization loss dE/dx for charged particles traversing the drift chamber is derived from the total charge deposited in each drift cell. It is computed as a truncated mean from the lowest 80% of the individual dE/dx measurements; various corrections are applied to remove several sources of bias (such, for instance, changes in gas gain due to temperature and pressure variations) that would degrade the accuracy of the primary ionization measurement. The left plot of Figure 2.17 shows the distribution of the reconstructed and corrected dE/dx from the drift chamber as a function of track momenta. The superimposed Bethe-Bloch curves for the individual particle species have been determined using various particle control samples. The resolution achieved to date is typically about 7.5% (as shown in the right plot of Figure 2.17 for e^\pm from Bhabha scattering), limited by the number of samplings and Landau fluctuations. A 3σ separation between kaons and pions can be achieved up to momenta of about 700 MeV/c [55].

2.5 The Cherenkov light detector

The Detector of Internally Reflected Cherenkov radiation (DIRC) is employed primarily for the separation of pions and kaons from about 500 MeV/c to the kinematic limit of

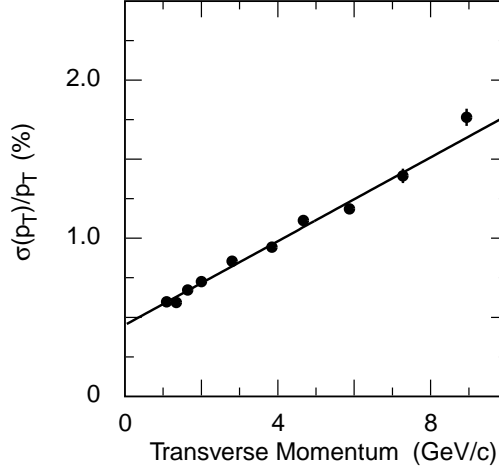


Figure 2.16: p_T resolution determined from cosmic ray muons.

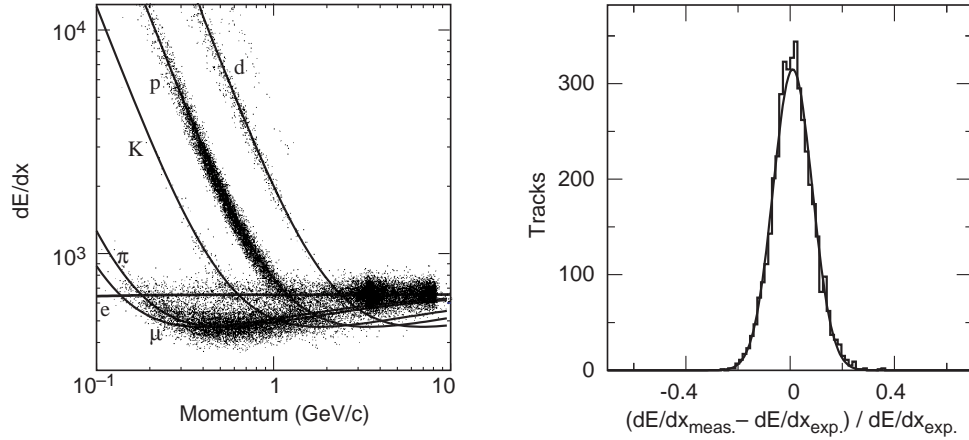


Figure 2.17: Left: reconstructed dE/dx as a function of track momenta. Right: difference between the measured and expected dE/dx for e^\pm from Bhabha scattering.

4 GeV/c. Excellent K/π separation is needed to tag with very low misidentification probability the flavor of neutral B mesons decaying to final states containing charged Kaons, where the charge of the Kaon determines the flavor of the B . It is also fundamental in the analysis described in this thesis, since it allows to discriminate between B decay channels that are otherwise very similar from a kinematical point of view, like $B \rightarrow D^0 K$ and $B \rightarrow D^0 \pi$.

2.5.1 Detector layout

The DIRC is a novel type of ring-imaging Cherenkov detector, based on the principle that the magnitudes of angles are maintained upon reflection from a flat surface [56]. Figure 2.18 shows a schematic of the DIRC geometry, while Figure 2.19 illustrates the principles of light production, transport, and imaging.

The radiator material of the DIRC is synthetic fused silica (refraction index $n = 1.473$)

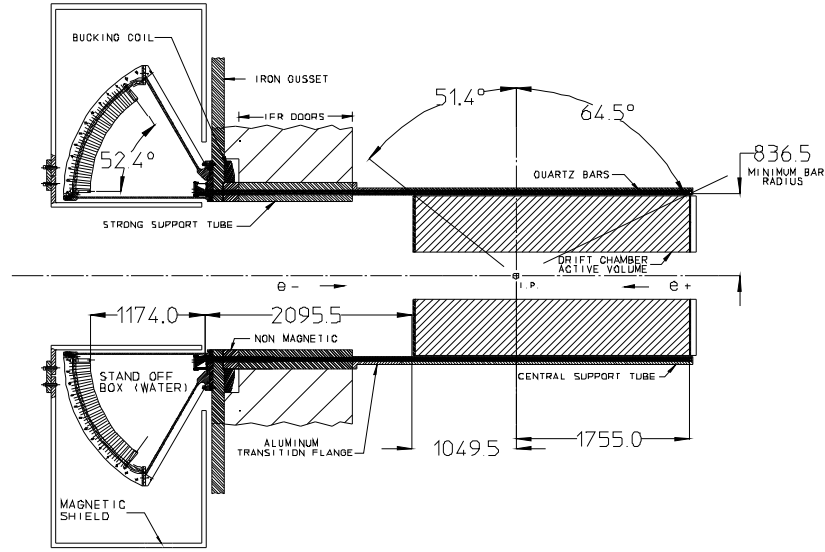


Figure 2.18: Schematics of the DIRC mechanical support structure.

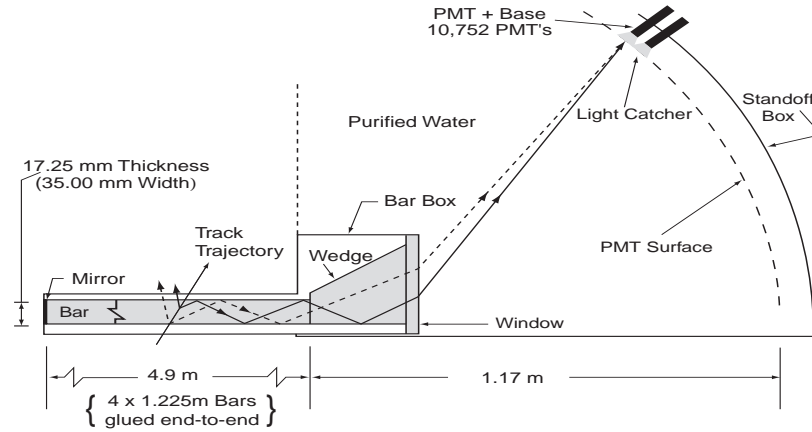


Figure 2.19: Schematics of the DIRC fused silica radiator bar and imaging region.

in the form of 144 long, thin bars with regular rectangular cross section. The bars, which are 17-mm-thick, 35-mm-wide and 4.9-m-long, are arranged in a 12-sided polygonal barrel, each side being composed of 12 adjacent bars. The solid angle subtended by the radiator bars corresponds to 94% of the azimuth and 83% of the cosine of the polar angle in the center-of-mass system. The total thickness of the DIRC material (bars and support structure) at normal incidence ($\theta = 90^\circ$) is only 8 cm, corresponding to 17% X_0 . Such a thin Cherenkov detector allows to have, at the same time, a large inner tracking volume, which is needed to achieve the desired momentum resolution, and a compact outer electromagnetic calorimeter, with improved angular resolution and limited costs.

The bars serve both as radiators and as light pipes for the portion of the light trapped in the radiator by total internal reflection (the internal reflection coefficient of the bar surfaces is greater than 0.9992 per bounce). A charged particle with velocity $v > c/n$, traversing the fused silica bar, generates a cone of Cherenkov photons of half-angle θ_c

with respect to the particle direction, where $\cos\theta_c = 1/\beta n$, $\beta = v/c$. For particles with $\beta \approx 1$, some photons will always lie within the total internal reflection limit, and will be transported to either one or both ends of the bar, depending on the particle incident angle. To avoid having to instrument both bar ends with photon detectors, a mirror is placed at the forward end, perpendicular to the bar axis, to reflect incident photons to the backward (instrumented) bar end.

Once photons arrive at the instrumented end, most of them emerge into an expansion region filled with 6000 litres of purified water ($n = 1.346$), called the stand-off box. A fused silica wedge at the exit of the bar reflects photons at large angles and thereby reduces the size of the required detection surface. The photons are detected by an array of densely packed photomultiplier tubes (PMTs), each surrounded by reflecting “light catcher” cones to capture light which would otherwise miss the PMT active area. The PMTs, arranged in 12 sectors of 896 phototubes each, have a diameter of 29 mm and are placed at a distance of about 1.2 m from the bar end. The expected Cherenkov light pattern at this surface is essentially a conic section, whose cone opening-angle is the Cherenkov production angle modified by refraction at the exit from the fused silica window.

The time taken for the photon to travel from the point of origin to the PMT is also related to the photon propagation angle $(\alpha_x, \alpha_y, \alpha_z)$ with respect to the bar axis. As the track position and angles are known from the tracking system, these three α angles can be used to (over-)determine the Cherenkov angle θ_c . This over-constraint on the angles is particularly useful in suppressing hits from beam-generated background and from other tracks in the same event, and also in resolving some ambiguities in the association between the PMT hits and the track (for instance, the forward-backward ambiguity between photons that have or haven’t been reflected by the mirror at the forward end of the bars). The relevant observable to distinguish between signal and background photons is the difference between the measured and expected photon time, δt_γ . It is calculated for each photon using the track-time of the PMT and the photon propagation time within the bar and the water filled standoff box. The resolution on this quantity, as measured in dimuon events (Figure 2.21(b) [48]), is 1.7 ns, close to the intrinsic 1.5 ns transit time spread of the photoelectrons in the PMTs. Applying the time information substantially improves the correct matching of photons with tracks and reduces the number of accelerator induced background hits by approximately a factor 40, as can be seen in Figure 2.20 [57].

2.5.2 Detector performance

In the absence of correlated systematic errors the resolution $\sigma_{\theta_{C,\text{track}}}$ on the track Cherenkov angle scale as

$$\sigma_{\theta_{C,\text{track}}} = \sigma_{\theta_{C,\gamma}} / \sqrt{N_\gamma}, \quad (2.2)$$

where $\sigma_{\theta_{C,\gamma}}$ is the single photon Cherenkov angle resolution and N_γ is the number of photons detected.

The single photon Cherenkov angle resolution has been measured in dimuon events to be 10.2 mrad (Figure 2.21(a) [48]). The main contributions to it come from the geometry of the detector (the size of the bars, the diameter of the PMTs and the distance between the bars and the PMTs give a 7 mrad contribution) and from the spread of the photon production angle, dominated by a 5.4 mrad chromatic term.

Figure 2.22 shows the number of photons detected as a function of the polar angle. It increases from a minimum of about 20 at the center of the barrel ($\theta \approx 90^\circ$) to well over 50 in the forward and backward directions, corresponding to the fact that the pathlength in the radiator is longer for tracks emitted at large dip angles (therefore the number of Cherenkov photons produced in the bars is greater) and the fraction of photons trapped by total internal reflection rises. This feature is very useful in the *BABAR* environment,

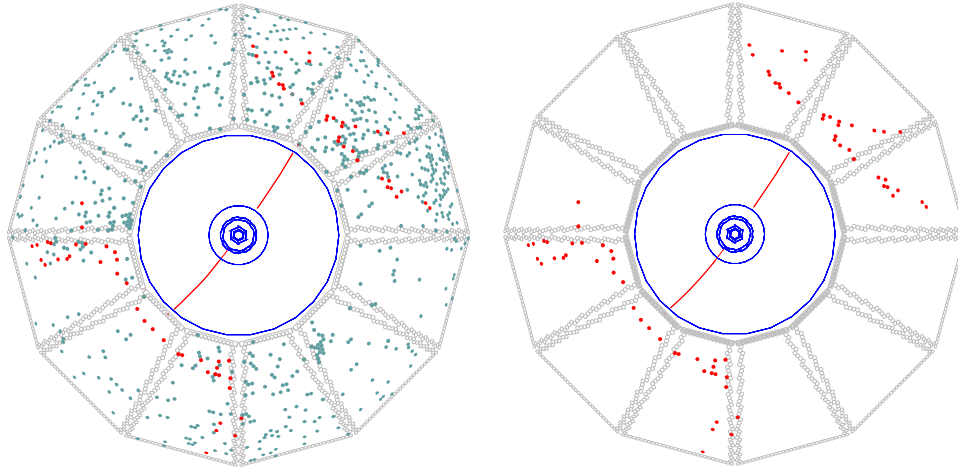


Figure 2.20: Display of one $e^+e^- \rightarrow \mu^+\mu^-$ event reconstructed in *BABAR* with two different time cuts. On the left, all DIRC PMTs that were hit within the ± 300 ns trigger window are shown. On the right, only those PMTs that were hit within 8 ns of the expected Cherenkov photon arrival time are displayed.

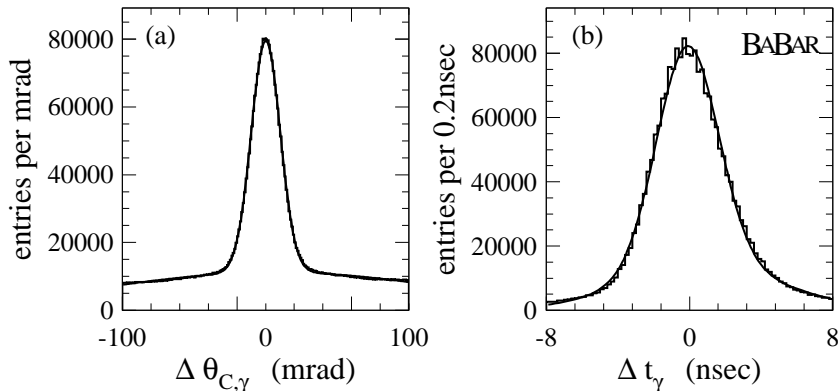


Figure 2.21: Difference between (a) the measured and the expected Cherenkov angle for single photons and (b) the measured and expected photon arrival time, as measured in muons produced in dimuon events.

where - due to the boost of the center-of-mass - particles are emitted preferentially in the forward direction. The bump at $\cos\theta = 0$ is a result of the fact that for tracks at small angles internal reflection of the Cherenkov photons occurs in both the forward and backward direction. The small decrease of the number of photons from the backward direction to the forward one is a consequence of the photon absorption along the bar before reaching the stand-off box in the backward end.

The combination of the single photon Cherenkov angle resolution, the distribution of the number of detected photons versus polar angle and the polar angle distribution of charged tracks yields a typical track Cherenkov angle resolution which is about 2.5 mrad for muons in di-muon events. A similar average resolution is found for charged kaons and pions in a sample of 430000 $D^{*+} \rightarrow D^0\pi^+(D^0 \rightarrow K^-\pi^+)$ decays reconstructed in data, where K^\mp/π^\pm tracks are identified through the charge correlation with the π^\pm from the

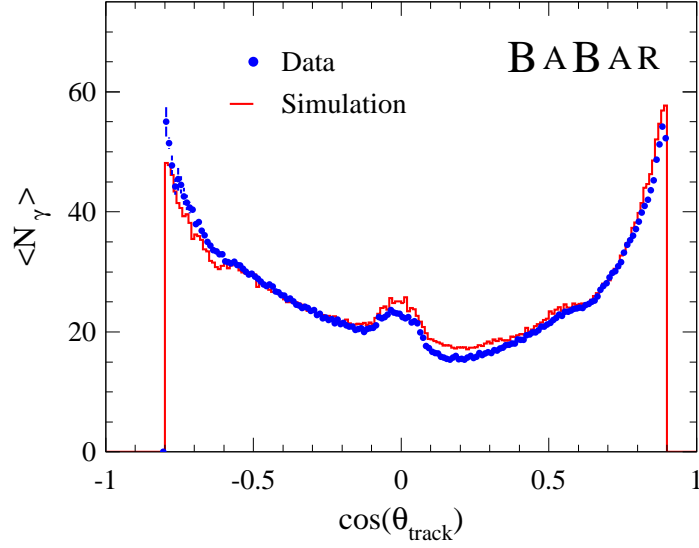


Figure 2.22: Number of detected photoelectrons versus track polar angle for reconstructed di-muon events in data and simulation.

$D^{*\pm}$ decay. From the measured single track resolution *vs.* momentum and the difference between the expected Cherenkov angles of charged pions (θ_C^π) and kaons (θ_C^K), the pion-kaon separation power of the DIRC, $|\theta_C^K - \theta_C^\pi|/\sigma_{\theta_C}$, can be inferred. As shown in Figure 2.23, the separation between kaons and pions at 3 GeV/ c is about 4.3σ .

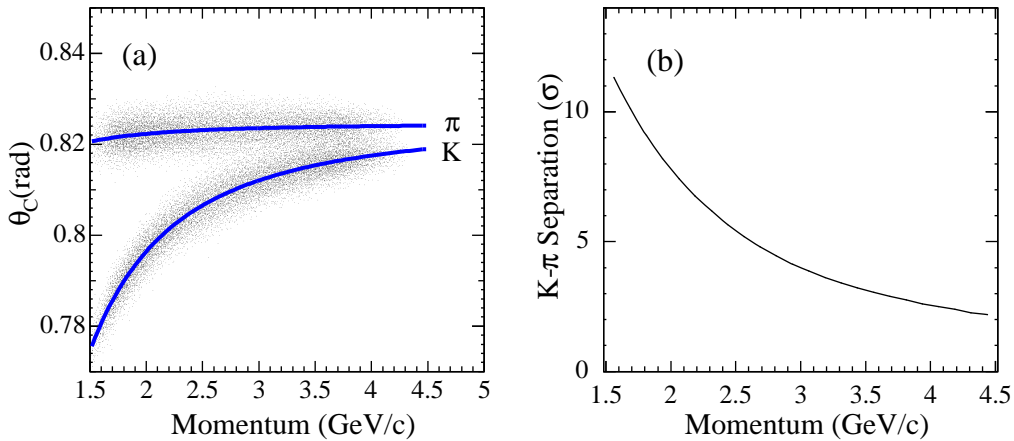


Figure 2.23: (a) The measured Cherenkov angle for pions (upper band) and kaons (lower band) from $D^* \rightarrow D^0\pi$, $D^0 \rightarrow K\pi$ decays reconstructed in data. The curves show the expected angle θ_C as a function of laboratory momentum, for the K and π mass hypothesis. (b) The average difference between the expected value of θ_C for kaons and pions, divided by the uncertainty, as a function of momentum.

2.6 The Electromagnetic Calorimeter

The *BABAR* electromagnetic calorimeter (EMC) is designed to detect and measure electromagnetic showers with high efficiency and very good energy and angular resolution over an energy range between 20 MeV (low-energy photons from π^0 mesons originating in B decays) and 9 GeV (electrons from Bhabha scattering). It is also the primary sub-detector providing electron-hadron separation.

Energy deposit clusters in the EMC with lateral shape consistent with the expected pattern from an electromagnetic shower are identified as photons when they are not associated to any charged tracks extrapolated from the SVT and the drift chamber, and as electrons if they are matched to a charged track and the ratio between the energy E measured in the EMC and the momentum p measured by the tracking system is $E/p \approx 1$.

The efficient reconstruction of extremely rare decays of B mesons containing π^0 s (e.g. $B^0 \rightarrow \pi^0\pi^0$) poses the most stringent design requirements on energy resolution of order 1% while excellent photon efficiency at low energy (~ 20 MeV) is required for efficient reconstruction of B meson decays containing multiple π^0 and η . Similar precision is required for efficient separation of electrons and hadrons with purities required at the 0.1% level for momentum as low as 500 MeV/ c . The π^0 mass resolution is dominated by the energy resolution at low energies (below 2 GeV) and by the angular resolution at high energies (above 2 GeV). The angular resolution is required to be a few milliradians in order to maintain good m_π^0 resolution ($\sigma_{m_\pi^0} \approx 6.5$ MeV) at all energies. The need for high efficiency requires hermetic coverage of the acceptance region while excellent resolution is achieved by minimising the material in front of and between the active detector elements.

2.6.1 Detector layout

The *BABAR* electromagnetic calorimeter (Figure 2.24) is a total-absorption calorimeter composed of 6580 CsI crystals doped with thallium iodide at about 1000 ppm [58]. The main properties of CsI(Tl) are summarized in Table 2.5: the high light yield and small Molière radius give the excellent energy and angular resolution required, while the short radiation length guarantees complete shower containment at *BABAR* energies with a relatively compact design. Furthermore, the high light yield and peak of the emission spectrum permit an efficient use of a silicon photodiode readout.

Each crystal is a truncated trapezoidal pyramid, with thickness between 29.6 cm ($16 X_0$) and 32.4 cm ($17.5 X_0$) and typical front face area 5×5 cm². The crystals are arranged quasi-projectively in a barrel structure of 48 θ rows by 120 crystals in azimuth (ϕ), with an inner radius of 90 cm. The forward end is closed by a separable end-cap capable of holding nine additional rows. This geometry provides full azimuthal coverage, while the polar angle coverage is $15.8^\circ < \theta_{\text{lab}} < 140.8^\circ$. To minimize the material in front of the calorimeter, the support structure of the crystals (which is made in carbon fiber) and the front-end electronics are located at the outer radius of the EMC. To recover the small fraction of light that is not internally reflected by the crystal surface, each crystal is wrapped with a diffuse reflective material (TYVEK). The scintillation light generated inside each crystal is detected by two independent 2×1 cm² silicon PIN photodiodes epoxied to its rear face.

2.6.2 Detector performance

Energy resolution

The limiting energy resolution of a homogeneous calorimeter is determined by fluctuations in the electromagnetic shower propagation and in the case of the *BABAR* crystal detector is empirically described as the quadratic sum of a stochastic term σ_1 and a constant term

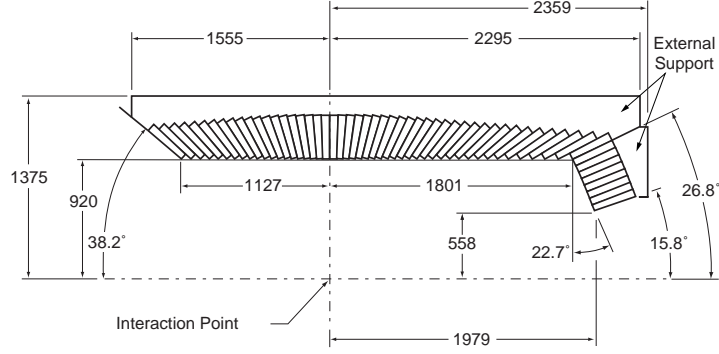


Figure 2.24: The crystal geometry of the Electromagnetic Calorimeter.

Parameter	Value
Radiation Length	1.86 cm
Molière Radius	3.8 cm
Density	4.53 g/cm ³
Light Yield	50000 γ /MeV
Light Yield Temperature Coefficient	0.28 %/°C
Peak Emission λ_{\max}	565 nm
Refractive Index (λ_{\max})	1.79

Table 2.5: Properties of CsI(Tl).

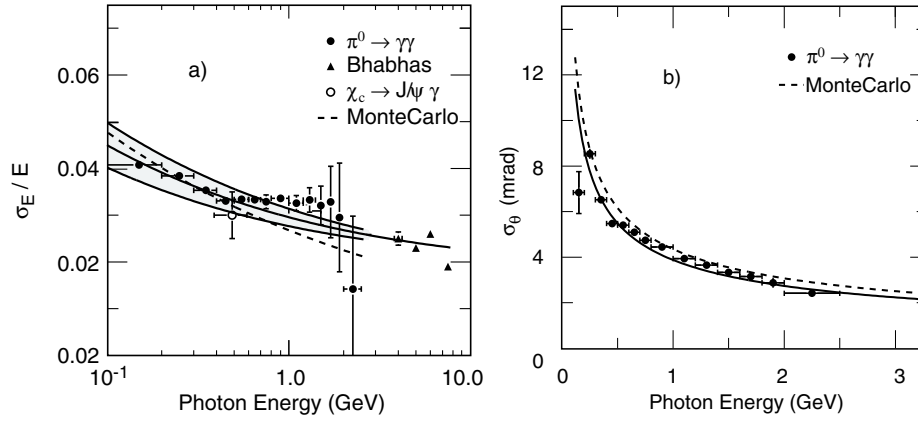


Figure 2.25: Left: the energy resolution for the electromagnetic calorimeter measured using photon and electron candidates. The solid curve is a fit to equation 2.3 and the shaded area denotes the one sigma error on the fit.

Right: the angular resolution for the electromagnetic calorimeter measured using photon candidates originating in π^0 and η decays. The solid curve is a fit to equation 2.5.

σ_2 :

$$\frac{\sigma_E}{E} = \sigma_1 E^{-\frac{1}{4}} \oplus \sigma_2 \quad (2.3)$$

The stochastic term $\sigma_1 E^{-\frac{1}{4}}$, which is dominant at low energies, arises primarily from fluctuations in photon statistics, but depends also on electronic noise in the readout chain and on the presence of beam-generated background. The constant term σ_2 , dominant at higher energies, arises from several effects of which the main are fluctuations in shower containment due to leakage out the rear of the crystal or absorption in the material between and in front of the crystals, and uncertainties in the calibrations.

In *BABAR* the energy resolution as a function of energy is measured on data on selected control samples, including electrons and positrons from Bhabha scattering (energies between 3 and 9 GeV), photons from π^0 and η decays (energies below 2 GeV) and from the decay $\chi_{c1} \rightarrow J/\psi \gamma$ ($E \approx 500$ MeV). At low energies the resolution is determined through weekly calibrations performed with a radioactive source ($^{16}\text{O}^*$) of 6.13 MeV photons. A fit to the resolution dependence on the energy with the empirical parameterization of Eqn 2.3, shown in Figure 2.25(a) [58], yields:

$$\frac{\sigma_E}{E} = \frac{(2.32 \pm 0.30)\%}{\sqrt[4]{E(\text{GeV})}} \oplus (1.85 \pm 0.12)\%, \quad (2.4)$$

The stochastic term is dominant for energies below about 2.5 GeV; above 2.5 GeV the constant term starts to be the limiting factor for the energy resolution.

Angular resolution

The angular resolution is determined by the transverse crystal size and the distance from the interaction point, and improves as the transverse size of the crystal decreases. On the other hand, since the electromagnetic shower has a natural lateral spread of the order of the Molière radius, the energy resolution would degrade if the transverse crystal size were chosen significantly smaller than the Molière radius, due to summing of the electronic noise from several crystals. The best compromise is obtained by choosing the transverse size of the crystals to be comparable to the Molière radius: this choice allows to achieve the required angular resolution² at low energies while maintaining the total number of crystals and readout channels limited to an acceptable noise and cost level.

Figure 2.25(b) [58] shows the angular resolution measured as a function of energy. The decays of π^0 and η candidates in which the two photons in the decay have approximately equal energy are used to infer angular resolution. It varies between about 12 milliradians at low energies and 3 milliradians at high energy. The data fit the empirical parameterisation:

$$\sigma_{\theta,\phi} = \left(\frac{(3.87 \pm 0.07)}{\sqrt{E(\text{GeV})}} + (0.00 \pm 0.04) \right) \text{ mrad} \quad (2.5)$$

π^0 Mass and Width

Figure 2.26 [48] shows the two-photon invariant mass for π^0 candidates. The π^0 candidates are taken from hadronic B meson decays. The invariant mass is stable to less than 1 % over the full photon energy range. The width of $6.9 \text{ MeV}/c^2$ compares to a Monte Carlo estimate of $6.8 \text{ MeV}/c^2$ in hadronic B meson events.

Electron-Hadron separation

Electron-hadron separation is accomplished by use of the shower energy, lateral shower shape and incident track parameters. The comparison of shower energy and incident momentum (E/p) is the most significant separation variable. Figure 2.27 [48] shows the electron efficiency and pion misidentification rate for different momenta using a very tight

²Few milliradians

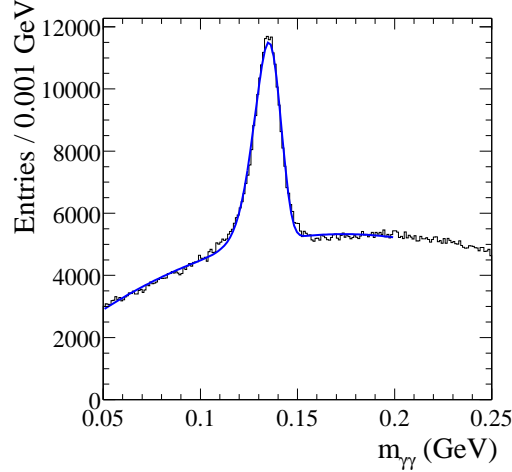


Figure 2.26: The π^0 mass peak reconstructed from photon candidates in hadronic events. The photon candidates are required to have an energy of at least 30 MeV and the energy of the π^0 must be greater than 300 MeV to reduce combinatoric backgrounds. The solid line is a fit to the data.

selection algorithm. The efficiency of electron identification is measured using electrons from radiative Bhabhas and $\gamma\gamma \rightarrow e^+e^-$ events. The pion misidentification probability is measured in three-prong τ decays. For momenta above 1 GeV/c the electron identification efficiency of this algorithm is 90.8 % with an average pion misidentification of 0.2 %.

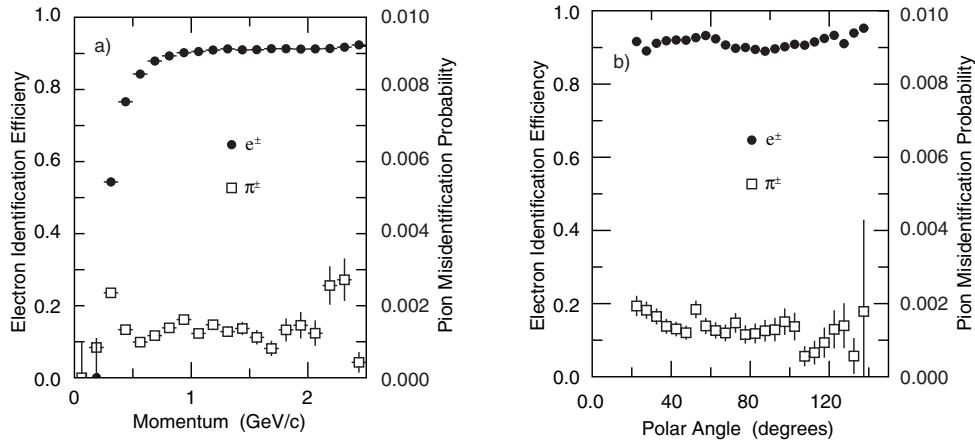


Figure 2.27: The electron efficiency and pion mis-identification rate for different momenta (left) and polar angles (right).

2.7 The Instrumented Flux Return

The Instrumented Flux Return (IFR) is designed to identify muons and neutral hadrons (primarily K_L^0 and neutrons). The principal requirements for IFR are large solid angle coverage, good efficiency and high background rejection for muons down to momenta

below 1 GeV/c. For neutral hadrons, high efficiency and good angular resolution are most important.

2.7.1 Detector layout

The IFR uses the steel flux return of the magnet as muon filter and hadron absorber. Single gap resistive plate chambers (RPC) with two-coordinate readout, operated in limited streamer mode constitute the active part of the detector [59]. The RPC are installed in the gaps of the finely segmented steel of the six barrel sectors and the two end-doors of the flux return, as illustrated in Figure 2.28. The steel segmentation has been optimised on the basis of Monte Carlo studies of muon penetration and charged and neutral hadron interactions. The steel is segmented into 18 plates, increasing in thickness from 2 cm of the inner 9 plates to 10 cm of outermost plates for a total 65 cm. In addition, two layers of cylindrical RPCs are installed between the EMC and the magnet cryostat to detect particles exiting the EMC.

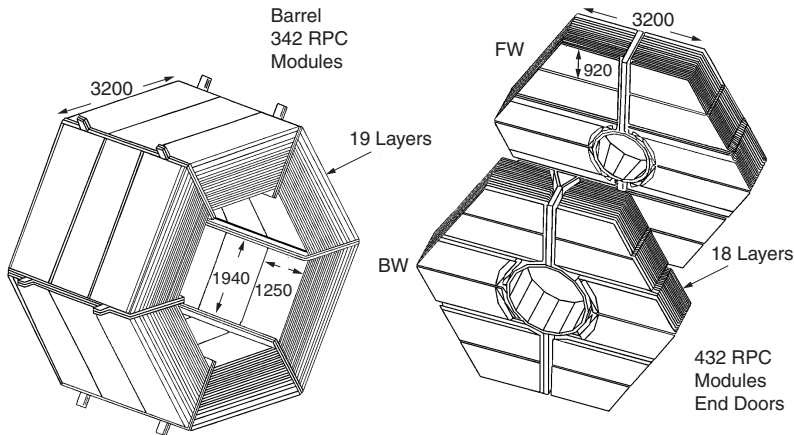


Figure 2.28: Overview of the IFR Barrel sectors and forward and backward end-doors; the shape of the RPC modules and the way they are stratified is shown.

Soon after the installation (which took place in Summer 1999), the efficiency of a significant fraction of the chambers (initially greater than 90%) has started to deteriorate at a rate of 0.5-1%/month. In order to solve some of the inefficiency problems an extensive improvement program has been developed and is making relevant advances. The RPCs in the forward end-cap region have been replaced in Summer 2002 with new ones based on the same base concept but with improved fabrication technique and quality controls: their efficiency has not significantly decreased over 2 years of running. The RPCs in the barrel region are being replaced with limited streamer tube (LST) detectors: two of the six sextants of the barrel have been replaced in Summer 2004 while the remaining four sextants should be replaced next year. Extensive quality control studies have been performed to check the reliability of these detectors, which are expected to operate until the end of the experiment with $\approx 90\%$ efficiency, as measured in cosmic ray runs.

2.7.2 Detector performance

Muon Identification

Charged particles that are reconstructed in the tracking systems and meet the criteria for minimum ionising particles in the EMC (i.e. tracks not depositing large amounts of

energy) are potential muon candidates. Their trajectories are extrapolated to the IFR taking into account the non-uniform magnetic field, multiple scattering and the average energy loss. The projected intersections with the RPC or LST planes are computed and for each readout plane all clusters (groups of adjacent hits in one of the two readout coordinates) detected within a maximum distance from the predicted intersection are associated with the track. For each cluster in the IFR associated with a charged track a number of variables are combined in a global likelihood function to discriminate muons from charged hadrons:

- the total number of interaction lengths traversed from the IP to the last RPC or LST layer with an associated cluster
- the difference between this measured number of interaction lengths and the number of interaction lengths predicted for a muon of the same momentum and angle
- the average number and the r.m.s. of the distribution of RPC or LST hits per layer
- the χ^2 for the geometric match between the projected track and the centroids of clusters in different RPC or LST layers

The performance of muon selection has been tested on samples of muons from $\mu\mu e e$ and $\mu\mu\gamma$ final states and pions from 3-prong τ decays and $K_s^0 \rightarrow \pi^+\pi^-$ decays. The selection of these control samples is based on kinematic variables, and not on variables used for muon selection. The muon identification efficiency and the pion misidentification probability as a function of the track momentum and polar angle are compared in Figure 2.29 for a loose selection criteria applied to the global likelihood: above 1 GeV/c the muon efficiency is greater than 80% with a pion misidentification probability between 5 and 10%.

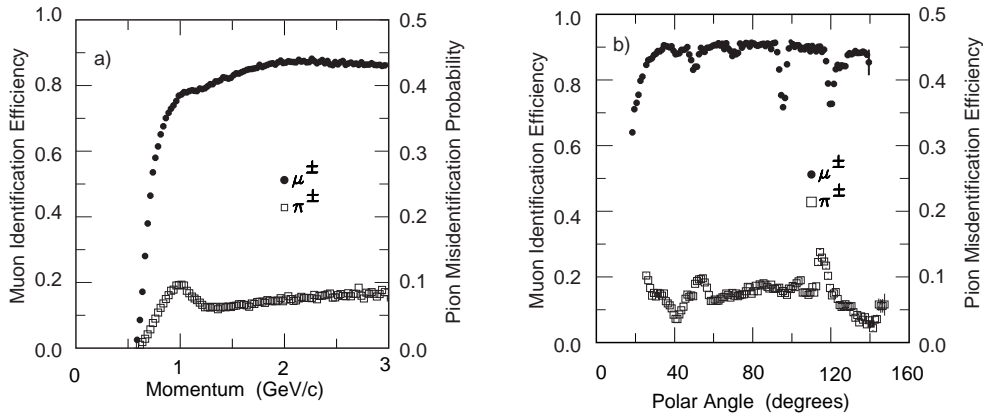


Figure 2.29: The muon efficiency and pion mis-identification rate for different momenta (left) and polar angles (right) obtained with loose selection criteria.

K_L^0 and Neutral Hadron Detection

K_L^0 and other neutral hadrons interact in the steel of the IFR and can be identified as clusters that are not associated with a charged track. Since neutral hadrons can interact also in the electromagnetic calorimeter, information from the EMC and the IFR is combined: neutral showers in the EMC are associated with the neutral hadrons detected in the IFR if their production angles, taken from the first interaction point in the detector, are consistent with each other.

The K_L^0 detection efficiency and angular resolution are measured on a control sample of K_L^0 produced in $e^+e^- \rightarrow \phi\gamma \rightarrow K_L^0 K_S^0 \gamma$ processes, where the true K_L^0 direction is inferred from the missing momentum calculated from the particles that are reconstructed in the final state (γ and K_S^0). The K_L^0 reconstruction efficiency increases roughly linearly with momentum between 20% at 1 GeV/c and 40% at 4 GeV/c (EMC and IFR combined), and the angular resolution is of the order of 50 mrad.

2.8 The *BABAR* Trigger

The *BABAR* trigger is designed to select a large variety of physics processes rejecting background events and keeping the total event rate under 280 Hz so as not to overload the downstream processing. The trigger must select the physics events of interest with very high and/or well understood efficiency, depending on the particular mode. Efficiency, diagnostic and background studies require the trigger to be able to select prescaled samples of Bhabha, di-muon and cosmic events. This kind of studies also demand random beam crossings and events that fail the trigger selection criteria.

The trigger system operates as a sequence of two independent stages, the second conditional upon the first. The Level 1 (L1) hardware trigger is performed first at the machine crossing rate. Its goal is to sufficiently reduce that rate to a level acceptable for the Level 3 (L3)³ software trigger which runs on a farm of commercial processors. The L1 trigger is optimised for simplicity and speed. It consists of a pipelined hardware processor. It is designed to provide an output trigger rate of the order of 2 kHz or less. The L1 trigger selection is based on a reduced data set from the DCH, EMC and IFR. Its maximum L1 response latency for a given collision is 12 μ s. Based on both the complete event and L1 trigger information, the L3 software algorithms select events of interest allowing them to be transferred to mass storage for further analysis. Dedicated L1 trigger processors receive data which is continuously clocked in from the DCH, EMC and IFR detector subsystems. The L1 trigger processor produces a 30 MHz clocked output to the *Fast Control and Timing System* (FCTS) that can optionally mask or prescale input triggers. The arrival of a L1-Accept signal by the data acquisition system causes a window of each subsystem's L1 latency buffer to be read out.

The Level 3 trigger is implemented as a software that makes use of the complete event information for taking its decision, including the output of the L1 trigger processors and of the FCTS. The selection decision is primarily taken by two set of orthogonal filters, one exclusively based on the DCH information, the other based on the EMC data only. The drift chamber filters select events containing at least one high p_T track ($p_T > 600$ MeV/c) or two low p_T tracks, originating from the interaction point. The EMC filters look for events characterized by an effective mass greater than 1.5 GeV. The effective mass is calculated from the cluster energy sums and the energy weighted centroid positions of all clusters in the event in the massless particles hypothesis. The events must also contain at least two clusters with c.m. energy greater than 350 MeV or at least four clusters. Table 2.6 shows the L3 and L1+L3 trigger efficiency for some relevant physics processes, derived from Monte Carlo simulation.

2.9 Conclusion

The *BABAR* detector, at the PEP-II *B*-Factory, is optimized for the study of *B* physics, with a large *B* meson sample (the number of $B\bar{B}$ pairs, 232×10^6 , is expected to increase up to $> 10^9$ in year 2008) and excellent vertex resolution, track and photon reconstruction

³An intermediate Level 2 software trigger was originally foreseen in the very early step of *BABAR* design, but it was soon merged in the L3 trigger

L3 Trigger	$\epsilon_{b\bar{b}}$	$\epsilon_{B \rightarrow \pi^0 \pi^0}$	$\epsilon_{B \rightarrow \tau \nu}$	$\epsilon_{c\bar{c}}$	ϵ_{uds}	$\epsilon_{\tau\tau}$
1 track filter	89.9	69.9	86.5	89.2	88.2	94.1
2 track filter	98.9	84.1	94.5	96.1	93.2	87.6
Combined DCH filters	99.4	89.1	96.6	97.1	95.4	95.5
2 cluster filter	25.8	91.2	14.5	39.2	48.7	34.3
4 cluster filter	93.5	95.2	62.3	87.4	85.5	37.8
Combined EMC filters	93.5	95.7	62.3	87.4	85.6	46.3
Combined DCH+EMC filters	>99.9	99.3	98.1	99.0	97.6	97.3
Combined L1+L3	>99.9	99.1	97.8	98.9	95.8	92.0

Table 2.6: L3 trigger efficiency (%) for various physics processes, derived from Monte Carlo simulation.

efficiency and charged particle identification. In particular, the large data sample, high reconstruction efficiency of charged and neutral particles produced in B and D decays and pion/kaon separation greater than 3σ over the momentum range $1.5 - 3.5$ GeV/ c allow to measure the rare $B \rightarrow D^0 K$ decays where the D^0 decays to a Cabibbo-suppressed CP eigenstate, as described in the next two Chapters.

Chapter 3

$B \rightarrow D_{(CP)}^0 K$ and $B \rightarrow D_{(CP)}^0 \pi$ selection

As stated in the Introduction to this manuscript, the goal of the analysis presented here is the reconstruction of the Cabibbo-suppressed $B \rightarrow D^0 K$ decay and of the Cabibbo-allowed $B \rightarrow D^0 \pi$ decay, with the D^0 decaying to CP -even, CP -odd and non- CP flavor eigenstates. The purpose is the measurement of the direct CP asymmetries $A_{CP\pm}$ and the charge-averaged branching fraction ratios R_{\pm} defined in Equations (1) and (2). The analysis is performed in two logical steps:

- the reconstruction of the $B \rightarrow D^0 K$ and $B \rightarrow D^0 \pi$ candidates (which will sometimes generically referred to as $B \rightarrow D^0 h$, $h = \pi, K$) from the charged and neutral particles in the final state detected by *BABAR*, and the application of selection criteria to remove or reduce the largest sources of background. These criteria are of different types: kinematical, topological, particle-identification, best candidate selection algorithms for events with multiple candidates, and so on.
- the extraction of the signal yields from the selected data sample by means of an unbinned maximum likelihood fit to two variables (ΔE and θ_C , defined later) whose probability density functions (PDFs) are different between $B \rightarrow D^0 \pi$, $B \rightarrow D^0 K$ and background events.

From the final yields and the selection efficiencies the branching fraction ratios and CP asymmetries are determined.

In this Chapter we describe the first step, that is the criteria used to reconstruct the $B \rightarrow D^0 h$ candidates and to suppress background due to mis-reconstructed $e^+e^- \rightarrow \Upsilon(4S) \rightarrow B\bar{B}$ or $e^+e^- \rightarrow q\bar{q}$ ($q = u, d, s, c$) events. The second step, the extraction of the signal yields from the selected sample and the measurement of the observables R_{\pm} and $A_{CP\pm}$, is discussed in next Chapter. The outline of the current Chapter is the following:

- in Section 3.1 we describe the D^0 decay modes that have been studied in this analysis and report the most updated measurements of their branching fractions.
- in Section 3.2 we summarize the amount of data and simulated events that have been used for the measurements presented in this thesis.
- in Section 3.3 we describe the selection of photons and charged pions and kaons that are produced in the final states of the $B \rightarrow D^0 h$ decay chain.
- in Section 3.4 we describe the reconstruction and selection criteria of short-lived particles ($\pi^0, K_s^0, \phi, \omega, D^0$ mesons) produced in the $B \rightarrow D^0 h$ decay chain.

- in Section 3.5 we describe B reconstruction and selection criteria.
- in Section 3.6 we show how background events due to random combinations of particles produced in $e^+e^- \rightarrow q\bar{q}$ collisions can be further suppressed by making use of some shape variables that exploit the different topologies, in the center-of-mass frame, of the $e^+e^- \rightarrow q\bar{q}$ and $e^+e^- \rightarrow \Upsilon(4S) \rightarrow B\bar{B}$ processes.
- in Section 3.7 a criterion to remove multiple selected candidates in the same event is studied and applied.
- in Section 3.8 the complete summary of the selection criteria, with the final selection efficiency for signal events, is provided.

The selection criteria have been optimized on simulated events, after scaling the luminosity of the generated samples to that of the data collected at the $\Upsilon(4S)$, by maximizing – separately for each D^0 decay mode – the ratio:

$$\frac{S}{\sqrt{S+B}} \quad (3.1)$$

where S is the expected number of signal $B \rightarrow D^0 K$ events in the final sample, and B is the expected number of background events in the final sample which populate the same $(\Delta E, \theta_C)$ region as the signal. This corresponds to minimizing the final statistical uncertainties on the $B \rightarrow D^0 K$ yields, and therefore on R_{\pm} and $A_{CP\pm}$, estimated through the unbinned maximum likelihood fit described in the following Chapter. The reliability of the simulation in estimating background level and signal and background efficiencies of the selection criteria has been checked by comparing data and simulated events after vetoing the $B \rightarrow D^0 K$ signal, as discussed in Section 3.9.

3.1 D^0 decay modes that have been studied and overall $B \rightarrow D^0 h$ branching fractions

In this study we have chosen to reconstruct the D^0 decay modes that are expected to be easier to identify, thanks to higher efficiencies or lower backgrounds, and have larger branching fractions (including secondary branching fractions of short-lived unstable particles produced in the D^0 decay). Based on these considerations, we have decided to reconstruct the D^0 candidates in the CP -even eigenstates K^+K^- , $\pi^+\pi^-$, in the CP -odd eigenstates $K_s^0\pi^0$, $K_s^0\phi$ and $K_s^0\omega$,¹ and in the non- CP eigenstate $K^-\pi^+$. Examples of D^0 decay modes that have been discarded are the CP -even $K_s^0K_s^0$ and $\pi^0\pi^0$, and the CP -odd $K_s^0\eta$ and $K_s^0\eta'$. The branching fractions for the decay modes of K_s^0 , π^0 , ϕ , ω that have been reconstructed in this analysis are listed in Table 3.1 The branching fractions for the D^0 decay modes that have been considered are listed in Table 3.2.

Decay mode	Measured branching fraction
$K_s^0 \rightarrow \pi^+\pi^-$	$(68.95 \pm 0.14)\%$
$\pi^0 \rightarrow \gamma\gamma$	$(98.798 \pm 0.032)\%$
$\phi \rightarrow K^+K^-$	$(49.1 \pm 0.6)\%$
$\omega \rightarrow \pi^+\pi^-\pi^0$	$(89.1 \pm 0.7)\%$

Table 3.1: Branching fractions of decay modes for the resonances produced in the D_{CP}^0 -decays [16].

¹With K_s^0 decaying to $\pi^+\pi^-$, and $\pi^0 \rightarrow \gamma\gamma$, $\phi \rightarrow K^+K^-$, $\omega \rightarrow \pi^+\pi^-\pi^0$

D^0 decay mode	Primary branching fraction (10^{-3})	Overall B.F. (10^{-3})
$K^- \pi^+$	38.0 ± 0.9	38.0 ± 0.9
$K^+ K^-$	3.89 ± 0.14	3.89 ± 0.14
$\pi^+ \pi^-$	1.38 ± 0.05	1.38 ± 0.05
$K_s^0 \pi^0$	11.5 ± 1.1	7.83 ± 0.75
$K_s^0 \phi$	4.70 ± 0.55	1.62 ± 0.21
$K_s^0 \omega$	11.5 ± 2.0	7.15 ± 1.40

Table 3.2: Branching fractions of the $D_{(CP\pm)}^0$ decays that have been studied in this analysis [16]. In the third column the D^0 branching fractions have been multiplied by the branching fractions of the K_s^0 , π^0 , ϕ and ω decays that are reconstructed in this analysis (see Table 3.1).

The branching fraction for the $B^- \rightarrow D^0 \pi^-$ process is $\mathcal{B}(B^- \rightarrow D^0 \pi^-) = (4.98 \pm 0.29) \times 10^{-3}$ [16] and the weighted average of the *BABAR*, Belle and Cleo measurements for the ratio $\mathcal{B}(B^- \rightarrow D^0 K^-)/\mathcal{B}(B^- \rightarrow D^0 \pi^-)$ is $(8.19 \pm 0.28)\%$, therefore the branching fraction for the $B^- \rightarrow D^0 K^-$ decay is $\mathcal{B}(B^- \rightarrow D^0 K^-) = (4.08 \pm 0.27) \times 10^{-4}$. The branching fractions for the $B \rightarrow D_{CP\pm}^0 K$ processes are $\mathcal{B}(B \rightarrow D_{CP\pm}^0 K) = \mathcal{B}(B^- \rightarrow D^0 K^-) \times R_{CP\pm}$, where $R_{CP\pm} = 1 + r_B^2 \pm 2r_B \cos \delta_B \cos \gamma$: the current measurements of r_B and γ [2, 3, 7, 8] favour $R_{CP\pm} \approx 0.85 - 1.15$, depending on the value of δ_B . Taking into account these numbers and the branching fractions listed in Tables 3.1 and 3.2, the total branching fractions for the $B \rightarrow D_{(CP)}^0 K$ decays that are reconstructed in this analysis are in the range $5 \times 10^{-7} - 2 \times 10^{-5}$: they are listed in Table 3.3, and should be compared with the total number of B^\pm decays collected so far (232×10^6) by the *BABAR* detector (see next Section).

D^0 decay mode	Overall $\mathcal{B}(B^- \rightarrow D^0 \pi^-)$	Overall $\mathcal{B}(B^- \rightarrow D^0 K^-)$
$K^- \pi^+$	$(18.9 \pm 1.2) \times 10^{-5}$	$(15.5 \pm 1.1) \times 10^{-6}$
$K^+ K^-$	$(19.4 \pm 1.3) \times 10^{-6}$	$R_{CP+} \times (15.9 \pm 1.2) \times 10^{-7}$
$\pi^+ \pi^-$	$(6.9 \pm 0.5) \times 10^{-6}$	$R_{CP+} \times (5.6 \pm 0.4) \times 10^{-7}$
$K_s^0(\pi^+ \pi^-) \pi^0(\gamma\gamma)$	$(39.0 \pm 4.4) \times 10^{-6}$	$R_{CP-} \times (31.9 \pm 3.8) \times 10^{-7}$
$K_s^0(\pi^+ \pi^-) \phi(K^+ K^-)$	$(8.1 \pm 1.2) \times 10^{-6}$	$R_{CP-} \times (6.6 \pm 1.0) \times 10^{-7}$
$K_s^0(\pi^+ \pi^-) \omega(\pi^+ \pi^- \pi^0(\gamma\gamma))$	$(35.6 \pm 7.3) \times 10^{-6}$	$R_{CP-} \times (29.2 \pm 5.8) \times 10^{-7}$

Table 3.3: Total branching fractions (including D^0 , K_s^0 , π^0 , ϕ and ω branching fractions) for the $B \rightarrow D^0 h$ decays that are reconstructed in this analysis. R_{CP+} and R_{CP-} are expected to lie approximately in the range 0.85-1.15.

3.2 Data and Monte Carlo sample

The analysis has been performed on the whole data sample collected by *BABAR* in the years 1999-2004, corresponding to $(231.8 \pm 2.6) \times 10^6$ $B\bar{B}$ pairs. The integrated luminosity of the data samples used to perform the analysis, the data taking periods and the number of collected $B\bar{B}$ pairs are summarized in Table 3.4, where we report both data collected at the $\Upsilon(4S)$ peak (on-resonance data, $\sqrt{s} = 10.58$ GeV) and data, used to study $e^+e^- \rightarrow q\bar{q}$ background events, collected 40 MeV below the $\Upsilon(4S)$ peak (off-resonance data, $\sqrt{s} = 10.54$ GeV).

To study the properties of background and signal events before looking at data, large samples of simulated (Monte Carlo) events have been analyzed, thus performing a so-called “blind” analysis, a technique largely in use in *BABAR* which allows to avoid introducing

Sample	Data taking period	Luminosity (fb^{-1})	$N(B\bar{B})/10^6$
RUN1 on-resonance	Oct. 1999 - Oct. 2000	19.5	21.2 ± 0.2
RUN1 off-resonance		2.3	
RUN2 on-resonance	Feb. 2001 - Jun. 2002	60.3	66.4 ± 0.7
RUN2 off-resonance		6.9	
RUN3 on-resonance	Nov. 2002 - Jul. 2003	31.1	34.1 ± 0.4
RUN3 off-resonance		2.4	
RUN4 on-resonance	Sep. 2003 - Jul. 2004	99.8	110.1 ± 1.2
RUN4 off-resonance		9.9	
RUN1-4 on-resonance	Oct. 1999 - Jul. 2004	210.5	231.8 ± 2.6
RUN1-4 off-resonance		21.6	

Table 3.4: Data sample used for the analysis. The effective $B\bar{B}$ cross section is 1.1 nb. The method used to evaluate the number of collected $B\bar{B}$ meson pairs is described in [61].

experimenter’s (subconscious) artificial biases in the measurement [60]. Selection criteria have been therefore optimized on Monte Carlo, and the reliability of the simulation has been checked by comparing its predictions with real data after explicitly vetoing, in the latter, signal $B \rightarrow D^0 h$ events. For the simulation of the physics of $B\bar{B}$ pair production and B decays the EvtGen package [62], designed by the CLEO and BABAR Collaborations, has been used. The branching fractions used in the simulation are taken from the most updated experimental measurements (where available), or from theoretical estimates. $e^+e^- \rightarrow q\bar{q}$ collisions and quark fragmentation in general have been simulated with the JetSet generator [63]. The GEANT [64] software has been used to simulate interactions of particles traversing the BABAR detector, taking properly into account the varying accelerator and detector conditions.

Table 3.5 lists the generic $e^+e^- \rightarrow q\bar{q}$ and $e^+e^- \rightarrow \Upsilon(4S) \rightarrow B\bar{B}$ Monte Carlo samples used to characterize background events, and the equivalent integrated luminosity. In the latter, signal events ($B \rightarrow D^0 K$ and $B \rightarrow D^0 \pi$ decays with D^0 decaying to the relevant final states) have been removed. Table 3.6 lists the exclusive Monte Carlo events that were generated and reconstructed in order to study the properties of the signal (about 54,000 signal events, $250 \text{ events}/\text{fb}^{-1}$, for each D^0 decay mode): in these events both a B^+ and a B^- mesons are generated, one decaying to $D^0 h$, and the other one decaying generically according to its known or estimated branching fraction ratios.

Sample	Events	Cross section (nb)	Luminosity (fb^{-1})
$e^+e^- \rightarrow q\bar{q}, q = u, d, s$	322×10^6	2.09	154
$e^+e^- \rightarrow c\bar{c}$	196×10^6	1.30	150
$e^+e^- \rightarrow \Upsilon(4S) \rightarrow B^0\bar{B}^0$	346×10^6	0.55	629
$e^+e^- \rightarrow \Upsilon(4S) \rightarrow B^+B^-$	341×10^6	0.55	620

Table 3.5: Generic Monte Carlo sample used for the analysis.

3.3 Reconstruction of charged and neutral particles in the final state

In this Section we describe how we select charged and neutral particles that are produced in the final state of the $B \rightarrow D^0 h$ decay chain and are detected in the BABAR tracking systems or calorimeters. In Figure 3.1 we show the π^\pm , K^\pm and π^0 expected momentum

D^0 mode	$B \rightarrow D^0 K$		$B \rightarrow D^0 \pi$	
	Events	Lumi (fb ⁻¹)	Events	Lumi (fb ⁻¹)
$K^- \pi^+$	53960	≈ 3164	53960	≈ 259
$K^+ K^-$	53960	≈ 30908	53960	≈ 2532
$\pi^+ \pi^-$	53960	≈ 87124	53960	≈ 610
$K_s^0 \pi^0, K_s^0 \rightarrow \pi^+ \pi^-$	53960	≈ 15171	53960	≈ 1243
$K_s^0 \phi, K_s^0 \rightarrow \pi^+ \pi^-, \phi \rightarrow K^+ K^-$	53960	≈ 74217	53960	≈ 6080
$K_s^0 \omega, K_s^0 \rightarrow \pi^+ \pi^-, \omega \rightarrow \pi^+ \pi^- \pi^0$	53960	≈ 16614	53960	≈ 1361

Table 3.6: Exclusive Monte Carlo samples used for the analysis

distributions in the laboratory frame as predicted by simulation.

3.3.1 Charged tracks selection

Charged particle tracks are reconstructed from the spatial hits in the SVT and the DCH: an iterative fitting algorithm based on the Kalman filter technique [65] performs pattern recognition and determines for each track the 5 parameters defined in Section 2.3.2. The full map of the magnetic field, the detailed distribution of the material in the detector and the expected energy loss of the particle as it traverses the detector are taken into account. Track parameter resolutions and reconstruction efficiency are shown in Section 2.3.2 and 2.4.2.

In this analysis all the charged tracks are required to be reconstructed in the fiducial volume of the tracking systems ($0.41 < \theta_{\text{lab}} < 2.41$). The geometrical acceptance is 85% in the CM frame, and the tracking efficiency is about 97% for momenta greater than 200 MeV/ c . With the exception of the pions from K_s^0 decays, which are typically originated 5-10 cm away from the primary interaction point (the K_s^0 mean energy in the D^0 decays considered here ranges between 1.3 GeV, in $D^0 \rightarrow K_s^0 \phi$, and 2.0 GeV, in $D^0 \rightarrow K_s^0 \pi^0$), all other charged particles produced in the $B \rightarrow D^0 h$ decay chains are generated from very short-lived particles (B, D^0, ϕ, ω) which travel at most few hundred microns from the IP: we therefore apply to their tracks the requirements $|d_0| < 1.5$ cm, $|z_0| < 10$ cm.

3.3.2 Charged particle identification

The charged particle identification system (PID) plays a crucial role in reducing the combinatorial background in the B, D^0, K_s^0, ϕ and ω reconstruction, and in discriminating – together with the invariant mass of the D^0 candidate – between similar D^0 decays, like $D^0 \rightarrow K^- \pi^+, D^0 \rightarrow K^+ K^-$ and $D^0 \rightarrow \pi^+ \pi^-$. It is also used, as will be described in next Chapter, to separate $B \rightarrow D^0 K$ and $B \rightarrow D^0 \pi$ candidates.

$\pi/K/p$ separation is achieved by means of the specific ionization loss dE/dx measured in the Silicon Vertex Tracker and in the Drift Chamber, and the Cherenkov angle θ_C and the number N_γ of Cherenkov photons reconstructed in the Detector of Internally Reflected Cherenkov light. The three sub-detectors are to a large extent complementary, in the sense that they exhibit their maximum $\pi/K/p$ discriminating power at different particle momentum ranges. The particle ID information from each of the three subdetectors is used to calculate a likelihood, for a given particle hypothesis. A subsystem provides particle information for a charged track if a number of minimal requirements are satisfied. The global likelihood for a given particle hypothesis is thus given by the product of the likelihoods of the subsystems that pass the requirements for that track. The requirements and momentum ranges are listed in Table 3.7: they are optimized to keep a very high acceptance efficiency.

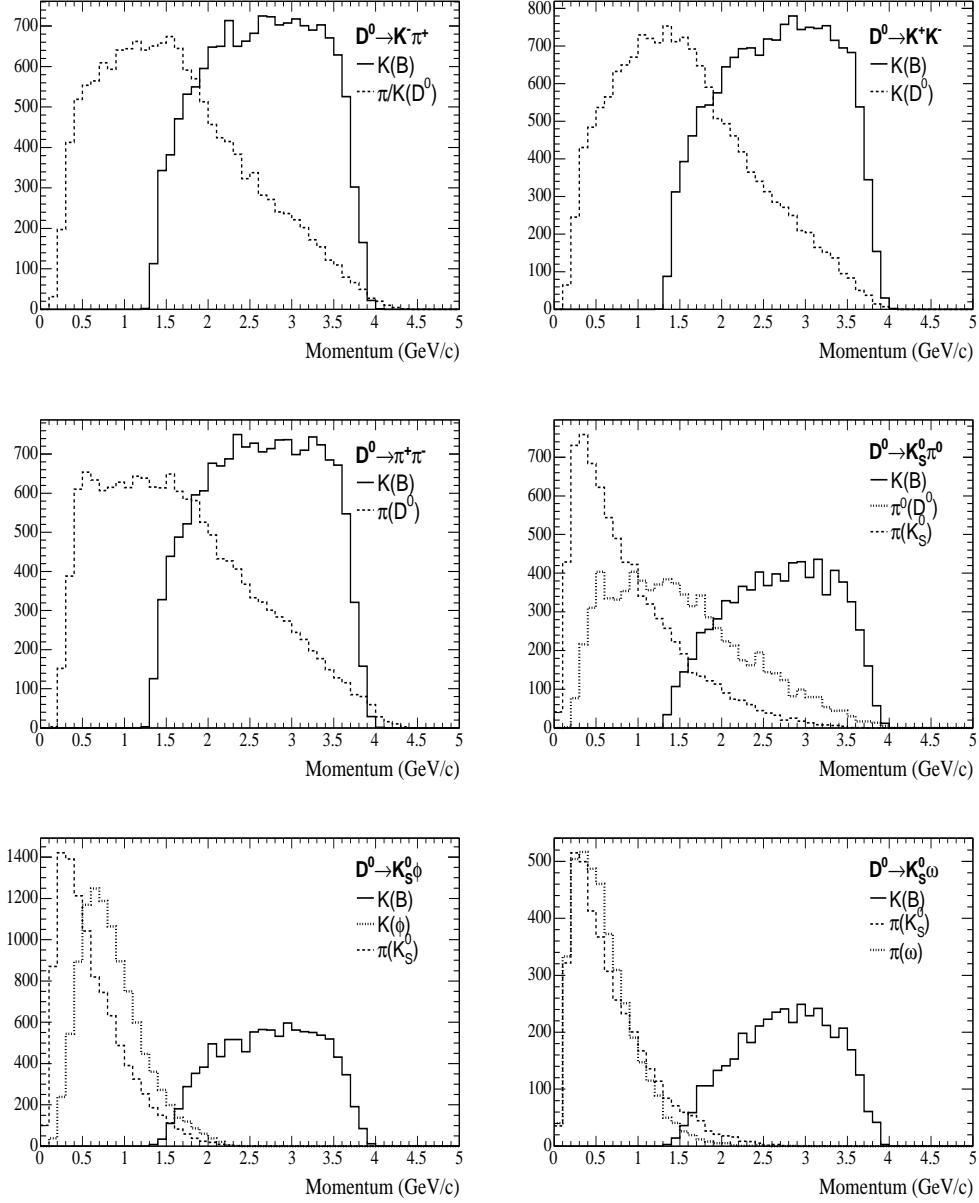


Figure 3.1: Momentum distribution of charged and neutral pions and charged kaons produced in the $B \rightarrow D^0 K$ decay chain. [Simulated $B \rightarrow D^0 K$ events]

The SVT and DCH likelihoods [66] are gaussian probability density functions (PDFs) whose mean and width are given by the expected central value and the estimated resolution of the truncated dE/dx mean. Both these parameters depend on the particle momentum. The DIRC likelihood [66] is expressed as the product of a Gaussian PDF associated to the measured Cherenkov angle θ_C and a Poissonian PDF for the number N_γ of detected Cherenkov photons. The mean and width of the Gaussian θ_C PDFs are given by the expected Cherenkov angle and the corresponding resolution, the mean of the Poissonian N_γ PDF is the expected number of photons: all these parameters

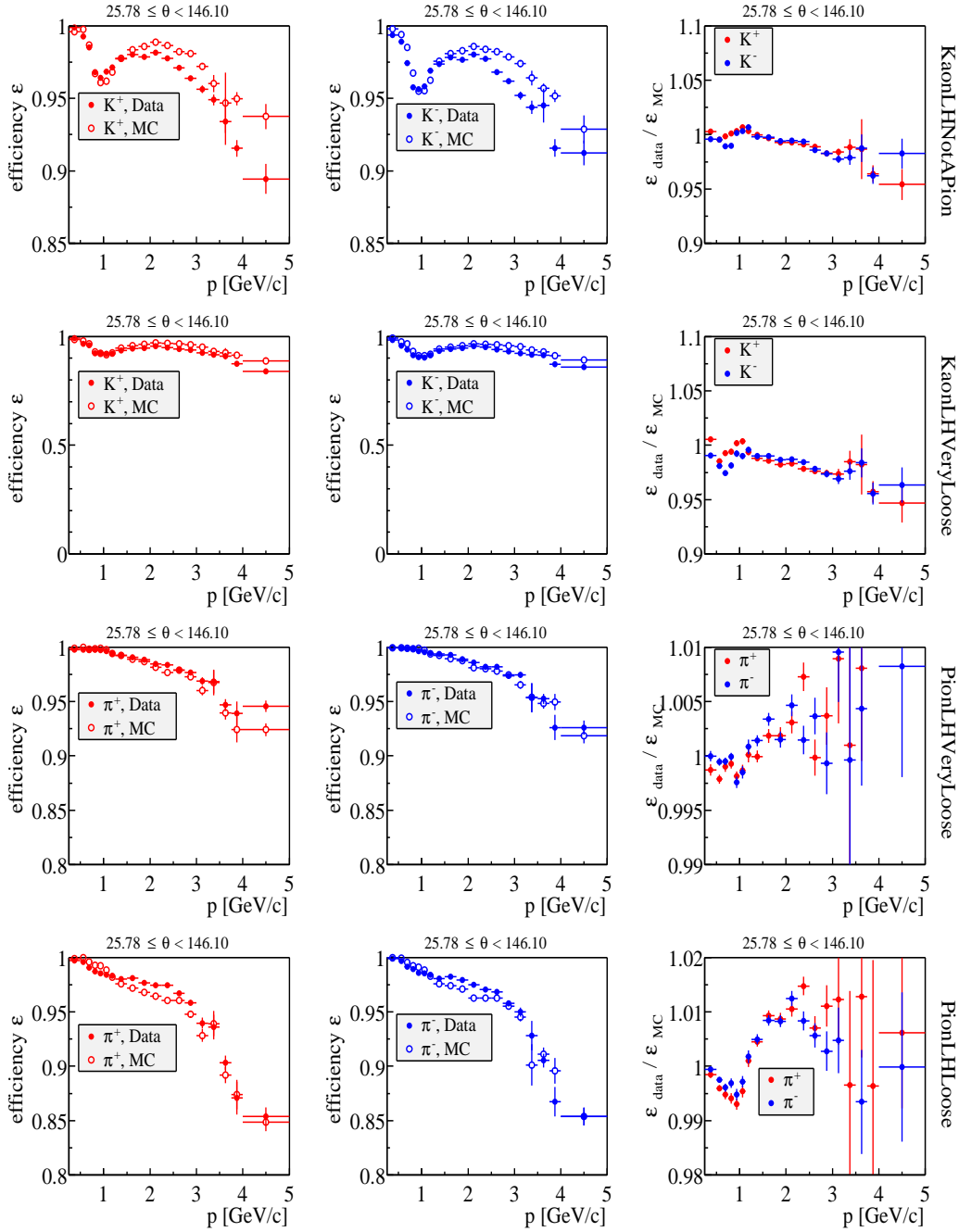


Figure 3.2: Efficiency of the four kaon and pion selectors used in this analysis: from top to bottom, KaonLHNotAPion (first row), KaonLHVeryLoose (second row), PionLHVeryLoose (third row), PionLHLoose (last row). The efficiencies of the kaon selectors are measured on a control sample of kinematically selected kaons, the efficiencies of the pion selectors are measured on a control sample of kinematically selected pions.

depend on the particle momentum and polar angle. The parameters entering the likelihood functions are determined on pure control samples of pions, kaons (typically from

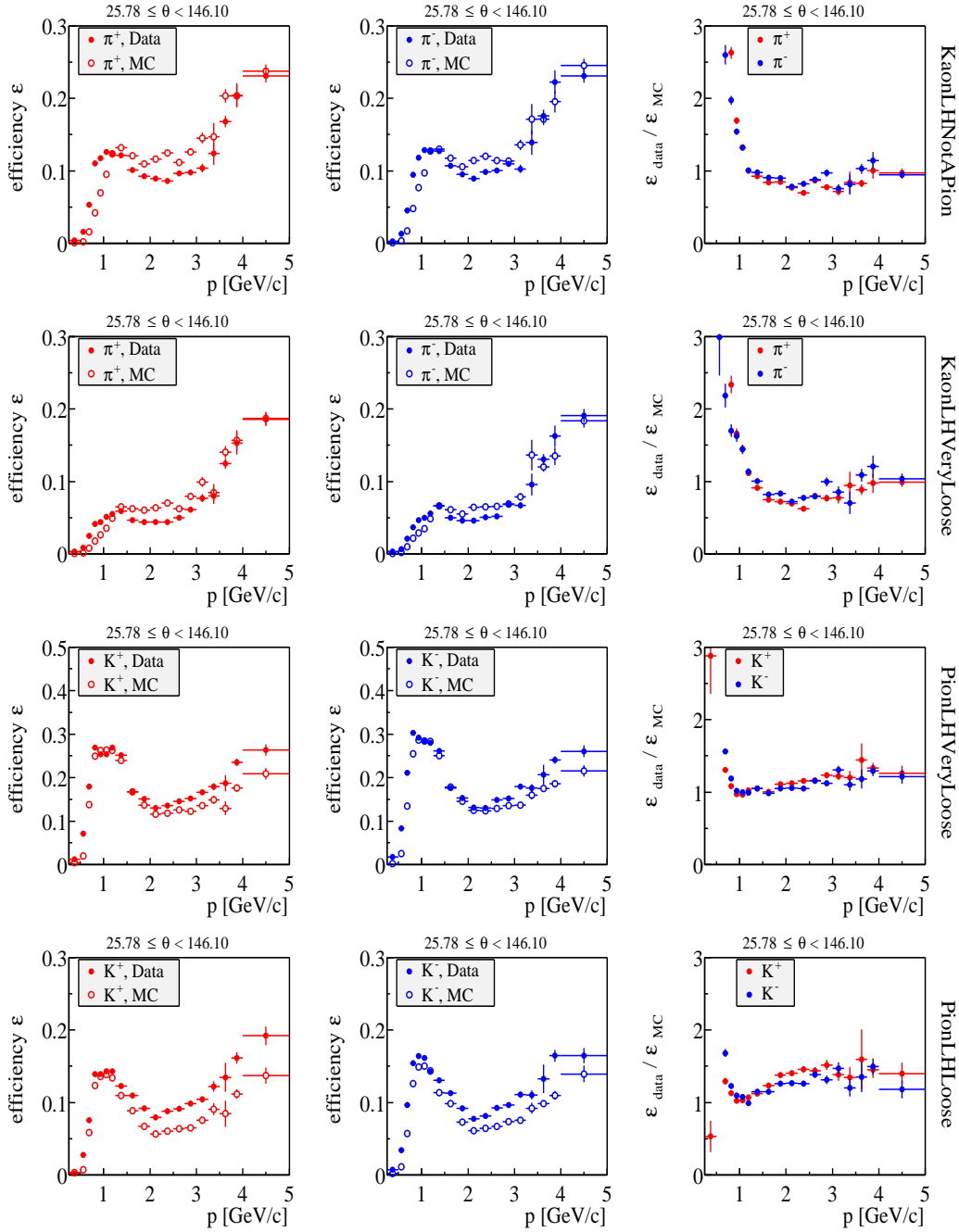


Figure 3.3: Mis-identification rate of the four kaon and pion selectors used in this analysis: from top to bottom, KaonLHNotAPion (first row), KaonLHVeryLoose (second row), PionLHVeryLoose (third row), PionLHLoose (last row). The mis-identification rates of the kaon selectors are measured on the pion control sample and viceversa.

$D^{*+} \rightarrow D^0 (\rightarrow K^- \pi^+) \pi^+$ and protons selected with kinematical requirements that do not make use of the PID information. Additional information from the EMC, as described in Section 2.6.2, or from the IFR, as described in Section 2.7.2, is used to compute the

detector	measured quantities	momentum range	requirements
SVT	dE/dx	$0.025 < p < 0.7 \text{ GeV}/c$ $p > 1.5 \text{ GeV}/c$	$> 3 \text{ dE/dx samplings}$
DCH	dE/dx	$0.090 < p < 0.7 \text{ GeV}/c$ $p > 1.5 \text{ GeV}/c$	$> 10 \text{ dE/dx samplings}$
DIRC	N_γ θ_C	$0.6 < p < 10 \text{ GeV}/c$	expected number of photons > 0

Table 3.7: Momentum domains and requirements that a charged track must satisfy in order that a subsystem provide particle information.

global likelihood for electrons and muons respectively.

In *BABAR* several ‘‘PID selectors’’ are defined, which – by applying requirements on likelihood ratios – allow to select charged particles with known efficiency ε and mis-identification rate r . Several selection criteria are provided, which are characterized by different combinations of (ε, r) (in general, the lower r , the lower ε). We make use of two kaon selectors, called *KaonLHNotAPion* and *KaonLHVeryLoose*, and two pion selectors, called *PionLHVeryLoose* and *PionLHLoose*. These selectors are optimized for high efficiency: the *PionLHLoose* and *KaonLHVeryLoose*, compared to the *PionLHVeryLoose* and *KaonLHNotAPion*, adopt more stringent criteria and have lower mis-identification rates, at the price of slightly lower efficiencies. The criteria used by these selectors are summarized in Table 3.8, where the likelihoods for the pion, kaon and proton hypothesis are indicated with L_π , L_K and L_p , respectively. The efficiency of

Selector	K/π	p	e
KaonLHNotAPion	$L_K/L_\pi > 0.2$	-	-
KaonLHVeryLoose	$L_K/L_\pi > 0.5$	$L_K/L_p > 0.018$	$ \mathbf{p} < 0.4 \text{ GeV}/c$ or $L_e/L_\pi < 0.95$
PionLHVeryLoose	$L_K/L_\pi < 0.98$	$L_p/L_\pi < 0.98$	-
PionLHLoose	$L_K/L_\pi < 0.82$	$L_p/L_\pi < 0.98$	$L_e/L_\pi < 0.95$

Table 3.8: Criteria applied for the identification of charged kaon and pions by four ‘‘selectors’’ provided in the *BABAR* analysis framework.

these selectors as a function of laboratory momentum p of the charged track is shown in Figure 3.2, while their mis-identification rate as a function of p is shown in Figure 3.3 [67].

3.3.3 Photon selection

Photon candidates are reconstructed in the electromagnetic calorimeter as reported in Section 2.6. In this analysis photons are required to have energy greater than 30 MeV and a lateral shower shape consistent with the expected pattern of energy deposit from an electromagnetic shower ($LAT < 0.8$).² The geometrical acceptance of the electromagnetic calorimeter is 90% in the center-of-mass frame, and the photon reconstruction efficiency of these selection criteria is above 96% for momenta greater than 600 MeV/c, and falls to 88-91% at lower momenta, as shown in Figure 3.4 [69].

²The lateral energy distribution LAT [68] is defined as

$$LAT = \frac{\sum_{i=3}^n E_i r_i^2}{\sum_{i=3}^n E_i r_i^2 + E_1 r_0^2 + E_2 r_0^2}, \quad E_1 \geq E_2 \geq \dots \geq E_n \quad (3.2)$$

where the sum extends over all crystals in a shower, $r_0 = 5 \text{ cm}$ is the average distance between two crystals frontfaces, and r_i is the distance between crystal i and the shower center (calculated as the center of gravity with linear energy-weighting of every crystal).

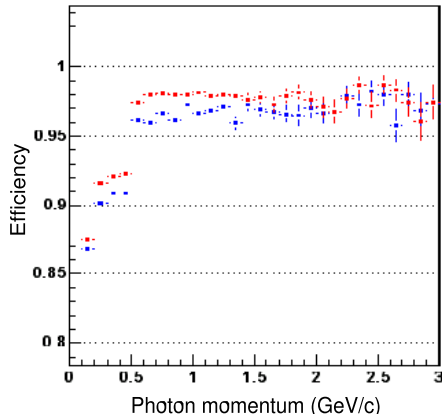


Figure 3.4: Efficiency, as a function of laboratory momentum, of the photon selection described in the text, as measured in a pure control sample of photons from $\pi^0 \rightarrow \gamma\gamma$ decays isolated in $\tau \rightarrow \rho(\rightarrow \pi^0 \pi)$ decays. Blue dots correspond to the efficiency measured in real data, red dots represent the expected efficiency from simulation.

3.4 “Composite” candidates reconstruction

In this Section we describe how very short-lived particles (π^0 , ϕ , ω and D^0 mesons) and short-lived K_s^0 mesons (which do not interact with the tracking systems, but decay before reaching the outer calorimeters), produced in the $B \rightarrow D^0 h$ decay chain, are identified by means of their charged and neutral decay products, selected with the criteria defined in the previous subsections. Background from random combinations of charged tracks or photons in the event is typically suppressed by selecting only the combinations which emerge from a common space-point (decay vertex) and whose invariant mass is sufficiently close to the known mean mass of the particle. Additional information such as, for instance, angular correlations due to the spin of the particles, can be used to further suppress background events.

3.4.1 π^0 reconstruction

π^0 candidates are reconstructed in the decay mode $\gamma\gamma$, from photon pairs with total energy greater than 200 MeV and invariant mass m_{π^0} (computed assuming that the photons are originated in proximity of the primary vertex) in the range 115–150 MeV/c^2 . This corresponds to a $\pm 2.5\sigma_{m_{\pi^0}}$ window around the mean value $\langle m_{\pi^0} \rangle$, where $\sigma_{m_{\pi^0}} \approx 7 \text{ MeV}/c^2$ is the π^0 mass resolution, as shown in Figure 3.5(a).

Photon pairs that pass the selection criteria, and are used in the $D^0 \rightarrow K_s^0 \pi^0$ and $\omega \rightarrow \pi^+ \pi^- \pi^0$ reconstruction, are kinematically fit [72] with their invariant mass constrained to the nominal π^0 mass [16]: the π^0 RMS momentum resolution is thus improved from 22.5 MeV/c to 19.0 MeV/c .

3.4.2 K_s^0 reconstruction

K_s^0 candidates are reconstructed in the decay mode $\pi^+ \pi^-$, from pairs of oppositely-charged tracks. The $\pi^+ \pi^-$ invariant mass $m_{K_s^0}$ – computed by assigning the pion mass to both tracks – must be within a $\pm 7.8 \text{ MeV}/c^2$ window around the mean value $\langle m_{K_s^0} \rangle$: this corresponds to a $\pm 3\sigma_{m_{K_s^0}}$ window, where $\sigma_{m_{K_s^0}} \approx 2.6 \text{ MeV}/c^2$ is the K_s^0 mass resolution, as shown in Figure 3.5(b). The efficiency of this cut is 94% due to the presence of

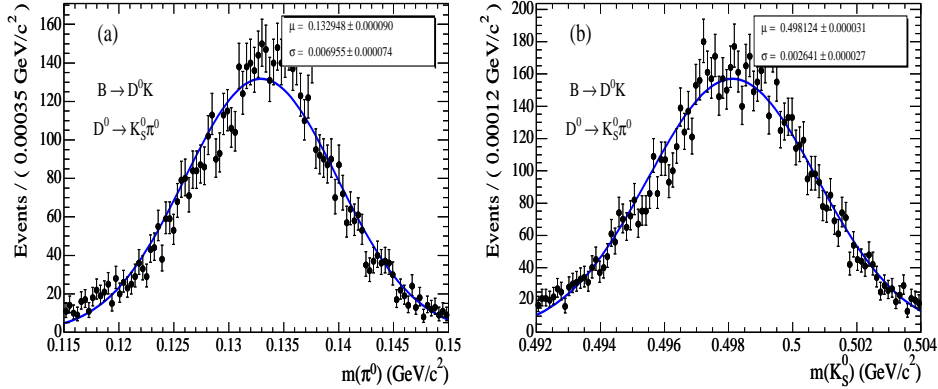


Figure 3.5: Invariant mass distribution of correctly-identified $\pi^0 \rightarrow \gamma\gamma$ (left) and $K_s^0 \rightarrow \pi^+\pi^-$ decays (right) in $B \rightarrow D^0 K$, $D^0 \rightarrow K_s^0 \pi^0$ simulated events.

non-Gaussian tails in the $m_{K_s^0}$ distribution of true K_s^0 candidates. The two pions are constrained to originate from the same point. We require that this point be significantly displaced, along the direction of the total momentum of the two pions, from the D^0 decay vertex, by retaining only candidates for which the ratio between the separation d_{xy} of the decay vertices of the K_s^0 and the D^0 in the transverse plane and its error $\sigma_{d_{xy}}$ is greater than 2, and the angle between the flight direction of the K_s^0 and the total momentum of the two pions in the transverse plane is lower than 90° . After having applied the previous criteria, fake K_s^0 candidates in which at least one of the two charged tracks does not correspond to a pion are negligible so we do not apply any PID requirement to the K_s^0 daughters.

3.4.3 ϕ reconstruction

ϕ candidates are reconstructed in the decay mode K^+K^- , from pairs of oppositely charged tracks with invariant mass m_ϕ – computed by assigning the kaon mass to both – within a ± 12 MeV/ c^2 window³ around the mean value $\langle m_\phi \rangle$. The two kaons are required to pass the KaonLHNNotAPion PID selector and are constrained to originate from the same point.

The m_ϕ distribution of true $\phi \rightarrow K^+K^-$ that are correctly reconstructed can be parameterized by means of a Breit-Wigner PDF, with mean $\langle m_\phi \rangle = 1019.42 \pm 0.03$ MeV/ c^2 and width (fixed to the PDG value) $\Gamma_\phi = 4.26$ MeV/ c^2 , convolved with a Gaussian resolution function with width $\sigma_{m_\phi} = 1.07 \pm 0.06$ MeV/ c^2 (see Figure 3.8). The requirement $|m_\phi - \langle m_\phi \rangle| < 12$ MeV/ c^2 has therefore an efficiency around 93% for true ϕ candidates. A comparison of the invariant mass distribution of ϕ candidates selected in the $B \rightarrow D^0 K$, $D^0 \rightarrow K_s^0 \phi$ analysis in signal and background simulated events is shown in the right plot of Figure 3.6.

Angular momentum conservation in the decay of a pseudoscalar D^0 meson to the vector ϕ and a pseudoscalar K_s^0 requires that the ϕ be produced with helicity 0. The subsequent decay of the ϕ into two kaons then yields a distribution of the cosine of the ϕ decay angle $\theta_{\text{hel}}(\phi)$ (the angle of the kaon in the ϕ rest frame with respect to the direction of the ϕ in the D^0 rest frame) which shows a characteristic $\cos^2 \theta_{\text{hel}}(\phi)$ behaviour. In background events the $\cos \theta_{\text{hel}}(\phi)$ distribution is flat for fake ϕ candidates reconstructed from random combinations of charged tracks, and is a sum of a constant and a $\cos^2 \theta_{\text{hel}}(\phi)$ distribution – due to partial polarization – for true ϕ candidates. The $\cos \theta_{\text{hel}}(\phi)$ distribution for signal

³The ϕ width is $\Gamma_\phi = 4.26 \pm 0.05$ MeV/ c^2

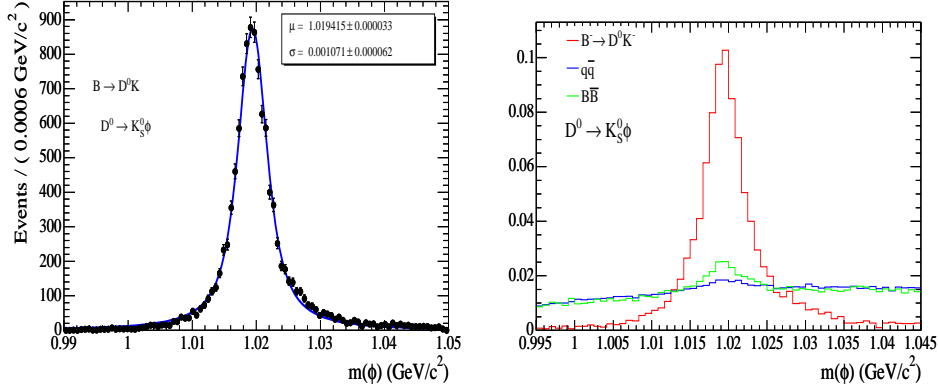


Figure 3.6: Left: invariant mass (m_ϕ) distribution of correctly identified $\phi \rightarrow K^+K^-$ mesons in $B \rightarrow D^0K$, $D^0 \rightarrow K_s^0\phi$ simulated events. Right: m_ϕ distributions of ϕ candidates reconstructed in the $B \rightarrow D^0K$, $D^0 \rightarrow K_s^0\phi$ analysis in signal ($B \rightarrow D^0K$) and background ($q\bar{q}$ and $B\bar{B}$) simulated events.

and background events (normalized to the same integral) is shown in Figure 3.7. We

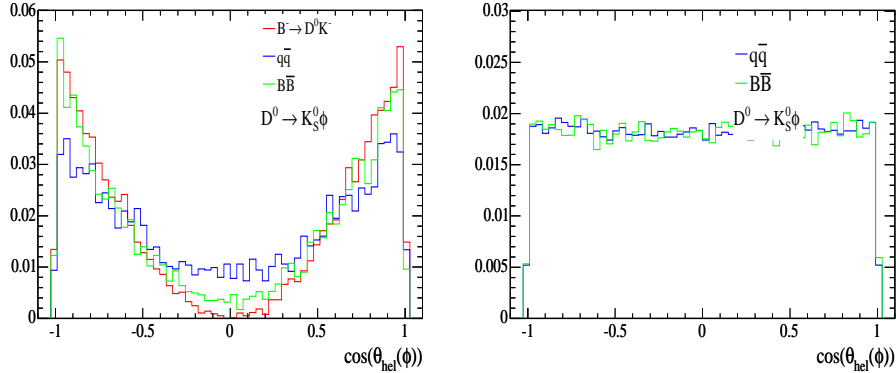


Figure 3.7: Helicity angle distribution of $\phi \rightarrow K^+K^-$ candidates reconstructed in the $B^- \rightarrow D^0K^-$, $D^0 \rightarrow K_s^0\phi$ analysis, in signal $B \rightarrow D^0K$, $q\bar{q}$ and $B\bar{B}$ simulated events. Left: correctly-identified $\phi \rightarrow K^+K^-$ decays. Right: fake ϕ candidates.

require:

$$|\cos(\theta_{\text{hel}}(\phi))| > 0.4, \quad (3.3)$$

thus rejecting 40% of fake ϕ candidates, while retaining about 94% of the true ϕ candidates reconstructed in $B \rightarrow D^0h$, $D^0 \rightarrow K_s^0\phi$ events.

3.4.4 ω reconstruction

ω candidates are reconstructed in the decay mode $\pi^+\pi^-\pi^0$ from combinations of two oppositely-charged tracks and a neutral π^0 with invariant mass m_ω – computed by assigning the pion mass to the two charged particles – inside a $\pm 18 \text{ MeV}/c^2$ around the

⁴The ω width is $\Gamma_\omega = 8.49 \pm 0.08 \text{ MeV}/c^2$

mean value $\langle m_\omega \rangle$. The two charged pions are required to pass the PionLHVeryLoose PID selector and are constrained to have a common vertex.

A comparison of the ω invariant mass in signal and background events on Monte Carlo is shown in Figure 3.8. The m_ω distribution in true $\omega \rightarrow \pi^+ \pi^- \pi^0$ decays can be described as the convolution of a Breit-Wigner, with mean $\langle m_\omega \rangle = 781.4 \pm 0.2$ MeV/ c^2 and width (fixed to the PDG value) $\Gamma_\omega = 8.49$ MeV/ c^2 , and a Gaussian resolution function with width $\sigma_{m_\omega} = 6.9 \pm 0.2$ MeV/ c^2 (see Figure 3.8). The requirement $|m_\omega - \langle m_\omega \rangle| < 18$ MeV/ c^2 has therefore an efficiency around 87% for true ω candidates.

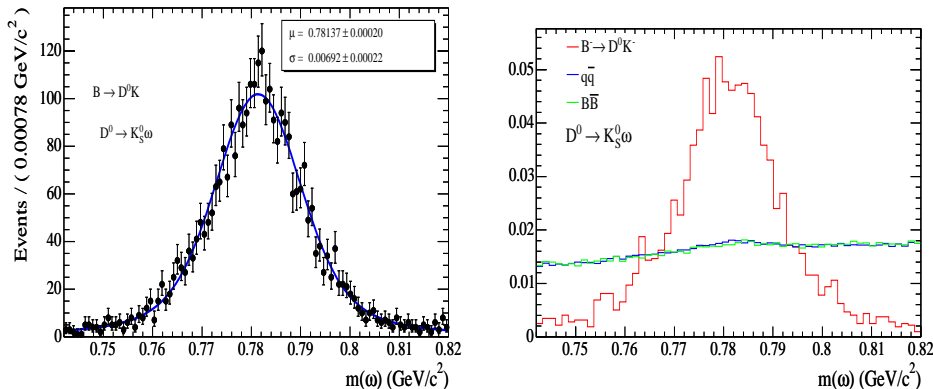


Figure 3.8: Left: invariant mass (m_ω) distribution of correctly identified $\omega \rightarrow \pi^+ \pi^- \pi^0$ mesons in $B \rightarrow D^0 K$, $D^0 \rightarrow K_s^0 \omega$ simulated events. Right: m_ω distributions of ω candidates reconstructed in the $B \rightarrow D^0 K$, $D^0 \rightarrow K_s^0 \omega$ analysis in signal ($B \rightarrow D^0 K$) and background ($q\bar{q}$ and $B\bar{B}$) simulated events.

In the $\omega \rightarrow \pi^+ \pi^- \pi^0$ decay the three daughter pions are produced, in the ω rest frame, in a plane. The normal helicity angle θ_N is the angle between the normal to this plane and the direction of the ω in the D^0 rest frame: for ω mesons produced in $D^0 \rightarrow K_s^0 \omega$ decays, which have helicity 0, $\cos \theta_N$ follows a $\cos^2 \theta_N$ distribution, while for unpolarized ω mesons or for fake ω candidates reconstructed from random combinations of two tracks and a π^0 the $\cos \theta_N$ distribution is roughly flat (see Figure 3.9). Another angular variable which characterizes the three-pion system is the Dalitz angle $\theta_{\pi\pi}$ between the flight direction of one of the three pions in the ω rest frame and the flight direction of one of the two other pions in their center-of-mass frame. In true $\omega \rightarrow \pi^+ \pi^- \pi^0$ decays (independently of the ω polarization) $\cos \theta_{\pi\pi}$ is distributed like $\sin^2 \theta_{\pi\pi}$, while fake ω candidates reconstructed from random combinations of two tracks and a π^0 exhibit an almost flat $\cos \theta_{\pi\pi}$ distribution (see Figure 3.9). We require

$$\cos^2 \theta_N \sin^2 \theta_{\pi\pi} > 0.08, \quad (3.4)$$

thus rejecting 45% of fake ω candidates while keeping 95% of the true ones selected in $B \rightarrow D^0 K$, $D^0 \rightarrow K_s^0 \omega$ decays.

3.4.5 D^0 reconstruction

D^0 candidates are reconstructed in the CP -odd eigenstates $K_s^0 \pi^0$, $K_s^0 \phi$, $K_s^0 \omega$, in the CP -even eigenstates $K^+ K^-$ and $\pi^+ \pi^-$ and in the non- CP eigenstate $K^- \pi^+$. Charged kaons and pions and neutral K_s^0 , π^0 , ϕ and ω mesons are selected according to the criteria described in the previous sections, and every two-body combination of these which is consistent with one of the six D^0 decay modes under study, with total center-of-mass momentum

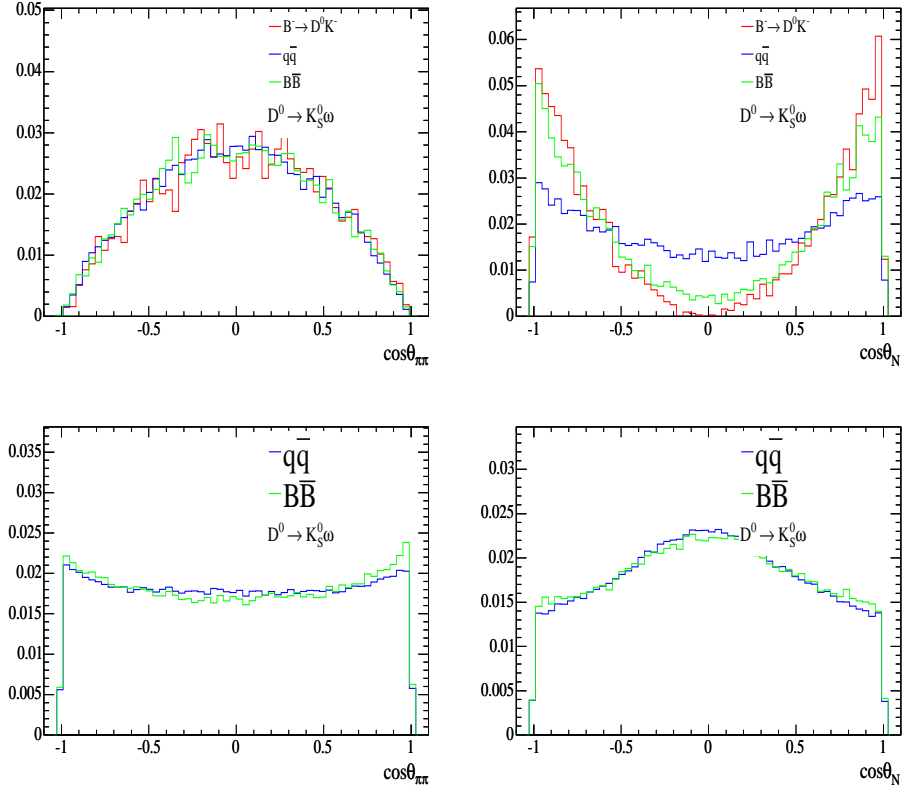


Figure 3.9: Distribution of the Dalitz angle $\cos\theta_{\pi\pi}$ (left column) and of the normal helicity angle $\cos\theta_N$ (right column) in signal and background simulated events reconstructed in the $B^- \rightarrow D^0 K^-, D^0 \rightarrow K_S^0 \omega$ analysis. The top plots correspond to correctly identified ω candidates: in background events $\cos\theta_N$ does not follow a pure $\cos^2\theta_N^2$ distribution since the ω is only partially polarized. The bottom plots correspond to fake ω candidates

$p^* > 1.3 \text{ GeV}/c$ and invariant mass m_{D^0} within a $\pm 2.5\sigma_{m_{D^0}}$ window around the mean value $\langle m_{D^0} \rangle$, is considered a D^0 candidate. With the exception of the $D^0 \rightarrow K_S^0 \pi^0$ case, the two D^0 daughters are constrained to have a common vertex. Kaons from $D^0 \rightarrow K^- \pi^+$ and $D^0 \rightarrow K^+ K^-$ are required to pass the KaonLHVeryLoose PID selector, pions from $D^0 \rightarrow \pi^+ \pi^-$ are required to pass the PionLHLoose PID selector. The decay angle $\theta_{\text{hel}}(D^0)$ of the D^0 , defined as the angle between the direction of one D^0 daughter in the D^0 rest frame and the direction of the D^0 in the B rest frame, is expected from angular momentum conservation to follow a flat $\cos\theta_{\text{hel}}(D^0)$ distribution, while $\cos\theta_{\text{hel}}(D^0)$ is peaked at ± 1 in background $e^+e^- \rightarrow q\bar{q}$ events where a fake D^0 is picked from a random combinations of tracks and neutral objects in the two light quark jets, as shown for instance in Figure 3.10 for the $D^0 \rightarrow \pi^+ \pi^-$ mode. In D^0 decay modes ($\pi^+ \pi^-$, $K_S^0 \pi^0$ and $K_S^0 \omega$) which are affected by a higher $e^+e^- \rightarrow q\bar{q}$ combinatorial background we require $|\cos\theta_{\text{hel}}(D^0)| < 0.9$.

The mean D^0 invariant mass $\langle m_{D^0} \rangle$ and its resolution $\sigma_{m_{D^0}}$, determined from Gaussian fits to the invariant mass distributions of true reconstructed D^0 candidates in simulated $B \rightarrow D^0 K$ events are summarized in Table 3.9. A comparison of the D^0 invariant mass in signal and background events on Monte Carlo is shown in Figure 3.11.

With a mass-constraint refit of the D^0 candidates, where m_D^0 is fixed to the nominal D^0 mass [16], the D^0 RMS momentum resolution is improved by about 35% in the $K^- \pi^+$,

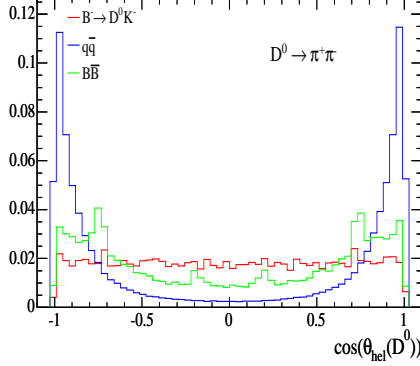


Figure 3.10: Distribution of the decay angle of the candidate D^0 reconstructed in the $B \rightarrow D^0 K, D^0 \rightarrow \pi^+ \pi^-$ analysis in signal ($B \rightarrow D^0 K^-$) and background ($q\bar{q}$ and $B\bar{B}$) simulated events.

D^0 mode	$\langle m_{D^0}^0 \rangle$ (MeV/ c^2)	$\sigma_{m_{D^0}^0}$ (MeV/ c^2)
$K^- \pi^+$	1864.5 ± 0.1	7.2 ± 0.1
$K^+ K^-$	1864.6 ± 0.1	6.5 ± 0.1
$\pi^+ \pi^-$	1864.5 ± 0.1	7.9 ± 0.1
$K_s^0 \pi^0$	1864.1 ± 0.3	20.0 ± 0.2
$K_s^0 \phi$	1865.4 ± 0.1	4.1 ± 0.1
$K_s^0 \omega$	1864.2 ± 0.2	9.2 ± 0.2

Table 3.9: D^0 invariant mass mean value $\langle m_{D^0} \rangle$ and resolution $\sigma_{m_{D^0}}$ in simulated $B \rightarrow D^0 K$ events.

$K^+ K^-$, $\pi^+ \pi^-$ (from ≈ 20 MeV/ c to ≈ 13 MeV/ c) and $K_s^0 \pi^0$ (from 31 to 20 MeV/ c) decay modes, and by about 15% in the $K_s^0 \phi$ and $K_s^0 \omega$ modes (from 22 to 19 MeV/ c and from 24 to 20 MeV/ c respectively).

3.5 B reconstruction

B mesons are reconstructed by combining a D^0 candidate with a charged track (“*bachelor*” or “*prompt*”) h . With the exception of the $D^0 \rightarrow K_s^0 \pi^0$ case, the prompt track and the D^0 are constrained to have a common vertex. The prompt particle is required to be detected by the DIRC with at least 5 Cherenkov photons ($N_\gamma \geq 5$), and its measured Cherenkov angle θ_C must be within $4 \sigma_{\theta_C}$ from the expected mean angle in the pion ($\theta_C^{\text{exp}}(\pi)$) or kaon ($\theta_C^{\text{exp}}(K)$) hypotheses, where σ_{θ_C} is the Cherenkov angle resolution. Information from the ElectroMagnetic Calorimeter and from the Instrumented Flux Return is used to reject tracks that are identified as electrons and muons, with very low pion mis-identification rates: 0.3% and 2% for e^\pm and μ^\pm , respectively [70, 71, 67].

One of the advantages of studying B physics in an $e^+ e^-$ collider at the $\Upsilon(4S)$ resonance is the kinematic constraint provided by the initial state. The energy of each B meson in the $\Upsilon(4S)$ frame must be equal to $\sqrt{s}/2$, where \sqrt{s} is the total $e^+ e^-$ CM energy. This constraint is exploited by introducing two almost uncorrelated kinematical variables [73],

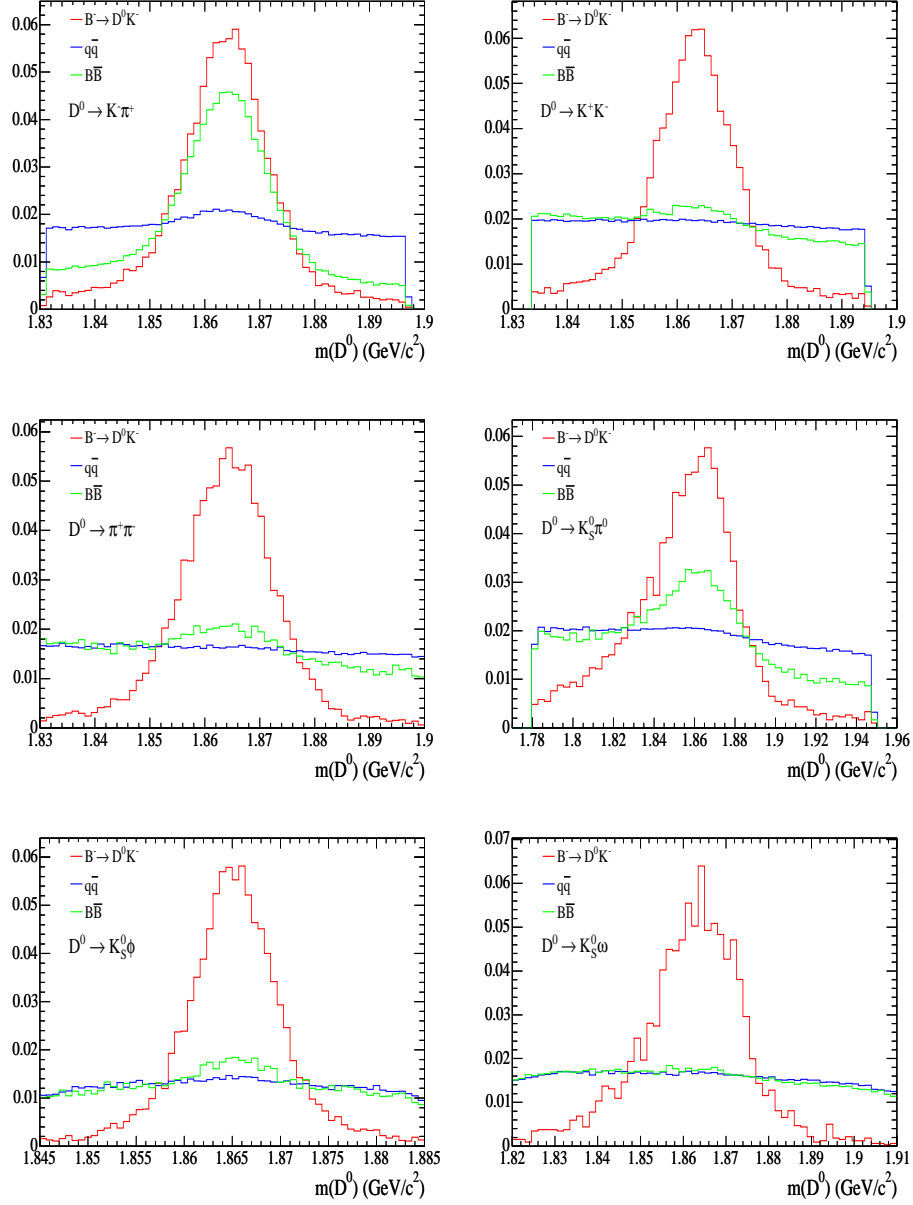


Figure 3.11: Invariant mass distribution of D^0 candidates reconstructed in signal ($B \rightarrow D^0 K$) and background ($q\bar{q}$ and $B\bar{B}$) simulated events, in each of the six decay D^0 modes under study. The distributions are normalized to the same area.

the *energy-substituted mass*:

$$m_{\text{ES}} \equiv \sqrt{\left(\frac{1}{2}s + \mathbf{p}_0 \cdot \mathbf{p}_B\right)^2 / E_0^2 - \mathbf{p}_B^2}. \quad (3.5)$$

and the *energy difference* ΔE :

$$\Delta E \equiv E_B^* - E_{\text{beam}}^* \quad (3.6)$$

The physical quantities \mathbf{p}_i ($i = 0, B$) and E_0 in (3.5) are measured in the laboratory frame and the subscript 0 and B refer to the e^+e^- system and the reconstructed B meson, respectively; E_B^* is the reconstructed CM energy of the candidate B . $E_{\text{beam}}^* = \sqrt{s}/2$ is the reconstructed CM beam energy. For correctly reconstructed B decays m_{ES} peaks at the B mass, as shown in Figure 3.12(a), while ΔE peaks at zero, as shown in Figure 3.12(b): their correlation is $\approx -8\%$, as shown in Figure 3.13.

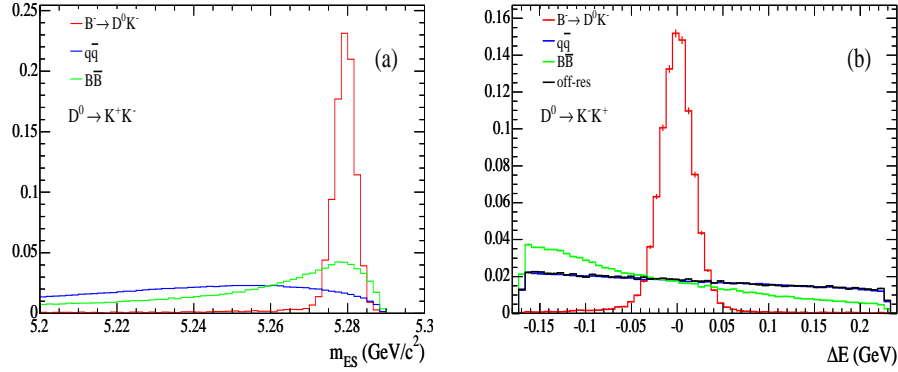


Figure 3.12: m_{ES} (left) and ΔE (right) distributions of B candidates reconstructed, in the $B \rightarrow D^0 K$, $D^0 \rightarrow K^+ K^-$ analysis, in signal ($B^- \rightarrow D^0 K^-$) and background ($q\bar{q}$ and $B\bar{B}$) simulated events. The distributions are normalized to the same area.

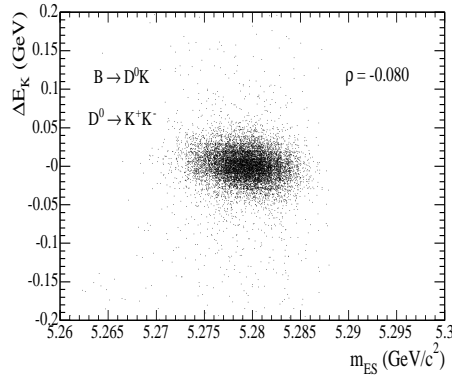


Figure 3.13: 2-dimensional $\{m_{\text{ES}}, \Delta E\}$ distribution of correctly identified B mesons reconstructed in the $B \rightarrow D^0 K$, $D^0 \rightarrow K^+ K^-$ analysis

By definition, m_{ES} depends on the B momentum in the laboratory frame but *not* on its energy, and is therefore independent of the mass hypothesis of the prompt particle, as shown in Figure 3.14(a). On the other hand, ΔE depends on the B energy and thus on the mass assignment of the prompt track h , as shown in Figure 3.14(b). When not explicitly stated, we reconstruct the ΔE variable by assigning the kaon mass to the bachelor track, otherwise the mass hypothesis of the prompt track will be explicitly indicated by writing ΔE_h , where $h = \pi$ or K . The dependence of ΔE on the mass of the prompt particle will be used in the unbinned maximum likelihood fit of Chapter 4 as a means to separate

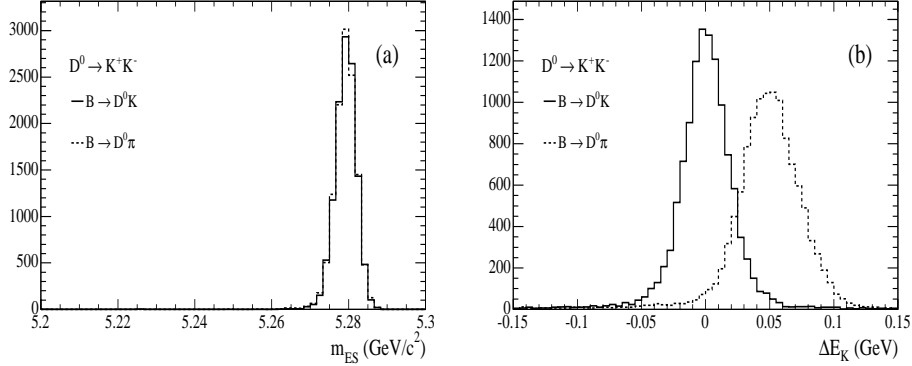


Figure 3.14: m_{ES} (left) and ΔE (right) distributions of correctly identified $B \rightarrow D^0 K$ and $B \rightarrow D^0 \pi$ decays in $B^- \rightarrow D^0 h^-$ simulated events.

$B^- \rightarrow D^0 \pi^-$ from $B^- \rightarrow D^0 K^-$ decays.

The m_{ES} resolution, $\sigma_{m_{\text{ES}}}$, is determined by the B meson true energy spread, which depends on event-by-event beam energy variations, $\sigma_{E_{\text{beam}}^*} \approx 2.6$ MeV [48], and by the B momentum measurement error in the $\Upsilon(4S)$ frame, $\sigma_{p_B^*} \approx 16$ MeV/ c :

$$\sigma_{m_{\text{ES}}}^2 \approx \sigma_{E_{\text{beam}}^*}^2 + \left(\frac{p_B^*}{M_B} \right)^2 \sigma_{p_B^*}^2. \quad (3.7)$$

Since in the $\Upsilon(4S)$ frame $p_B^*/M_B \simeq 0.06$, $\sigma_{m_{\text{ES}}}^2$ is dominated by the beam energy fluctuations: the m_{ES} distribution of correctly reconstructed $B \rightarrow D^0 K$ decays is therefore independent of the D^0 decay mode, as observed in simulated signal events. The m_{ES} distribution of correctly identified $B \rightarrow D^0 K$ ($D^0 \rightarrow K^+ K^-$) decays is shown in Figure 3.15(a). It has been parameterized with the sum of two Gaussian functions, $N \left(f_1 \times \frac{1}{\sqrt{2\pi}\sigma_1} e^{-\frac{1}{2} \left(\frac{m_{\text{ES}} - \mu_1}{\sigma_1} \right)^2} + (1 - f_1) \times \frac{1}{\sqrt{2\pi}\sigma_2} e^{-\frac{1}{2} \left(\frac{m_{\text{ES}} - \mu_2}{\sigma_2} \right)^2} \right)$, since for a small fraction ($1 - f_1 \approx 4\%$) of the candidates the B energy is slightly underestimated due to photon radiation in the final state. The width of the core Gaussian function is $\sigma_{m_{\text{ES}}} \equiv \sigma_1 = (2.51 \pm 0.03)$ MeV/ c^2 . We select B candidates with m_{ES} within a $\pm 3 \sigma_{m_{\text{ES}}}$ range from the mean value $\langle m_{\text{ES}} \rangle \equiv \mu_1$, where – since the m_{ES} distribution for signal events is the same in all channels – we use the values of $\langle m_{\text{ES}} \rangle$ and $\sigma_{m_{\text{ES}}}$ determined on $B^- \rightarrow D^0 \pi^-$, $D^0 \rightarrow K^- \pi^+$ candidates. In off-resonance data, which are collected at a center-of-mass energy 40 MeV below the $\Upsilon(4S)$ peak, the m_{ES} distribution is shifted – with respect to that of $q\bar{q}$ events in on-resonance data – by -20 MeV: for this reason, the off-resonance sample is selected by requiring $|m_{\text{ES}} + 20 \text{ MeV} - \langle m_{\text{ES}} \rangle| < 3\sigma_{m_{\text{ES}}}$.

The r.m.s. spread of the ΔE distribution in $B \rightarrow D^0 K$ decays depends on the B energy measurement resolution $\sigma_{E_B^*}$ and on the spread in E_{beam}^* :

$$\sigma_{\Delta E}^2 = \sigma_{E_{\text{beam}}^*}^2 + \sigma_{E_B^*}^2. \quad (3.8)$$

Since $\sigma_{E_B^*} \approx 17$ MeV for B mesons reconstructed in the decay modes studied in the analysis, while $\sigma_{E_{\text{beam}}^*} \approx 2.6$ MeV, $\sigma_{\Delta E}$ is dominated by the energy measurement error. Due to the D^0 mass-constraint, $\sigma_{E_B^*}$ is almost independent on the D^0 channel, and the final ΔE resolution for correctly reconstructed $B^- \rightarrow D^0 K^-$ candidates is almost the same

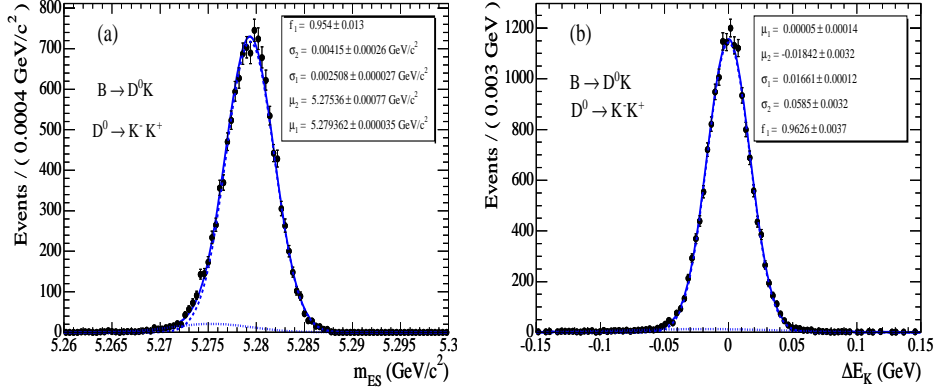


Figure 3.15: m_{ES} (left) and ΔE (right) distribution for true reconstructed $B^- \rightarrow D^0 K^-$, $D^0 \rightarrow K^+ K^-$ decays.

in every channel, $\sigma_{\Delta E} \approx 17$ MeV (Figure 3.15(b)). Like the m_{ES} one, also the ΔE distribution of true $B \rightarrow D^0 K$ candidates has been parameterized with the sum of two Gaussian functions, $N\left(f_1 \times \frac{1}{\sqrt{2\pi}\sigma_1} e^{-\frac{1}{2}\left(\frac{\Delta E - \mu_1}{\sigma_1}\right)^2} + (1-f_1) \times \frac{1}{\sqrt{2\pi}\sigma_2} e^{-\frac{1}{2}\left(\frac{\Delta E - \mu_2}{\sigma_2}\right)^2}\right)$, to take into account the small fraction $1 - f_1$ of B candidates whose energy is slightly underestimated. The width of the core Gaussian function is $\sigma_{\Delta E} \equiv \sigma_1 = (16.6 \pm 0.1)$ MeV.

For true $B^- \rightarrow D^0 \pi^-$ decays the assignment of the kaon mass to the prompt pion leads to overestimate its center-of-mass energy and therefore its measured ΔE is shifted by a quantity

$$\Delta E_{\text{shift}} \equiv \Delta E_K - \Delta E_\pi = \gamma \left(\sqrt{m_K^2 + p^2} - \sqrt{m_\pi^2 + p^2} \right) \quad (3.9)$$

with respect to the true value, where $\gamma \equiv E_{\mathcal{Y}(4S)}/M_{\mathcal{Y}(4S)} \approx 1.144$ and p is the bachelor track momentum in the lab frame. As the momenta of the reconstructed prompt tracks are almost equivalently distributed in the range $[1.5, 4.0]$ GeV/ c , it follows: ⁵

$$\begin{aligned} \Delta E_{\text{shift}} &\in [30, 85] \text{ MeV} \\ \langle \Delta E_{\text{shift}} \rangle &\simeq 50 \text{ MeV} \\ \sigma_{\Delta E}(B \rightarrow D^0 \pi) &\approx 21 \text{ MeV} \end{aligned} \quad (3.12)$$

This is shown in Figure 3.14, where the ΔE_K distributions of correctly identified $B \rightarrow D^0 \pi$ and $B \rightarrow D^0 K$ candidates in simulated $B \rightarrow D^0 h$ events are overlaid, and in Figure 3.16.

Since ΔE is used as a discriminating variable in the final fit, only a loose cut is applied to it: B candidates with ΔE in the range $[-160, 230]$ MeV are selected. The asymmetry of the selection cut takes into account the shift from zero by ≈ 50 MeV of the $B \rightarrow D^0 \pi$ ΔE distribution.

⁵It is easily seen that ΔE_{shift} can be written

$$\Delta E_{\text{shift}} = \gamma p \left(\sqrt{1 + (m_K/p)^2} - \sqrt{1 + (m_\pi/p)^2} \right) \quad (3.10)$$

$$\approx \gamma p \left(\left(1 + \frac{1}{2} \frac{m_K^2}{p^2} \right) - \left(1 + \frac{1}{2} \frac{m_\pi^2}{p^2} \right) \right) = \frac{\gamma}{2p} (m_K^2 - m_\pi^2) \approx \frac{0.128 \text{ GeV}/c}{p} \quad (3.11)$$

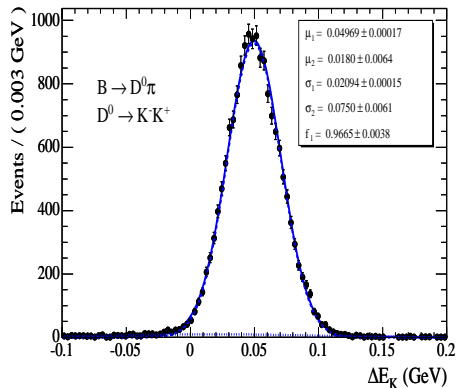


Figure 3.16: ΔE distribution for true reconstructed $B^- \rightarrow D^0\pi^-$, $D^0 \rightarrow K^+K^-$ decays. The distribution has been parameterized (solid line) with the sum of two Gaussian functions. The width of the core Gaussian is $\sigma_{\Delta E} = \sigma_1 = (20.9 \pm 0.2)$ MeV.

3.5.1 Additional selection criteria

In the channel $B^- \rightarrow D^0K^-$, $D^0 \rightarrow \pi^+\pi^-$, a significant contribution to the $B\bar{B}$ background in the ΔE signal region $[-50, 50]$ MeV comes from the much more abundant processes $B^- \rightarrow D^0\pi^-$, $D^0 \rightarrow K^-\pi^+$, and $B^- \rightarrow \bar{K}_X^{*0}[K^-\pi^+]\pi^-$ (where K_X^{*0} can be $K^{*0}(892)$, $K^{*0}(1430)$ or nearby resonances), where the prompt pion is incorrectly identified as a D^0 daughter and the charged kaon from the D^0 or K_X^{*0} is incorrectly identified as a B daughter. We remove this background contributions by requiring that the invariant mass of the system given by the prompt track and the pion from D^0 with opposite charge be greater than $1.9 \text{ GeV}/c^2$.

3.6 Continuum background suppression through event-shape variables

After having reconstructed and selected $B \rightarrow D^0h$, $D^0 \rightarrow X_1X_2$ candidates ($X_1X_2 = K^-\pi^+$, K^+K^- , ...) as described in previous Sections, surviving background candidates arise primarily from $e^+e^- \rightarrow q\bar{q}$ ($q = u, d, s, c$) events, in which random combinations of tracks and photons in the event are picked up in the reconstruction, and from misreconstructed $e^+e^- \rightarrow \Upsilon(4S) \rightarrow B\bar{B}$ events. In this section we describe how $q\bar{q}$ background is further (partially) suppressed: its final separation from the signal is done in the final fit, described in Chapter 4, together with the $B\bar{B}$ background measurement.

We reduce fake B candidates from $q\bar{q}$ events by making use of some event shape variables that exploit the different topologies of $e^+e^- \rightarrow q\bar{q}$ and $B\bar{B}$ events in the center-of-mass frame, the $\Upsilon(4S)$ rest frame. The two B mesons produced in $\Upsilon(4S) \rightarrow B\bar{B}$ decays are in fact almost at rest in the center-of-mass frame, there is no direction preferred by their decay products and the $B\bar{B}$ events are thus *spherical*. On the other hand, the light quarks from $e^+e^- \rightarrow q\bar{q}$ are produced with a significant momentum and their decay products are contained in two more or less collimated back-to-back jets.

All the shape variables that we have investigated are defined in terms of quantities (momenta and angles) measured in the center-of-mass (CM) frame. Two recurring concepts in their definitions are those of:

- *rest-of-event* (ROE), i.e. the set of all detected tracks and photons in the event that

have not been used to reconstruct the $B \rightarrow D^0 h$ candidate.

- thrust axis (\hat{T}) and thrust (T) [74]. The thrust axis is the direction \hat{T} , in the CM frame, that maximizes the thrust:

$$T = \max \left(\frac{\sum_i |\hat{T} \cdot \mathbf{p}_i^*|}{\sum_i |\mathbf{p}_i^*|} \right) \quad (3.13)$$

\mathbf{p}_i^* is the center-of-mass momentum of the i -th (charged or neutral) particle. The thrust can be computed by summing over all tracks and photons in the event (T), or considering only objects belonging to the B decay tree (T^B) or to the ROE (T^{ROE}).

The event-shape variables that we have considered are:

- The Legendre monomials, a set of momentum-weighted sums of the tracks and neutrals in the ROE [75]:

$$L_j = \sum_i^{\text{ROE}} p_i^* \times |\cos(\theta_i^*)|^j \quad (3.14)$$

θ_i^* is the CM angle between \mathbf{p}_i^* and the thrust axis \hat{T}^B of the B candidate. We have considered only the L_0, L_2 pair, since many analyses in *BABAR* have shown that adding other L_j ($j \neq 0, 2$) to the set of discriminating variables does not improve its signal/background separating power.

- the thrust computed using tracks and photons in the rest-of-event, T^{ROE} .
- R_2^{ROE} , the ratio of the Fox-Wolfram moments $H_2^{\text{ROE}}/H_0^{\text{ROE}}$, computed using tracks and photons in the rest-of-event. H_l^{ROE} is defined as [76] :

$$H_l^{\text{ROE}} \equiv \sum_{i,j}^{\text{ROE}} \frac{|\mathbf{p}_i^*| |\mathbf{p}_j^*|}{E_{\text{vis}}^{*2}} P_l(\cos \theta_{ij}^*) \quad (3.15)$$

P_l are the Legendre polynomials, θ_{ij} is the opening angle between \mathbf{p}_i^* and \mathbf{p}_j^* , and E_{vis}^* is the total visible energy of the event. For jet-like continuum events $|x| = |\cos \theta_{ij}|$ is peaked at zero, while for spherical $B\bar{B}$ events $|\cos \theta_{ij}|$ is more uniformly distributed: since $P_2(x) = \frac{1}{2}(3x^2 - 1)$, then R_2^{ROE} is shifted towards one in $q\bar{q}$ events and towards zero in $B\bar{B}$ events.

Other shape variables have been investigated but have not been used since they do not provide significant signal/background discrimination.

Additional signal/continuum background separation can be gained using quantities that are known from angular momentum conservation to have different distributions in signal and $q\bar{q}$ events. We consider the following two quantities:

- $|\cos(\mathbf{p}_B^*, \hat{z})|$ is the cosine of the angle of the B candidate momentum with respect to the beam (z) axis. In $\Upsilon(4S) \rightarrow B\bar{B}$ decays it follows a $\sin^2(\mathbf{p}_B^*, \hat{z})$ distribution while it is flat in $q\bar{q}$ events (modulo distortions due to the detector acceptance).
- $|\cos(\hat{T}^B, \hat{z})|$ is the cosine of the angle of the B candidate thrust axis with respect to the z axis. Modulo acceptance effects, signal events have an almost uniform distribution⁶ and background events follow a $1 + \cos^2(\hat{T}^B, \hat{z})$ shape.

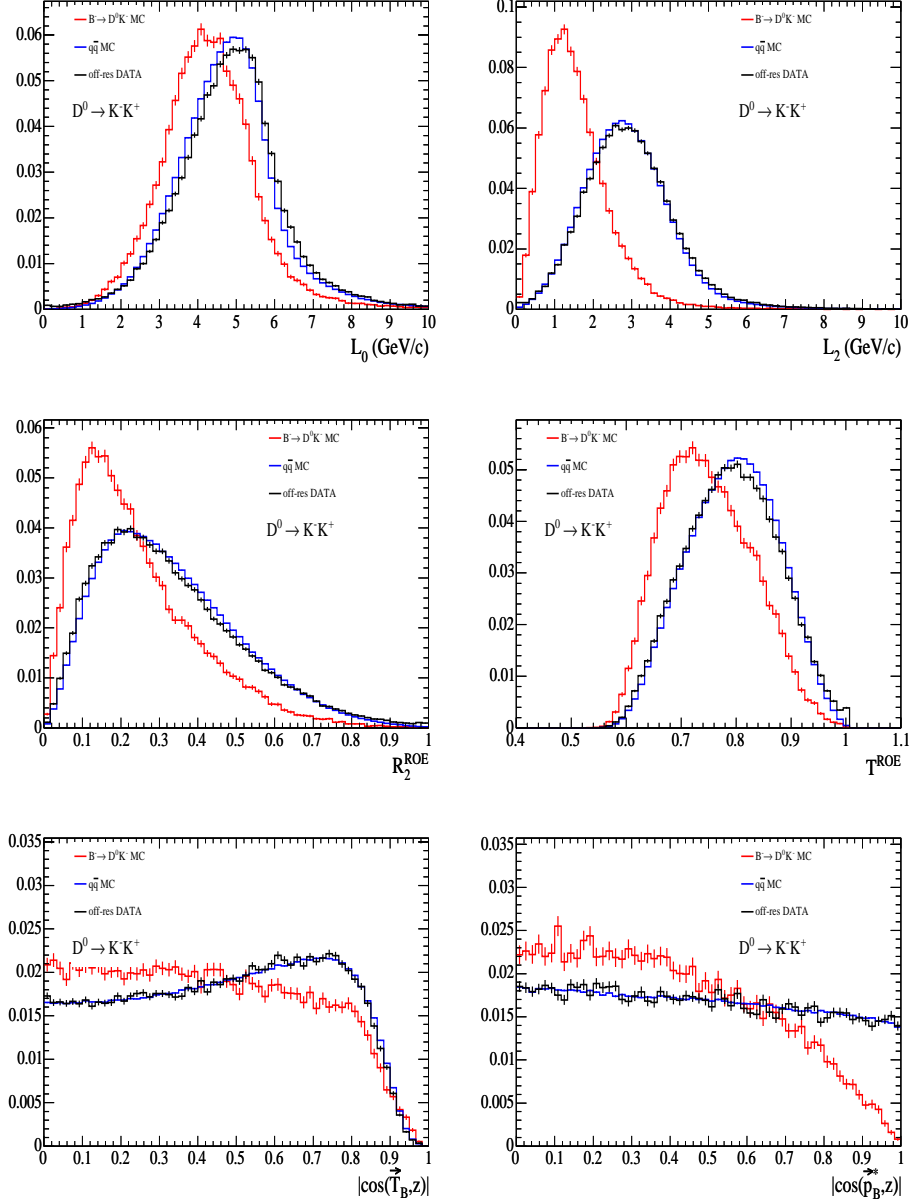


Figure 3.17: Distributions of the six event-shape variables considered in the analysis, in simulated $B^- \rightarrow D^0 K^-, q\bar{q}$ and $B\bar{B}$ simulated events, where the D^0 is reconstructed in the $D^0 \rightarrow K^+ K^-$ decay mode.

The distribution of the six quantities L_0 , L_2 , T^{ROE} , R_2^{ROE} , $|\cos(\hat{T}^B, \hat{z})|$ and $|\cos(\vec{p}_B^*, \hat{z})|$, for simulated $B \rightarrow D^0 K, D^0 \rightarrow K^+ K^-$ and $q\bar{q}$ events and for events selected in off-resonance data in the $D^0 \rightarrow K^+ K^-$ analysis, are shown in Figure 3.17.

To take into account the correlations between the event shape variables and achieve a better signal/continuum background separation we have combined them into a linear

⁶The distribution is not perfectly flat, within the statistical fluctuations, because of the small – but not zero – B momentum in the $\Upsilon(4S)$ frame.

combination (Fisher discriminant [77]). The coefficients of the Fisher discriminant have been optimised for maximum statistical separation following a standard procedure [78] using MC samples of true signal events and $q\bar{q}$ events. Replacing $q\bar{q}$ simulated events with off-resonance data has yielded optimized coefficients that are consistent with those found in the previous case. The statistical separation that has been maximised is defined as:

$$\text{separation} = \frac{\mu(\text{signal}) - \mu(q\bar{q} \text{ background})}{\sqrt{\sigma(\text{signal})^2 + \sigma(q\bar{q} \text{ background})^2}} \quad (3.16)$$

where $\mu, \sigma(\text{signal})$ and $\mu, \sigma(q\bar{q} \text{ background})$ are the mean and width of the Fisher discriminant distributions for the signal and the continuum background, and depend on the shape variables included in the linear combination and on their coefficients.

We have considered, for all the six decay modes under investigation, seven different Fisher discriminants with various combinations of discriminating variables:

- F_1 : L_0, L_2
- F_2 : $L_0, L_2, |\cos(\mathbf{p}_B^*, \hat{z})|$
- F_3 : $L_0, L_2, |\cos(\hat{T}_B, \hat{z})|$
- F_4 : $L_0, L_2, R_2^{\text{ROE}}$
- F_5 : L_0, L_2, T^{ROE}
- F_6 : $L_0, L_2, |\cos(\hat{T}_B, \hat{z})|, |\cos(\mathbf{p}_B^*, \hat{z})|$
- F_7 : $L_0, L_2, |\cos(\hat{T}_B, \hat{z})|, |\cos(\mathbf{p}_B^*, \hat{z})|, R_2^{\text{ROE}}, T^{\text{ROE}}$

We have studied on Monte Carlo the simultaneous efficiency for signal and for continuum background of different selection criteria for all the Fisher discriminants that have been described. The signal efficiency versus continuum background efficiency, not very different among the seven combinations under study, is shown in Figure 3.18.

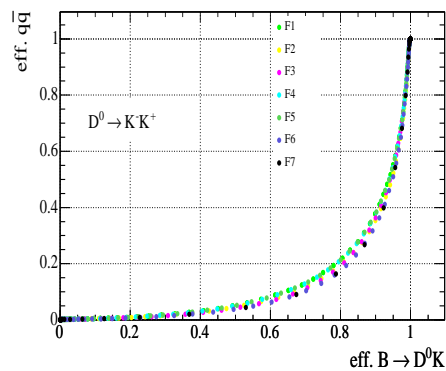


Figure 3.18: Signal efficiency versus continuum background efficiency for different selection criteria and different combinations of the discriminating shape variables. [Simulated $B \rightarrow D^0 K$ and $q\bar{q}$ events]

The combination that gives the best discriminating power and is defined with the minimum number of variables is $F \equiv F_6$, whose distribution in signal and $q\bar{q}$ background events is reported in Figure 3.19 for the six D^0 decay channels. In all the six decay modes,

the F distribution of correctly identified $B \rightarrow D^0 K$ candidates peaks at $\mu(\text{signal}) \approx -0.41$ and has a width $\sigma(\text{signal}) \approx 0.43$, while the F -distribution in $q\bar{q}$ events peaks at $\mu(q\bar{q}) \approx 0.38$ and has a width $\sigma(q\bar{q}) \approx 0.48$: the separation is about 1.23 in all the six cases. We have required $F < 0.28$ for events in which the D^0 is reconstructed in the $K^-\pi^+$ and $K_S^0\phi$ modes, and $F < 0.0$ for events in which the D^0 is reconstructed in the remaining four decay modes, where the level of continuum background is higher. The signal selection efficiency is 93% in the first case and 82% in the second case; the $q\bar{q}$ background rejection rates are 58% and 79% for $F < 0.28$ and $F < 0.0$, respectively.

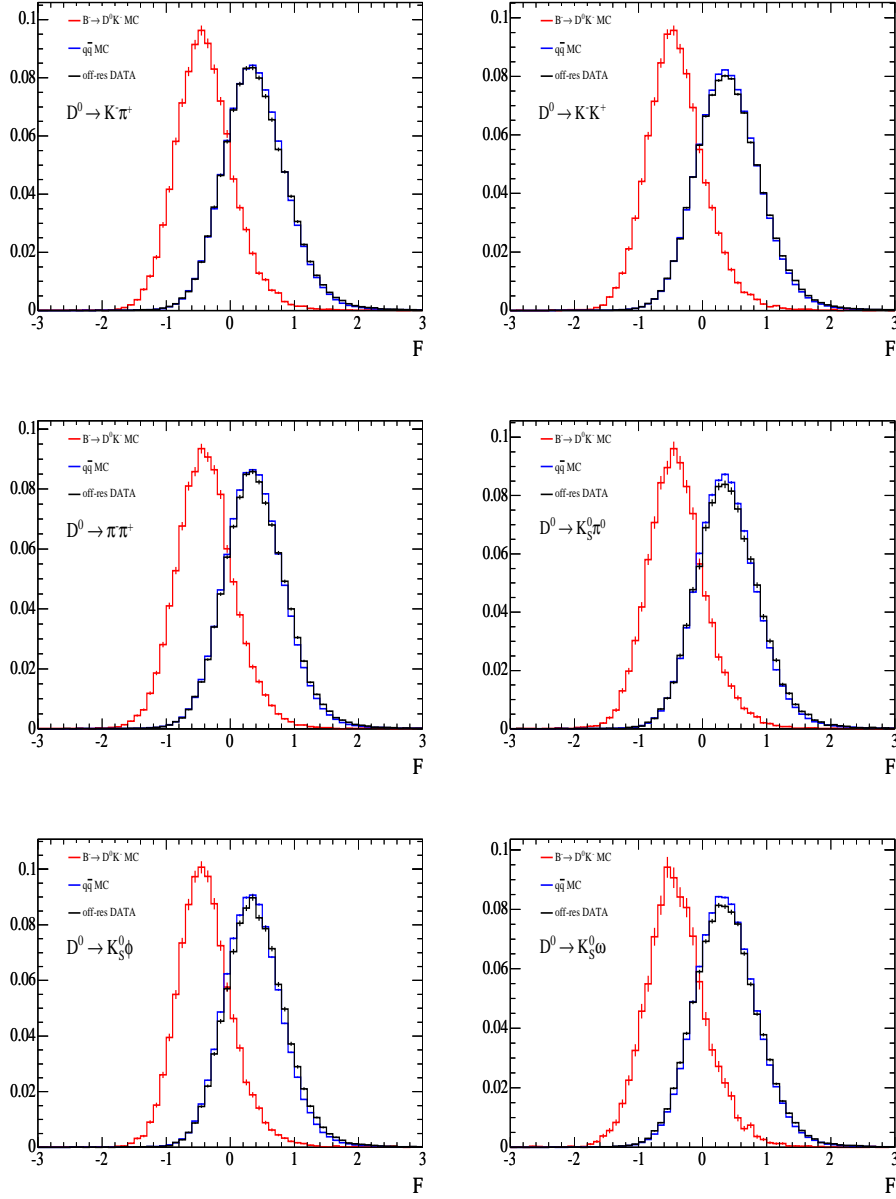


Figure 3.19: Distribution of the Fisher discriminant adopted to reduce the continuum background in simulated $B^- \rightarrow D^0 K^-$ and $q\bar{q}$ events and in off-resonance data.

3.7 Arbitration of multiple candidates

When reconstructing B candidates, it can sometimes happen that more than one combination satisfies the selection criteria in the same event. The rate at which this occurs depends on the reconstructed decay mode and on the selection cuts. It is very small when the D^0 is selected in the $K^-\pi^+$, K^+K^- , $\pi^+\pi^-$ and $K_S^0\phi$ final states, but it increases when a $D^0 \rightarrow K_S^0\pi^0$ or $D^0 \rightarrow K_S^0\omega$ is reconstructed, because the probability to select a fake candidate (due especially to misreconstructed ω or π^0 candidates) is higher.

We define the *multiplicity* as the ratio of the total number of selected candidates to the number of events in which at least one candidate is found. Figure 3.20 displays the distribution of $B \rightarrow D^0h$ candidates per event, selected in data with the standard selection summarized in Tables 3.11, 3.12, 3.13. The resulting multiplicity is reported on each plot. The multiplicity differs from 1 by less than 1% for the $K^-\pi^+$, K^+K^- , $\pi^+\pi^-$,

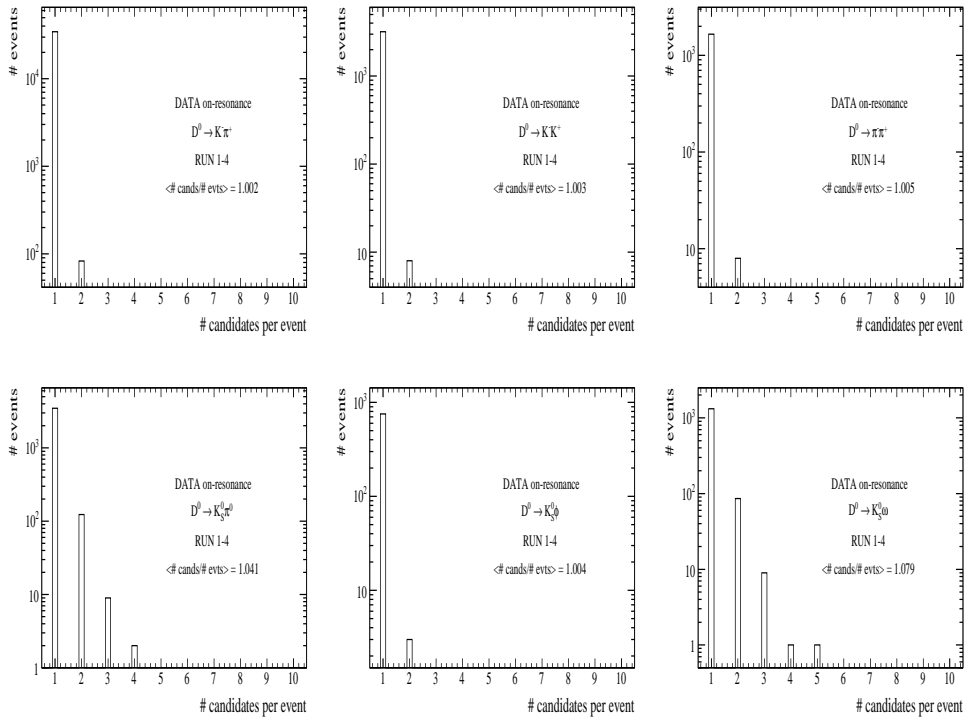


Figure 3.20: Distribution of the number of selected B candidates per event, before the application of the arbitration algorithm. The multiplicity values are shown. The B candidates are selected in data.

$K_S^0\phi$ selection, by 5% for the $K_S^0\pi^0$ selection and by 7% for the $K_S^0\omega$ selection.

In order to select only one candidate per event it is necessary to define a criterion that permits to identify, as far as possible, the combination with the larger probability to be a true signal $B \rightarrow D^0h$ decay. The D^0 invariant mass and the energy-substituted mass are chosen as discriminating quantities in all the channels. For the $D^0 \rightarrow CP$ -odd channels we also include, in the set of the discriminating variables, the invariant masses of the candidate ϕ , ω and π^0 . In events with multiplicity greater than one, the candidate with the minimum value of χ^2 is selected, with χ^2 defined as:

- in the $D^0 \rightarrow K^- \pi^+, K^+ K^-, \pi^+ \pi^-$ case:

$$\chi^2 = \frac{(m_{D^0} - \langle m_{D^0} \rangle)^2}{\sigma_{m_{D^0}}^2} + \frac{(m_{\text{ES}} - \langle m_{\text{ES}} \rangle)^2}{\sigma_{m_{\text{ES}}}^2} \quad (3.17)$$

- in the $D^0 \rightarrow K_S^0 \pi^0$ case:

$$\chi^2 = \frac{(m_{D^0} - \langle m_{D^0} \rangle)^2}{\sigma_{m_{D^0}}^2} + \frac{(m_{\text{ES}} - \langle m_{\text{ES}} \rangle)^2}{\sigma_{m_{\text{ES}}}^2} + \frac{(m_{\pi^0} - \langle m_{\pi^0} \rangle)^2}{\sigma_{m_{\pi^0}}^2} \quad (3.18)$$

- in the $D^0 \rightarrow K_S^0 \phi$ case:

$$\chi^2 = \frac{(m_{D^0} - \langle m_{D^0} \rangle)^2}{\sigma_{m_{D^0}}^2} + \frac{(m_{\text{ES}} - \langle m_{\text{ES}} \rangle)^2}{\sigma_{m_{\text{ES}}}^2} + \frac{(m_{\phi} - \langle m_{\phi} \rangle)^2}{\sigma_{m_{\phi}}^2 + \Gamma_{\phi}^2} \quad (3.19)$$

- in the $D^0 \rightarrow K_S^0 \omega$ case:

$$\chi^2 = \frac{(m_{D^0} - \langle m_{D^0} \rangle)^2}{\sigma_{m_{D^0}}^2} + \frac{(m_{\text{ES}} - \langle m_{\text{ES}} \rangle)^2}{\sigma_{m_{\text{ES}}}^2} + \frac{(m_{\pi^0} - \langle m_{\pi^0} \rangle)^2}{\sigma_{m_{\pi^0}}^2} + \frac{(m_{\omega} - \langle m_{\omega} \rangle)^2}{\sigma_{m_{\omega}}^2 + \Gamma_{\omega}^2} \quad (3.20)$$

The effect of the criterion has been fully investigated on simulated $B \rightarrow D^0 h$ decays. Table 3.10 lists, for all the six D^0 decay modes under study, the average multiplicity m in background events, the fraction f of signal events in which, after all the other selection criteria have been applied, more than one candidate is found, and the *right choice rate* r . The latter is defined as the number of events, with multiplicity greater than one, in which the true B candidate has been chosen by the arbitration algorithm, divided by the total number of events, with multiplicity greater than one, in which the true B candidate is present. In other words, the right choice rate is a measure of how many times, in events with multiple candidates, the arbitration algorithm selects – if present – the correct $B \rightarrow D^0 h$ candidate. In the end, in the selected samples, the fraction of rejected background candidates, equal to $m-1$, is very small (between 0.2 and 0.6%) in the $K^- \pi^+, K^+ K^-, \pi^+ \pi^-$ and $K_S^0 \phi$ modes, while it is about 5% in the $K_S^0 \pi^0$ mode and 8% in the $K_S^0 \omega$ mode. The fraction of signal candidates that are removed by the arbitration, equal to $f \times (1 - r)$, is about 0.1% in the $K^- \pi^+, K^+ K^-, \pi^+ \pi^-$ and $K_S^0 \phi$ modes, 0.7% in the $K_S^0 \pi^0$ mode and 1.7% in the $K_S^0 \omega$ mode.

D^0 decay mode	Multiplicity in bkg events	Fraction of $B \rightarrow D^0 h$ events with multiple B candidates	right choice rate (%)
$K^- \pi^+$	1.002	0.5%	68 ± 3
$K^+ K^-$	1.002	0.3%	78 ± 4
$\pi^+ \pi^-$	1.006	0.4%	71 ± 4
$K_S^0 \pi^0$	1.049	3.8%	82 ± 2
$K_S^0 \phi$	1.004	0.3%	97 ± 2
$K_S^0 \omega$	1.079	8.7%	81 ± 2

Table 3.10: Average multiplicity m in simulated background events, fraction f of simulated signal $B \rightarrow D^0 h$ events with multiple candidates and right choice rate r of the arbitration algorithm.

Parameter	Criterion
ΔE_K (MeV)	$[-160, 230]$
$ m_{\text{ES}} - \langle m_{\text{ES}} \rangle $	$< 3 \sigma$
prompt PID	VeryTightElectron=false and VeryTightMuon=false
prompt θ_C	$ \theta_C - \theta_C(\pi) < 4\sigma$ or $ \theta_C - \theta_C(K) < 4\sigma$
prompt N_γ	≥ 5
$ m_{D^0} - \langle m_{D^0} \rangle $	$< 2.5 \sigma$

Table 3.11: $B \rightarrow D^0 h$ selection criteria that are common to all the six D^0 decay modes under investigation. The mean and width of m_{D^0} are listed in Table 3.9.

3.8 Summary of the selection criteria

In this Section we summarize the $B \rightarrow D^0 h$ selection criteria, described in the previous paragraphs. Criteria that are common to all D^0 decay modes are listed in Table 3.11. We report in Tables 3.12 and 3.13 the selection criteria that depend on the D^0 decay mode under study and the final selection efficiencies, evaluated on signal Monte Carlo, for true $B^- \rightarrow D^0 K^-$ and $B^- \rightarrow D^0 \pi^-$ candidates: they are approximately 40% in the $D^0 \rightarrow K^- \pi^+$ mode, 30% in the $K^+ K^-$ and $\pi^+ \pi^-$ modes, 20% in the $K_s^0 \pi^0$ and $K_s^0 \phi$ modes and 7% in the $K_s^0 \omega$ mode.

	$D^0 \rightarrow K^- \pi^+$	$D^0 \rightarrow K^+ K^-$	$D^0 \rightarrow \pi^+ \pi^-$
Fisher discriminant	< 0.28	< 0.0	< 0.0
D^0 vertex probability	$> 0.01\%$	$> 0.01\%$	$> 0.01\%$
$D^0 \cos \theta_{\text{hel}} $	-	-	< 0.9
PID 1st D^0 daughter	KaonLHVeryLoose	KaonLHVeryLoose	PionLHLoose
PID 2nd D^0 daughter	-	KaonLHVeryLoose	PionLHLoose
other requirements	-	-	$m(h\pi) > 1.9 \text{ GeV}/c^2$ ($m_h = m_K$)
reco. efficiency			
<i>after</i> arbitration			
$B \rightarrow D^0 \pi$	$39.90 \pm 0.21 \%$	$31.24 \pm 0.20 \%$	$30.62 \pm 0.20 \%$
$B \rightarrow D^0 K$	$39.49 \pm 0.21 \%$	$30.73 \pm 0.20 \%$	$30.27 \pm 0.20 \%$

Table 3.12: Selection criteria used to select the candidate samples on which the unbinned maximum likelihood fit is performed. The mean and width of m_{D^0} are listed in Table 3.9.

3.9 Data-MC comparison

We show in Figures 3.21, 3.22, 3.23, 3.24 and 3.25 a comparison between Monte Carlo and data for the distributions of the most relevant quantities that are used in the selection or will be used in the final fit. The distribution of each variable is plotted after applying the selection criteria to all the other quantities. The Monte Carlo sample is scaled to the luminosity of the on-resonance data. At this stage we want to remain blind with respect to the $B^- \rightarrow D^0 K^-$ signal, therefore we select only candidates within a ± 50 MeV ΔE_π window around zero (with the exception of Figure 3.21, where we consider a large ΔE_π region) and apply a tight kaon veto to the prompt track. The agreement is good: the overall background and signal normalizations are correctly estimated by the Monte Carlo, and the small discrepancies in the mean or the width of the distributions of a few quantities (m_{ES} , $m(\pi^0)$, $m(D^0[\rightarrow K_s^0 \pi^0])$) are easily taken into account by adjusting the corresponding criteria when selecting the $B \rightarrow D^0 h$ candidates on data. We can therefore

	$D^0 \rightarrow K_S^0 \pi^0$	$D^0 \rightarrow K_S^0 \phi$	$D^0 \rightarrow K_S^0 \omega$
Fisher discriminant	< 0.0	< 0.28	< 0.0
D^0 vertex probability	-	> 0.01%	> 0.01%
D^0 $ \cos \theta_{\text{hel}} $	< 0.9	-	< 0.9
$ m_{K_S^0} - \langle m_{K_S^0} \rangle $ (MeV/ c^2)	< 7.8	< 7.8	< 7.8
K_S^0 signed 2D flight-length	> 2σ	> 2σ	> 2σ
$E(\pi^0)$ (MeV)	> 200	-	> 200
$m(\pi^0)$ (MeV/ c^2)	[115, 150]	-	[115, 150]
$ m_\phi - \langle m_\phi \rangle $ (MeV/ c^2)	-	< 12	-
$ \cos \theta_{\text{hel}}(\phi) $	-	> 0.4	-
PID ϕ daughters	-	KaonLHNNotAPion	-
$ m_\omega - \langle m_\omega \rangle $ (MeV/ c^2)	-	-	< 18
PID ω daughters	-	-	PionLHVeryLoose
ω helicity angles	-	-	$\cos^2 \theta_N \sin^2 \theta_{\pi\pi} > 0.08$
reco. efficiency			
<i>after arbitration</i>			
$B \rightarrow D^0 \pi$	17.75 ± 0.17 %	20.58 ± 0.17 %	6.99 ± 0.11 %
$B \rightarrow D^0 K$	17.08 ± 0.16 %	20.11 ± 0.17 %	6.94 ± 0.11 %

Table 3.13: Selection criteria used to select the candidate samples on which the unbinned maximum likelihood fit is performed. The mean and width of m_{D^0} are listed in Table 3.9.

proceed to the signal yield extraction with the final fit.

3.10 Expected signal yields

The $B \rightarrow D^0 \pi$ and $B \rightarrow D^0 K$ signal yields expected, from Monte Carlo simulation, in a statistics corresponding to that of the on-resonance data sample ($\mathcal{L} = 210.7 \text{ fb}^{-1}$, $N(B^\pm) = 231.8 \times 10^6$) are given in Table 3.14. The uncertainties from the number of B^\pm (1.1% [61], see Table 3.4) and from B , D^0 and secondary branching fractions (from PDG) are included (see Table 3.3). We also take into account uncertainties in the estimated efficiencies, due to the limited statistics of the Monte Carlo samples and to possible discrepancies between simulated and real events. Since absolute efficiencies are not relevant for the final measurements presented in this thesis, as we quote only asymmetries and branching fraction ratios in which most of the systematic errors on the efficiencies cancel, we do not go into details in the treatment of these uncertainties, which are summarized in Table 3.15. The tracks, π^0 , K_S^0 reconstruction efficiency and PID selection efficiency uncertainties have been evaluated according to the recipes provided by *BABAR* collaborators who have compared pure control samples selected in data and Monte Carlo [79, 80, 81]. The uncertainty on the efficiency of the selection criteria has been estimated through a comparison with the similar $B \rightarrow D_{(CP^\pm)}^0 K^*$ analysis that has been performed in *BABAR*. About 150 $B^\pm \rightarrow D_{CP^+}^0 K^\pm$ and 200 $B^\pm \rightarrow D_{CP^-}^0 K^\pm$ are expected.

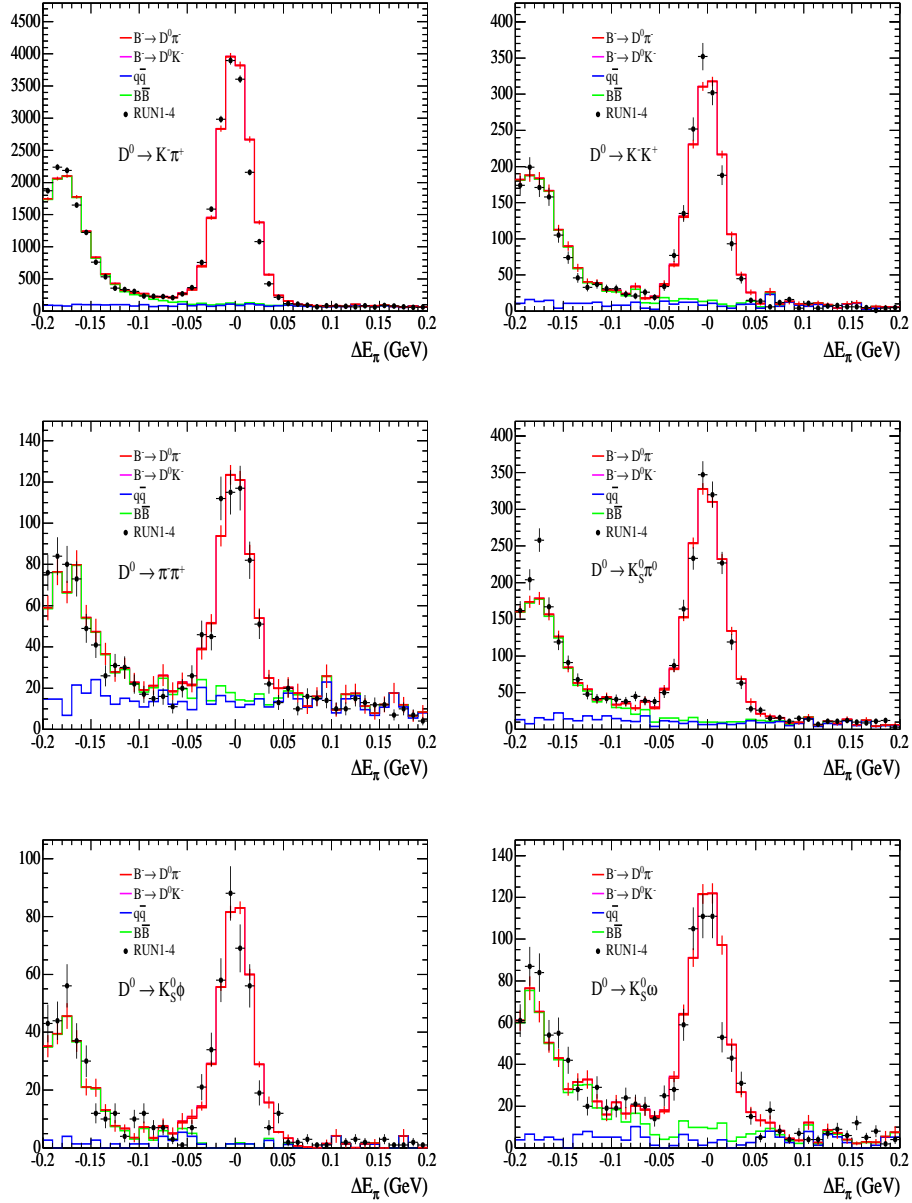


Figure 3.21: ΔE_π distribution of $B \rightarrow D^0 h$ candidates selected in data and in Monte Carlo. All the selection criteria listed in Tables 3.11, 3.12 and 3.13 have been applied. In addition a tight kaon veto has been applied to the prompt track h .

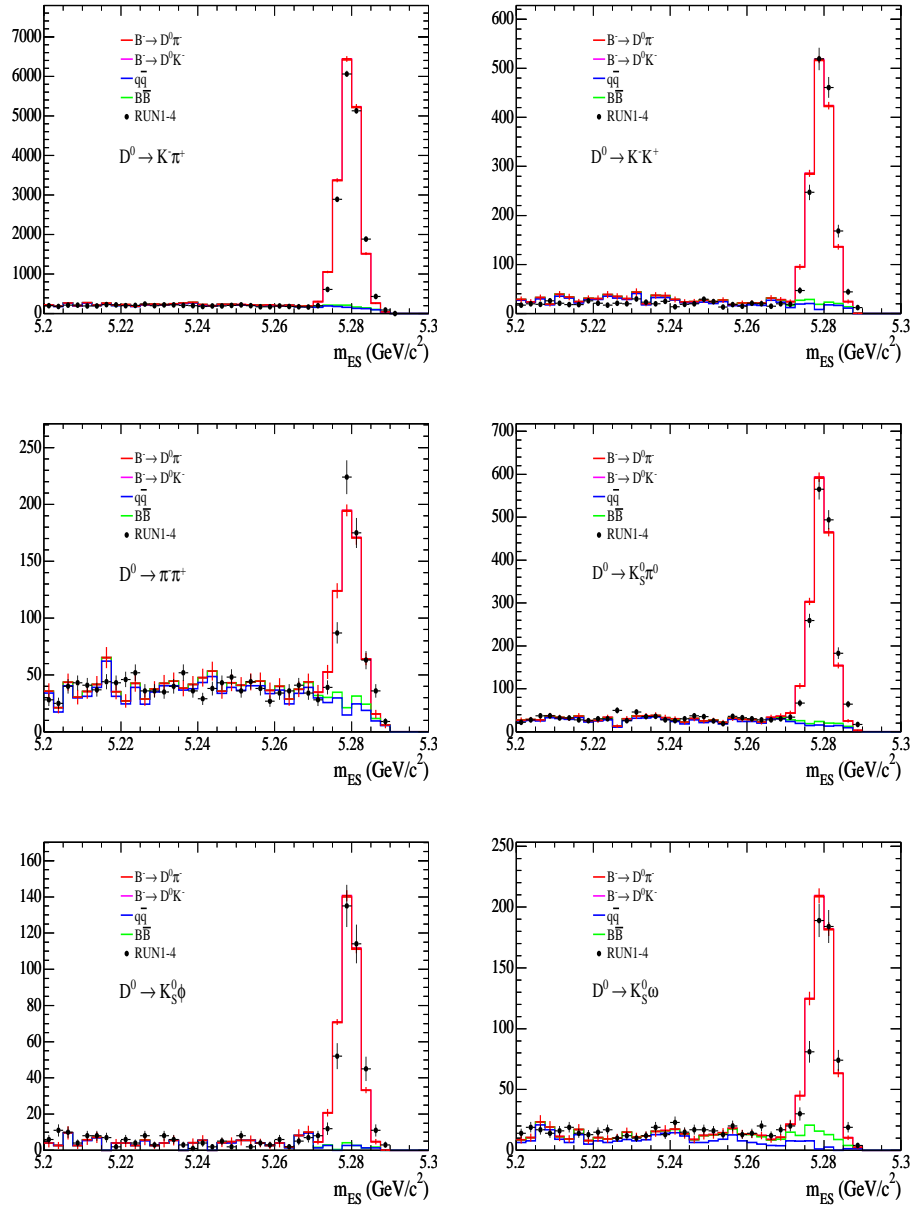


Figure 3.22: m_{ES} distribution of $B \rightarrow D^0 h$ candidates selected in data and in Monte Carlo. All the selection criteria listed in Tables 3.11, 3.12 and 3.13 have been applied, with the exception of that on m_{ES} . In addition a tight kaon veto has been applied to the prompt track h , and ΔE_π has been required to be in the range $[-50, 50]$ MeV.

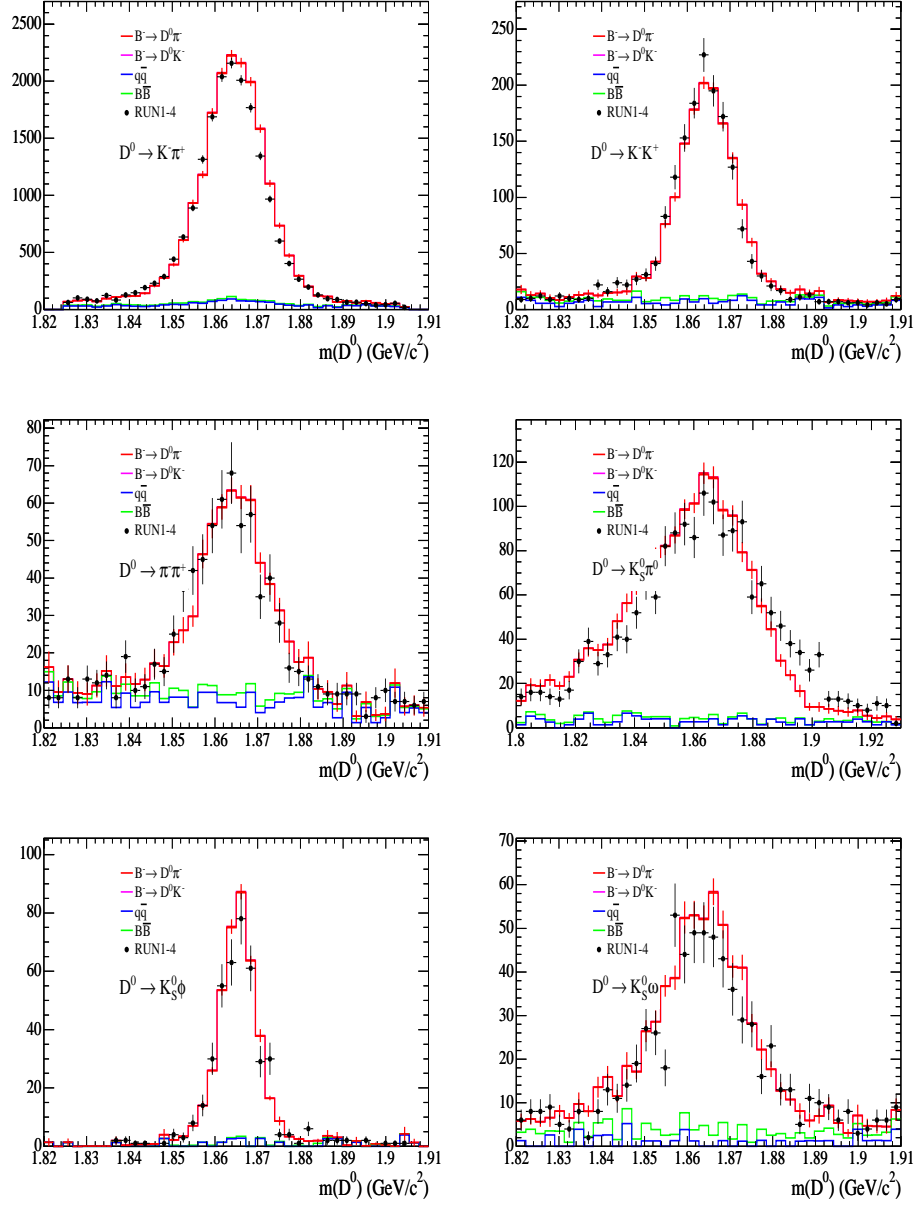


Figure 3.23: D^0 invariant mass distribution of $B \rightarrow D^0 h$ candidates selected in data and in Monte Carlo. All the selection criteria listed in Tables 3.11, 3.12 and 3.13 have been applied, with the exception of that on the D^0 mass. In addition a tight kaon veto has been applied to the prompt track h , and ΔE_π has been required to be in the range $[-50, 50]$ MeV.

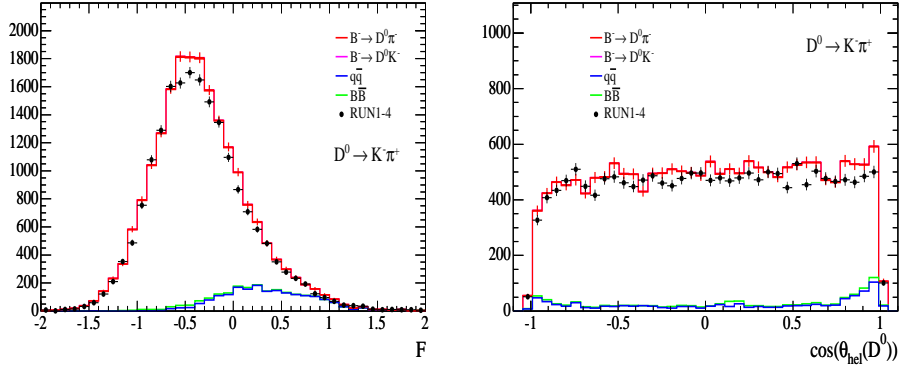


Figure 3.24: Fisher discriminant (F) and D^0 helicity angle ($\theta_{\text{hel}}(D^0)$) distributions of $B \rightarrow D^0 h$, $D^0 \rightarrow K^- \pi^+$ candidates selected in data and in Monte Carlo. All the selection criteria listed in Tables 3.11, 3.12 and 3.13 have been applied, with the exception of those on the plotted quantities. In addition a tight kaon veto has been applied to the prompt track h , and ΔE_π has been required to be in the range $[-50, 50]$ MeV.

D^0 decay mode	$N(D^0 K)$	$N(D^0 \pi)$
$K^- \pi^+$	$1419 \pm 38 \pm 84 \pm 34 \pm 89$	$17502 \pm 132 \pm 1033 \pm 415 \pm 932$
$K^+ K^-$	$113 \pm 11 \pm 7 \pm 4 \pm 8$	$1403 \pm 37 \pm 83 \pm 50 \pm 80$
$\pi^+ \pi^-$	$39 \pm 6 \pm 2 \pm 1 \pm 3$	$488 \pm 22 \pm 29 \pm 18 \pm 28$
$K_S^0 \pi^0$	$126 \pm 11 \pm 7 \pm 12 \pm 10$	$1604 \pm 40 \pm 95 \pm 154 \pm 116$
$K_S^0 \phi$	$31 \pm 6 \pm 2 \pm 4 \pm 3$	$385 \pm 20 \pm 23 \pm 50 \pm 29$
$K_S^0 \omega$	$47 \pm 7 \pm 3 \pm 9 \pm 4$	$577 \pm 24 \pm 34 \pm 113 \pm 51$

Table 3.14: $B \rightarrow D^0 K$ and $B \rightarrow D^0 \pi$ signal yields expected from simulation, for each of the six D^0 decay modes under study, in a statistics corresponding to that of the on-resonance data sample. The four uncertainties on the yields come respectively from (1) statistical fluctuations, (2) number of B^\pm and $\mathcal{B}(B \rightarrow D^0 \pi)$, (3) D^0 branching fraction ratios, (4) uncertainties on the selection efficiency and, for the $B \rightarrow D^0 K$ yield, $\mathcal{B}(B \rightarrow D^0 K)/\mathcal{B}(B \rightarrow D^0 \pi)$. Here we have assumed $\mathcal{B}(B \rightarrow D^0 K)/\mathcal{B}(B \rightarrow D^0 \pi) = 8.19\%$, and $R_{CP+} = R_{CP-} = 1$.

	$K^- \pi^+$	$K^+ K^-$	$\pi^+ \pi^-$	$K_S^0 \pi^0$	$K_S^0 \phi$	$K_S^0 \omega$
Tracks selection	2.1%	2.1%	2.1%	2.1%	2.7%	2.7%
PID efficiency	2.8%	3.5%	3.5%	2.0%	3.5%	3.5%
K_S^0 reconstruction	-	-	-	3.0%	3.0%	3.0%
π^0 reconstruction	-	-	-	3.0%	-	3.0%
All other selection criteria	4.0%	4.0%	4.0%	5.0%	5.0%	6.0%
MC stat.	0.5%	0.6%	0.7%	0.9%	0.8%	1.6%
Total	5.4%	5.7%	5.8%	7.2%	7.4%	8.7%

Table 3.15: Breakdown of the different contributions to the systematic uncertainty on the absolute $B \rightarrow D^0 K$ and $B \rightarrow D^0 \pi$ efficiencies.

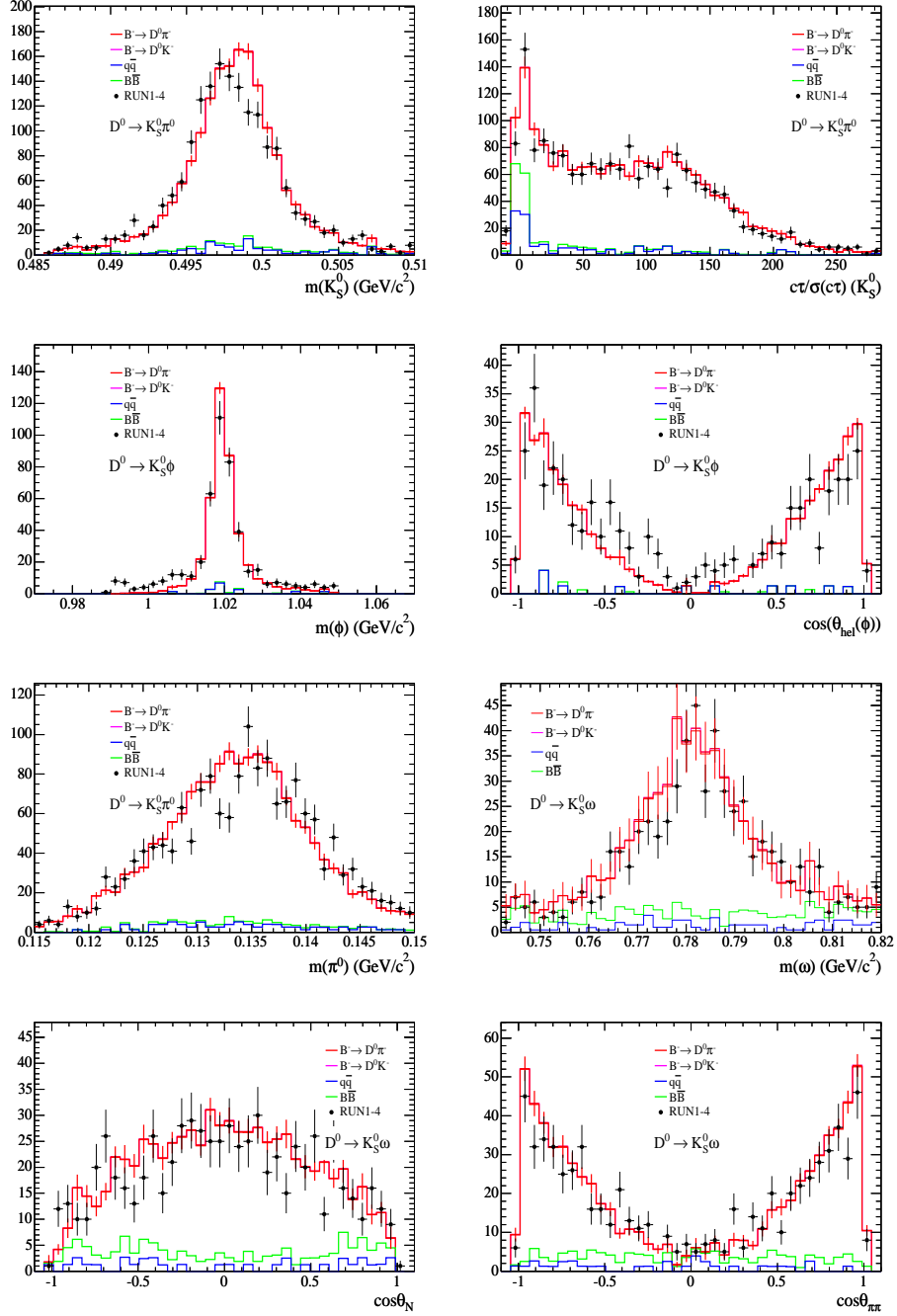


Figure 3.25: Distributions, for $B \rightarrow D^0 h$ candidates selected in data and in Monte Carlo, of (from top to bottom, left to right): K_S^0 invariant mass and flight length significance, ϕ invariant mass and helicity angle, π^0 invariant mass, ω invariant mass and helicity and Dalitz angles. All the selection criteria listed in Tables 3.11, 3.12 and 3.13 have been applied, with the exception of those on the plotted quantities. In addition a tight kaon veto has been applied to the prompt track h , and ΔE_π has been required to be in the range $[-50, 50]$ MeV.

Chapter 4

Measurement of the $B^\pm \rightarrow D_{(CP)}^0 h^\pm$ yields and of the GLW observables

In this Chapter the $B \rightarrow D^0 K$ and $B \rightarrow D^0 \pi$ yields are extracted, performing a maximum likelihood fit to two discriminating variables, the energy difference $\Delta E \equiv \Delta E_K$ of the B candidate and the Cherenkov angle θ_C of the prompt track h . Fits are done for each of the six samples of $B \rightarrow D^0 h$, $D^0 \rightarrow X_1 X_2$ candidates ($X_1 X_2 = K^- \pi^+$, $K^+ K^-$, $\pi^+ \pi^-$, $K_s^0 \pi^0$, $K_s^0 \phi$, $K_s^0 \omega$) that have been selected with the criteria described in the previous Chapter. Correcting the yields with the different $B \rightarrow D^0 K$ and $B \rightarrow D^0 \pi$ selection efficiencies, the branching fraction ratios $\mathcal{B}(B \rightarrow D_{(CP\pm)}^0 K)/\mathcal{B}(B \rightarrow D_{(CP\pm)}^0 \pi)$ and the double ratios R_\pm are determined. Performing the fits separately to the B^+ and B^- samples allows to measure the yields for $B^+ \rightarrow D_{CP\pm}^0 K^+$ and $B^- \rightarrow D_{CP\pm}^0 K^-$ and thus the CP asymmetries $A_{CP\pm}$. To most effectively use all available information, we choose to perform an unbinned fit, since this approach is known to yield smaller statistical uncertainties on the fit parameters than a corresponding binned fit. Moreover, the choice of the unbinned fit allows us to use probability density functions which depend on parameters that are computed on a event-by-event basis (for instance the mean of the θ_C distribution, which is the expected angle and therefore depends on the momentum p of the prompt track in the selected event).

Here is the outline of the Chapter:

- we first investigate, in Section 4.1, the composition of background events that pass our selection criteria. These events are classified, according to their ΔE and θ_C distributions, in different background categories.
- in Section 4.2 we describe the unbinned maximum likelihood fit procedure used to extract the signal ($B \rightarrow D^0 K$ and $B \rightarrow D^0 \pi$) yields.
- in Sections 4.3 and 4.4 we describe the parameterization respectively of the θ_C and ΔE probability density functions for the two signals and the various background categories.
- in Section 4.5 the unbinned maximum likelihood fit reliability to return unbiased estimates of the signal yields is validated by means of extensive Monte Carlo studies.
- in Section 4.6 we perform the unbinned maximum likelihood fit, for the six D^0 decay channels, on the samples selected in *BABAR* simulated events, and compare the results with expectations.

- in Section 4.7 the yields of the $B \rightarrow D^0\pi$ and $B \rightarrow D^0K$ signals in the six D^0 decay channels, resulting from the maximum likelihood fit on data, are quoted.
- in Section 4.8 we summarize the results of the fits performed, as a control check, on background samples.
- in Section 4.9 the main systematic errors are discussed and evaluated.
- finally, in Sections 4.10 and 4.11, the GLW observables $A_{CP\pm}$ and R_{\pm} are evaluated and discussed.

4.1 Background characterization

In order to measure $B \rightarrow D^0\pi$, $B \rightarrow D^0K$ and background yields through a maximum likelihood fit, an accurate knowledge of the background sources and how the discriminating variables are distributed in background events is required. To this purpose we have studied the nature of the background candidates selected in about 150 fb^{-1} of $e^+e^- \rightarrow q\bar{q}$ simulated events and about 620 fb^{-1} of $e^+e^- \rightarrow B\bar{B}$ simulated events (Section 3.2, Table 3.5), and in the off-resonance data sample (21.6 fb^{-1} , see Section 3.2, Table 3.4).

After having applied the selection criteria of the previous Chapter we find from these studies that only in 2% or less of the background B candidates in the final sample the prompt track is neither a pion nor a kaon. In these rare cases the prompt track is typically a mis-identified high-momentum lepton (a muon in 80-90% of the times), whose Cherenkov angle usually differs by less than one σ_{θ_C} (where σ_{θ_C} is the θ_C resolution) from the expected value in the pion hypothesis, while it differs by more than four σ_{θ_C} (typically about 6-7 standard deviations) from the expected value in the kaon hypothesis. When exploiting the Cherenkov angle measurement, therefore, these background events can be assimilated to those where the prompt track is a true pion, and we can distinguish, according to the nature of the bachelor track, the following two background categories: the background in which the bachelor track is a real kaon, which will be denoted as “ $B \rightarrow D^0K$ background”, and the background in which the bachelor track is not a kaon, usually a pion (or in a few cases, as stated above, a lepton), which will be denoted as “ $B \rightarrow D^0\pi$ background”. The θ_C probability density function (PDF) of the $B \rightarrow D^0K$ background is identical to that of the $B \rightarrow D^0K$ signal, and the θ_C PDF of the $B \rightarrow D^0\pi$ background is identical to that of the $B \rightarrow D^0\pi$ signal: they will be discussed in detail in Section 4.3. Separation between the $B \rightarrow D^0K$ signal and the $B \rightarrow D^0K$ background (and, similarly, between the $B \rightarrow D^0\pi$ signal and the $B \rightarrow D^0\pi$ background) is achieved by exploiting, in the fit, their different ΔE distributions.

The nature of the $B \rightarrow D^0\pi$ and $B \rightarrow D^0K$ backgrounds is substantially similar: both of them are composed by two main sources, one coming from continuum production of light quark pairs and one coming from the misreconstructed decays of B mesons produced in $e^+e^- \rightarrow B\bar{B}$ collisions. These two background sources are characterized by quite different ΔE distributions and for this reason they are treated separately. Whenever the distinction of the nature of the bachelor track will be necessary, the continuum and $B\bar{B}$ backgrounds will be labeled with $q\bar{q}(h)$ ($h = \pi, K$) and $B\bar{B}(h)$ ($h = \pi, K$), respectively. In $B\bar{B}$ events there are special sources of background that are particularly difficult to deal with, backgrounds that are peaking in the ΔE signal region. In the following we shall refer to this effect as “peaking” $B\bar{B}$ background.

$q\bar{q}$ and $B\bar{B}$ (non-peaking) backgrounds

Figures 4.1(a-f) show the ΔE distribution of the $B \rightarrow D^0\pi$ background, as obtained from generic Monte Carlo events with the standard selection criteria and an additional tight kaon veto applied to the bachelor track. Figures 4.2(a-f) show the ΔE distribution of

the $B \rightarrow D^0 K$ distribution, as obtained from generic Monte Carlo events selected with the same standard criteria and the additional requirement that the kaon veto fails for the prompt track. $B\bar{B}$ peaking backgrounds have been removed. In all these figures both the continuum and $B\bar{B}$ components are shown, normalized to the same integrated luminosity (corresponding to the luminosity of the data sample) in order to compare their relative magnitude. As can be seen, background B candidates selected in $e^+e^- \rightarrow q\bar{q}$ events are characterized by a linear ΔE distribution, since they are reconstructed from random combinations of tracks and (true or fake) D^0 candidates: their ΔE PDF parameterization will be discussed in detail in Section 4.4.2. The ΔE distribution of the $B\bar{B}$ background, as can be seen in Figures 4.1 and 4.2, has a more complex structure, concentrating at negative ΔE values, and can be understood by looking in detail at the composition of the background from $B\bar{B}$ events. The main contributions originate in fact from the processes:

- $B^- \rightarrow D^{*0} h^-$, $D^{*0} \rightarrow D^0 \pi^0$ or $D^{*0} \rightarrow D^0 \gamma$, $D^0 \rightarrow X_1 X_2$, in which the π^0 or γ from the D^{*0} is missed
- $B^- \rightarrow D^0 \rho^-$, $D^0 \rightarrow X_1 X_2$, $\rho^- \rightarrow \pi^- \pi^0$, and $B^- \rightarrow D^0 K^{*-}$, $D^0 \rightarrow X_1 X_2$, $K^{*-} \rightarrow K^- \pi^0$, in which the π^0 from the ρ^- or K^{*-} is missed

These types of $B\bar{B}$ background events are characterized by the fact that a neutral pion or a photon is not assigned to the candidate B , therefore the reconstructed B energy is lower than the true value, and ΔE is shifted towards negative values. Let us consider, as an example, a $B^- \rightarrow D^{*0} K^-$, $D^{*0} \rightarrow D^0 \pi^0$, $D^0 \rightarrow K^- \pi^+$ decay characterized by a typical π^0 momentum $p_{\pi^0} = 110 \text{ MeV}/c$ in the $\Upsilon(4S)$ CM frame. If the π^0 is missed and the decay is identified as a $B \rightarrow D^0 K$, the energy E_B^* of the reconstructed B candidate is shifted by $-E_{\pi^0}^* = -\sqrt{m_{\pi^0}^2 + p_{\pi^0}^2} \approx -175 \text{ MeV}$ and its momentum lies in the range $\sim [230, 350] \text{ MeV}/c$ (B mesons have a momentum of about $340 \text{ MeV}/c$ in the $\Upsilon(4S)$ frame). Consequently, ΔE is shifted by -175 MeV , apart from the reconstruction uncertainties, and m_{ES} lies in the range $[5.270, 5.285] \text{ GeV}/c^2$. Only a fraction of these background events is thus removed by the requirements $\Delta E > -0.160 \text{ GeV}$ and $|m_{\text{ES}} - \langle m_{\text{ES}} \rangle| < 3\sigma_{m_{\text{ES}}}$ ($\langle m_{\text{ES}} \rangle \approx 5.280 \text{ GeV}/c^2$, $\sigma_{m_{\text{ES}}} \approx 2.5 \text{ MeV}/c^2$): the remaining ones tend to accumulate near the low ΔE boundary, -160 MeV . The ΔE distribution of the $B\bar{B}(\pi)$ background is similar in shape to the corresponding $B\bar{B}(K)$ background: however, because of the difference between the kaon and pion mass, the distribution is shifted by about 50 MeV in the positive direction. This consideration explains why the $B\bar{B}(\pi)$ background is concentrated around $\Delta E \approx -0.125 \text{ MeV}$.

The amount of $B\bar{B}$ background with a correctly reconstructed D^0 candidate rapidly drops down as the ΔE increases, and it is usually quite small in the $B \rightarrow D^0 h$ signal region. However, in a small fraction of $B\bar{B}$ events background B candidates are selected from a random combination of a charged track and a fake D^0 candidate, reconstructed with one or more tracks or neutral objects not belonging to a real D^0 decay. In this case the B candidate can have larger values of ΔE : as for the $q\bar{q}$ background, these events are spread throughout the whole ΔE region, therefore a fraction of them occupies the ΔE signal region.

As a last comment on Figures 4.1 and 4.2, we can observe that data-MC agreement is very good, giving us a high confidence in the background comprehension.

$B\bar{B}$ peaking backgrounds

A first, but small and irreducible type of peaking background arises from charmless $B^- \rightarrow X_1 X_2 h^-$ decays, which have the same final states as the $B^- \rightarrow D^0 (\rightarrow X_1 X_2) h^-$ signal. This background is therefore undistinguishable from the signal, when exploiting

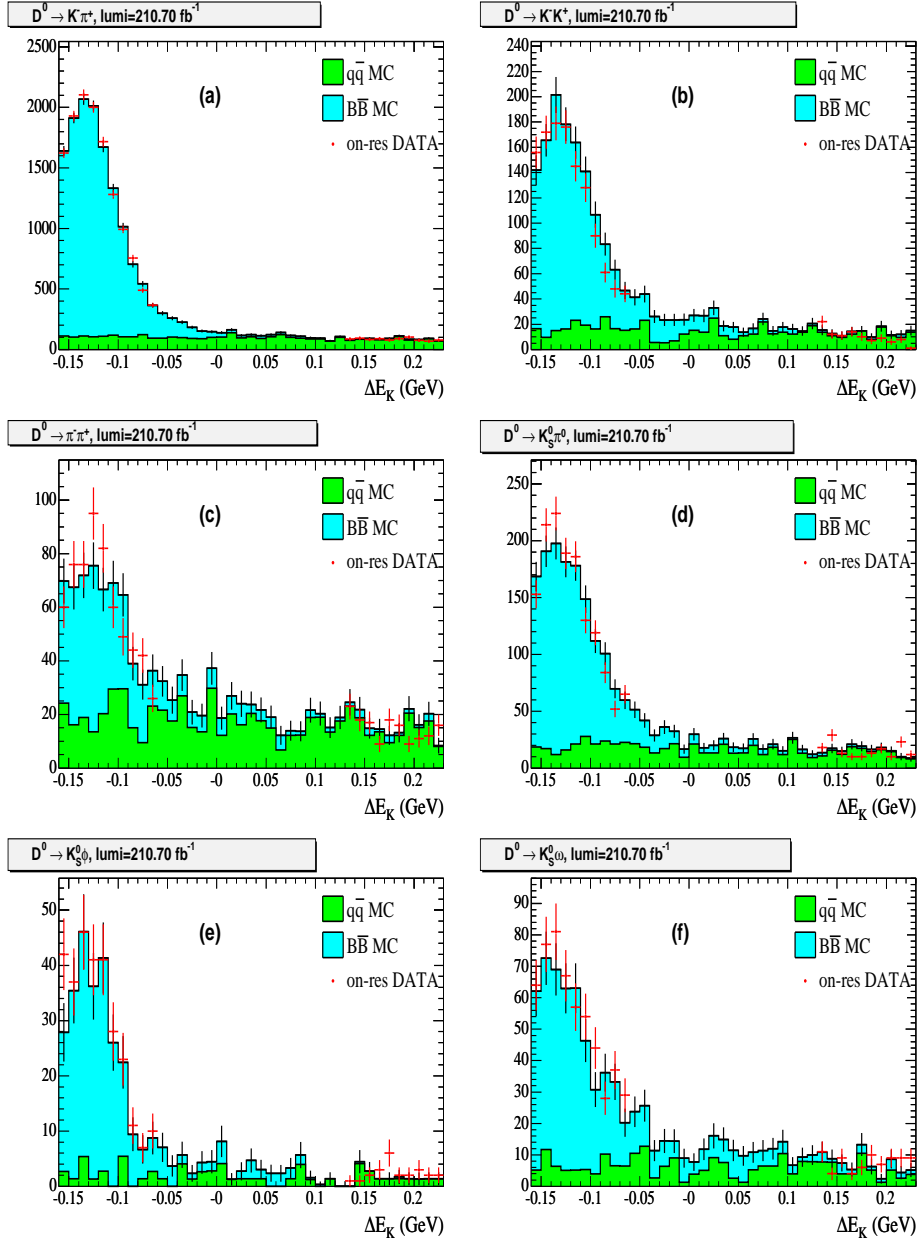


Figure 4.1: ΔE distribution of the $B \rightarrow D^0\pi$ background (solid histograms). Fake B candidates have been selected, with the standard criteria of Chapter 3 and an additional tight kaon veto, in $q\bar{q}$ and $B\bar{B}$ background events (i.e., $B \rightarrow D^0K$ and $B \rightarrow D^0\pi$ events are explicitly vetoed). Overlaid (red dots) is the distribution of B candidates selected in data (with the same criteria) outside of the $B \rightarrow D^0K$ and $B \rightarrow D^0\pi$ signal regions ($\Delta E < -80$ MeV or $\Delta E > 130$ MeV).

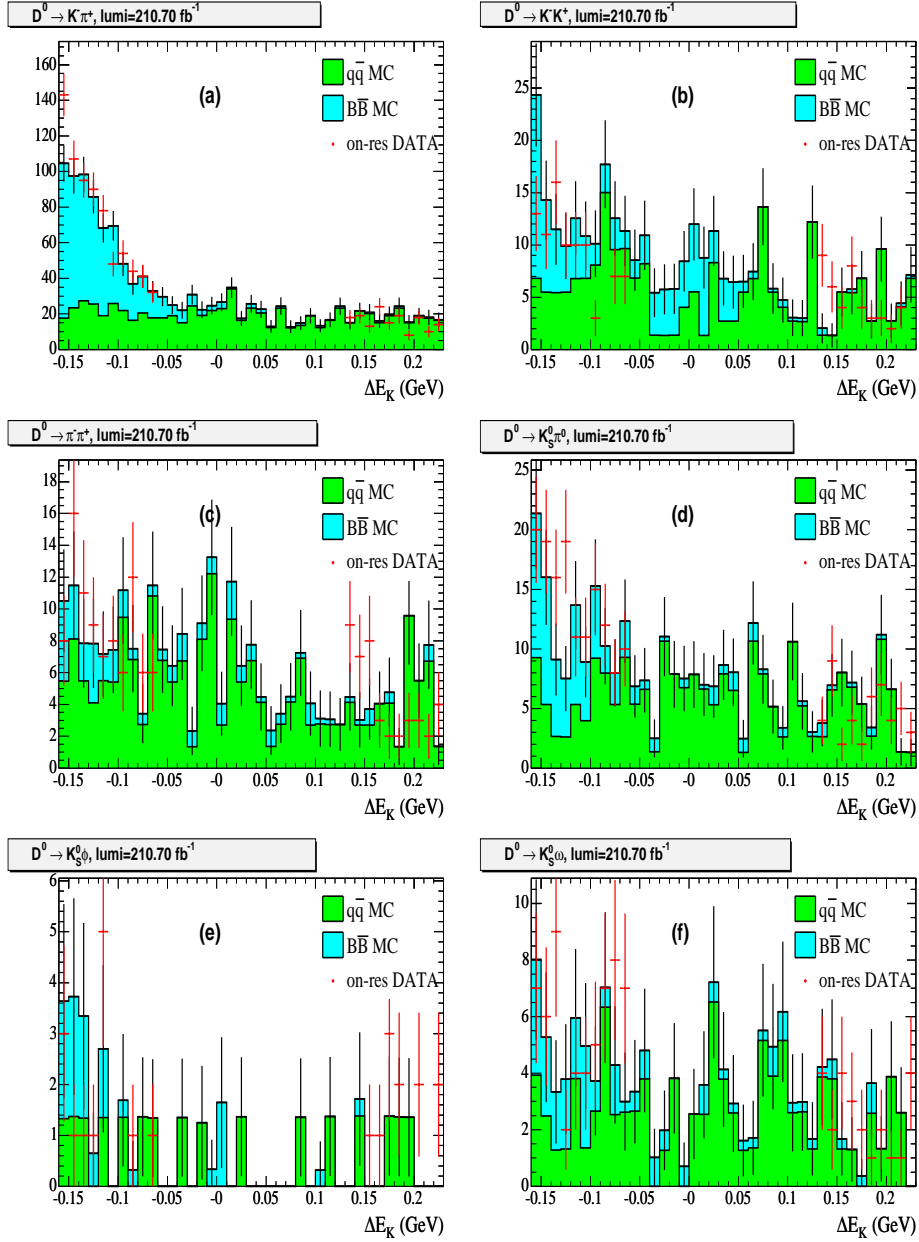


Figure 4.2: ΔE distribution of the $B \rightarrow D^0 K$ background. Fake B candidates have been selected, with the standard criteria of Chapter 3 and requiring that the prompt track fails a tight kaon veto, in $q\bar{q}$ and $B\bar{B}$ background events (i.e., $B \rightarrow D^0 K$ and $B \rightarrow D^0 \pi$ events are explicitly vetoed). Overlaid (red dots) is the distribution of B candidates selected in data (with the same criteria) outside of the $B \rightarrow D^0 \pi$ and $B \rightarrow D^0 K$ signal regions ($\Delta E < -80$ MeV or $\Delta E > 130$ MeV).

the ΔE and θ_C variables.¹ In the $D^0 \rightarrow K^- \pi^+$ mode the peaking background is totally negligible, because $\mathcal{B}(B^- \rightarrow K^- \pi^+ K^-) < 1.3 \times 10^{-6}$ at 90% C.L. and $\mathcal{B}(B^- \rightarrow K^- \pi^+ \pi^-) = (5.7 \pm 0.4) \times 10^{-5}$: taking into account a selection efficiency which is about 0.5%, as evaluated on simulated $B^- \rightarrow K^- \pi^+ h^-$ decays, the expected peaking events are about 2 for $h = K$ and 66 for $h = \pi$, to be compared with more than one thousand $B \rightarrow D^0 K$ and more than fifteen thousand $B \rightarrow D^0 \pi$ expected signal events. In the other D^0 modes, where the signal yields are by a factor more than ten lower than in the $K^- \pi^+$ case, the upper limits for $B^- \rightarrow X_1 X_2 h^-$ are at the 10^{-5} level, and with selection efficiencies around 0.5% we cannot exclude a priori a relevant peaking background contribution. We estimate this background by exploiting the D^0 mass sidebands and counting the number of background events that survive our selection (apart from the D^0 mass cut) and for which the invariant mass $m(X_1 X_2)$ lies outside the D^0 mass signal window. This number is scaled by the ratio of the width of the D^0 signal window and the width of the D^0 sideband region: these events will be subtracted from the signal inside the fit procedure (Section 4.2). The counting is done by performing a fit, similar to that used to extract the signal yields described in next Sections, to the $\{\Delta E, \theta_C\}$ distribution of events in the D^0 mass sidebands. The background ΔE PDF is a straight line with floating slope, because in the D^0 mass sidebands there is only combinatorial background, as the $B\bar{B}$ background from $B \rightarrow D^{*0} h$ and $B \rightarrow D^0 \rho$ or $B \rightarrow D^0 K^*$ is removed by vetoing the D^0 mass signal window. The $X_1 X_2 h$ ΔE PDFs and the kaon and pion θ_C PDFs are the same as the ones used in the final fit and are described in Sections 4.4.3 and 4.3.

The sideband region definitions are reported in Table 4.1, together with the number of events that survive the selection. The number of peaking events has a certain relevance only for the $B \rightarrow D^0 K$, $D^0 \rightarrow K^+ K^-$ mode, where $(64 \pm 14) \times 0.34 = (21 \pm 5)$ events will be subtracted in the fit. The sideband window choice is determined from three considerations:

- In the pre-selection of D^0 candidates, only the ones with invariant mass inside the range $[1774.5 - 1.9145]$ MeV/ c^2 are reconstructed in the $K^+ K^-$, $\pi^+ \pi^-$ and $K_s^0 \pi^0$ modes, and the range is reduced to $[1794.5 - 1.8945]$ MeV/ c^2 in the $K_s^0 \phi$ and $K_s^0 \omega$ modes.
- It is necessary to avoid contamination from signal $B \rightarrow D^0 h$ events with D^0 invariant mass in the tails of the $m(D^0)$ distribution, so, the larger the $m(D^0)$ resolution, the narrower the available sideband.
- in the $K^+ K^-$ mode, there is a not negligible number of $B \rightarrow D^0 h$, $D^0 \rightarrow K^- \pi^+$ decays (due to the higher $D^0 \rightarrow K^- \pi^+$ branching fraction) selected in the upper D^0 sideband, around 1.94 GeV/ c^2 , arising from misidentification of the pion from D^0 as a kaon. The ΔE distribution of these events is partially peaked in the signal region and would lead to an overestimate of the $K^+ K^- h$ background, and therefore we veto the region $m(D^0) > 1.9145$ GeV/ c^2 in this mode. Analogously, in the $\pi^+ \pi^-$ mode $B \rightarrow D^0 h$, $D^0 \rightarrow K^- \pi^+$ decays where the D^0 kaon is misidentified as a pion are selected in the lower D^0 mass sideband, around 1.78 GeV/ c^2 , and therefore we veto the region $m(D^0) < 1.8145$ GeV/ c^2 .

A second type of peaking background affects only the $B \rightarrow D^0 h$, $D^0 \rightarrow K_s^0 \phi (\rightarrow K^+ K^-)$ and $B \rightarrow D^0 h$, $D^0 \rightarrow K_s^0 \omega (\rightarrow \pi^+ \pi^- \pi^0)$ channels, and is constituted by $B \rightarrow D^0 h$ decays followed by a D^0 decay to the same final states that we reconstruct, $K_s^0 K^+ K^-$ and $K_s^0 \pi^+ \pi^- \pi^0$, without the intermediate production of a ϕ or a ω resonance. This

¹Actually, the ΔE distribution of the $B^- \rightarrow X_1 X_2 K^-$ background is about 75% larger than the one of the $B \rightarrow D^0 K$ signal. This is due to the fact that in the reconstruction of the signal decay chain a mass fit is performed on the $X_1 X_2$ system forming the D^0 . The D^0 mass fit improves the energy resolution of the $X_1 X_2$ system if it originates from a true D^0 , otherwise it worsens the resolution.

D^0 mode	$m(D^0)$ sideband region (MeV/ c^2)	peaking events (K)	peaking events (π)	scale factor
K^+K^-	[1774.5 – 1834.5], [1884.5 – 1914.5]	64 ± 14	0_{-0}^{+15}	0.34
$\pi^+\pi^-$	[1814.5 – 1839.5], [1889.5 – 1954.5]	12 ± 12	0_{-0}^{+7}	0.38
$K_S^0\pi^0$	[1774.5 – 1804.5], [1924.5 – 1954.5]	0_{-0}^{+6}	0_{-0}^{+5}	1.67
$K_S^0\phi$	[1794.5 – 1834.5], [1894.5 – 1934.5]	0_{-0}^{+2}	0_{-0}^{+1}	0.28
$K_S^0\omega$	[1794.5 – 1829.5], [1899.5 – 1934.5]	9 ± 8	0_{-0}^{+4}	0.69

Table 4.1: D^0 mass sideband region definitions and number of peaking background events. The expected yields in the signal D^0 window are obtained by multiplying these yields for the scale factor, which is defined as the ratio of the widths of the D^0 mass signal and sideband regions.

background is potentially very dangerous since the D^0 final state can have opposite CP with respect to that of our signal (the s -wave, non-resonant amplitudes $D^0 \rightarrow K_S^0 K^+ K^-$ and $D^0 \rightarrow K_S^0 \pi^+ \pi^- \pi^0$ are CP -even) and therefore dilutes the measured CP asymmetries. This effect can be monitored and subtracted using the $B \rightarrow D^0 \pi$, $D^0 \rightarrow K_S^0 \phi$ and $B \rightarrow D^0 \pi$, $D^0 \rightarrow K_S^0 \omega$ as control samples, as explained in Section 4.9.5.

4.2 Fit procedure

The $B \rightarrow D^0 K$, $B \rightarrow D^0 \pi$ and background yields in the event sample selected with the criteria described in the previous Chapter are determined through an unbinned maximum likelihood fit. The likelihood \mathcal{L} for the selected sample is given by the product of the probabilities for each individual candidate and a Poisson factor:

$$\mathcal{L} = \frac{e^{-N'} (N')^N}{N!} \prod_{i=1}^N \mathcal{P}_i. \quad (4.1)$$

The probability \mathcal{P}_i for a candidate in the event i is the sum of the signal and background terms:

$$\begin{aligned} \mathcal{P}_i(\Delta E, \theta_C) = & \frac{N_{D^0\pi}}{N'} \mathcal{P}_i^{D^0\pi} + \frac{N_{D^0K}}{N'} \mathcal{P}_i^{D^0K} + \\ & \frac{N_{q\bar{q}(\pi)}}{N'} \mathcal{P}_i^{q\bar{q}(\pi)} + \frac{N_{q\bar{q}(K)}}{N'} \mathcal{P}_i^{q\bar{q}(K)} + \\ & \frac{N_{B\bar{B}(\pi)}}{N'} \mathcal{P}_i^{B\bar{B}(\pi)} + \frac{N_{B\bar{B}(K)}}{N'} \mathcal{P}_i^{B\bar{B}(K)} + \\ & \frac{N_{X_1 X_2 K}}{N'} \mathcal{P}_i^{X_1 X_2 K}. \end{aligned} \quad (4.2)$$

where $N' = N_{D^0\pi} + N_{D^0K} + N_{q\bar{q}(\pi)} + N_{q\bar{q}(K)} + N_{B\bar{B}(\pi)} + N_{B\bar{B}(K)} + N_{X_1 X_2 K}$. Each addendum on the right-hand side of equation (4.2) is the product of two different terms. The ratio N_J/N' ($J = D^0\pi, D^0K, \dots$) represents the probability to choose a candidate of type J after the selection criteria are applied; the term \mathcal{P}_i^J is the probability density function for measuring the particular set of physical quantities $\{\Delta E, \theta_C\}_i$ in the i^{th} event, once the candidate of type J has been selected:

$$\mathcal{P}_i^J = \mathcal{P}_{\Delta E, i}^J \mathcal{P}_{\theta_C, i}^J. \quad (4.3)$$

Here and from now on, unless otherwise stated, $B\bar{B}(\pi)$ and $B\bar{B}(K)$ are referred to the non-peaking $B\bar{B}$ component.

The first factor in the likelihood definition (equation 4.1) is a poissonian term describing the probability of observing N events (the number of candidates of the sample on which the fit is performed) when N' is the expected number. It correctly takes into account the statistical fluctuations in the estimate of the *a priori* composition of each type of candidate after the selection criteria are applied. If the poissonian term were not present, the fit would estimate the composition of that particular selected sample, and *not* the *a priori* composition after the application of the selection criteria. This is reflected in a different estimation of the errors of the parameters N_J : in fact we must note that the presence of the poissonian term also constrains the sum N' of the extracted number of candidates to be equal to N , the total number of selected candidates. The likelihood defined in (4.1) is called an *extended maximum likelihood*[82]. The fits are performed using the MINUIT package[83].

In the fit, the free parameters are the six signal and background yields: $N_{D^0\pi}$, N_{D^0K} , $N_{q\bar{q}(\pi)}$, $N_{q\bar{q}(K)}$, $N_{B\bar{B}(\pi)}$, $N_{B\bar{B}(K)}$, and two parameters of the ΔE signal PDF, $\mathcal{P}_{\Delta E}^{D^0K}$, as it will be shown in Section 4.4.1. The number of peaking background events $N_{X_1X_2K}$ is fixed to the values in the third column of Table 4.1, scaled by the corresponding value in the last column of the same Table. When performing the fit to the B^+ and B^- samples separately, to extract the signal asymmetries, the number of peaking events is fixed to half the values in Table 4.1 (i.e. we assume no charge asymmetry in this background and equal statistical fluctuations for positive and negative X_1X_2K decays): the corresponding systematic uncertainty is evaluated in Section 4.9. All other parameters contained in all other PDFs (but $\mathcal{P}_{\Delta E}^{D^0K}$) are fixed: the way they are obtained is described in the next two Sections.

4.3 Particle ID probability density functions

The probability $\mathcal{P}_{\theta_C, i}^J$ is defined as:

$$\mathcal{P}_{\theta_C, i}^J = \begin{cases} \mathcal{P}_{\theta_C, i}^K & J = D^0K, q\bar{q}(K), B\bar{B}(K) \text{ or } X_1X_2K \\ \mathcal{P}_{\theta_C, i}^\pi & J = D^0\pi, q\bar{q}(\pi) \text{ or } B\bar{B}(\pi) \end{cases} \quad (4.4)$$

where $\mathcal{P}_{\theta_C}^K$ and $\mathcal{P}_{\theta_C}^\pi$ are the probability density functions for the Cherenkov angle in the hypothesis that the prompt track be either a charged kaon or pion. These probability density functions are derived from the value of the Cherenkov angle (θ_C) as measured in the DIRC. The parameterization is the same as developed in *BABAR* for the $B^0 \rightarrow K^-\pi^+$ analysis [22], and has been determined on kaon and pion tracks from D^0 decays in a $D^{*+} \rightarrow D^0\pi^+$, $D^0 \rightarrow K^-\pi^+$ control sample. The correlation between the charge of the D^0 daughters and that of the D^* is exploited: the $\pi(K)$ track is always the one with the same (opposite) charge as the D^* . Only the tracks from the D^0 decay have been used, as the soft pion momentum is well below the interesting kinematic range. The control sample is selected by means of kinematic criteria only (invariant masses of the D^0 and D^{*+} candidates, $D^{*+}-D^0$ mass difference, χ^2 probabilities of the vertex fit to the D^0 and D^{*0} daughters) and has a purity around 96%. Only tracks that are reconstructed in the DIRC are used to form the D^0 candidate. The same “quality” cuts that have been used in this analysis to select the candidate prompt tracks are applied to the kaon and pion candidates in the control sample: the number of observed signal photons in the DIRC must be greater than 5, in order to decrease the number of poor θ_C fits and hence improve the θ_C resolution, the measured Cherenkov angle must be consistent within 4σ with that expected either for a kaon or a pion of same momentum, and tracks identified as leptons by the VeryTight electron and muon *BABAR* selectors are rejected. From the selected control sample, the θ_C PDFs are determined with the following method, detailed in [85]:

- the θ_C pulls, $(\theta_C - \theta_C^{\text{exp}}) / \sigma_{\theta_C}$, in bins of both momentum and $\cos \theta$, are computed. θ is the polar angle of the track, $\theta_C^{\text{exp}} = \cos^{-1} \frac{1}{\beta n}$ is the expected Cherenkov angle given

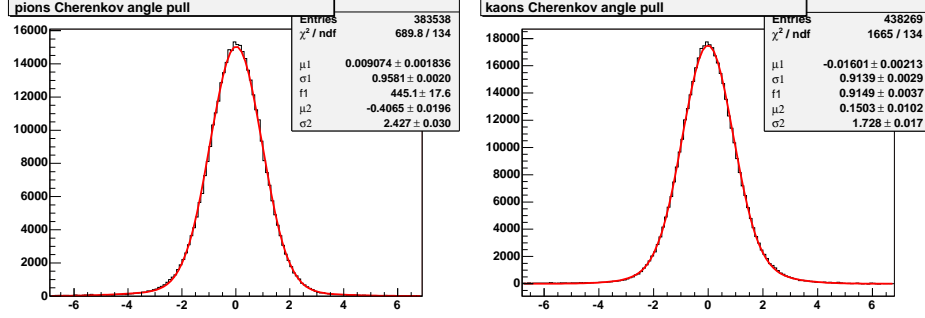


Figure 4.3: Final θ_C pull distributions for pions (left) and kaons (right).

the refraction index $n = 1.473$ of the DIRC radiator material and the velocity $\beta = p/E$ of the track, and σ_{θ_C} is the expected Cherenkov angle resolution stored in the BABAR database. The data are binned in 20 $\cos\theta$ bins and 20 momentum bins from 0.5 GeV/c to 7 GeV/c. The pull distributions of tracks in sidebands of the $D^{*+} - D^0$ mass difference and D^0 invariant mass distributions are subtracted from the pull distributions of tracks in the signal regions in order to remove contributions from background tracks. The background-subtracted pull distribution in each $p - \cos\theta$ bin is then fit to a single Gaussian. The means and widths of these Gaussian fits are tabulated as correction parameters (“offsets”, μ_{θ_C} , and “scale factors”, s_{θ_C}) that are henceforth used to correct the measurements of θ_C and σ_{θ_C} (a bi-dimensional linear interpolation between the values found in adjacent bins is used to smooth the binning effects).

- After correction, the new pull $\theta_C^{\text{pull}} \equiv (\theta_C - \theta_C^{\text{exp}} - s_{\theta_C} \mu_{\theta_C}) / s_{\theta_C} \sigma_{\theta_C}$ does not depend anymore on momentum and polar angle. The corrected pulls for kaons and pions are therefore integrated over polar angle and momentum, and fit to a double-Gaussian function of the form:

$$f_1 \times \frac{1}{\sqrt{2\pi}\sigma_1} e^{-\frac{1}{2} \left(\frac{\theta_C^{\text{pull}} - \mu_1}{\sigma_1} \right)^2} + (1-f_1) \times \frac{1}{\sqrt{2\pi}\sigma_2} e^{-\frac{1}{2} \left(\frac{\theta_C^{\text{pull}} - \mu_2}{\sigma_2} \right)^2}. \quad (4.5)$$

The results of these fit, which are shown in Figure 4.3, give us the parameters of our kaon and pion θ_C pull PDFs, and are summarized in Table 4.2.

The same procedure is performed on control samples derived from Monte Carlo in order to produce the PDFs we use in fits to simulated events.

Parameter	pions	kaons
μ_1	0.0091 ± 0.0018	-0.0160 ± 0.0021
σ_1	0.9581 ± 0.0020	0.9139 ± 0.0029
μ_2	-0.407 ± 0.020	0.150 ± 0.010
σ_2	2.427 ± 0.030	1.728 ± 0.017
f_1	0.9704 ± 0.0022	0.9149 ± 0.0037

Table 4.2: Parameters of the double-Gaussian PDFs used to describe the distributions of the corrected θ_C pull of pions and kaons, obtained from the $D^{*+} \rightarrow D^0\pi^+$, $D^0 \rightarrow K^-\pi^+$ control sample.

4.4 ΔE probability density function

4.4.1 Signal ΔE parameterization

The $B \rightarrow D^0 K$ signal is parameterized with a single Gaussian, whose mean and sigma are denoted in the following with $\mu(D^0 K)$ and $\sigma(D^0 K)$. The $B \rightarrow D^0 \pi$ ΔE PDF would be the same as the $B \rightarrow D^0 K$ one if the prompt track would be assigned the pion mass; since ΔE is computed by assigning the kaon mass, it is shifted by a quantity $\Delta E_{\text{shift}}(\gamma, p) = \gamma \left(\sqrt{m_K^2 + p^2} - \sqrt{m_\pi^2 + p^2} \right)$ which depends on the momentum \vec{p} of the prompt track in the lab frame. Therefore we parameterize the $B \rightarrow D^0 \pi$ ΔE PDF with a single Gaussian whose mean is computed, event-per-event, as $\mu(D^0 \pi) = \mu(D^0 K) + \Delta E_{\text{shift}}(\gamma, p)$, and whose width is the same as that of the $B \rightarrow D^0 K$ PDF ($\sigma(D^0 \pi) = \sigma(D^0 K)$). We are thus left with only two parameters, $\mu(D^0 K)$ and $\sigma(D^0 K)$. These are left floating in the fit, and are directly determined from the same data used to extract the yields.

We have anticipated in the previous Chapter that the ΔE distribution of selected signal B candidates, at the end of the selection, is distributed according to a double-Gaussian function. We are allowed to use in the fit a single Gaussian, instead of a more complex double-Gaussian PDF, provided we scale the selection efficiency ε to $\tilde{\varepsilon} \equiv \varepsilon \times f_1$, where f_1 is the fraction of events in the main Gaussian. The validity of this assumption has been checked with detailed Monte Carlo studies, as described in Section 4.5. f_1 values are in the range 90-96% for $B \rightarrow D^0 K$ candidates, as estimated from simulated signal events: these values are summarized in Tables 4.3 and 4.4.

In Figures 4.4 and 4.5 the ΔE_π distribution of the selected $B \rightarrow D^0 \pi$ Monte Carlo events and the ΔE_K distribution of selected $B \rightarrow D^0 K$ Monte Carlo events is shown, with the superimposed fit to a double-Gaussian function.

	$K^- \pi^+$	$K^+ K^-$	$\pi^+ \pi^-$	$K_S^0 \pi^0$	$K_S^0 \phi$	$K_S^0 \omega$
f_1 (%)	94.19±0.33	95.08±0.33	94.99±0.33	92.18±0.63	94.08±0.47	87.1±1.1
μ_1 (MeV)	-0.44±0.13	-0.53±0.14	-0.12±0.14	-0.77±0.22	0.52±0.18	-0.28±0.37
σ_1 (MeV)	16.94±0.11	17.15±0.12	16.96±0.12	19.15±0.21	17.58±0.17	18.62±0.35
μ_2 (MeV)	-32.8±2.4	-34.6±3.2	-38.4±3.4	-26.9±3.4	-33.3±3.6	-25.1±4.1
σ_2 (MeV)	62.6±1.7	67.5±2.4	69.4±2.5	70.4±3.0	64.4±2.5	72.0±3.6

Table 4.3: Parameters of the double-Gaussian PDF used to fit the ΔE_π distribution of selected $B \rightarrow D^0 \pi$ events.

	$K^- \pi^+$	$K^+ K^-$	$\pi^+ \pi^-$	$K_S^0 \pi^0$	$K_S^0 \phi$	$K_S^0 \omega$
f_1 (%)	96.35±0.24	96.97±0.25	96.94±0.24	95.31±0.43	96.18±0.36	90.6±0.9
μ_2 (MeV/c)	-19.7±3.5	-22.8±4.3	-17.7±4.5	-21.6±5.1	-9.9±4.1	-13.7±4.8
σ_2 (MeV/c)	74.1±3.3	72.0±3.9	77.1±4.4	76.1±4.9	69.5±4.0	73.3±4.7

Table 4.4: Parameters of the double-Gaussian PDF used to fit the ΔE_K distribution of selected $B \rightarrow D^0 K$ events. The mean and sigma of the core Gaussian function are fixed to the values of the $B \rightarrow D^0 \pi$ ΔE_π core Gaussian PDF.

4.4.2 $q\bar{q}$ background ΔE parameterization

Background $e^+ e^- \rightarrow q\bar{q}$ events have a flat ΔE distribution, because the candidate B is reconstructed from random combinations of tracks and photons, therefore we parameterize the ΔE PDF of the $q\bar{q}$ background with a first order polynomial. The $B \rightarrow D^0 K$ continuum background is expected to have the same ΔE shape than the $B \rightarrow D^0 \pi$ continuum background, as they differ only in the nature of the bachelor track. This has been

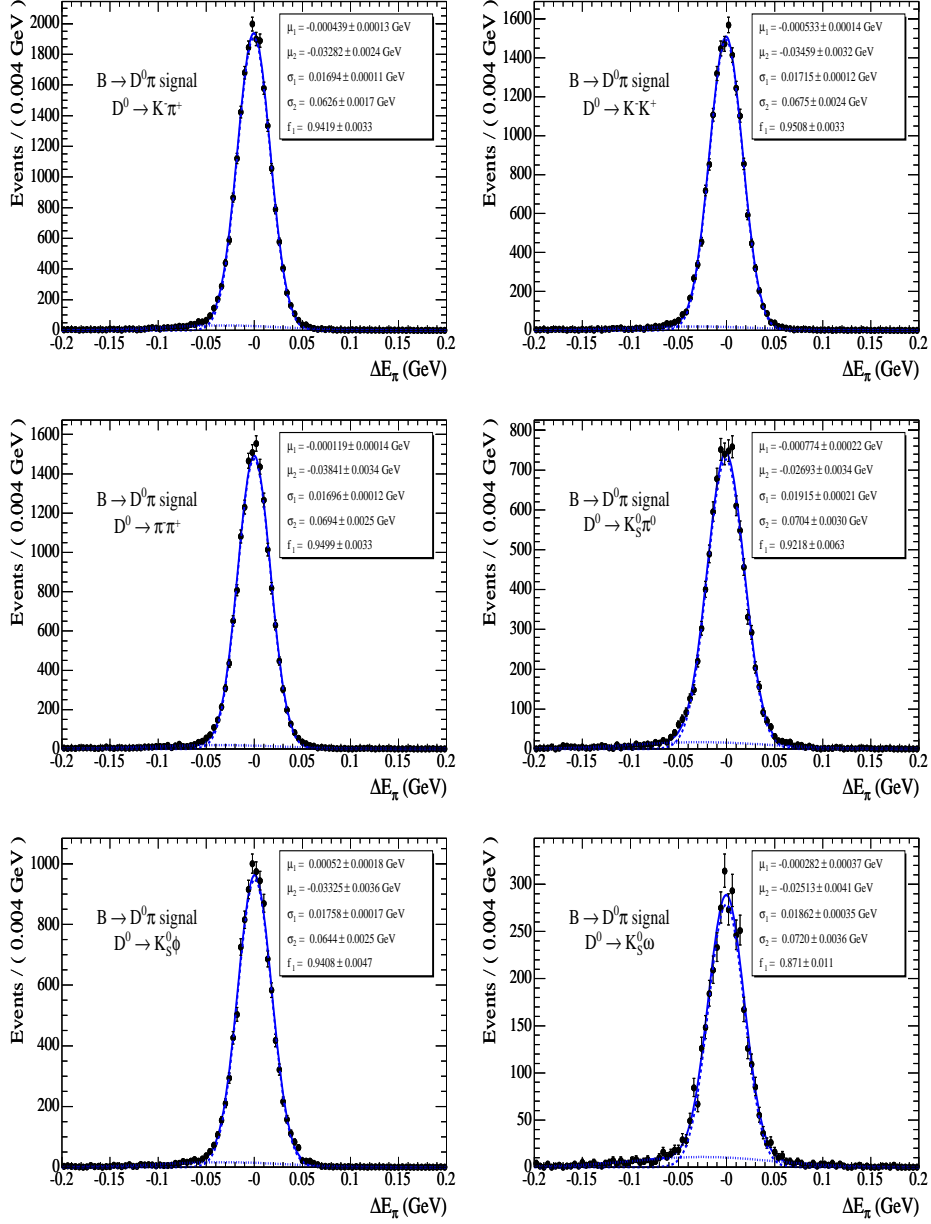


Figure 4.4: ΔE_π distribution of true $B \rightarrow D^0\pi$ candidates selected in $B \rightarrow D^0\pi$ simulated events for each of the six D^0 decay modes under study. All selection criteria have been applied. The results of a double-Gaussian fit are overlaid.

confirmed by looking separately at $q\bar{q}(\pi)$ and $q\bar{q}(K)$ background events in the selected samples and comparing the fit slopes of their distributions: as shown in Figure 4.6 and in Table 4.5 they are consistent with each other. Therefore in the final fit the ΔE $q\bar{q}(\pi)$ and $q\bar{q}(K)$ probability density functions are parameterized by means of the same function, a straight line with a fixed slope, whose shape is determined with the following methods:

- for Monte Carlo samples, the slope is fixed to the value determined from a linear

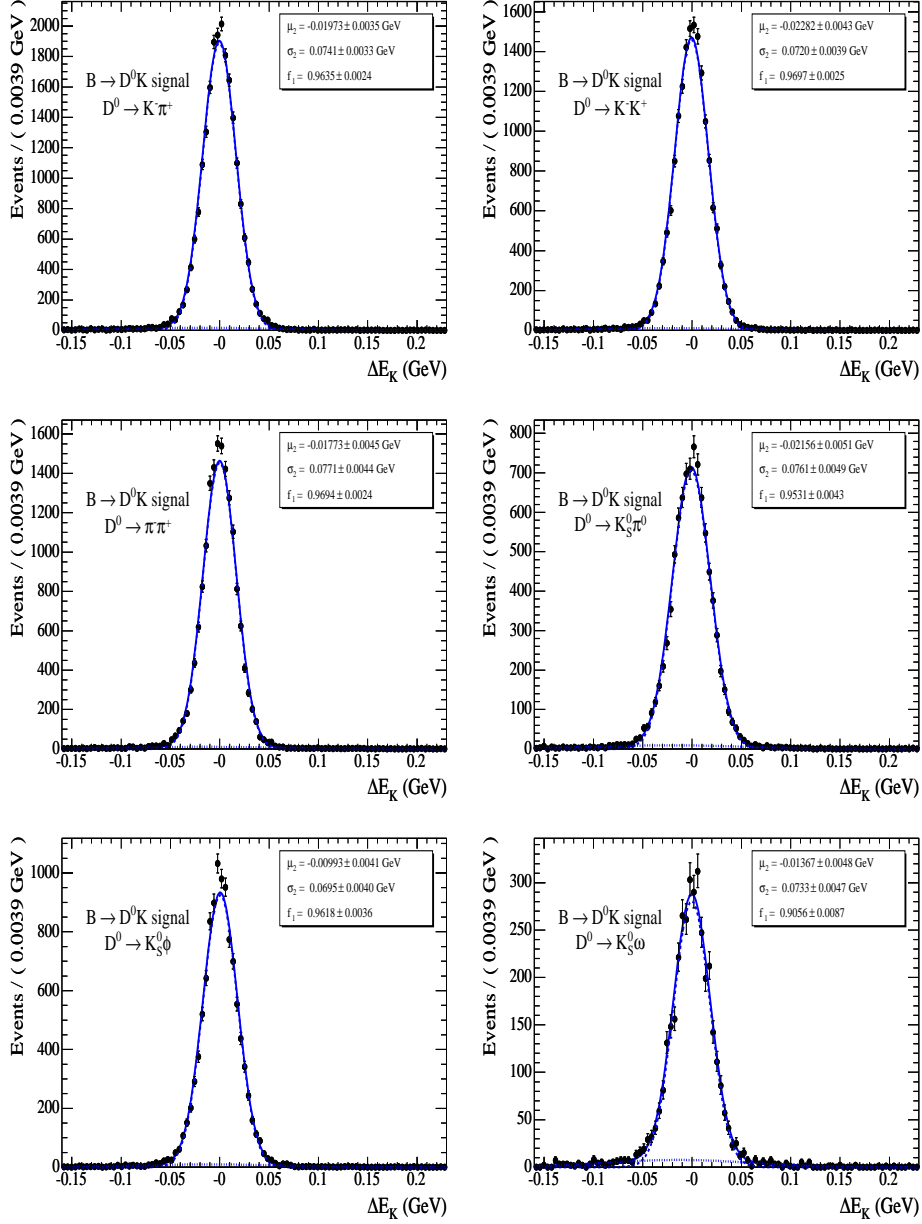


Figure 4.5: ΔE_K distribution of true $B \rightarrow D^0 K$ candidates selected in $B \rightarrow D^0 K$ simulated events for each of the six D^0 decay modes under study. All selection criteria have been applied. The results of a double-Gaussian fit (with the mean and width of the core Gaussian fixed to the same values of the $B \rightarrow D^0 \pi$ ΔE_π core Gaussian) are overlaid.

fit to the ΔE distribution of the B candidates, selected with the standard criteria of Chapter 3 in simulated $q\bar{q}$ events. Final values are reported in the last row of Table 4.5, corresponding to the plots in Figure 4.7.

- for data samples, the slope is fixed to the value determined from a linear fit to the

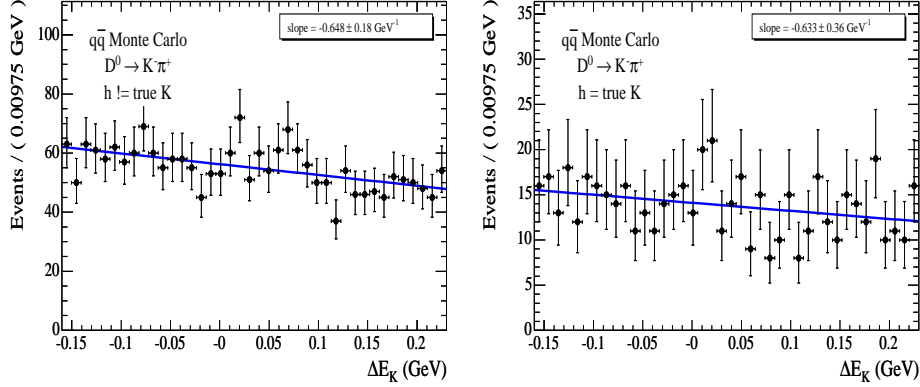


Figure 4.6: ΔE distribution and straight line fit for fake B candidates selected in $q\bar{q}(\pi)$ (left) and $q\bar{q}(K)$ events. D^0 candidates are reconstructed in the $K^-\pi^+$ channel. All selection criteria have been applied.

MC sample	Slope (GeV^{-1})					
	$D^0 \rightarrow K^-\pi^+$	$D^0 \rightarrow K^+K^-$	$D^0 \rightarrow \pi^+\pi^-$	$D^0 \rightarrow K_S^0\pi^0$	$D^0 \rightarrow K_S^0\phi$	$D^0 \rightarrow K_S^0\omega$
$q\bar{q}(\pi)$	-0.65 ± 0.18	-0.6 ± 0.6	-0.9 ± 0.5	-1.5 ± 0.5	-1.5 ± 1.3	-1.3 ± 0.8
$q\bar{q}(K)$	-0.63 ± 0.36	-1.0 ± 0.6	-1.5 ± 0.6	-0.7 ± 0.7	-1.6 ± 1.7	-0.5 ± 1.0
$q\bar{q}(\pi+K)$	-0.65 ± 0.16	-0.80 ± 0.42	-1.07 ± 0.37	-1.17 ± 0.38	-1.5 ± 1.0	-0.9 ± 0.6

Table 4.5: Slope of the linear PDF used to parameterize the ΔE distribution of B candidates selected, for each of the six D^0 decay modes under study, in the simulated $q\bar{q}$ sample. The standard selection criteria of Chapter 3 have been applied.

ΔE distribution of (fake) B candidates selected in the off-resonance data-sample, which – having been collected below the $B\bar{B}$ production threshold – does not include misreconstructed B candidates. All the selection criteria of Chapter 3 are applied, with the exception of the m_{ES} cut. The release of the m_{ES} requirement, because of the negligible correlation (below 2%) between m_{ES} and ΔE in $q\bar{q}$ events (Figure 4.8), does not affect significantly the ΔE distribution, and at the same time allows to reduce by a factor 3 the uncertainty on the slope, which is quite large due to the poor statistics of the off-resonance data sample. The results of such fits are shown in Figure 4.9 and are summarized in the last row of Table 4.6.

The parameters are found to be consistent between positive and negative B candidates.

off-res. sample	Slope (GeV^{-1})					
	$D^0 \rightarrow K^-\pi^+$	$D^0 \rightarrow K^+K^-$	$D^0 \rightarrow \pi^+\pi^-$	$D^0 \rightarrow K_S^0\pi^0$	$D^0 \rightarrow K_S^0\phi$	$D^0 \rightarrow K_S^0\omega$
all cuts	-0.9 ± 0.5	-0.3 ± 1.5	-0.3 ± 1.1	-1.6 ± 1.0	4.7 ± 5.3	-1.6 ± 1.9
no m_{ES} cut	-0.50 ± 0.16	-0.2 ± 0.5	-1.25 ± 0.34	-1.15 ± 0.35	-1.4 ± 0.8	-1.6 ± 0.5

Table 4.6: Slope of the linear PDF used to parameterize the ΔE distribution of B candidates selected, for each of the six D^0 decay modes under study, in the off-resonance data sample.

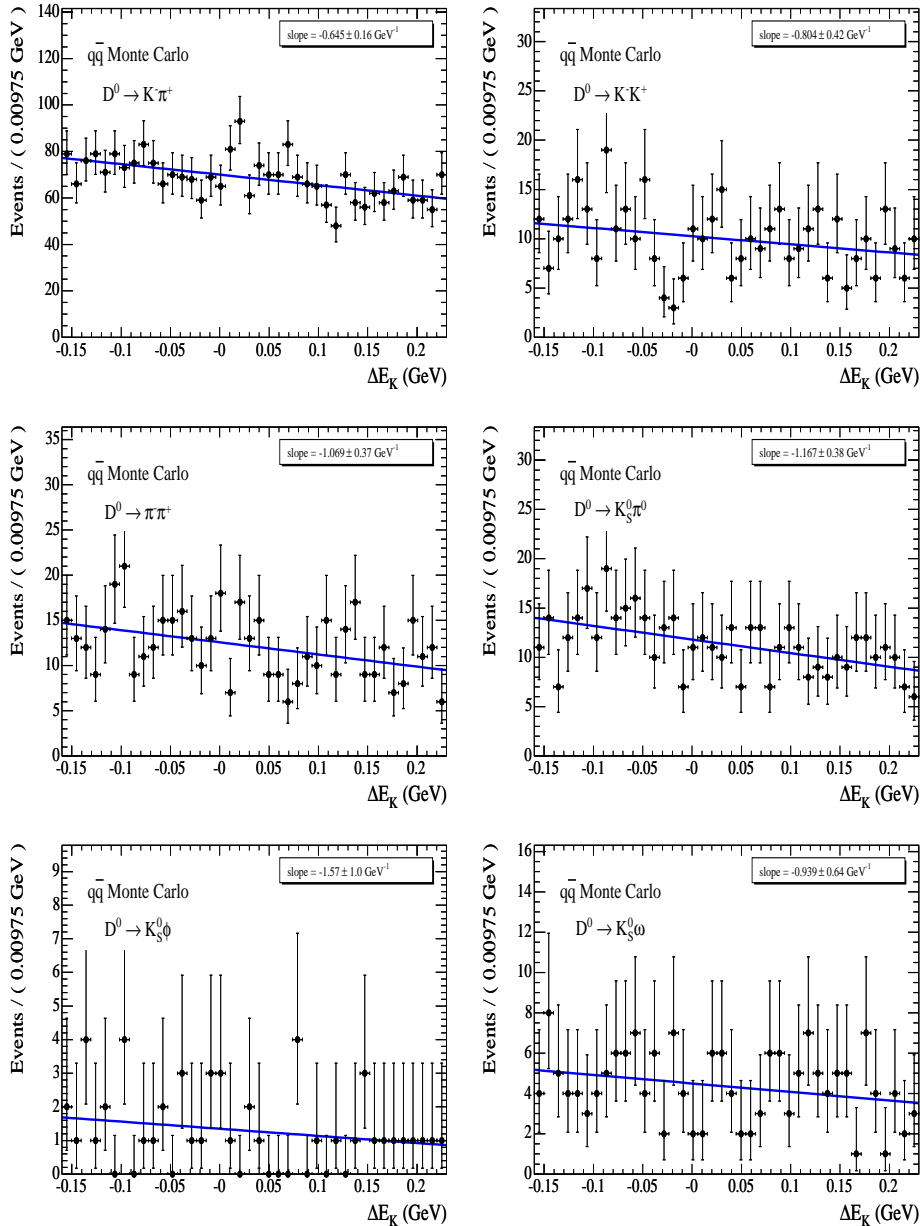


Figure 4.7: ΔE distribution and straight line fit for fake B candidates selected in $q\bar{q}$ simulated events for each of the six D^0 decay modes under study. All selection criteria have been applied.

4.4.3 $B\bar{B}$ background ΔE parameterization

The ΔE shapes of the $B\bar{B}(h)$ non-peaking components are parameterized from the generic Monte Carlo, which – as shown in Figures 4.1 and 4.2 – is found to correctly reproduce the behaviour observed in real data, apart from a small shift ($\approx +2$ MeV with respect to data). We find that a good empirical parameterization of the ΔE distribution of the $B\bar{B}(\pi)$ background is given by a “Crystal-Ball” lineshape [84], a Gaussian with an

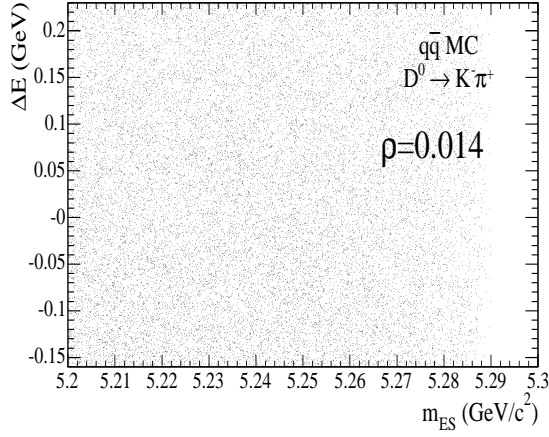


Figure 4.8: m_{ES} vs ΔE distribution of fake B candidates selected in $q\bar{q}$ events. D^0 candidates are reconstructed in the $K^-\pi^+$ channel. All selection criteria but the m_{ES} one have been applied.

exponential tail at higher ΔE values:

$$f_{\text{CB}}(\Delta E) = N \times \begin{cases} e^{-\frac{1}{2}\left(\frac{\Delta E - \mu}{\sigma}\right)^2} & \frac{\Delta E - \mu}{\sigma} < -\alpha \\ \left(\frac{n}{|\alpha|}\right)^n e^{-\frac{\alpha^2}{2}} \times \left[\frac{n}{|\alpha|} + \alpha + \frac{\Delta E - \mu}{\sigma}\right]^{-n} & \frac{\Delta E - \mu}{\sigma} > -\alpha \end{cases} \quad (4.6)$$

The Gaussian takes into account the increase of the background at negative values of ΔE (≈ -125 MeV for the $B\bar{B}(\pi)$ background and ≈ -175 MeV for the $B\bar{B}(K)$ background), while the exponential tail describes the ΔE distribution at positive values of $B\bar{B}$ combinatorial background candidates. The parameters are estimated on generic $B\bar{B}$ Monte Carlo, after having removed peaking backgrounds with the same final state as the signal, and requiring that the prompt track be a true kaon (for the $B\bar{B}(K)$ background, Figure 4.10) or not (for the $B\bar{B}(\pi)$ background, Figure 4.11). The values of the parameters μ , σ , α and n are reported in Tables 4.7 and 4.8. For the $K_s^0\phi$ channel the combinatorial $B\bar{B}(K)$ background at the end of the selection is found to be negligible and only the gaussian part is relevant (see again the $K_s^0\phi$ plot in Figure 4.10), so the parameters α and n are not computed. When performing the fit on data we shift the mean of the $B\bar{B}$ ΔE PDFs, determined on Monte Carlo, by -2 MeV as suggested by the data-MC comparison. The other parameters remain the same. The parameters are found to be consistent between positive and negative B candidates.

In addition, the contributions from charmless peaking backgrounds $B \rightarrow X_1 X_2 K$ are included, as reported in Section 4.1. The shape of the ΔE distributions of these peaking backgrounds is parameterized as a Gaussian, with same mean as the $B \rightarrow D^0 K$ signal, and width $\sigma(X_1 X_2 K) = f \times \sigma(D^0 K)$, where the scale factor f (1.80 ± 0.10) is determined from samples of simulated $B \rightarrow X_1 X_2 K$ events.

4.5 Fit validation with Monte Carlo studies

In order to evaluate the reliability of the fit to return unbiased values for the signal yields and asymmetries we have performed intensive Monte Carlo studies. In detail, we have implemented a “toy” Monte Carlo that generates 500 “experiments”, in which the ΔE

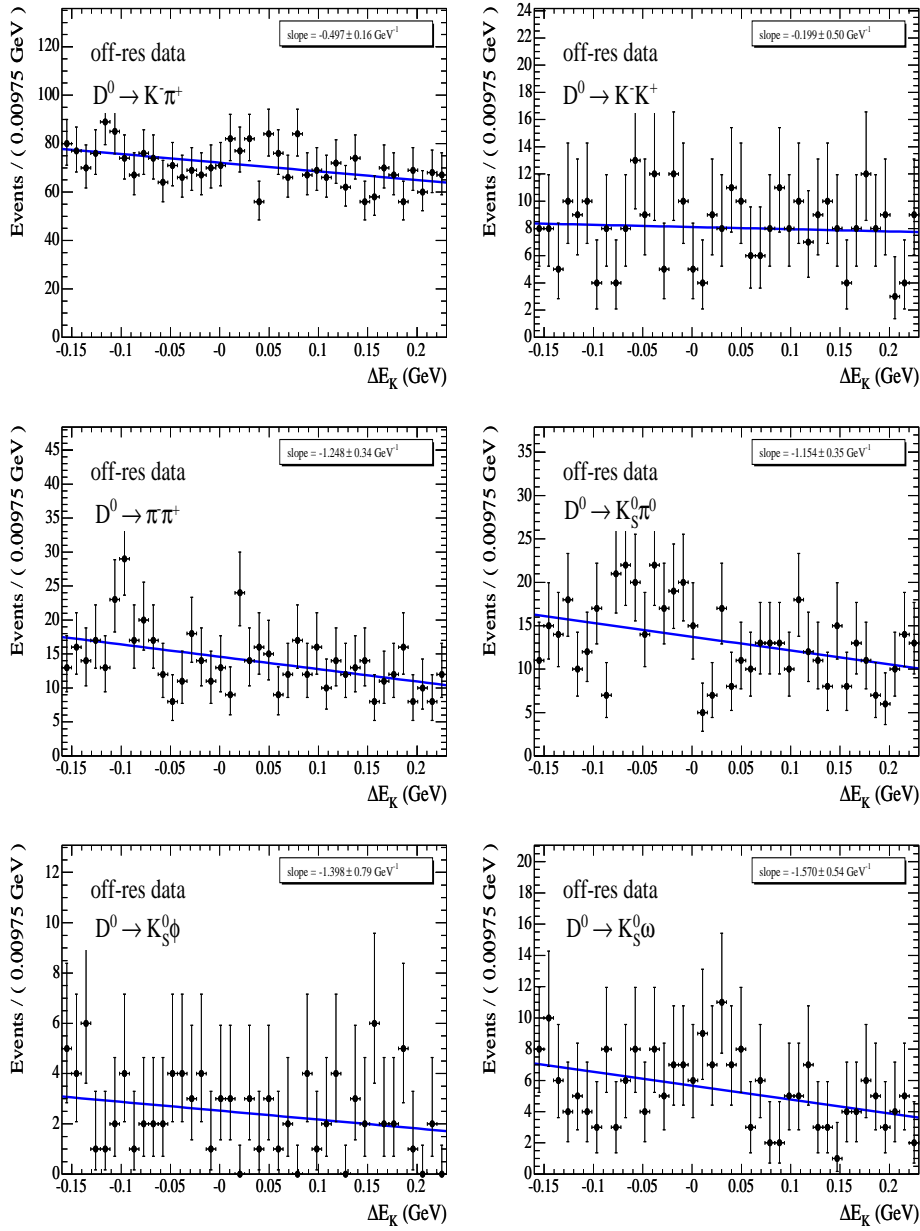


Figure 4.9: ΔE distribution and straight line fit for fake B candidates selected in off-resonance data for each of the six D^0 decay modes under study. All selection criteria but the m_{ES} one have been applied.

and θ_C distributions of $B \rightarrow D^0\pi$, $B \rightarrow D^0K$ and background (both $q\bar{q}$ and $B\bar{B}$) events are simulated, according to their distribution as determined on Monte Carlo. The number of “candidates” of each contribution in an experiment is similar to the number expected (from Monte Carlo) with the same integrated luminosity as that of the data sample. We have performed these studies for two D^0 modes, the K^+K^- and $K_S^0\pi^0$ ones, which are the most relevant CP -even and CP -odd channels considered here.

For each experiment the distribution of $\{p, \theta, \sigma_{\theta_C}\}$ (respectively the momentum, po-

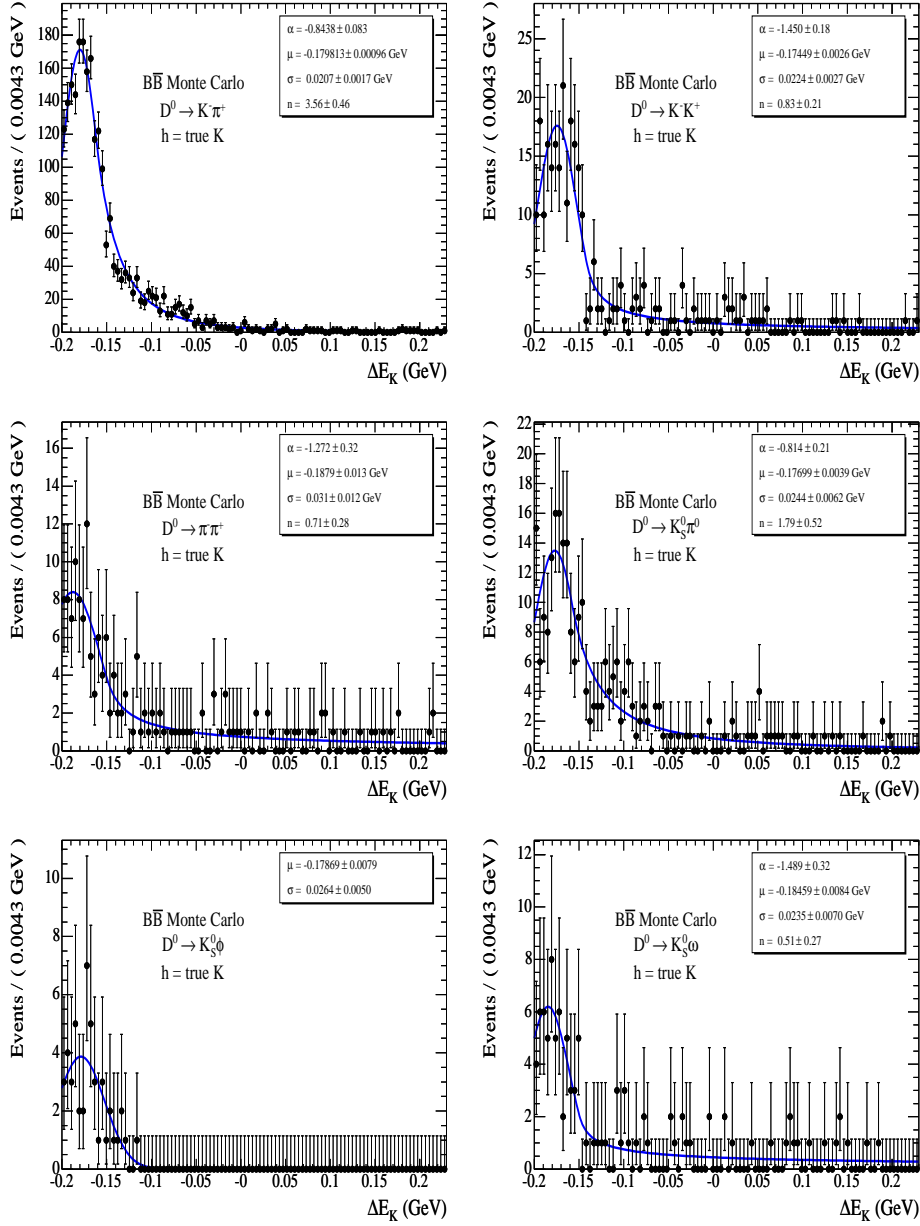


Figure 4.10: ΔE distribution of fake B candidates selected in $e^+e^- \rightarrow B\bar{B}(K)$ simulated events for each of the six D^0 decay modes under study. Signal and peaking background events have been explicitly vetoed. All selection criteria have been applied. The results of a fit with a Crystal Ball lineshape have been overlaid. The values of the parameters μ , σ , α and n are reported in Tables 4.7 and 4.8. For the $K_S^0\phi$ channel the combinatorial $B\bar{B}(K)$ background is negligible and the ΔE distribution has been fit with a single Gaussian PDF.

lar angle and expected Cherenkov angle resolution of the prompt track) is taken from randomly selected events in the generic Monte Carlo, then ΔE and θ_C are generated according to the type of candidate:

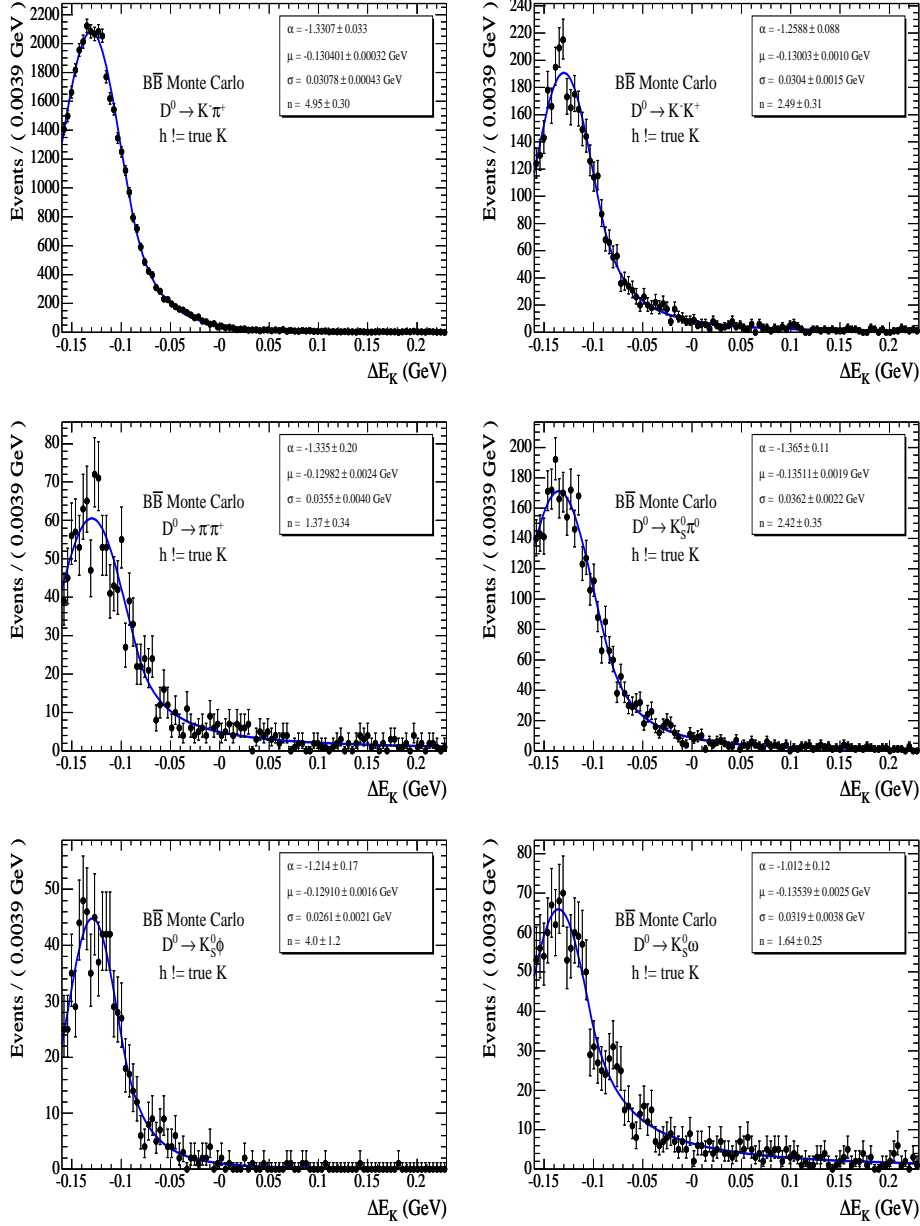


Figure 4.11: ΔE distribution of fake B candidates selected in $e^+e^- \rightarrow B\bar{B}(\pi)$ simulated events for each of the six D^0 decay modes under study. Signal events have been explicitly vetoed. All selection criteria have been applied. The results of a fit with a Crystal Ball lineshape have been overlaid.

- The $B \rightarrow D^0 K$ ΔE is generated from a double-Gaussian function

$$f_1 \times \frac{1}{\sqrt{2\pi}\sigma_1} e^{-\frac{1}{2}\left(\frac{\Delta E - \mu_1}{\sigma_1}\right)^2} + (1-f_1) \times \frac{1}{\sqrt{2\pi}\sigma_2} e^{-\frac{1}{2}\left(\frac{\Delta E - \mu_2}{\sigma_2}\right)^2} \quad (4.7)$$

with the parameters μ_1 , σ_1 listed in Table 4.3 and the parameters f_1 , μ_2 and σ_2 listed in Table 4.4.

D^0 mode	μ (MeV)	σ (MeV)	α	n
$K^- \pi^+$	-179.8 ± 1.0	20.7 ± 1.7	-0.84 ± 0.08	3.56 ± 0.46
$K^+ K^-$	-174.5 ± 2.6	22.4 ± 2.7	-1.45 ± 0.18	0.83 ± 0.21
$\pi^+ \pi^-$	-188 ± 13	31 ± 12	-1.27 ± 0.32	0.71 ± 0.28
$K_s^0 \pi^0$	-177.0 ± 3.9	24 ± 6	-0.81 ± 0.21	1.79 ± 0.52
$K_s^0 \phi$	-179 ± 8	26 ± 5	-	-
$K_s^0 \omega$	-185 ± 8	24 ± 7	-1.49 ± 0.32	0.51 ± 0.27

Table 4.7: Parameters of the Crystal Ball PDF used to fit the ΔE distribution of B candidates selected, for each of the six D^0 decay modes under study, in simulated $B\bar{B}(K)$ background (non-peaking) events. For the $K_s^0 \phi$ channel the combinatorial $B\bar{B}(K)$ background is negligible and only the gaussian part is relevant, so the parameters α and n are not computed.

D^0 mode	μ (MeV)	σ (MeV)	α	n
$K^- \pi^+$	-130.4 ± 0.3	30.8 ± 0.4	-1.33 ± 0.03	4.95 ± 0.30
$K^+ K^-$	-130.0 ± 1.0	30.4 ± 1.5	-1.26 ± 0.09	2.49 ± 0.31
$\pi^+ \pi^-$	-129.8 ± 2.4	35.5 ± 4.0	-1.34 ± 0.20	1.37 ± 0.34
$K_s^0 \pi^0$	-135.1 ± 1.9	36.2 ± 2.2	-1.37 ± 0.11	2.42 ± 0.35
$K_s^0 \phi$	-129.1 ± 1.6	26.1 ± 2.1	-1.21 ± 0.17	4.0 ± 1.2
$K_s^0 \omega$	-135.4 ± 2.5	31.9 ± 3.8	-1.01 ± 0.12	1.64 ± 0.25

Table 4.8: Parameters of the Crystal Ball PDF used to fit the ΔE distribution of B candidates selected, for each of the six D^0 decay modes under study, in simulated $B\bar{B}(\pi)$ background (non-peaking) events.

- The $B \rightarrow D^0 \pi$ ΔE is generated from a double-Gaussian function with parameters $\mu_1, \sigma_1, \mu_2, \sigma_2$ and f_1 listed in Table 4.3 and shifted event-by-event by a momentum-dependent quantity, according to Eq. (3.9) discussed in the previous Chapter
- the continuum ΔE is generated as a linear polynomial distribution with slope taken from the last row of Table 4.5
- the $B\bar{B}(K)$ and $B\bar{B}(\pi)$ ΔE are generated from Crystal Ball functions (Eq. 4.6) with the parameters reported in Table 4.7 and 4.8
- the $B \rightarrow D^0 K, q\bar{q}(K)$ and $B\bar{B}(K)$ θ_C are simulated by first generating the corrected pull θ_C^{pull} from a double-Gaussian function (Eq. 4.5) with the parameters in the right column of Table 4.2, and then computing θ_C from $\theta_C = \theta_C^{\text{exp}} + s_{\theta_C} \mu_{\theta_C} + s_{\theta_C} \sigma_{\theta_C} \theta_C^{\text{pull}}$, where θ_C^{exp} is the expected Cherenkov angle for a given momentum p in the kaon hypothesis
- the $B \rightarrow D^0 \pi, q\bar{q}(\pi)$ and $B\bar{B}(\pi)$ θ_C are generated similarly to the $B \rightarrow D^0 K, q\bar{q}(K)$ and $B\bar{B}(K)$ θ_C , with obvious substitutions (the parameters of the θ_C^{pull} double Gaussian PDF are those in the middle column of Table 4.2, the expected Cherenkov angle θ_C^{exp} is computed with the pion hypothesis, and the correction parameters μ_{θ_C} and s_{θ_C} are those determined on the pion control sample).

For these studies we have not included a peaking background $B \rightarrow X_1 X_2 h$ component.

A set of 500 toy experiments have been simulated, each one containing the sum of six populations with the above ΔE and θ_C distributions. The number of candidates of each contribution in a toy experiment is generated from a Poisson distribution with a fixed mean for each type of population, which is simply the expected number of candidates for that population as predicted from the BABAR simulation (the numbers in the second

column of Tables 4.12 and 4.18). The sample generated in each experiment is fit with the same PDFs used to generate the sample, with the exception of the $B \rightarrow D^0\pi$ and $B \rightarrow D^0K$ ΔE distribution, which are fit – like in our nominal fit – with a single Gaussian PDF. In each experiment the pulls $\delta_J = (N_J^{fit} - N_J^{gen})/\sigma_J$ are built, where $J = D^0\pi, D^0K$. N_J^{gen} is the mean value of the poissonian generator of J -type candidates, scaled by the mean value f_1 of the core $\Delta E B \rightarrow D^0h$ Gaussian, N_J^{fit} is the fit value of the number of candidates J and σ_J is the associated error.

The distribution of $\delta_{D\pi}$ and δ_{DK} obtained in the 500 toy experiments are shown in Figure 4.12. The distributions are fit with a gaussian. The means are compatible with zero and the widths are compatible with one, as expected in the case where the fit result is unbiased. The same behavior is observed in the pulls of the D^0K and $D^0\pi$ yield asymmetries $\delta A_J = (A_J^{fit} - A_J^{gen})/\sigma_{A_J}$, where $J = D^0\pi, D^0K$, $A_{D^0h} \equiv \frac{N(D^0h^-) - N(D^0h^+)}{N(D^0h^-) + N(D^0h^+)}$, as shown in Figure 4.13.

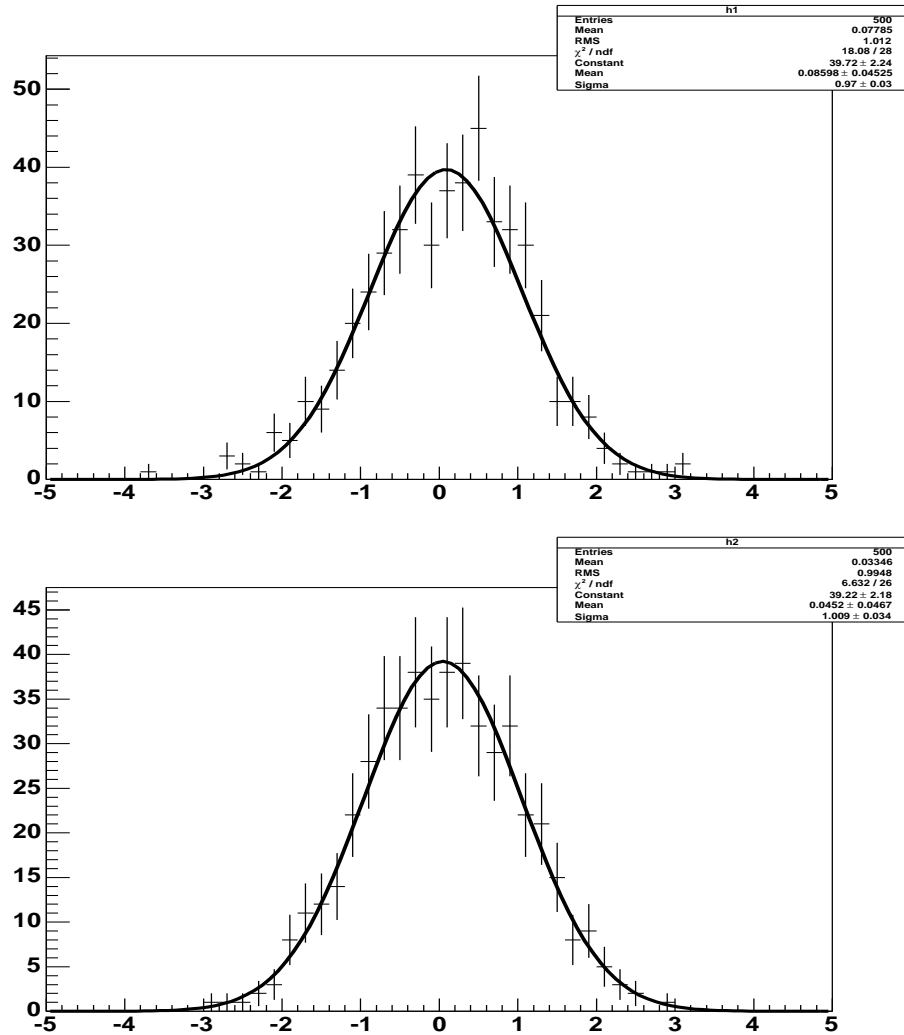


Figure 4.12: Pulls of the signal yields, $\delta_{D^0K} = (N_{D^0K}^{fit} - N_{D^0K}^{gen})/\sigma_{D^0K}$ (top) and $\delta_{D^0\pi} = (N_{D^0\pi}^{fit} - N_{D^0\pi}^{gen})/\sigma_{D^0\pi}$ (bottom), obtained with 500 toy experiments. The results of a Gaussian fit are overlaid.

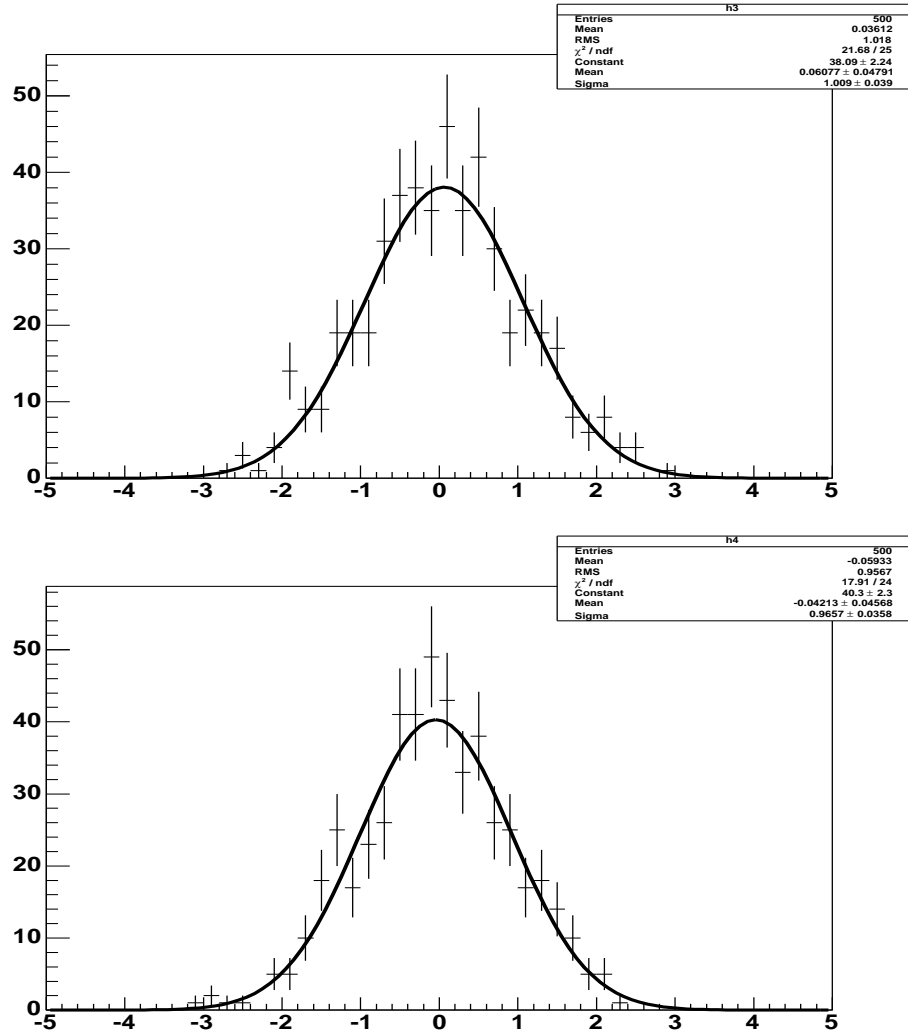


Figure 4.13: Pulls of the charge asymmetries of the $B \rightarrow D^0 h$ signals, $A(D^0 K)$ (top) and $A(D^0 \pi)$ (bottom), obtained with 500 toy experiments. The results of a Gaussian fit are overlaid.

4.6 Fit to generic Monte Carlo

Before moving to the final fit on data, the analysis has been performed on the generic Monte Carlo in order to check the $B \rightarrow D^0 K$ and $B \rightarrow D^0 \pi$ yield extraction with a much more complete simulation with respect to the “toy” Monte Carlo described in the previous Section. The particle-identification PDF used for this analysis has been tuned on simulated $D^{*+} \rightarrow D^0 \pi^+$, $D^0 \rightarrow K^- \pi^+$ events, and the Monte Carlo sample has been scaled to the same luminosity of the data sample (210.7 fb^{-1}). In the following Tables (4.9-4.24) we summarize for each channel the number of expected signal and background events and their asymmetries, and we report the fit results. For the expected signal $B \rightarrow D^0 \pi$ and $B \rightarrow D^0 K$ yields we report in parentheses the numbers scaled by the main ΔE Gaussian fraction f_1 defined in 4.4.1. From these checks we shall see that the

parameters of the ΔE Gaussian PDF for the $D^0 K$ signal are correctly estimated from the final fit, and so are the signal yields, provided we compare them with the expected number of events scaled by f_1 .

$K^- \pi^+$

generic Monte Carlo – Fit Results ($K^- \pi^+$)				
Parameter	True value	Fitted value	B^+	B^-
$\mu(D^0 K)$	-0.44 ± 0.13	-0.47 ± 0.14	-	-
$\sigma(D^0 K)$	16.94 ± 0.11	17.11 ± 0.12	-	-
$N_{D^0 \pi}$	17502 (16485 \pm 53)	16755 \pm 138	8479 \pm 97	8277 \pm 96
$N_{D^0 K}$	1419 (1367 \pm 3)	1409 \pm 43	723 \pm 30	686 \pm 30
$N_{q\bar{q}(\pi)}$	3076	3758 \pm 107	1899 \pm 73	1858 \pm 72
$N_{q\bar{q}(K)}$	760	914 \pm 46	464 \pm 33	450 \pm 32
$N_{B\bar{B}(\pi)}$	12532	12432 \pm 126	6286 \pm 898	6144 \pm 89
$N_{B\bar{B}(K)}$	292	366 \pm 31	193 \pm 23	172 \pm 22

Table 4.9: True yields and maximum likelihood fit results in the generic Monte Carlo analysis of the $B^- \rightarrow D^0 K^-$, $D^0 \rightarrow K^- \pi^+$ analysis.

generic Monte Carlo – Fit Results ($K^- \pi^+$)		
Species	True asymmetry	Fitted asymmetry
$D^0 \pi$	-1.0%	$-(1.2 \pm 0.8)\%$
$D^0 K$	-1.3%	$-(2.6 \pm 3.0)\%$
$q\bar{q}(\pi)$	-3.7%	$-(1.1 \pm 2.7)\%$
$q\bar{q}(K)$	-3.8%	$-(1.5 \pm 5.0)\%$
$B\bar{B}(\pi)$	-0.9%	$-(1.1 \pm 1.0)\%$
$B\bar{B}(K)$	0.0%	$-(5.7 \pm 8.7)\%$

Table 4.10: True and fitted asymmetries in the generic Monte Carlo analysis of the $B^- \rightarrow D^0 K^-$, $D^0 \rightarrow K^- \pi^+$ analysis.

Param.	$\mu(D^0 K)$	$\sigma(D^0 K)$	$N_{D^0 \pi}$	$N_{D^0 K}$	$N_{q\bar{q}(\pi)}$	$N_{q\bar{q}(K)}$	$N_{B\bar{B}(\pi)}$	$N_{B\bar{B}(K)}$
$\mu(D^0 K)$	1.000	-0.038	-0.024	0.032	0.015	-0.018	0.007	0.011
$\sigma(D^0 K)$	-0.038	1.000	0.155	0.055	-0.288	-0.056	0.072	0.011
$N_{D^0 \pi}$	-0.024	0.155	1.000	-0.002	-0.208	-0.020	0.055	0.005
$N_{D^0 K}$	0.032	0.055	-0.002	1.000	-0.018	-0.202	0.005	0.048
$N_{q\bar{q}(\pi)}$	0.015	-0.288	-0.208	-0.018	1.000	0.012	-0.326	0.010
$N_{q\bar{q}(K)}$	-0.018	-0.056	-0.020	-0.202	0.012	1.000	0.002	-0.428
$N_{B\bar{B}(\pi)}$	0.007	0.072	0.055	0.005	-0.326	0.002	1.000	-0.030
$N_{B\bar{B}(K)}$	0.011	0.011	0.005	0.048	0.010	-0.428	-0.030	1.000

Table 4.11: Correlation coefficients of parameters from the fit on the $B^- \rightarrow D^0 K^-$, $D^0 \rightarrow K^- \pi^+$ MC sample.

K^+K^-

generic Monte Carlo – Fit Results (K^+K^-)				
Parameter	True value	Fitted value	B^+	B^-
$\mu(D^0K)$	-0.53 ± 0.14	-0.5 ± 0.5	-	-
$\sigma(D^0K)$	17.15 ± 0.12	17.0 ± 0.5	-	-
$N_{D^0\pi}$	1403 (1334 \pm 5)	1330 \pm 40	656 \pm 28	674 \pm 28
N_{D^0K}	113 (110 \pm 1)	99 \pm 14	53 \pm 10	46 \pm 9
$N_{q\bar{q}(\pi)}$	321	400 \pm 37	221 \pm 26	179 \pm 24
$N_{q\bar{q}(K)}$	226	249 \pm 26	142 \pm 19	107 \pm 17
$N_{B\bar{B}(\pi)}$	1229	1205 \pm 42	609 \pm 30	596 \pm 29
$N_{B\bar{B}(K)}$	46	62 \pm 18	31 \pm 13	31 \pm 12

Table 4.12: True yields and maximum likelihood fit results in the generic Monte Carlo analysis of the $B^- \rightarrow D^0K^-$, $D^0 \rightarrow K^+K^-$ analysis.

generic Monte Carlo – Fit Results (K^+K^-)		
Species	True asymmetry	Fitted asymmetry
$D^0\pi$	1.0%	(1.4 \pm 3.0)%
D^0K	-1.0%	-(1 \pm 14)%
$q\bar{q}(\pi)$	-9%	-(11 \pm 9)%
$q\bar{q}(K)$	-12%	-(15 \pm 10)%
$B\bar{B}(\pi)$	-2.2%	-(1.1 \pm 3.5)%
$B\bar{B}(K)$	-8%	(0 \pm 29)%

Table 4.13: True and fitted asymmetries in the generic Monte Carlo analysis of the $B^- \rightarrow D^0K^-$, $D^0 \rightarrow K^+K^-$ analysis.

Param.	$\mu(D^0K)$	$\sigma(D^0K)$	$N_{D^0\pi}$	N_{D^0K}	$N_{q\bar{q}(\pi)}$	$N_{q\bar{q}(K)}$	$N_{B\bar{B}(\pi)}$	$N_{B\bar{B}(K)}$
$\mu(D^0K)$	1.000	-0.019	0.020	-0.044	0.002	-0.021	-0.015	-0.011
$\sigma(D^0K)$	-0.019	1.000	-0.194	-0.087	0.292	-0.056	-0.077	-0.013
$N_{D^0\pi}$	0.020	-0.194	1.000	0.008	-0.236	0.017	0.064	0.004
N_{D^0K}	-0.044	-0.087	0.008	1.000	-0.026	0.252	0.007	0.073
$N_{q\bar{q}(\pi)}$	0.002	0.292	-0.236	-0.026	1.000	0.018	-0.399	0.014
$N_{q\bar{q}(K)}$	-0.021	-0.056	0.017	0.252	0.018	1.000	-0.008	0.608
$N_{B\bar{B}(\pi)}$	-0.015	-0.077	0.064	0.007	-0.399	-0.008	1.000	-0.025
$N_{B\bar{B}(K)}$	-0.011	-0.013	0.004	0.073	0.014	0.608	-0.025	1.000

Table 4.14: Correlation coefficients of parameters from the fit on the $B^- \rightarrow D^0K^-$, $D^0 \rightarrow K^+K^-$ MC sample.

$\pi^+\pi^-$

generic Monte Carlo – Fit Results ($\pi^+\pi^-$)				
Parameter	True value	Fitted value	B^+	B^-
$\mu(D^0K)$ (MeV)	-0.12 ± 0.14	-0.4 ± 0.9	-	-
$\sigma(D^0K)$ (MeV)	16.96 ± 0.12	15.4 ± 0.9	-	-
$N_{D^0\pi}$	488(463 ± 1)	443 ± 26	215 ± 17	228 ± 18
N_{D^0K}	39(38 ± 1)	44 ± 10	23 ± 7	21 ± 7
$N_{q\bar{q}(\pi)}$	473	540 ± 41	261 ± 27	279 ± 28
$N_{q\bar{q}(K)}$	201	182 ± 30	65 ± 20	117 ± 18
$N_{B\bar{B}(\pi)}$	459	434 ± 33	211 ± 23	223 ± 23
$N_{B\bar{B}(K)}$	30	38^{+25}_{-18}	38 ± 18	0^{+17}_{-0}

Table 4.15: True yields and maximum likelihood fit results in the generic Monte Carlo analysis of the $B^- \rightarrow D^0K^-$, $D^0 \rightarrow \pi^+\pi^-$ analysis.

generic Monte Carlo – Fit Results ($\pi^+\pi^-$)		
Species	True asymmetry	Fitted asymmetry
$D^0\pi$	1.4%	$(3 \pm 6)\%$
D^0K	0.7%	$-(5 \pm 24)\%$
$q\bar{q}(\pi)$	11%	$(3 \pm 7)\%$
$q\bar{q}(K)$	11%	$(29 \pm 16)\%$
$B\bar{B}(\pi)$	5%	$(2 \pm 7)\%$
$B\bar{B}(K)$	-1%	$-(100^{+0}_{-89})\%$

Table 4.16: True and fitted asymmetries in the generic Monte Carlo analysis of the $B^- \rightarrow D^0K^-$, $D^0 \rightarrow \pi^+\pi^-$ analysis.

Param.	$\mu(D^0K)$	$\sigma(D^0K)$	$N_{D^0\pi}$	N_{D^0K}	$N_{q\bar{q}(\pi)}$	$N_{q\bar{q}(K)}$	$N_{B\bar{B}(\pi)}$	$N_{B\bar{B}(K)}$
$\mu(D^0K)$	1.000	-0.012	-0.020	0.047	0.003	0.025	0.009	-0.017
$\sigma(D^0K)$	-0.012	1.000	0.298	0.126	-0.285	0.058	0.121	-0.018
$N_{D^0\pi}$	-0.020	0.298	1.000	0.035	-0.313	0.019	0.134	-0.006
N_{D^0K}	0.047	0.126	0.035	1.000	-0.041	0.230	0.018	-0.091
$N_{q\bar{q}(\pi)}$	0.003	-0.285	-0.313	-0.041	1.000	0.012	-0.573	-0.014
$N_{q\bar{q}(K)}$	0.025	0.058	0.019	0.230	0.012	1.000	-0.014	-0.816
$N_{B\bar{B}(\pi)}$	0.009	0.121	0.134	0.018	-0.573	-0.014	1.000	0.027
$N_{B\bar{B}(K)}$	-0.017	-0.018	-0.006	-0.091	-0.014	-0.816	0.027	1.000

Table 4.17: Correlation coefficients of parameters from the fit on the $B^- \rightarrow D^0K^-$, $D^0 \rightarrow \pi^+\pi^-$ MC sample.

$K_S^0\pi^0$

generic Monte Carlo – Fit Results ($K_S^0\pi^0$)				
Parameter	True value	Fitted value	B^+	B^-
$\mu(D^0K)$ (MeV)	-0.77 ± 0.22	-0.3 ± 0.6	-	-
$\sigma(D^0K)$ (MeV)	19.15 ± 0.21	19.0 ± 0.5	-	-
$N_{D^0\pi}$	1604(1479 \pm 10)	1471 \pm 43	749 \pm 30	722 \pm 29
N_{D^0K}	126(120 \pm 1)	122 \pm 15	65 \pm 11	57 \pm 10
$N_{q\bar{q}(\pi)}$	392	524 \pm 45	259 \pm 30	265 \pm 30
$N_{q\bar{q}(K)}$	251	285 \pm 27	153 \pm 20	132 \pm 19
$N_{B\bar{B}(\pi)}$	1163	1156 \pm 43	568 \pm 30	588 \pm 31
$N_{B\bar{B}(K)}$	42	21 \pm 17	9^{+13}_{-9}	12 \pm 12

Table 4.18: True yields and maximum likelihood fit results in the generic Monte Carlo analysis of the $B^- \rightarrow D^0K^-$, $D^0 \rightarrow K_S^0\pi^0$ analysis.

generic Monte Carlo – Fit Results ($K_S^0\pi^0$)		
Species	True asymmetry	Fitted asymmetry
$D^0\pi$	-1.7%	$-(1.8 \pm 2.8)\%$
D^0K	-0.5%	$-(7 \pm 12)\%$
$q\bar{q}(\pi)$	3%	$(1 \pm 8)\%$
$q\bar{q}(K)$	-7%	$-(7 \pm 10)\%$
$B\bar{B}(\pi)$	1.0%	$(1.7 \pm 3.7)\%$
$B\bar{B}(K)$	-1%	$(14^{+7}_{-9})\%$

Table 4.19: True and fitted asymmetries in the generic Monte Carlo analysis of the $B^- \rightarrow D^0K^-$, $D^0 \rightarrow K_S^0\pi^0$ analysis.

Param.	$\mu(D^0K)$	$\sigma(D^0K)$	$N_{D^0\pi}$	N_{D^0K}	$N_{q\bar{q}(\pi)}$	$N_{q\bar{q}(K)}$	$N_{B\bar{B}(\pi)}$	$N_{B\bar{B}(K)}$
$\mu(D^0K)$	1.000	0.007	0.015	0.043	0.010	0.027	0.020	0.017
$\sigma(D^0K)$	0.007	1.000	0.237	-0.080	-0.341	-0.054	-0.116	-0.018
$N_{D^0\pi}$	0.015	0.237	1.000	-0.009	-0.288	-0.021	-0.101	-0.008
N_{D^0K}	0.043	-0.080	-0.009	1.000	0.028	0.295	0.011	0.109
$N_{q\bar{q}(\pi)}$	0.010	-0.341	-0.288	0.028	1.000	-0.007	0.466	-0.011
$N_{q\bar{q}(K)}$	0.027	-0.054	-0.021	0.295	-0.007	1.000	-0.005	0.647
$N_{B\bar{B}(\pi)}$	0.020	-0.116	-0.101	0.011	0.466	-0.005	1.000	-0.027
$N_{B\bar{B}(K)}$	0.017	-0.018	-0.008	0.109	-0.011	0.647	-0.027	1.000

Table 4.20: Correlation coefficients of parameters from the fit on the $B^- \rightarrow D^0K^-$, $D^0 \rightarrow K_S^0\pi^0$ MC sample.

$K_S^0\phi$

generic Monte Carlo – Fit Results ($K_S^0\phi$)				
Parameter	True value	Fit value	B^+	B^-
$\mu(D^0K)$ (MeV)	0.52 ± 0.18	0.43 ± 0.98	-	-
$\sigma(D^0K)$ (MeV)	17.58 ± 0.17	17.91 ± 0.85	-	-
$N_{D^0\pi}$	399(375 \pm 2)	380 ± 21	189 ± 14	191 ± 15
N_{D^0K}	33(32 \pm 1)	33 ± 6	18 ± 5	15 ± 4
$N_{q\bar{q}(\pi)}$	45	58 ± 14	31 ± 10	27 ± 10
$N_{q\bar{q}(K)}$	24	22 ± 6	8 ± 4	14 ± 5
$N_{B\bar{B}(\pi)}$	252	258 ± 18	122 ± 13	136 ± 13
$N_{B\bar{B}(K)}$	5	6 ± 3	2 ± 2	4 ± 3

Table 4.21: True yields and maximum likelihood fit results in the generic Monte Carlo analysis of the $B^- \rightarrow D^0K^-$, $D^0 \rightarrow K_S^0\phi$ analysis.

generic Monte Carlo – Fit Results ($K_S^0\phi$)		
Species	True asymmetry	Fit asymmetry
$D^0\pi$	0.7%	(1 \pm 5)%
D^0K	-1.0%	-(9 \pm 19)%
$q\bar{q}(\pi)$	29%	-(7 \pm 24)%
$q\bar{q}(K)$	8.3%	(27 \pm 28)%
$B\bar{B}(\pi)$	0%	(5 \pm 7)%
$B\bar{B}(K)$	0%	(33 \pm 56)%

Table 4.22: True and fit asymmetries in the generic Monte Carlo analysis of the $B^- \rightarrow D^0K^-$, $D^0 \rightarrow K_S^0\phi$ analysis.

Param.	$\mu(D^0K)$	$\sigma(D^0K)$	$N_{D^0\pi}$	N_{D^0K}	$N_{q\bar{q}(\pi)}$	$N_{q\bar{q}(K)}$	$N_{B\bar{B}(\pi)}$	$N_{(B\bar{B}(K))}$
$\mu(D^0K)$	1.000	0.120	0.049	0.028	-0.061	0.011	-0.000	0.002
$\sigma(D^0K)$	0.120	1.000	0.162	-0.033	-0.313	-0.043	0.068	-0.009
$N_{D^0\pi}$	0.049	0.162	1.000	0.006	-0.209	-0.016	0.051	-0.003
N_{D^0K}	0.028	-0.033	0.006	1.000	0.020	0.206	-0.005	0.046
$N_{q\bar{q}(\pi)}$	-0.061	-0.313	-0.209	0.020	1.000	-0.022	-0.325	-0.011
$N_{q\bar{q}(K)}$	0.011	-0.043	-0.016	0.206	-0.022	1.000	-0.012	0.224
$N_{B\bar{B}(\pi)}$	-0.000	0.068	0.051	-0.005	-0.325	-0.012	1.000	0.035
$N_{B\bar{B}(K)}$	0.002	-0.009	-0.003	0.046	-0.011	0.224	0.035	1.000

Table 4.23: Correlation coefficients of parameters from the fit on the $B^- \rightarrow D^0K^-$, $D^0 \rightarrow K_S^0\phi$ MC sample.

$K_S^0\omega$

generic Monte Carlo – Fit Results ($K_S^0\omega$)				
Parameter	True value	Fit value	B^+	B^-
$\mu(D^0K)$ (MeV)	-0.28 ± 0.37	0.0 ± 1.0	-	-
$\sigma(D^0K)$ (MeV)	18.62 ± 0.35	18.3 ± 0.9	-	-
$N_{D^0\pi}$	590(515 \pm 7)	515 \pm 26	263 \pm 18	252 \pm 18
N_{D^0K}	47(43 \pm 1)	39 \pm 9	17 \pm 6	22 \pm 6
$N_{q\bar{q}(\pi)}$	133	229 \pm 35	131 \pm 24	98 \pm 23
$N_{q\bar{q}(K)}$	105	131 \pm 25	74 \pm 18	57 \pm 17
$N_{B\bar{B}(\pi)}$	492	465 \pm 32	235 \pm 23	230 \pm 22
$N_{B\bar{B}(K)}$	17	5 $^{+23}_{-5}$	1 $^{+16}_{-1}$	4 $^{+16}_{-4}$

Table 4.24: True yields and maximum likelihood fit results in the generic Monte Carlo analysis of the $B^- \rightarrow D^0K^-$, $D^0 \rightarrow K_S^0\omega$ analysis.

generic Monte Carlo – Fit Results ($K_S^0\omega$)		
Species	True asymmetry	Fit asymmetry
$D^0\pi$	-2.0%	-(2 \pm 5)%
D^0K	1.2%	(13 \pm 22)%
$q\bar{q}(\pi)$	-5.3%	-(14 \pm 15)%
$q\bar{q}(K)$	-16%	-(13 \pm 19)%
$B\bar{B}(\pi)$	-4.5%	-(1 \pm 7)%
$B\bar{B}(K)$	5.9%	(60 $^{+40}_{-160}$)%

Table 4.25: True and fit asymmetries in the generic Monte Carlo analysis of the $B^- \rightarrow D^0K^-$, $D^0 \rightarrow K_S^0\omega$ analysis.

Param.	$\mu(D^0K)$	$\sigma(D^0K)$	$N_{D^0\pi}$	N_{D^0K}	$N_{q\bar{q}(\pi)}$	$N_{q\bar{q}(K)}$	$N_{B\bar{B}(\pi)}$	$N_{B\bar{B}(K)}$
$\mu(D^0K)$	1.000	0.009	-0.023	0.061	0.006	-0.032	0.022	0.017
$\sigma(D^0K)$	0.009	1.000	-0.261	-0.092	-0.309	0.051	-0.119	-0.023
$N_{D^0\pi}$	-0.023	-0.261	1.000	0.015	0.294	-0.018	0.116	0.008
N_{D^0K}	0.061	-0.092	0.015	1.000	0.028	-0.281	0.012	0.129
$N_{q\bar{q}(\pi)}$	0.006	-0.309	0.294	0.028	1.000	0.015	0.613	-0.015
$N_{q\bar{q}(K)}$	-0.032	0.051	-0.018	-0.281	0.015	1.000	0.016	-0.837
$N_{B\bar{B}(\pi)}$	0.022	-0.119	0.116	0.012	0.613	0.016	1.000	-0.028
$N_{B\bar{B}(K)}$	0.017	-0.023	0.008	0.129	-0.015	-0.837	-0.028	1.000

Table 4.26: Correlation coefficients of parameters from the fit on the $B^- \rightarrow D^0K^-$, $D^0 \rightarrow K_S^0\omega$ MC sample.

In conclusion, the signal yields and asymmetries returned from the fit are consistent, within the estimated uncertainties, with the expected values from the simulation. We summarize them in Tables 4.27 and 4.28. $B\bar{B}(\pi)$ and $B\bar{B}(K)$ yields are also correctly estimated. $q\bar{q}(\pi)$ and $q\bar{q}(K)$ yields are overestimated, because the fraction $1 - f_1$ of $B \rightarrow D^0 h$ events that are not contained in the main ΔE Gaussian is mis-identified as a $q\bar{q}(h)$ background in the fit: this behaviour has also been observed in the “toy” Monte Carlo studies, and is not a concern since for our measurements we are interested only in the signal yields. In all the fits a significant (20-30%) correlation between the $B \rightarrow D^0 h$ and the $q\bar{q}(h)$ fit yields is observed: this correlation has also been reproduced in the Monte Carlo pseudo-experiments described in previous Section, which have shown that – even in the presence of such a correlation – the signal yields are not biased and their uncertainties are correctly estimated.

D^0 mode	$D^0\pi$ yield		D^0K yield	
	True	Fit	True	Fit
$K^-\pi^+$	16485 ± 53	16755 ± 138	1367 ± 3	1409 ± 43
K^+K^-	1334 ± 5	1330 ± 40	110 ± 1	99 ± 14
$\pi^+\pi^-$	463 ± 1	443 ± 26	38 ± 1	42 ± 10
$K_S^0\pi^0$	1479 ± 10	1471 ± 43	120 ± 1	122 ± 15
$K_S^0\phi$	375 ± 2	379 ± 21	32 ± 1	32 ± 6
$K_S^0\omega$	515 ± 7	515 ± 26	43 ± 1	39 ± 9

Table 4.27: True versus fit $B \rightarrow D^0\pi$ and $B \rightarrow D^0K$ yields, for each of the six D^0 modes, in the analysis performed on BABAR simulated events scaled to the same integrated luminosity as the data sample.

D^0 mode	$D^0\pi$ asymmetry (%)		D^0K asymmetry (%)	
	True	Fit	True	Fit
$K^-\pi^+$	-1.0	-1.2 ± 0.8	-1.3	-2.6 ± 3.0
K^+K^-	1.0	1.4 ± 3.0	-1.0	-1 ± 14
$\pi^+\pi^-$	1.4	3 ± 6	0.7	-5 ± 24
$K_S^0\pi^0$	-1.7	-1.8 ± 2.8	-0.5	-7 ± 12
$K_S^0\phi$	0.7	1 ± 5	-1.0	-9 ± 19
$K_S^0\omega$	-2.0	-2 ± 5	1.2	13 ± 22

Table 4.28: True versus fit $B \rightarrow D^0\pi$ and $B \rightarrow D^0K$ asymmetries, for each of the six D^0 modes, in the analysis performed on BABAR simulated events scaled to the same integrated luminosity as the data sample.

4.7 Fit results on data

In this section we report the results of the measurement of the $B \rightarrow D^0 K$ and $B \rightarrow D^0 \pi$ yields on data after the unblinding.

In Tables 4.29, 4.31, 4.33, 4.35, 4.37 and 4.39 we summarize the fit yields for each D^0 mode with their uncertainties. In the last column the charge asymmetries of each signal and background category, defined as the ratio between the difference and the sum of negative and positive B candidates in each category, are shown.

In Tables 4.30, 4.32, 4.34, 4.36, 4.38, 4.40 we put the correlation matrices of the fit parameters.

The ΔE and θ_C distributions of the selected samples with the projection of the fit result for each D^0 mode are shown in the two top plots of Figures 4.14-4.19.

The ΔE distributions, with the projection of the fit result, for each D^0 mode for the separate B^+ and B^- samples are shown in the two plots in the middle row of the same Figures.

In order to provide the evidence of the presence of the $B \rightarrow D^0 K$ signal, and to see what the components of the event sample look like in the ΔE variable when integrating over θ_C , we use the following weighting technique [86]. For each event, a weight for h to be a kaon or a pion is derived from the numbers $N(\pi) \equiv N(D^0 \pi) + N(q\bar{q}(\pi)) + N(B\bar{B}(\pi))$ and $N(K) \equiv N(D^0 K) + N(q\bar{q}(K)) + N(B\bar{B}(K)) + N(X_1 X_2 K)$ estimated from the fit and from the probability distributions in the θ_C variable. Using these weights, the data is then plotted in the ΔE variable. These plots, called “sPlots”, are shown in the bottom row of the Figures already introduced. For comparison, also shown are the sum of the $D^0 \pi$, $q\bar{q}(\pi)$ and $B\bar{B}(\pi)$ contributions (estimated from the nominal fit) in the case where the $h = \pi$ weight is used, and the sum of the $D^0 K$, $q\bar{q}(K)$, $B\bar{B}(K)$ and $X_1 X_2 K$ in the case where the $h = K$ weight is used.

4.7.1 $K^- \pi^+$

on-resonance data – Fit Results ($K^- \pi^+$)				
Parameter	Fitted value	B^+	B^-	Asym(%)
$\mu(D^0 K)$ (MeV)	-2.62 ± 0.14	-	-	
$\sigma(D^0 K)$ (MeV)	16.74 ± 0.12	-	-	
$N_{D^0 \pi}$	16050 ± 135	8151 ± 95	7899 ± 93	-1.6 ± 0.8
$N_{D^0 K}$	1260 ± 40	649 ± 29	611 ± 28	-3.0 ± 3.2
$N_{q\bar{q}(\pi)}$	3590 ± 104	1922 ± 73	1668 ± 68	-7.1 ± 2.8
$N_{q\bar{q}(K)}$	669 ± 42	317 ± 30	352 ± 30	5 ± 6
$N_{B\bar{B}(\pi)}$	12660 ± 127	6420 ± 90	6238 ± 88	-1.4 ± 1.0
$N_{B\bar{B}(K)}$	386 ± 32	217 ± 23	169 ± 22	-12 ± 8

Table 4.29: Maximum likelihood fit results in the on-resonance data sample of selected $B^- \rightarrow D^0 K^-$, $D^0 \rightarrow K^- \pi^+$ candidates.

The measured branching fraction ratio, taking into account selection and fit efficiency:

$$\tilde{\varepsilon}(B \rightarrow D^0 K) / \tilde{\varepsilon}(B \rightarrow D^0 \pi) = 101.3\% \quad (4.8)$$

and the correlation between the $B \rightarrow D^0 \pi$ and $B \rightarrow D^0 K$ yields returned from the fit (Table 4.30), is

$$\frac{\mathcal{B}(B \rightarrow D^0 K)}{\mathcal{B}(B \rightarrow D^0 \pi)} = \frac{N(B \rightarrow D^0 K) / N(B \rightarrow D^0 \pi)}{\tilde{\varepsilon}(B \rightarrow D^0 K) / \tilde{\varepsilon}(B \rightarrow D^0 \pi)} = (7.75 \pm 0.26(\text{stat}))\% \quad (4.9)$$

Param.	$\mu(D^0 K)$	$\sigma(D^0 K)$	$N_{D^0 \pi}$	$N_{D^0 K}$	$N_{q\bar{q}(\pi)}$	$N_{q\bar{q}(K)}$	$N_{B\bar{B}(\pi)}$	$N_{B\bar{B}(K)}$
$\mu(D^0 K)$	1.000	-0.038	-0.026	0.040	0.013	-0.017	0.008	0.012
$\sigma(D^0 K)$	-0.038	1.000	0.159	0.050	-0.291	-0.054	0.068	0.006
$N_{D^0 \pi}$	-0.026	0.159	1.000	-0.005	-0.205	-0.021	0.051	0.004
$N_{D^0 K}$	0.040	0.050	-0.005	1.000	-0.018	-0.191	0.004	0.035
$N_{q\bar{q}(\pi)}$	0.013	-0.291	-0.205	-0.018	1.000	-0.033	-0.312	0.020
$N_{q\bar{q}(K)}$	-0.017	-0.054	-0.021	-0.191	-0.033	1.000	0.010	-0.419
$N_{B\bar{B}(\pi)}$	0.008	0.068	0.051	0.004	-0.312	0.010	1.000	-0.049
$N_{B\bar{B}(K)}$	0.012	0.006	0.004	0.035	0.020	-0.419	-0.049	1.000

Table 4.30: Correlation coefficients of parameters from the fit on the $B^- \rightarrow D^0 K^-$, $D^0 \rightarrow K^- \pi^+$ on-resonance sample.

The $B \rightarrow D^0 h$ charge asymmetries are

$$A(D^0 \pi) = \frac{N(D^0 \pi^-) - N(\bar{D}^0 \pi^+)}{N(D^0 \pi^-) + N(\bar{D}^0 \pi^+)} = -(1.6 \pm 0.8(\text{stat}))\% \quad (4.10)$$

$$A(D^0 K) = \frac{N(D^0 K^-) - N(\bar{D}^0 K^+)}{N(D^0 K^-) + N(\bar{D}^0 K^+)} = -(3.0 \pm 3.2(\text{stat}))\% \quad (4.11)$$

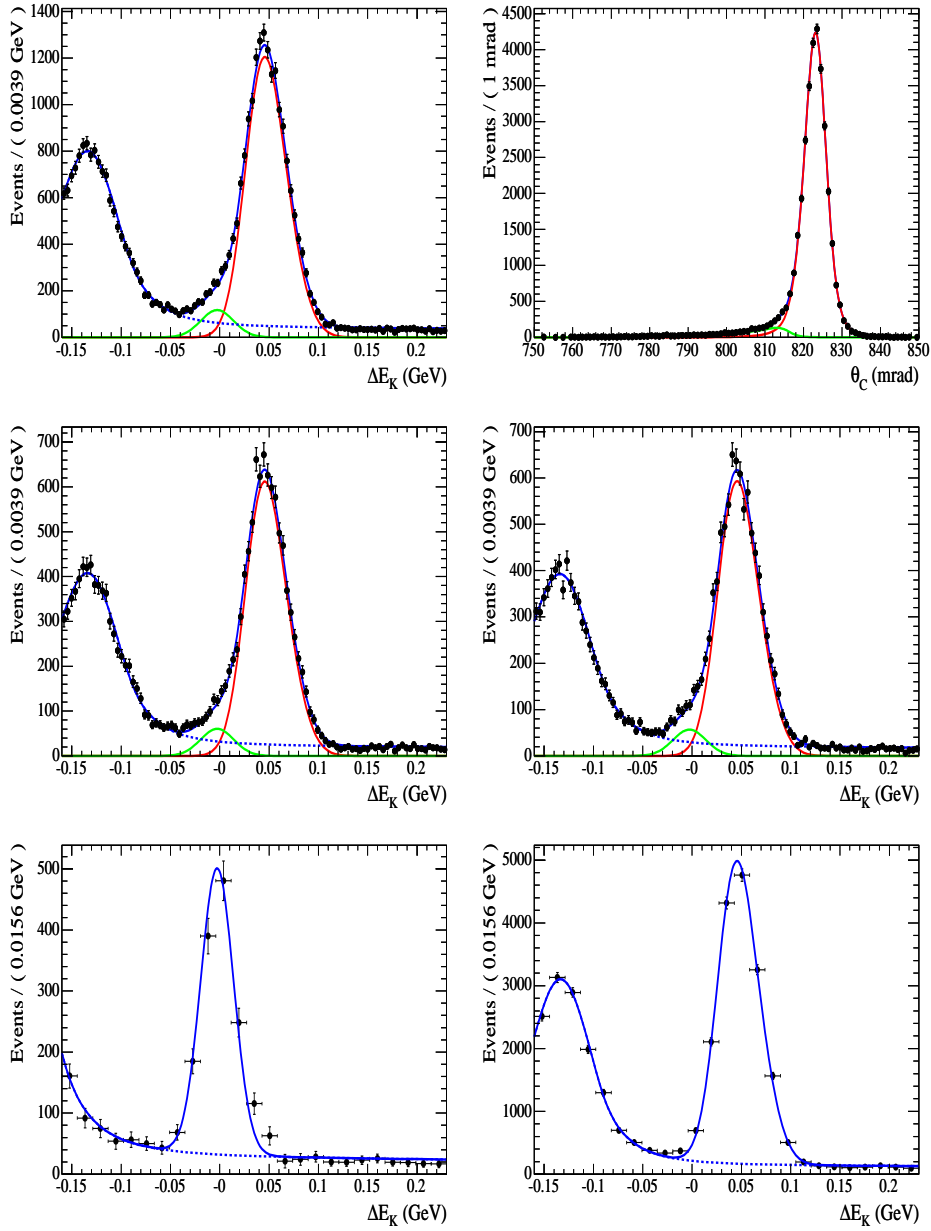


Figure 4.14: Top: ΔE (left) and θ_C (right) distribution of selected $B \rightarrow D^0 h, D^0 \rightarrow K^- \pi^+$ events in the on-resonance data sample. Middle: ΔE distribution of positive (left) and negative (right) B candidates. Bottom: ΔE distribution of selected events that have been weighted based on the probability, computed according to the θ_C measured value and its PDF, of $h = K$ (left) or $h = \pi$ (right). In the first four plots, the blue solid line represents the projection of the likelihood in the plotted variable. In the top-left and the two central plots the red solid line, the green solid line and the blue dashed line represent the ΔE projection of the $B \rightarrow D^0 \pi$, $B \rightarrow D^0 K$ and background components of the likelihood. In the top-right plot, the red and the green lines represent the θ_C projection of the “pion” ($B \rightarrow D^0 \pi$, $q\bar{q}(\pi)$ and $B\bar{B}(\pi)$) and “kaon” ($B \rightarrow D^0 K$, $q\bar{q}(K)$, $B\bar{B}(K)$) of the likelihood. In the two bottom plots, the solid lines represent the ΔE projections of the kaon component (left) and the pion component (right) of the likelihood, while the dashed lines represent the projections of the background kaon or pion components.

4.7.2 K^+K^-

on-resonance data – Fit Results (K^+K^-)				
Parameter	Fitted value	B^+	B^-	Asym(%)
$\mu(D^0K)$ (MeV)	-2.7 ± 0.5	-	-	
$\sigma(D^0K)$ (MeV)	17.3 ± 0.5	-	-	
$N_{D^0\pi}$	1395 ± 40	705 ± 28	690 ± 28	-1.1 ± 2.8
N_{D^0K}	96 ± 13	26 ± 9	70 ± 10	46 ± 15
$N_{q\bar{q}(\pi)}$	273 ± 33	130 ± 22	143 ± 24	5 ± 12
$N_{q\bar{q}(K)}$	185 ± 23	118 ± 18	67 ± 15	-28 ± 13
$N_{B\bar{B}(\pi)}$	1188 ± 41	588 ± 28	600 ± 29	1.0 ± 3.3
$N_{B\bar{B}(K)}$	34 ± 16	14 ± 12	20 ± 12	18 ± 51

Table 4.31: Maximum likelihood fit results in the on-resonance data sample of selected $B^- \rightarrow D^0K^-$, $D^0 \rightarrow K^+K^-$ candidates.

Param.	$\mu(D^0K)$	$\sigma(D^0K)$	$N_{D^0\pi}$	N_{D^0K}	$N_{q\bar{q}(\pi)}$	$N_{q\bar{q}(K)}$	$N_{B\bar{B}(\pi)}$	$N_{B\bar{B}(K)}$
$\mu(D^0K)$	1.000	-0.034	0.024	0.025	-0.003	0.010	-0.015	-0.008
$\sigma(D^0K)$	-0.034	1.000	-0.163	0.105	0.280	0.067	-0.070	-0.018
$N_{D^0\pi}$	0.024	-0.163	1.000	-0.008	-0.213	-0.021	0.055	0.007
N_{D^0K}	0.025	0.105	-0.008	1.000	0.033	0.267	-0.009	-0.080
$N_{q\bar{q}(\pi)}$	-0.003	0.280	-0.213	0.033	1.000	-0.012	-0.401	0.013
$N_{q\bar{q}(K)}$	0.010	0.067	-0.021	0.267	-0.012	1.000	0.007	-0.625
$N_{B\bar{B}(\pi)}$	-0.015	-0.070	0.055	-0.009	-0.401	0.007	1.000	-0.036
$N_{B\bar{B}(K)}$	-0.008	-0.018	0.007	-0.080	0.013	-0.625	-0.036	1.000

Table 4.32: Correlation coefficients of parameters from the fit on the $B^- \rightarrow D^0K^-$, $D^0 \rightarrow K^+K^-$ on-resonance sample.

The measured branching fraction ratio, taking into account selection and fit efficiency:

$$\tilde{\varepsilon}(B \rightarrow D^0K)/\tilde{\varepsilon}(B \rightarrow D^0\pi) = 100.3\% \quad (4.12)$$

and the correlation between the $B \rightarrow D^0\pi$ and $B \rightarrow D^0K$ yields returned from the fit, is:

$$\frac{\mathcal{B}(B \rightarrow D^0K)}{\mathcal{B}(B \rightarrow D^0\pi)} = \frac{N(B \rightarrow D^0K)/N(B \rightarrow D^0\pi)}{\tilde{\varepsilon}(B \rightarrow D^0K)/\tilde{\varepsilon}(B \rightarrow D^0\pi)} = (6.9 \pm 1.0(\text{stat}))\% \quad (4.13)$$

The double branching fraction ratio is:

$$\frac{\frac{\mathcal{B}(B \rightarrow D^0K, D^0 \rightarrow K^+K^-)}{\mathcal{B}(B \rightarrow D^0\pi, D^0 \rightarrow K^+K^-)}}{\frac{\mathcal{B}(B \rightarrow D^0K, D^0 \rightarrow K^- \pi^+)}{\mathcal{B}(B \rightarrow D^0\pi, D^0 \rightarrow K^- \pi^+)}} = (89 \pm 13(\text{stat}))\% \quad (4.14)$$

The $B \rightarrow D^0h$ charge asymmetries are

$$A(D^0\pi) = \frac{N(D^0\pi^-) - N(\bar{D}^0\pi^+)}{N(D^0\pi^-) + N(\bar{D}^0\pi^+)} = -(1.1 \pm 2.8(\text{stat}))\% \quad (4.15)$$

$$A(D^0K) = \frac{N(D^0K^-) - N(\bar{D}^0K^+)}{N(D^0K^-) + N(\bar{D}^0K^+)} = (46 \pm 15(\text{stat}))\% \quad (4.16)$$

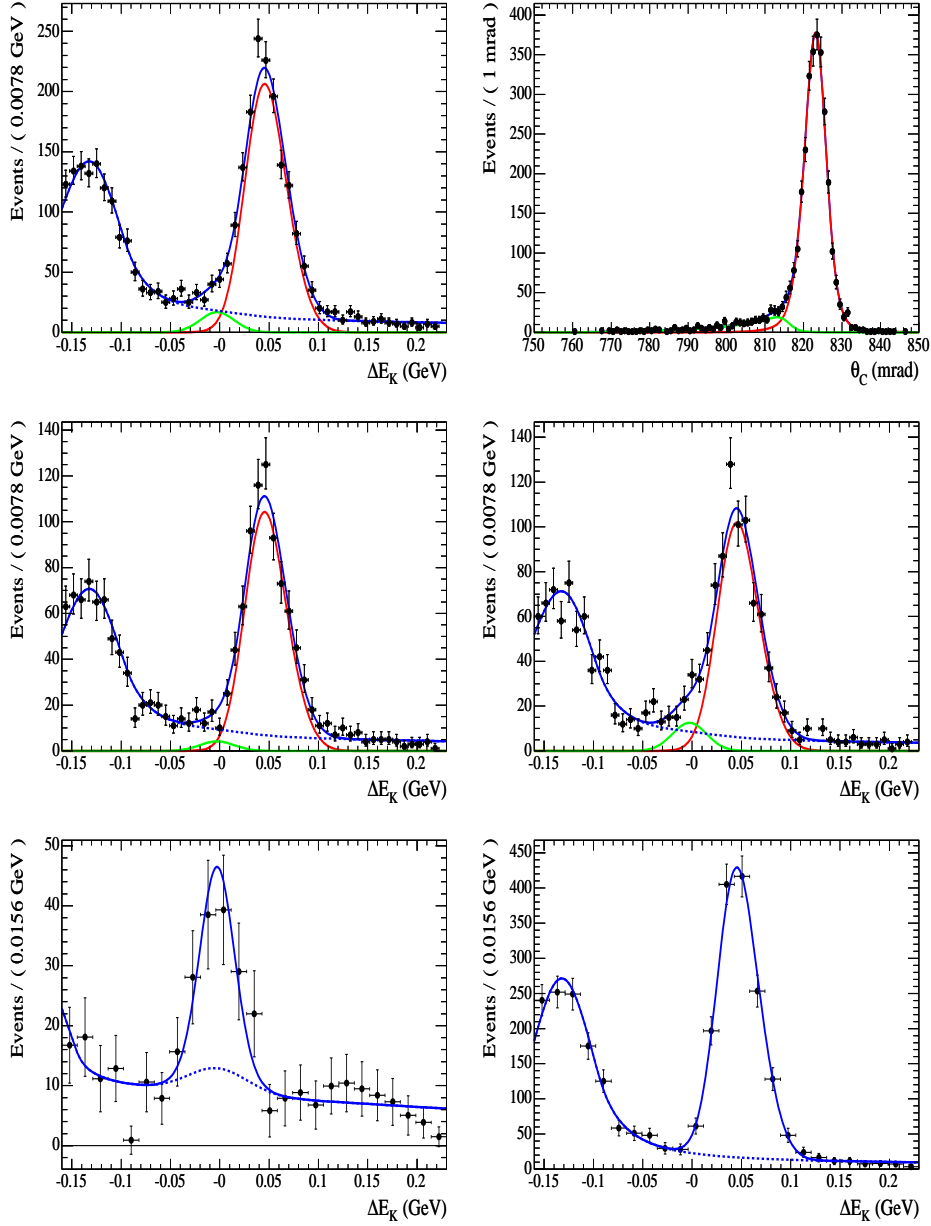


Figure 4.15: Top: ΔE (left) and θ_C (right) distribution of selected $B \rightarrow D^0 h, D^0 \rightarrow K^+ K^-$ events in the on-resonance data sample. Middle: ΔE distribution of positive (left) and negative (right) B candidates. Bottom: ΔE distribution of selected events that have been weighted based on the probability, computed according to the θ_C measured value and its PDF, of $h = K$ (left) or $h = \pi$ (right). In the first four plots, the blue solid line represents the projection of the likelihood in the plotted variable. In the top-left and the two central plots the red solid line, the green solid line and the blue dashed line represent the ΔE projection of the $B \rightarrow D^0 \pi$, $B \rightarrow D^0 K$ and background components of the likelihood. In the top-right plot, the red and the green lines represent the θ_C projection of the “pion” ($B \rightarrow D^0 \pi, q\bar{q}(\pi)$ and $B\bar{B}(\pi)$) and “kaon” ($B \rightarrow D^0 K, q\bar{q}(K)$, $B\bar{B}(K)$ and $X_1 X_2 K$) of the likelihood. In the two bottom plots, the solid lines represent the ΔE projections of the kaon component (left) and the pion component (right) of the likelihood, while the dashed lines represent the projections of the background kaon or pion components.

4.7.3 $\pi^+\pi^-$

on-resonance data – Fit Results ($\pi^+\pi^-$)				
Parameter	Fitted value	B^+	B^-	Asym(%)
$\mu(D^0K)$ (MeV)	-1.6 ± 1.0	-	-	
$\sigma(D^0K)$ (MeV)	16.9 ± 0.9	-	-	
$N_{D^0\pi}$	475 ± 26	256 ± 18	219 ± 17	-8 ± 5
N_{D^0K}	35 ± 10	18 ± 7	17 ± 7	-3 ± 28
$N_{q\bar{q}(\pi)}$	415 ± 38	206 ± 25	209 ± 26	1 ± 9
$N_{q\bar{q}(K)}$	215 ± 32	112 ± 11	103 ± 11	-4 ± 7
$N_{B\bar{B}(\pi)}$	485 ± 33	240 ± 23	245 ± 23	1 ± 7
$N_{B\bar{B}(K)}$	32 ± 26	17^{+20}_{-17}	15^{+19}_{-15}	-6^{+80}_{-77}

Table 4.33: Maximum likelihood fit results in the on-resonance data sample of selected $B^- \rightarrow D^0K^-$, $D^0 \rightarrow \pi^+\pi^-$ candidates.

Param.	$\mu(D^0K)$	$\sigma(D^0K)$	$N_{D^0\pi}$	N_{D^0K}	$N_{q\bar{q}(\pi)}$	$N_{q\bar{q}(K)}$	$N_{B\bar{B}(\pi)}$	$N_{B\bar{B}(K)}$
$\mu(D^0K)$	1.000	0.083	-0.046	-0.017	-0.034	0.016	0.000	-0.011
$\sigma(D^0K)$	0.083	1.000	-0.296	0.039	-0.305	-0.018	0.116	0.006
$N_{D^0\pi}$	-0.046	-0.296	1.000	-0.009	0.318	0.015	-0.124	-0.007
N_{D^0K}	-0.017	0.039	-0.009	1.000	-0.014	-0.272	0.007	0.112
$N_{q\bar{q}(\pi)}$	-0.034	-0.305	0.318	-0.014	1.000	-0.024	-0.553	0.018
$N_{q\bar{q}(K)}$	0.016	-0.018	0.015	-0.272	-0.024	1.000	0.018	-0.817
$N_{B\bar{B}(\pi)}$	0.000	0.116	-0.124	0.007	-0.553	0.018	1.000	-0.031
$N_{B\bar{B}(K)}$	-0.011	0.006	-0.007	0.112	0.018	-0.817	-0.031	1.000

Table 4.34: Correlation coefficients of parameters from the fit on the $B^- \rightarrow D^0K^-$, $D^0 \rightarrow \pi^+\pi^-$ on-resonance sample.

The measured branching fraction ratio, taking into account selection and fit efficiency:

$$\tilde{\varepsilon}(B \rightarrow D^0K)/\tilde{\varepsilon}(B \rightarrow D^0\pi) = 100.9\% \quad (4.17)$$

and the correlation between the $B \rightarrow D^0\pi$ and $B \rightarrow D^0K$ yields returned from the fit, is:

$$\frac{\mathcal{B}(B \rightarrow D^0K)}{\mathcal{B}(B \rightarrow D^0\pi)} = \frac{N(B \rightarrow D^0K)/N(B \rightarrow D^0\pi)}{\tilde{\varepsilon}(B \rightarrow D^0K)/\tilde{\varepsilon}(B \rightarrow D^0\pi)} = (7.3 \pm 2.1(\text{stat}))\% \quad (4.18)$$

The double branching fraction ratio is:

$$\frac{\frac{\mathcal{B}(B \rightarrow D^0K, D^0 \rightarrow \pi^+\pi^-)}{\mathcal{B}(B \rightarrow D^0\pi, D^0 \rightarrow \pi^+\pi^-)}}{\frac{\mathcal{B}(B \rightarrow D^0K, D^0 \rightarrow K^-\pi^+)}{\mathcal{B}(B \rightarrow D^0\pi, D^0 \rightarrow K^-\pi^+)}} = (94 \pm 28(\text{stat}))\% \quad (4.19)$$

The $B \rightarrow D^0h$ charge asymmetries are

$$A(D^0\pi) = \frac{N(D^0\pi^-) - N(\bar{D}^0\pi^+)}{N(D^0\pi^-) + N(\bar{D}^0\pi^+)} = -(8 \pm 5(\text{stat}))\% \quad (4.20)$$

$$A(D^0K) = \frac{N(D^0K^-) - N(\bar{D}^0K^+)}{N(D^0K^-) + N(\bar{D}^0K^+)} = -(3 \pm 28(\text{stat}))\% \quad (4.21)$$

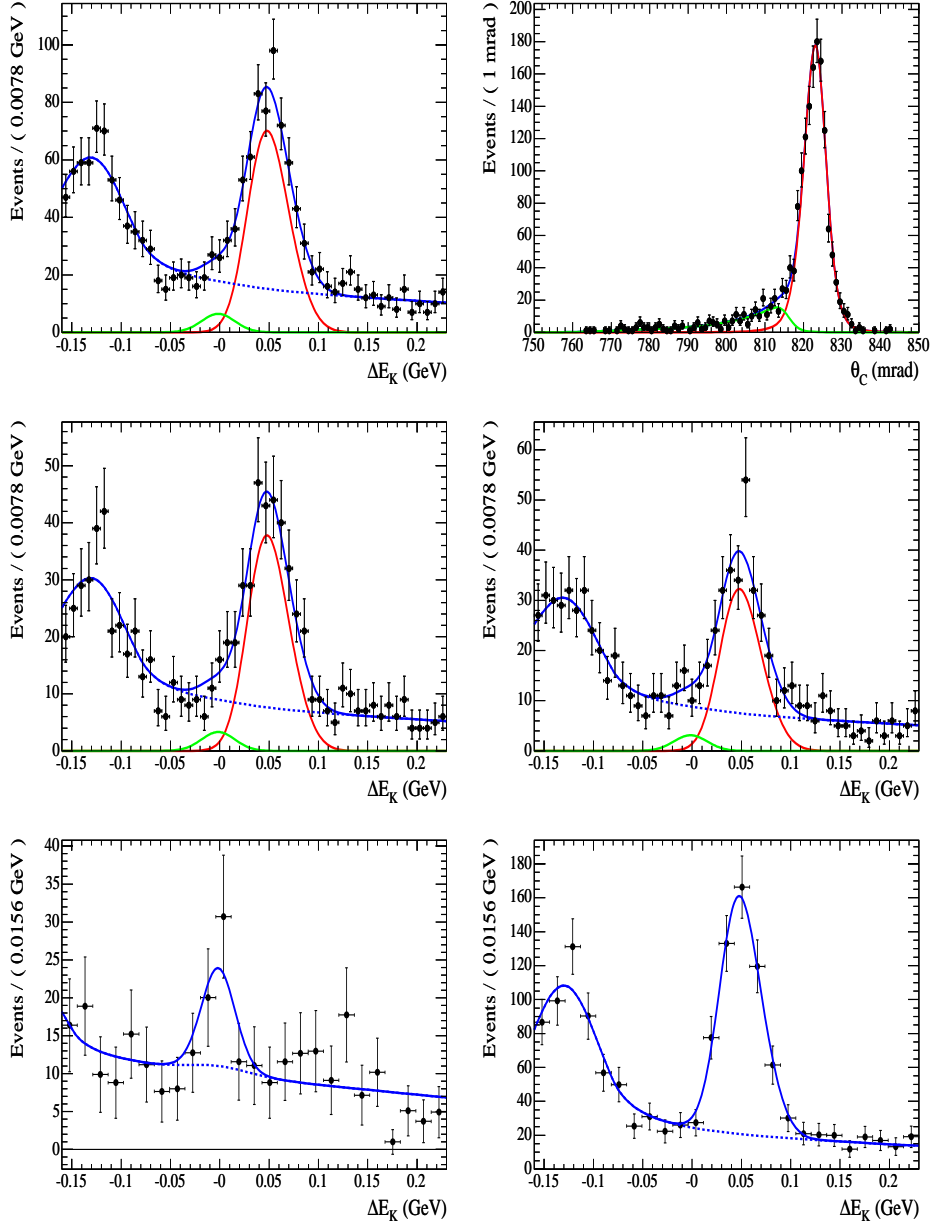


Figure 4.16: Top: ΔE (left) and θ_C (right) distribution of selected $B \rightarrow D^0 h$, $D^0 \rightarrow \pi^+ \pi^-$ events in the on-resonance data sample. Middle: ΔE distribution of positive (left) and negative (right) B candidates. Bottom: ΔE distribution of selected events that have been weighted based on the probability, computed according to the θ_C measured value and its PDF, of $h = K$ (left) or $h = \pi$ (right). In the first four plots, the blue solid line represents the projection of the likelihood in the plotted variable. In the top-left and the two central plots the red solid line, the green solid line and the blue dashed line represent the ΔE projection of the $B \rightarrow D^0 \pi$, $B \rightarrow D^0 K$ and background components of the likelihood. In the top-right plot, the red and the green lines represent the θ_C projection of the “pion” ($B \rightarrow D^0 \pi$, $q\bar{q}(\pi)$ and $B\bar{B}(\pi)$) and “kaon” ($B \rightarrow D^0 K$, $q\bar{q}(K)$, $B\bar{B}(K)$ and $X_1 X_2 K$) of the likelihood. In the two bottom plots, the solid lines represent the ΔE projections of the kaon component (left) and the pion component (right) of the likelihood, while the dashed lines represent the projections of the background kaon or pion components.

4.7.4 $K_S^0\pi^0$

on-resonance data – Fit Results ($K_S^0\pi^0$)				
Parameter	Fitted value	B^+	B^-	Asym(%)
$\mu(D^0K)$ (MeV)	-1.6 ± 0.6	-	-	
$\sigma(D^0K)$ (MeV)	17.6 ± 0.5	-	-	
$N_{D^0\pi}$	1384 ± 42	707 ± 29	677 ± 29	-2.2 ± 3.0
N_{D^0K}	81 ± 13	39 ± 9	42 ± 9	4 ± 16
$N_{q\bar{q}(\pi)}$	545 ± 46	250 ± 30	295 ± 31	8 ± 8
$N_{q\bar{q}(K)}$	227 ± 27	90 ± 18	137 ± 21	21 ± 12
$N_{B\bar{B}(\pi)}$	1315 ± 46	684 ± 33	631 ± 32	-4.0 ± 3.5
$N_{B\bar{B}(K)}$	57 ± 20	34 ± 14	23 ± 15	-19 ± 37

Table 4.35: Maximum likelihood fit results in the on-resonance data sample of selected $B^- \rightarrow D^0K^-$, $D^0 \rightarrow K_S^0\pi^0$ candidates.

Param.	$\mu(D^0K)$	$\sigma(D^0K)$	$N_{D^0\pi}$	N_{D^0K}	$N_{q\bar{q}(\pi)}$	$N_{q\bar{q}(K)}$	$N_{B\bar{B}(\pi)}$	$N_{B\bar{B}(K)}$
$\mu(D^0K)$	1.000	-0.055	0.034	0.044	0.018	0.025	0.010	0.015
$\sigma(D^0K)$	-0.055	1.000	-0.250	0.034	-0.337	0.026	0.106	0.007
$N_{D^0\pi}$	0.034	-0.250	1.000	0.001	0.281	-0.018	-0.092	-0.007
N_{D^0K}	0.044	0.034	0.001	1.000	-0.014	0.289	0.005	0.096
$N_{q\bar{q}(\pi)}$	0.018	-0.337	0.281	-0.014	1.000	0.033	-0.453	0.024
$N_{q\bar{q}(K)}$	0.025	0.026	-0.018	0.289	0.033	1.000	-0.019	0.663
$N_{B\bar{B}(\pi)}$	0.010	0.106	-0.092	0.005	-0.453	-0.019	1.000	-0.046
$N_{B\bar{B}(K)}$	0.015	0.007	-0.007	0.096	0.024	0.663	-0.046	1.000

Table 4.36: Correlation coefficients of parameters from the fit on the $B^- \rightarrow D^0K^-$, $D^0 \rightarrow K_S^0\pi^0$ on-resonance sample.

The measured branching fraction ratio, taking into account selection and fit efficiency:

$$\tilde{\varepsilon}(B \rightarrow D^0K)/\tilde{\varepsilon}(B \rightarrow D^0\pi) = 99.5\% \quad (4.22)$$

and the correlation between the $B \rightarrow D^0\pi$ and $B \rightarrow D^0K$ yields returned from the fit, is:

$$\frac{\mathcal{B}(B \rightarrow D^0K)}{\mathcal{B}(B \rightarrow D^0\pi)} = \frac{N(B \rightarrow D^0K)/N(B \rightarrow D^0\pi)}{\tilde{\varepsilon}(B \rightarrow D^0K)/\tilde{\varepsilon}(B \rightarrow D^0\pi)} = (5.9 \pm 1.0(\text{stat}))\% \quad (4.23)$$

The double branching fraction ratio is:

$$\frac{\frac{\mathcal{B}(B \rightarrow D^0K, D^0 \rightarrow K_S^0\pi^0)}{\mathcal{B}(B \rightarrow D^0\pi, D^0 \rightarrow K_S^0\pi^0)}}{\frac{\mathcal{B}(B \rightarrow D^0K, D^0 \rightarrow K^-\pi^+)}{\mathcal{B}(B \rightarrow D^0\pi, D^0 \rightarrow K^-\pi^+)}} = (76 \pm 13(\text{stat}))\% \quad (4.24)$$

The $B \rightarrow D^0h$ charge asymmetries are

$$A(D^0\pi) = \frac{N(D^0\pi^-) - N(\bar{D}^0\pi^+)}{N(D^0\pi^-) + N(\bar{D}^0\pi^+)} = -(2.2 \pm 3.0(\text{stat}))\% \quad (4.25)$$

$$A(D^0K) = \frac{N(D^0K^-) - N(\bar{D}^0K^+)}{N(D^0K^-) + N(\bar{D}^0K^+)} = -(4 \pm 16(\text{stat}))\% \quad (4.26)$$

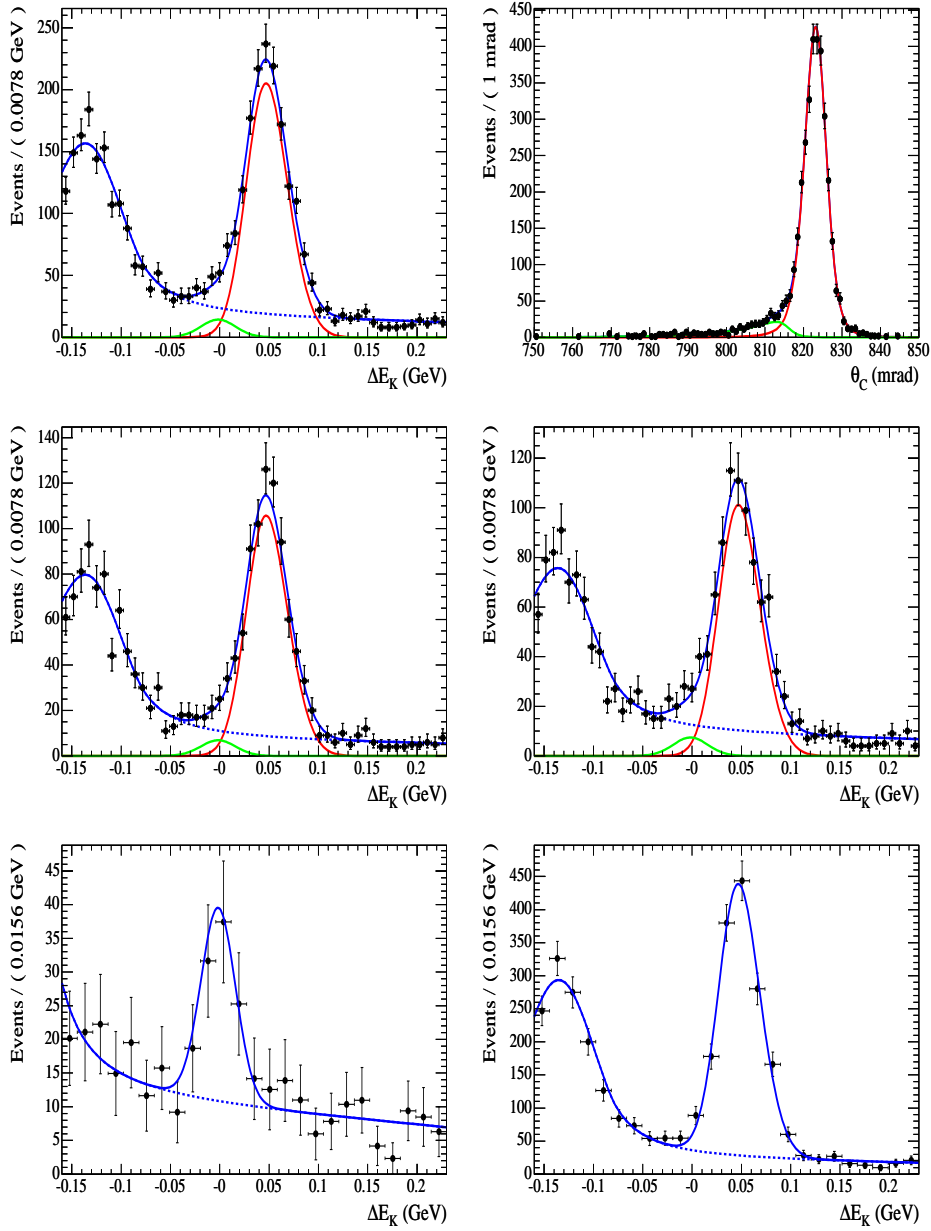


Figure 4.17: Top: ΔE (left) and θ_C (right) distribution of selected $B \rightarrow D^0 h, D^0 \rightarrow K_S^0 \pi^0$ events in the on-resonance data sample. Middle: ΔE distribution of positive (left) and negative (right) B candidates. Bottom: ΔE distribution of selected events that have been weighted based on the probability, computed according to the θ_C measured value and its PDF, of $h = K$ (left) or $h = \pi$ (right). In the first four plots, the blue solid line represents the projection of the likelihood in the plotted variable. In the top-left and the two central plots the red solid line, the green solid line and the blue dashed line represent the ΔE projection of the $B \rightarrow D^0 \pi$, $B \rightarrow D^0 K$ and background components of the likelihood. In the top-right plot, the red and the green lines represent the θ_C projection of the “pion” ($B \rightarrow D^0 \pi$, $q\bar{q}(\pi)$ and $B\bar{B}(\pi)$) and “kaon” ($B \rightarrow D^0 K$, $q\bar{q}(K)$, $B\bar{B}(K)$ and $X_1 X_2 K$) of the likelihood. In the two bottom plots, the solid lines represent the ΔE projections of the kaon component (left) and the pion component (right) of the likelihood, while the dashed lines represent the projections of the background kaon or pion components.

4.7.5 $K_S^0\phi$

on-resonance data – Fit Results ($K_S^0\phi$)				
Parameter	Fitted value	B^+	B^-	Asym(%)
$\mu(D^0K)$ (MeV)	-2.1 ± 1.0	-	-	
$\sigma(D^0K)$ (MeV)	17.2 ± 0.8	-	-	
$N_{D^0\pi}$	333 ± 20	176 ± 14	157 ± 13	-6 ± 6
N_{D^0K}	28 ± 6	15 ± 5	13 ± 4	-7 ± 23
$N_{q\bar{q}(\pi)}$	80 ± 17	32 ± 10	48 ± 12	20 ± 19
$N_{q\bar{q}(K)}$	41 ± 8	27 ± 7	14 ± 5	-32 ± 20
$N_{B\bar{B}(\pi)}$	272 ± 19	132 ± 13	140 ± 14	3 ± 7
$N_{B\bar{B}(K)}$	3_{-2}^{+3}	3_{-2}^{+3}	0_{-0}^{+1}	-100_{-0}^{+67}

Table 4.37: Maximum likelihood fit results in the on-resonance data sample of selected $B^- \rightarrow D^0K^-$, $D^0 \rightarrow K_S^0\phi$ candidates.

Param.	$\mu(D^0K)$	$\sigma(D^0K)$	$N_{D^0\pi}$	N_{D^0K}	$N_{q\bar{q}(\pi)}$	$N_{q\bar{q}(K)}$	$N_{B\bar{B}(\pi)}$	$N_{B\bar{B}(K)}$
$\mu(D^0K)$	1.000	0.054	0.003	-0.073	-0.034	0.035	-0.022	-0.009
$\sigma(D^0K)$	0.054	1.000	-0.161	-0.047	-0.294	0.041	-0.090	-0.011
$N_{D^0\pi}$	0.003	-0.161	1.000	-0.009	0.223	-0.021	0.068	0.005
N_{D^0K}	-0.073	-0.047	-0.009	1.000	0.012	-0.250	0.008	0.069
$N_{q\bar{q}(\pi)}$	-0.034	-0.294	0.223	0.012	1.000	0.020	0.373	-0.010
$N_{q\bar{q}(K)}$	0.035	0.041	-0.021	-0.250	0.020	1.000	-0.012	-0.275
$N_{B\bar{B}(\pi)}$	-0.022	-0.090	0.068	0.008	0.373	-0.012	1.000	-0.029
$N_{B\bar{B}(K)}$	-0.009	-0.011	0.005	0.069	-0.010	-0.275	-0.029	1.000

Table 4.38: Correlation coefficients of parameters from the fit on the $B^- \rightarrow D^0K^-$, $D^0 \rightarrow K_S^0\phi$ on-resonance sample.

The measured branching fraction ratio, taking into account selection and fit efficiency:

$$\tilde{\varepsilon}(B \rightarrow D^0K)/\tilde{\varepsilon}(B \rightarrow D^0\pi) = 99.9\% \quad (4.27)$$

and the correlation between the $B \rightarrow D^0\pi$ and $B \rightarrow D^0K$ yields returned from the fit, is:

$$\frac{\mathcal{B}(B \rightarrow D^0K)}{\mathcal{B}(B \rightarrow D^0\pi)} = \frac{N(B \rightarrow D^0K)/N(B \rightarrow D^0\pi)}{\tilde{\varepsilon}(B \rightarrow D^0K)/\tilde{\varepsilon}(B \rightarrow D^0\pi)} = (8.4 \pm 1.9(\text{stat}))\% \quad (4.28)$$

The double branching fraction ratio is:

$$\frac{\frac{\mathcal{B}(B \rightarrow D^0K, D^0 \rightarrow K_S^0\phi)}{\mathcal{B}(B \rightarrow D^0\pi, D^0 \rightarrow K_S^0\phi)}}{\frac{\mathcal{B}(B \rightarrow D^0K, D^0 \rightarrow K^-\pi^+)}{\mathcal{B}(B \rightarrow D^0\pi, D^0 \rightarrow K^-\pi^+)}} = (109 \pm 25(\text{stat}))\% \quad (4.29)$$

The $B \rightarrow D^0h$ charge asymmetries are

$$A(D^0\pi) = \frac{N(D^0\pi^-) - N(\bar{D}^0\pi^+)}{N(D^0\pi^-) + N(\bar{D}^0\pi^+)} = -(6 \pm 6(\text{stat}))\% \quad (4.30)$$

$$A(D^0K) = \frac{N(D^0K^-) - N(\bar{D}^0K^+)}{N(D^0K^-) + N(\bar{D}^0K^+)} = -(7 \pm 23(\text{stat}))\% \quad (4.31)$$

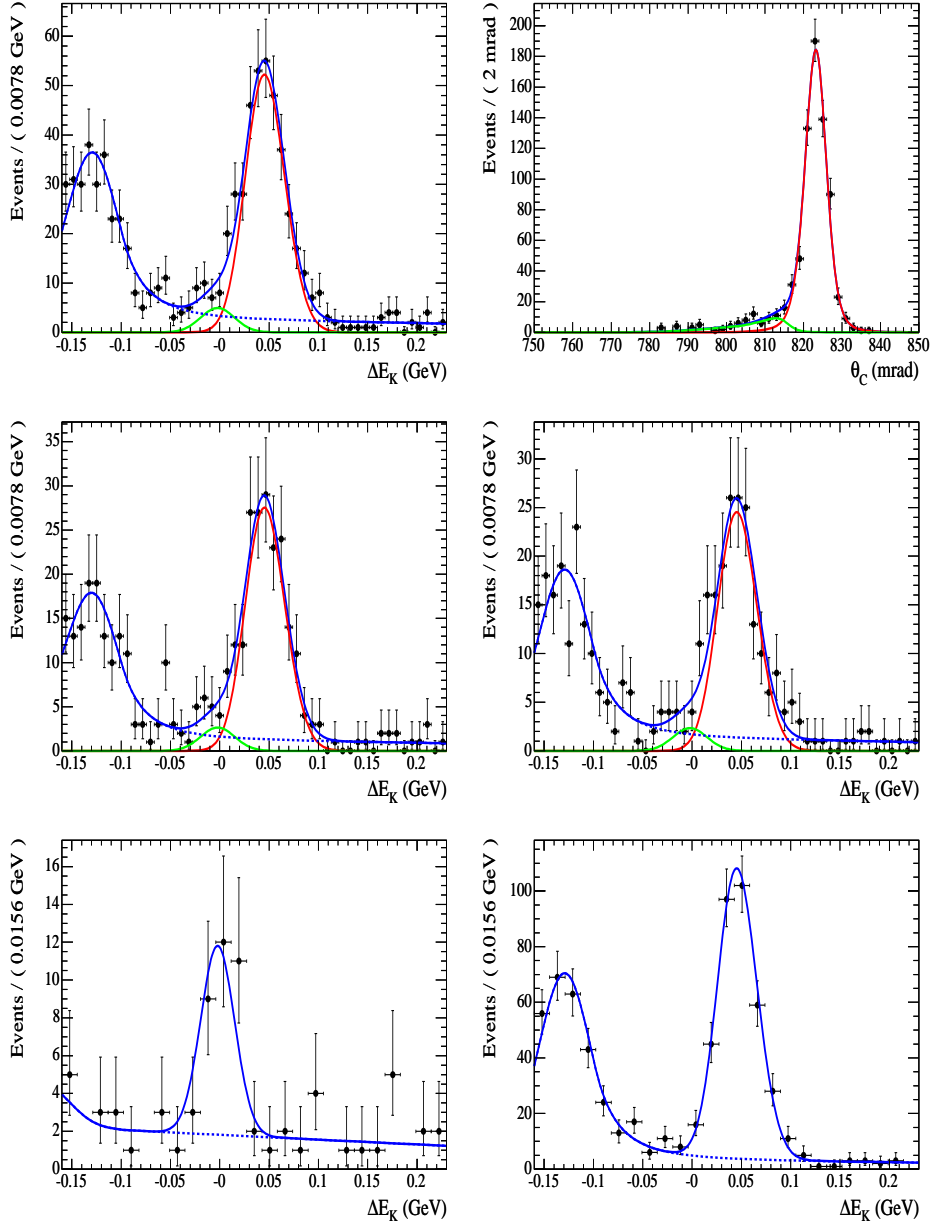


Figure 4.18: Top: ΔE (left) and θ_C (right) distribution of selected $B \rightarrow D^0 h$, $D^0 \rightarrow K_s^0 \phi$ events in the on-resonance data sample. Middle: ΔE distribution of positive (left) and negative (right) B candidates. Bottom: ΔE distribution of selected events that have been weighted based on the probability, computed according to the θ_C measured value and its PDF, of $h = K$ (left) or $h = \pi$ (right). In the first four plots, the blue solid line represents the projection of the likelihood in the plotted variable. In the top-left and the two central plots the red solid line, the green solid line and the blue dashed line represent the ΔE projection of the $B \rightarrow D^0 \pi$, $B \rightarrow D^0 K$ and background components of the likelihood. In the top-right plot, the red and the green lines represent the θ_C projection of the “pion” ($B \rightarrow D^0 \pi$, $q\bar{q}(\pi)$ and $B\bar{B}(\pi)$) and “kaon” ($B \rightarrow D^0 K$, $q\bar{q}(K)$, $B\bar{B}(K)$ and $X_1 X_2 K$) of the likelihood. In the two bottom plots, the solid lines represent the ΔE projections of the kaon component (left) and the pion component (right) of the likelihood, while the dashed lines represent the projections of the background kaon or pion components.

4.7.6 $K_s^0\omega$

on-resonance data – Fit Results ($K_s^0\omega$)				
Parameter	Fitted value	B^+	B^-	Asym(%)
$\mu(D^0K)$ (MeV)	-2.6 ± 1.0	-	-	
$\sigma(D^0K)$ (MeV)	17.6 ± 0.9	-	-	
$N_{D^0\pi}$	465 ± 25	235 ± 17	230 ± 17	-1 ± 5
N_{D^0K}	39 ± 9	25 ± 7	14 ± 6	-28 ± 24
$N_{q\bar{q}(\pi)}$	211 ± 34	84 ± 23	127 ± 24	20 ± 16
$N_{q\bar{q}(K)}$	126 ± 26	59 ± 20	67 ± 10	6 ± 18
$N_{B\bar{B}(\pi)}$	547 ± 34	294 ± 24	253 ± 24	-8 ± 6
$N_{B\bar{B}(K)}$	18_{-16}^{+23}	18_{-16}^{+20}	0_{-0}^{+6}	-100_{-0}^{+200}

Table 4.39: Maximum likelihood fit results in the on-resonance data sample of selected $B^- \rightarrow D^0K^-$, $D^0 \rightarrow K_s^0\omega$ candidates.

Param.	$\mu(D^0K)$	$\sigma(D^0K)$	$N_{D^0\pi}$	N_{D^0K}	$N_{q\bar{q}(\pi)}$	$N_{q\bar{q}(K)}$	$N_{B\bar{B}(\pi)}$	$N_{B\bar{B}(K)}$
$\mu(D^0K)$	1.000	-0.003	-0.012	0.057	-0.024	-0.026	-0.029	0.015
$\sigma(D^0K)$	-0.003	1.000	-0.255	-0.129	0.286	0.071	0.102	-0.030
$N_{D^0\pi}$	-0.012	-0.255	1.000	0.021	-0.285	-0.025	-0.102	0.011
N_{D^0K}	0.057	-0.129	0.021	1.000	-0.037	-0.279	-0.016	0.123
$N_{q\bar{q}(\pi)}$	-0.024	0.286	-0.285	-0.037	1.000	-0.020	0.602	0.020
$N_{q\bar{q}(K)}$	-0.026	0.071	-0.025	-0.279	-0.020	1.000	-0.016	-0.826
$N_{B\bar{B}(\pi)}$	-0.029	0.102	-0.102	-0.016	0.602	-0.016	1.000	0.036
$N_{B\bar{B}(K)}$	0.015	-0.030	0.011	0.123	0.020	-0.826	0.036	1.000

Table 4.40: Correlation coefficients of parameters from the fit on the $B^- \rightarrow D^0K^-$, $D^0 \rightarrow K_s^0\omega$ on-resonance sample.

The measured branching fraction ratio, taking into account selection and fit efficiency:

$$\tilde{\varepsilon}(B \rightarrow D^0K)/\tilde{\varepsilon}(B \rightarrow D^0\pi) = 103.3\%. \quad (4.32)$$

and the correlation between the $B \rightarrow D^0\pi$ and $B \rightarrow D^0K$ yields returned from the fit, is:

$$\frac{\mathcal{B}(B \rightarrow D^0K)}{\mathcal{B}(B \rightarrow D^0\pi)} = \frac{N(B \rightarrow D^0K)/N(B \rightarrow D^0\pi)}{\tilde{\varepsilon}(B \rightarrow D^0K)/\tilde{\varepsilon}(B \rightarrow D^0\pi)} = (8.2 \pm 1.9(\text{stat}))\% \quad (4.33)$$

The double branching fraction ratio is:

$$\frac{\frac{\mathcal{B}(B \rightarrow D^0K, D^0 \rightarrow K_s^0\omega)}{\mathcal{B}(B \rightarrow D^0\pi, D^0 \rightarrow K_s^0\omega)}}{\frac{\mathcal{B}(B \rightarrow D^0K, D^0 \rightarrow K^-\pi^+)}{\mathcal{B}(B \rightarrow D^0\pi, D^0 \rightarrow K^-\pi^+)}} = (105 \pm 25(\text{stat}))\% \quad (4.34)$$

The $B \rightarrow D^0h$ charge asymmetries are

$$A(D^0\pi) = \frac{N(D^0\pi^-) - N(\bar{D}^0\pi^+)}{N(D^0\pi^-) + N(\bar{D}^0\pi^+)} = -(1 \pm 5(\text{stat}))\% \quad (4.35)$$

$$A(D^0K) = \frac{N(D^0K^-) - N(\bar{D}^0K^+)}{N(D^0K^-) + N(\bar{D}^0K^+)} = -(28 \pm 24(\text{stat}))\% \quad (4.36)$$

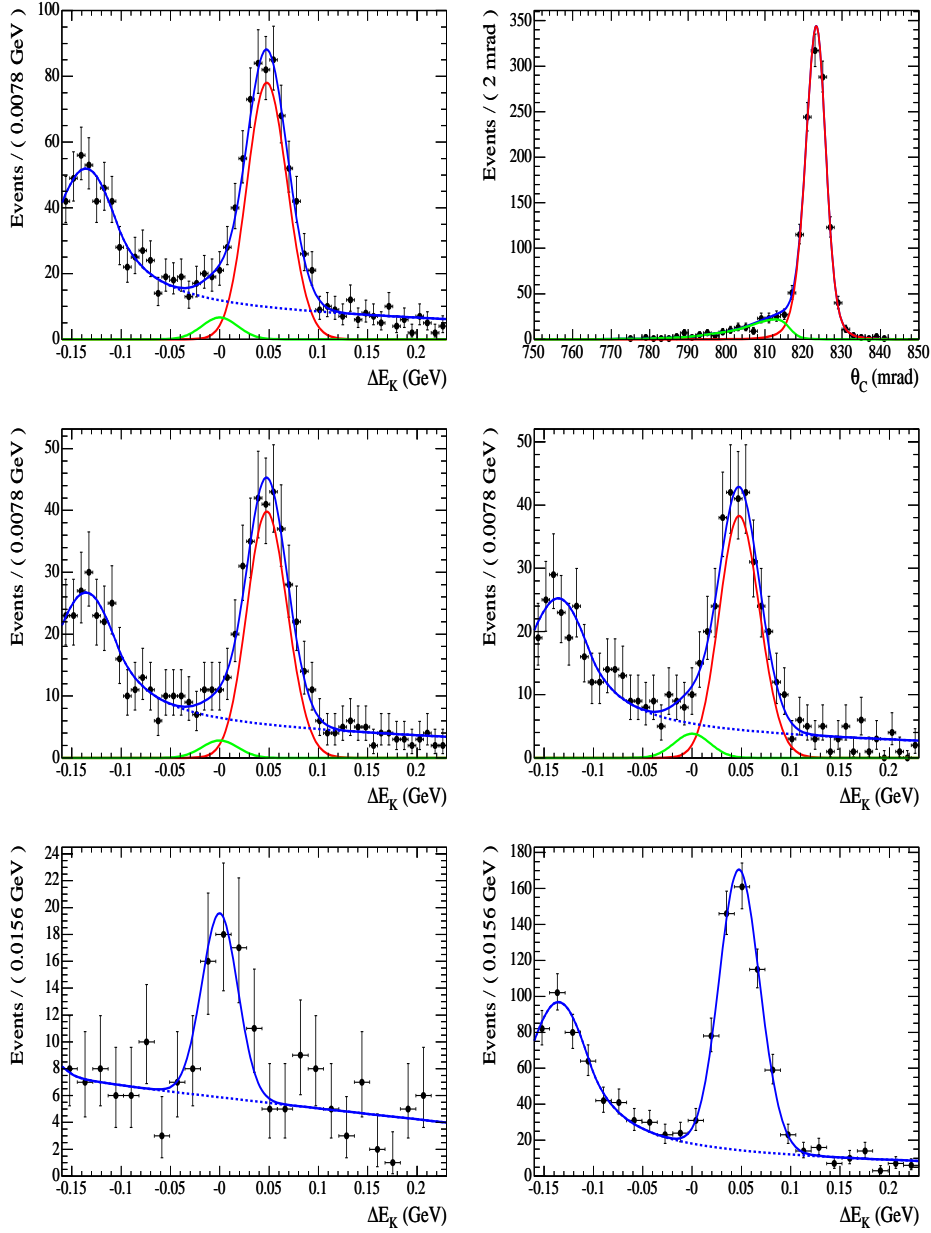


Figure 4.19: Top: ΔE (left) and θ_C (right) distribution of selected $B \rightarrow D^0 h$, $D^0 \rightarrow K_S^0 h$ events in the on-resonance data sample. Middle: ΔE distribution of positive (left) and negative (right) B candidates. Bottom: ΔE distribution of selected events that have been weighted based on the probability, computed according to the θ_C measured value and its PDF, of $h = K$ (left) or $h = \pi$ (right). In the first four plots, the blue solid line represents the projection of the likelihood in the plotted variable. In the top-left and the two central plots the red solid line, the green solid line and the blue dashed line represent the ΔE projection of the $B \rightarrow D^0 \pi$, $B \rightarrow D^0 K$ and background components of the likelihood. In the top-right plot, the red and the green lines represent the θ_C projection of the “pion” ($B \rightarrow D^0 \pi$, $q\bar{q}(\pi)$ and $B\bar{B}(\pi)$) and “kaon” ($B \rightarrow D^0 K$, $q\bar{q}(K)$, $B\bar{B}(K)$ and $X_1 X_2 K$) of the likelihood. In the two bottom plots, the solid lines represent the ΔE projections of the kaon component (left) and the pion component (right) of the likelihood, while the dashed lines represent the projections of the background kaon or pion components.

4.8 Fit on background-only data samples

If the fit behaves properly, it must give a number of signal candidates compatible with zero when it is performed on a sample of candidates selected in off-resonance data, or in on-resonance data after vetoing signal events. We have thus performed the nominal $\{\Delta E, \theta_C\}$ fit on each of the six samples of $B \rightarrow D^0 h$ candidates selected in off-resonance data, after all selection criteria described in the previous Chapter have been applied (sample A) and also after having loosened or completely removed some selection criteria in order to increase the statistics of the selected sample (B-E). We have also performed the fit to selected candidates in on-resonance data, limiting ourselves to the region $\Delta E > 0.14$ GeV (sample F) or $m_{ES} < 5.26$ GeV/ c^2 (samples G and H) where no $B \rightarrow D^0 h$ events are expected. In all the eight cases, for each of the six D^0 modes, the $B \rightarrow D^0 \pi$ and $B \rightarrow D^0 K$ fit yields have been found to be consistent with zero. Also the number of $B\bar{B}(\pi)$ and $B\bar{B}(K)$ returned from the fit is consistent with zero. We have then redone the fits after fixing the $B \rightarrow D^0 h$ and $B\bar{B}(h)$ yields to zero, to measure the charge asymmetries of the background and check whether asymmetries significantly different from zero (which would indicate a detector charge bias) are seen. The results of these fits are listed in Table 4.41: no significant charge asymmetry is observed either in the $q\bar{q}(\pi)$ or in the $q\bar{q}(K)$ background.

sample	$K^-\pi^+$		K^+K^-		$\pi^+\pi^-$	
	$A(q\bar{q}(\pi))(\%)$	$A(q\bar{q}(K))(\%)$	$A(q\bar{q}(\pi))(\%)$	$A(q\bar{q}(K))(\%)$	$A(q\bar{q}(\pi))(\%)$	$A(q\bar{q}(K))(\%)$
A	2.8 ± 6.3	-11 ± 15	33 ± 27	-20 ± 34	5 ± 15	9 ± 39
B	2.4 ± 2.1	0.6 ± 4.9	4 ± 8	-14 ± 9	10 ± 5	5 ± 8
C	-2.4 ± 5.0	-20 ± 10	7 ± 10	-18 ± 16	11 ± 7	-2 ± 13
D	1.0 ± 1.6	0.9 ± 3.5	-0.8 ± 3.5	-1.4 ± 4.7	2.8 ± 2.5	-1.1 ± 4.1
E	1.6 ± 4.2	-13 ± 9	-3 ± 10	11 ± 14	-1 ± 5	0 ± 9
F	-0.5 ± 1.2	-3.8 ± 2.5	-0.7 ± 2.4	-1.1 ± 3.6	0.9 ± 1.8	-4.8 ± 3.0
G	-0.8 ± 0.6	-1.0 ± 1.3	-0.9 ± 1.1	-1.5 ± 1.7	-0.3 ± 0.9	0.6 ± 1.4
H	-1.2 ± 0.8	-0.1 ± 1.7	-1.8 ± 2.5	4.1 ± 3.4	0.1 ± 1.8	0.3 ± 2.7

sample	$K_S^0 \pi^0$		$K_S^0 \phi$		$K_S^0 \omega$	
	$A(q\bar{q}(\pi))(\%)$	$A(q\bar{q}(K))(\%)$	$A(q\bar{q}(\pi))(\%)$	$A(q\bar{q}(K))(\%)$	$A(q\bar{q}(\pi))(\%)$	$A(q\bar{q}(K))(\%)$
A	-20 ± 21	-31 ± 20	-33^{+67}_{-51}	60^{+29}_{-47}	0 ± 35	-29 ± 24
B	-1 ± 6	-2 ± 7	-20 ± 14	27 ± 16	-4 ± 9	-3 ± 11
C	-14 ± 16	-28 ± 17	-50 ± 42	43 ± 48	5 ± 17	-18 ± 22
D	5.8 ± 4.4	0 ± 6	-7 ± 10	13 ± 14	-3 ± 6	-2 ± 7
E	-2 ± 5	-5 ± 7	11 ± 39	27 ± 30	-4 ± 11	-5 ± 14
F	0.3 ± 3.1	-0.9 ± 4.4	-7 ± 8	-7 ± 9	-1.2 ± 3.8	-1 ± 5
G	0.5 ± 1.5	-3.8 ± 2.1	4.2 ± 3.6	-9 ± 5	-1.1 ± 1.8	-0.5 ± 2.6
H	0.2 ± 1.9	-3.8 ± 2.7	2 ± 5	-16 ± 7	-3.7 ± 2.9	-0.7 ± 3.7

Table 4.41: Charge asymmetries of the $q\bar{q}(\pi)$ and $q\bar{q}(K)$ backgrounds estimated from a $\{\Delta E, \theta_C\}$ fit to several background samples. The uncertainties are statistical only, as obtained from the errors on the fit yields. The sample that have been considered are the following:

- A = off-res data after final selection.
- B = off-res data, m_{ES} cut removed.
- C = off-res data, $m(D^0)$ cut removed.
- D = off-res data, no m_{ES} and $m(D^0)$ cuts.
- E = off-res data, no event shape cuts.
- F = on-res data, no m_{ES} and $m(D^0)$ cuts, $\Delta E > 0.14$ GeV.
- G = on-res data, $m_{ES} \leq 5.26$ GeV/ c^2 , no $m(D^0)$ cuts.
- H = on-res data, $m_{ES} \leq 5.26$ GeV/ c^2 .

4.9 Systematic errors evaluation

The main sources of systematic uncertainty on the yields and derived quantities (the CP asymmetry and the ratio of the branching fraction) are listed in the following.

4.9.1 Parameterization of the ΔE $B\bar{B}$ and $q\bar{q}$ distribution

The PDFs describing the probability associated to the value of ΔE for the different background contributions depend on a number of parameters. The way these parameters are estimated has been described in section 4.4. All the PDF parameters have been determined through a fit on the ΔE distributions obtained on real data or Monte Carlo samples. Thus each value has its own associated error. Each PDF parameter is increased or decreased by 1σ , while all the others are kept fixed at their central value. The resulting change of each fit parameter is considered as the associated systematic error. In the evaluation of the total systematic error the single contributions are considered uncorrelated, and the square of the total error is computed as the sum of the squares of the single contributions.

4.9.2 Parameterization of PDF(θ_C)

The parameterization of the particle-identification PDF is performed by fitting with a double-Gaussian function the background-subtracted distribution of the corrected pull θ_C^{pull} . Therefore, the significant parameters for the θ_C PDFs are the two sets of five parameters listed in Table 4.2. The systematic error associated with the particle-identification PDF is estimated by varying by $\pm 1\sigma$ the double-Gaussian parameters of the kaon and pion θ_C distributions and taking the sum in quadrature of the resulting shifts in $A_{CP\pm}$ and R_{\pm} as the systematic errors.

4.9.3 Evaluation of the peaking backgrounds

The uncertainties on the number of peaking background events ($B \rightarrow X_1 X_2 K$) estimated from the D^0 mass sidebands are listed in Table 4.1 and take into account possible statistical fluctuations of the $B \rightarrow X_1 X_2 K$ yield. These fluctuations introduce a systematic uncertainty on the $B \rightarrow D_{CP\pm}^0 K$ yield and therefore on R_{\pm} : therefore we perform the fit after floating the $B \rightarrow X_1 X_2 K$ yield by its uncertainty and take the shift in R_{\pm} as the associated systematic uncertainty. The uncertainties on the asymmetries are evaluated from the observed shifts in $A_{CP\pm}$ when the fits to the B^+ and B^- samples are redone after allowing independent Poisson fluctuations of the $B^+ \rightarrow X_1 X_2 K^+$ and $B^- \rightarrow X_1 X_2 K^-$ candidates, and also allowing a 20% CP asymmetry for the peaking backgrounds. Finally, we take into account the uncertainty on the ΔE shape of the peaking background by adding in quadrature to the systematic uncertainty on R_{\pm} and $A_{CP\pm}$ the shift that is obtained after repeating the fit with the parameters of the ΔE distribution of the peaking background varied by $\pm 1\sigma$.

4.9.4 Detector charge asymmetry

A source of bias that must be investigated arises from a potential charge asymmetry of the $BABAR$ detector, due to a possible charge bias in tracking efficiency (e.g., K^+ vs K^-) and/or particle identification. In order to understand if this effect can bring a significant bias to the asymmetry measurement a number of control samples, from both Monte Carlo and real data, are studied. When we say “significant bias” we must keep in mind that the statistical uncertainty on the $B \rightarrow D^0 K$, $D^0 \rightarrow K^+ K^-$ asymmetry is of the order of 15%.

The charge asymmetry has been measured on data for the processes $B \rightarrow D^0\pi$ [$D^0 \rightarrow K^-\pi^+$], $B \rightarrow D^0K$ [$D^0 \rightarrow K^-\pi^+$], $B \rightarrow D^0\pi$ [$D^0 \rightarrow K^+K^-$], $B \rightarrow D^0\pi$ [$D^0 \rightarrow \pi^+\pi^-$], $B \rightarrow D^0\pi$ [$D^0 \rightarrow K_s^0\pi^0$], $B \rightarrow D^0\pi$ [$D^0 \rightarrow K_s^0\phi$], $B \rightarrow D^0\pi$ [$D^0 \rightarrow K_s^0\omega$], where the CP asymmetry is expected to be negligible; the same check has been performed on Monte Carlo for the same control samples and for the signal $B \rightarrow D^0K$ [$D^0 \rightarrow K^-\pi^+$]. The results of the measured charge asymmetries are reported in table 4.42; all the results show that there is no evidence of a charge asymmetry of the *BABAR* detector. The average asymmetry found in Monte Carlo is $-(0.4 \pm 0.3)\%$, while in data control samples it is $(-1.8 \pm 0.9)\%$. Hence no corrections are applied to the measured CP asymmetries: we just add (in quadrature) an extra contribution $(1.8 + 0.9)\% = 2.7\%$ to the systematic error on them.

decay mode	A_{CP} (%)
$B \rightarrow D^0\pi, D^0 \rightarrow K^+K^-$ signal MC	$+0.7 \pm 0.8$
$B \rightarrow D^0\pi, D^0 \rightarrow \pi^+\pi^-$ signal MC	$+1.1 \pm 0.8$
$B \rightarrow D^0\pi, D^0 \rightarrow K_s^0\pi^0$ signal MC	-1.5 ± 1.0
$B \rightarrow D^0\pi, D^0 \rightarrow K_s^0\phi$ signal MC	$+0.7 \pm 0.9$
$B \rightarrow D^0\pi, D^0 \rightarrow K_s^0\omega$ signal MC	-2.0 ± 1.6
$B \rightarrow D^0\pi, D^0 \rightarrow K^-\pi^+$ signal MC	-1.0 ± 0.7
$B \rightarrow D^0K, D^0 \rightarrow K^-\pi^+$ signal MC	-1.3 ± 0.7
$B \rightarrow D^0\pi, D^0 \rightarrow K^+K^-$ DATA	-1.1 ± 2.8
$B \rightarrow D^0\pi, D^0 \rightarrow \pi^+\pi^-$ DATA	-7.8 ± 5.2
$B \rightarrow D^0\pi, D^0 \rightarrow K_s^0\pi^0$ DATA	-2.2 ± 3.0
$B \rightarrow D^0\pi, D^0 \rightarrow K_s^0\phi$ DATA	-5.7 ± 5.7
$B \rightarrow D^0\pi, D^0 \rightarrow K_s^0\omega$ DATA	-1.1 ± 5.2
$B \rightarrow D^0\pi, D^0 \rightarrow K^-\pi^+$ DATA	-1.6 ± 0.8
$B \rightarrow D^0K, D^0 \rightarrow K^-\pi^+$ DATA	-3.0 ± 3.2

Table 4.42: Charge asymmetries measured on signal Monte Carlo or data for different B decays.

4.9.5 S-wave Pollution in $B \rightarrow D^0K, D^0 \rightarrow K_s^0\phi$ and $B \rightarrow D^0K, D^0 \rightarrow K_s^0\omega$

The measured CP asymmetry in $B \rightarrow D^0K, D^0 \rightarrow K_s^0\phi$ can be diluted by the presence, in the selected sample, of $B \rightarrow D^0K$ decays with D^0 decaying to the same final state $K_s^0K^+K^-$ as $K_s^0\phi, \phi \rightarrow K^+K^-$ but with opposite CP content. The same can happen in the $B \rightarrow D^0K, D^0 \rightarrow K_s^0\omega$ analysis with backgrounds from $B \rightarrow D^0K, D^0 \rightarrow K_s^0\pi^+\pi^-\pi^0$. Moreover, as will be shown later, also the measured ratio R_- is, to a small extent, affected by the presence of this peculiar background. The Dalitz plot for the $D^0 \rightarrow K_s^0K^+K^-$ decay has been studied in detail in *BABAR* in D^0 produced in $D^{*+} \rightarrow D^0\pi^+$ decays [87] and from these it is found that the $D^0 \rightarrow K_s^0K^+K^-$ amplitude can be described as the sum of only two amplitudes, $D^0 \rightarrow K_s^0\phi$ ($CP = -1$) and $D^0 \rightarrow K_s^0a_0$ ($CP = +1$, since the a_0 is scalar). On the other hand, the full amplitude of $D^0 \rightarrow K_s^0\pi^+\pi^-\pi^0$ is not known yet, although it could be measured either in *BABAR* or in charm factories like *CLEO-c*.

Let us see how the presence of the CP -even $D^0 \rightarrow K_s^0a_0$ affects the CP -asymmetry and the branching fraction ratio measured in the $K_s^0\phi$ channel. Neglecting CP violation in the D^0 system, the $K_s^0\phi$ final state is accessible only to $D_2 \equiv \frac{D^0 - \bar{D}^0}{\sqrt{2}}$, while $K_s^0a_0$ is accessible only to $D_1 \equiv \frac{D^0 + \bar{D}^0}{\sqrt{2}}$. The $B^- \rightarrow K_s^0K^+K^-\pi^-$ amplitude is therefore:

$$A_{\pi^-} \equiv A(B^- \rightarrow K_s^0K^+K^-\pi^-)$$

$$\begin{aligned}
&= A(B^- \rightarrow D^0 \pi^-) \times A(D^0 \rightarrow K_s^0 K^+ K^-) \\
&= A(B^- \rightarrow D^0 \pi^-) \times \frac{A(D_1 \rightarrow K_s^0 a_0) + A(D_2 \rightarrow K_s^0 \phi)}{\sqrt{2}} \quad (4.37)
\end{aligned}$$

Here we have neglected the term $A(B^- \rightarrow \bar{D}^0 \pi^-) \times A(\bar{D}^0 \rightarrow K_s^0 K^+ K^-)$ since it is suppressed by a factor $r_B \lambda^2 \approx 0.5 - 1\%$ with respect to the term $A(B^- \rightarrow D^0 \pi^-) \times A(D^0 \rightarrow K_s^0 K^+ K^-)$. Since the a_0 is scalar and the ϕ is a vector, the amplitudes for the D decays, in terms of the helicity angle θ_H of the two kaons,² can be written: [88]

$$A(D_1 \rightarrow a_0 K_s^0) = A_1 \quad (4.38)$$

$$A(D_2 \rightarrow \phi K_s^0) = A_2 \sqrt{3} \cos \theta_H \quad (4.39)$$

Therefore:

$$\begin{aligned}
A_\pi^- &= A(B^- \rightarrow D^0 \pi^-) \times \frac{A_1 + A_2 \sqrt{3} \cos \theta_H}{\sqrt{2}} \\
&= \frac{A_\pi A_2}{\sqrt{2}} \times [z + \sqrt{3} \cos \theta_H] \quad (4.40)
\end{aligned}$$

where

$$z \equiv \frac{A_1}{A_2} \quad (4.41)$$

is a complex number and

$$A_\pi \equiv A(B^- \rightarrow D^0 \pi^-) \quad (4.42)$$

Similarly, the $B^+ \rightarrow K_s^0 K^+ K^- \pi^+$ amplitude is:

$$\begin{aligned}
A_\pi^+ &\equiv A(B^+ \rightarrow K_s^0 K^+ K^- \pi^+) \\
&= A(B^+ \rightarrow \bar{D}^0 \pi^+) \times A(\bar{D}^0 \rightarrow K_s^0 K^+ K^-) \\
&= A(B^+ \rightarrow \bar{D}^0 \pi^+) \times \frac{A(D_1 \rightarrow K_s^0 a_0) - A(D_2 \rightarrow K_s^0 \phi)}{\sqrt{2}} \\
&= \frac{A_\pi A_2}{\sqrt{2}} \times [z - \sqrt{3} \cos \theta_H] \quad (4.43)
\end{aligned}$$

with the phase convention such that $A(B^+ \rightarrow \bar{D}^0 \pi^+) = A(B^- \rightarrow D^0 \pi^-)$.

Now let us turn to the $B^\pm \rightarrow K_s^0 K^+ K^- K^\pm$ amplitudes. Here we take into account also the terms that we have neglected in the $B \rightarrow D\pi$ case, since suppression is much weaker:

$$\begin{aligned}
A_K^- &\equiv A(B^- \rightarrow K_s^0 K^+ K^- K^-) \\
&= A(B^- \rightarrow D^0 K^-) \times A(D^0 \rightarrow K_s^0 K^+ K^-) + \\
&\quad A(B^- \rightarrow \bar{D}^0 K^-) \times A(\bar{D}^0 \rightarrow K_s^0 K^+ K^-) \\
&= A(B^- \rightarrow D^0 K^-) \times \left[\frac{A(D_1 \rightarrow K_s^0 a_0) + A(D_2 \rightarrow K_s^0 \phi)}{\sqrt{2}} + \right. \\
&\quad \left. r_B e^{i(\delta_B - \gamma)} \frac{A(D_1 \rightarrow K_s^0 a_0) - A(D_2 \rightarrow K_s^0 \phi)}{\sqrt{2}} \right] \\
&= \frac{A_K A_2}{\sqrt{2}} \times [z(1 + r_B e^{i(\delta_B - \gamma)}) + \sqrt{3} \cos \theta_H (1 - r_B e^{i(\delta_B - \gamma)})] \quad (4.44)
\end{aligned}$$

²In Chapter 3 this angle was denoted with $\theta_{\text{hel}}(\phi)$

where have used:

$$\frac{A(B^- \rightarrow \bar{D}^0 K^-)}{A(B^- \rightarrow D^0 K^-)} = r_B e^{i(\delta_B - \gamma)} \quad (4.45)$$

For the B^+ amplitude we must take into account that

$$\frac{A(B^+ \rightarrow D^0 K^+)}{A(B^+ \rightarrow \bar{D}^0 K^+)} = r_B e^{i(\delta_B + \gamma)} \quad (4.46)$$

and find, with the phase choice such that $A(B^+ \rightarrow \bar{D}^0 K^+) = A(B^- \rightarrow D^0 K^-) = A_K$,

$$\begin{aligned} A_K^+ &\equiv A(B^+ \rightarrow K_s^0 K^+ K^- K^+) \\ &= A(B^+ \rightarrow \bar{D}^0 K^+) \times A(\bar{D}^0 \rightarrow K_s^0 K^+ K^-) + \\ &\quad A(B^+ \rightarrow D^0 K^+) \times A(D^0 \rightarrow K_s^0 K^+ K^-) \\ &= A(B^+ \rightarrow \bar{D}^0 K^+) \times \left[\frac{A(D_1 \rightarrow K_s^0 a_0) - A(D_2 \rightarrow K_s^0 \phi)}{\sqrt{2}} + \right. \\ &\quad \left. r_B e^{i(\delta_B + \gamma)} \frac{A(D_1 \rightarrow K_s^0 a_0) + A(D_2 \rightarrow K_s^0 \phi)}{\sqrt{2}} \right] \\ &= \frac{A_K A_2}{\sqrt{2}} \times [z(1 + r_B e^{i(\delta_B + \gamma)}) - \sqrt{3} \cos \theta_H (1 - r_B e^{i(\delta_B + \gamma)})] \end{aligned} \quad (4.47)$$

We then compute $|A|^2 = AA^*$:

$$|A_\pi^-|^2 = \frac{|A_\pi A_2|^2}{2} [|z|^2 + 3 \cos^2 \theta_H + 2\sqrt{3} \cos \theta_H \Re z] \quad (4.48)$$

$$|A_\pi^+|^2 = \frac{|A_\pi A_2|^2}{2} [|z|^2 + 3 \cos^2 \theta_H - 2\sqrt{3} \cos \theta_H \Re z] \quad (4.49)$$

$$\begin{aligned} |A_K^-|^2 &= \frac{|A_K A_2|^2}{2} \left[(1 + r_B^2 + 2r_B \cos(\delta_B - \gamma)) |z|^2 + \right. \\ &\quad (1 + r_B^2 - 2r_B \cos(\delta_B - \gamma)) 3 \cos^2 \theta_H + \\ &\quad \left. ((1 - r_B^2) \Re z - 2r_B \sin(\delta_B - \gamma) \Im z) 2\sqrt{3} \cos \theta_H \right] \end{aligned} \quad (4.50)$$

$$\begin{aligned} |A_K^+|^2 &= \frac{|A_K A_2|^2}{2} \left[(1 + r_B^2 + 2r_B \cos(\delta_B + \gamma)) |z|^2 + \right. \\ &\quad (1 + r_B^2 - 2r_B \cos(\delta_B + \gamma)) 3 \cos^2 \theta_H - \\ &\quad \left. ((1 - r_B^2) \Re z - 2r_B \sin(\delta_B + \gamma) \Im z) 2\sqrt{3} \cos \theta_H \right] \end{aligned} \quad (4.51)$$

Therefore:

$$|A_\pi^-|^2 + |A_\pi^+|^2 = |A_\pi A_2|^2 \times [|z|^2 + 3 \cos^2 \theta_H] \quad (4.52)$$

$$|A_\pi^-|^2 - |A_\pi^+|^2 = |A_\pi A_2|^2 \times 2\sqrt{3} \Re z \cos \theta_H \quad (4.53)$$

$$\begin{aligned} |A_K^-|^2 + |A_K^+|^2 &= |A_K A_2|^2 [(1 + r_B^2 + 2r_B \cos \delta_B \cos \gamma) |z|^2 + \\ &\quad (1 + r_B^2 - 2r_B \cos \delta_B \cos \gamma) 3 \cos^2 \theta_H + \\ &\quad - 4r_B \cos \delta_B \sin \gamma \Im z \sqrt{3} \cos \theta_H] \end{aligned} \quad (4.54)$$

$$\begin{aligned} |A_K^-|^2 - |A_K^+|^2 &= |A_K A_2|^2 [r_B \sin \delta_B \sin \gamma (|z|^2 - 3 \cos^2 \theta_H) + \\ &\quad ((1 - r_B^2) \Re z - 2r_B \sin \delta_B \cos \gamma \Im z) \sqrt{3} \cos \theta_H] \end{aligned} \quad (4.55)$$

If we integrate the above expressions in $\cos \theta_H$ over a symmetric $\cos \theta_H$ range, $[\pm \Delta, \pm 1]$ (in this analysis $\Delta = 0.4$), the linear terms in $\cos \theta_H$, which are also linear in z , cancel. The observed CP asymmetry in the DK channel is therefore:

$$\begin{aligned}
A_{CP-}^{\text{obs}}(DK) &= \frac{\int [|A_K^-|^2 - |A_K^+|^2] d(\cos \theta_H)}{\int [|A_K^-|^2 + |A_K^+|^2] d(\cos \theta_H)} \\
&= -\frac{2r_B \sin \delta_B \sin \gamma (A - B|z|^2)}{A(1 + r_B^2 - 2r_B \cos \delta_B \cos \gamma) + B|z|^2(1 + r_B^2 + 2r_B \cos \delta_B \cos \gamma)} \\
&= -\frac{2r_B \sin \delta_B \sin \gamma}{1 + r_B^2 - 2r_B \cos \delta_B \cos \gamma} \frac{1 - B/A |z|^2}{1 + B/A |z|^2 \frac{1+r_B^2+2r_B \cos \delta_B \cos \gamma}{1+r_B^2-2r_B \cos \delta_B \cos \gamma}} \\
&= A_{CP-} \frac{1 - B/A |z|^2}{1 + B/A |z|^2 \frac{R_{CP+}}{R_{CP-}}} \tag{4.56}
\end{aligned}$$

where

$$A \equiv \int_{\Delta}^1 3 \cos^2 \theta_H d \cos \theta_H = 1 - \Delta^3 \tag{4.57}$$

$$B \equiv \int_{\Delta}^1 d \cos \theta_H = 1 - \Delta \tag{4.58}$$

If $\Delta = 0.4$ then $B/A = 0.64$ and

$$A_{CP-}^{\text{obs}} = A_{CP-} \frac{1 - 0.64|z|^2}{1 + 0.64|z|^2 \frac{R_{CP+}}{R_{CP-}}} \tag{4.59}$$

For the branching fraction ratio we have:

$$\begin{aligned}
N(D^0 \pi) \propto \int |A_{\pi^-}|^2 + |A_{\pi^+}|^2 &= |A_{\pi} A_2|^2 \int [|z|^2 + 3 \cos^2 \theta_H] d \cos \theta_H \\
&= |A_{\pi} A_2|^2 \times \left(1 + \frac{\int |z|^2 d \cos \theta_H}{\int 3 \cos^2 \theta_H d \cos \theta_H} \right) \\
&= |A_{\pi} A_2|^2 (1 + B/A |z|^2) \tag{4.60}
\end{aligned}$$

and

$$\begin{aligned}
N(D^0 K) \propto \int |A_K^-|^2 + |A_K^+|^2 &= |A_K A_2|^2 \int [(1 + r_B^2 + 2r_B \cos \delta_B \cos \gamma) |z|^2 + \\
&\quad (1 + r_B^2 - 2r_B \cos \delta_B \cos \gamma) 3 \cos^2 \theta_H] d \cos \theta_H \\
&= |A_K A_2|^2 (1 + r_B^2 - 2r_B \cos \delta_B \cos \gamma) \times \\
&\quad \left(1 + \frac{1 + r_B^2 + 2r_B \cos \delta_B \cos \gamma}{1 + r_B^2 - 2r_B \cos \delta_B \cos \gamma} \frac{\int |z|^2 d \cos \theta_H}{\int 3 \cos^2 \theta_H d \cos \theta_H} \right) \\
&= |A_K A_2|^2 (1 + r_B^2 - 2r_B \cos \delta_B \cos \gamma) \times \\
&\quad \left(1 + B/A |z|^2 \frac{R_{CP+}}{R_{CP-}} \right) \tag{4.61}
\end{aligned}$$

Therefore the observed branching fraction ratio is

$$\begin{aligned}
R_-^{\text{obs}} = \frac{N(D^0 K)}{N(D^0 \pi)} &= (1 + r_B^2 - 2r_B \cos \delta_B \cos \gamma) \times \frac{1 + B/A |z|^2 \frac{R_{CP+}}{R_{CP-}}}{1 + B/A |z|^2} \\
&= R_{CP-} \times \frac{1 + B/A |z|^2 \frac{R_{CP+}}{R_{CP-}}}{1 + B/A |z|^2} \tag{4.62}
\end{aligned}$$

In the case $\Delta = 0.4$, $B/A = 0.64$:

$$R_-^{\text{obs}} = R_{CP-} \times \frac{1 + 0.64|z|^2 \frac{R_{CP+}}{R_{CP-}}}{1 + 0.64|z|^2} \quad (4.63)$$

We can thus correct, with the expressions (4.59) and (4.63), the CP -asymmetry A_{CP-} and the double branching fraction ratio R_- in the $K_s^0\phi$ channel and determine the true values, which are related to γ , r_B and δ_B through the standard GLW relations (Introduction, Eqs. (3) and (4)). To this extent we use the value of R_+ measured with the CP -even modes K^+K^- and $\pi^+\pi^-$ (0.90 ± 0.12) and the value of R_- measured with the CP -odd mode $K_s^0\pi^0$ (0.76 ± 0.13), which are not affected by this dilution effect. $|z|^2$ has been estimated by one of the *BABAR* collaborators working on the $D^0 \rightarrow K_s^0 K^+ K^-$ Dalitz analysis to be $(25 \pm 1)\%$ [89]: this is consistent with the value that we find ($33 \pm 9\%$) by studying the distribution of the number of $D^0\pi$ candidates as a function of $\cos\theta_H$. $B \rightarrow D^0\pi$ candidates selected in our sample are in fact expected to follow a $|z|^2 + 3\cos^2\theta_H$ distribution (Eq. (4.52)), from which $|z|^2$ can be extracted. To this purpose we select in data a pure sample of $B \rightarrow D^0\pi$, $D^0 \rightarrow K_s^0\phi$ decays by applying all the standard criteria described in the previous Chapter (but the $\cos\theta_{\text{hel}}(\phi)$ one), plus a 2.5σ cut on ΔE_π around zero and the request that the prompt track h fails the KaonLHVeryTight selector, and plot their $\cos\theta_H$ distribution after having subtracted the expected $\cos\theta_H$ distribution of continuum and $B\bar{B}$ (non-peaking) backgrounds obtained from Monte Carlo. The distribution is then fit with a $|z|^2 + 3\cos^2\theta_H$ PDF, and $|z|^2 = 0.33 \pm 0.09$ is found, as shown in Figure 4.20. We have checked on simulated signal $B \rightarrow D^0\pi$, $D^0 \rightarrow K_s^0\phi$ events that the acceptance

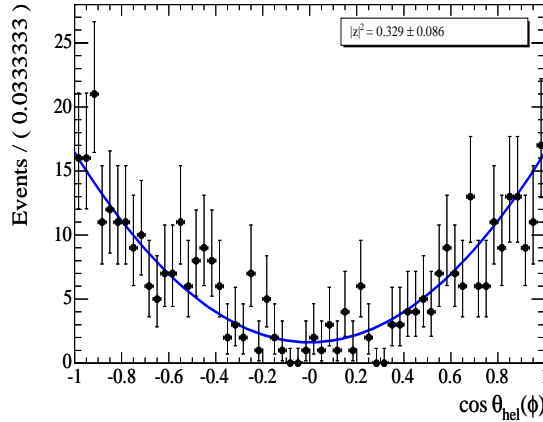


Figure 4.20: $\cos\theta_H$ distribution of $B \rightarrow D^0\pi$, $D^0 \rightarrow K_s^0\phi$ candidates selected in data. Background expected from $q\bar{q}$ and $B\bar{B}$ (non peaking) simulated events has been subtracted.

is uniform as a function of $\cos\theta_H$ and therefore the $\cos\theta_H$ distribution is parabolic by fitting it with a $|z|^2 + 3\cos^2\theta_H$ PDF: in that case we find indeed $|z|^2 = 0.0032 \pm 0.0029$, which is consistent with zero.

We therefore have, for the $K_s^0\phi$ channel:

$$\begin{aligned} A_{CP-}^{\text{obs}} &= A_{CP-}^{\text{true}} \times \frac{1 - 0.64 \times (0.25 \pm 0.01)}{1 + 0.64 \times (0.25 \pm 0.01) \times \frac{0.90 \pm 0.12}{0.76 \pm 0.13}} \\ &= A_{CP-}^{\text{true}} \times (0.71 \pm 0.03) \end{aligned} \quad (4.64)$$

$$\begin{aligned}
R_-^{\text{obs}} &= R_-^{\text{true}} \times \frac{1 + 0.64 \times (0.25 \pm 0.01) \times \frac{0.90 \pm 0.12}{0.76 \pm 0.13}}{1 + 0.64 \times (0.25 \pm 0.01)} \\
&= R_-^{\text{true}} \times (1.03 \pm 0.04)
\end{aligned} \tag{4.65}$$

For the $K_s^0 \omega$ channel the situation, unfortunately, is complicated by the fact that the full structure of the $D^0 \rightarrow K_s^0 \pi^+ \pi^- \pi^0$ decay amplitude is not known at present. We therefore proceed in the following way. In the worst scenario, the $B \rightarrow D^0 h$, $D^0 \rightarrow K_s^0 \pi^+ \pi^- \pi^0$ background has $CP = +1$ and the asymmetry is maximally diluted, by

$$A_{CP}^{\text{obs}} = A_{CP}^{\text{true}}(D^0 K) \frac{1 - f|z|^2}{1 + f|z|^2 \frac{R_+}{R_-}} \tag{4.66}$$

where $f = 0.55/0.95 = 0.58$ is the ratio of $D^0 \rightarrow K_s^0 \pi^+ \pi^- \pi^0$ and $D^0 \rightarrow K_s^0 \omega$ efficiencies of the selection criterion $\cos^2 \theta_N \sin^2 \theta_{\pi\pi} > 0.08$ applied to our final sample (see Subsection 3.4.4). $|z|^2$ can be extracted from a $|z|^2 + 3 \cos^2 \theta_N$ fit to the dipion helicity angle ($\cos \theta_N$) distribution of the ω candidate in the $B \rightarrow D^0 \pi$, $D^0 \rightarrow K_s^0 \omega$ control sample, selected with the standard selection criteria (but the $\cos^2 \theta_N \sin^2 \theta_{\pi\pi}$ one) of the previous Chapter, plus a 2.5σ cut on ΔE_π around zero and the request that the prompt track h fails the KaonLHVeryTight selector. As shown in Figure 4.21, we find $|z|^2 = 42 \pm 8\%$, and the corresponding asymmetry dilution would be:

$$\begin{aligned}
A_{CP-}^{\text{obs}} &= A_{CP-}^{\text{true}} \times \frac{1 - 0.58 \times (0.42 \pm 0.08)}{1 + 0.58 \times (0.42 \pm 0.08) \times \frac{0.90 \pm 0.12}{0.76 \pm 0.13}} \\
&= A_{CP-}^{\text{true}} \times (0.59 \pm 0.05)
\end{aligned}$$

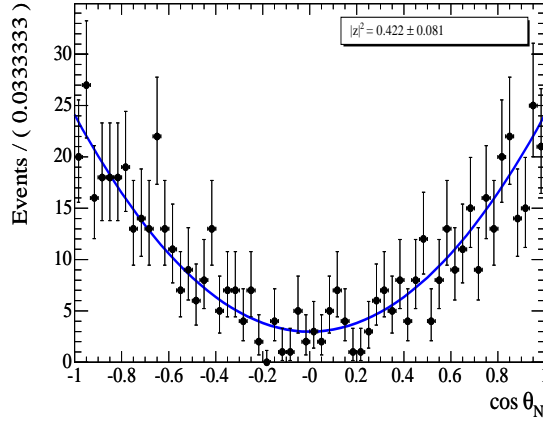


Figure 4.21: $\cos \theta_N$ distribution of $B \rightarrow D^0 \pi$, $D^0 \rightarrow K_s^0 \omega$ candidates selected in data. Background expected from $q\bar{q}$ and $B\bar{B}$ (non peaking) simulated events has been subtracted.

However, the $D^0 \rightarrow K_s^0 \pi^+ \pi^- \pi^0$ decay can have mixed CP content due to the presence of intermediate K^* or ρ resonances. Therefore the dilution will be somewhere in between 0.59 ± 0.05 and 1: we assume here the average value 0.8 and assign to it an uncertainty ± 0.2 , therefore in the $K_s^0 \omega$ channel:

$$A_{CP-}^{\text{obs}} = A_{CP-}^{\text{true}} \times (0.8 \pm 0.2) \tag{4.67}$$

For the ratio R_- , in presence of a pure $CP = +1$ $D^0 \rightarrow K_s^0 \pi^+ \pi^- \pi^0$ background we would have $R_-^{\text{obs}} = R_-^{\text{true}} \times (1.03 \pm 0.08)$: here we assume therefore

$$R_{CP-}^{\text{obs}} = R_{CP-}^{\text{true}} \times (1.02 \pm 0.09) \quad (4.68)$$

As for the $K_s^0 \phi$ channel, also in this case uniformity of acceptance as a function of $\cos \theta_N$ has been evaluated by fitting the $\cos \theta_N$ distribution of signal $B \rightarrow D^0 \pi$, $D^0 \rightarrow K_s^0 \omega$ with a $|z|^2 + 3 \cos^2 \theta_N$ PDF: in this case we find $|z|^2 = 0.0000 \pm 0.0018$, consistent with a pure parabolic distribution which would be obtained if the acceptance were uniform in $\cos \theta_N$.

For both the $K_s^0 \phi$ and $K_s^0 \omega$ channels, the central value and the statistical errors of the CP -asymmetries and the branching fraction ratios are scaled by the mean values of the correction factors computed in this Section: the uncertainties on the correction factors are taken into account in the systematic errors.

4.10 Measurement of the direct CP asymmetry

One of the main goals of this analysis is to perform a measurement of the direct CP asymmetry

$$A_{CP\pm} \stackrel{\text{def}}{=} \frac{\mathcal{B}(B^- \rightarrow D_{CP\pm}^0 K^-) - \mathcal{B}(B^+ \rightarrow D_{CP\pm}^0 K^+)}{\mathcal{B}(B^- \rightarrow D_{CP\pm}^0 K^-) + \mathcal{B}(B^+ \rightarrow D_{CP\pm}^0 K^+)}. \quad (4.69)$$

The measurement of the CP asymmetry is performed by using the measured yields of positive and negative $B \rightarrow D^0 K$ decays in the CP -eigenstates $K^+ K^-$, $\pi^+ \pi^-$, $K_s^0 \pi^0$, $K_s^0 \phi$ and $K_s^0 \omega$ that are listed in Tables 4.31, 4.33, 4.35, 4.37 and 4.39. The asymmetries in the $K_s^0 \phi$ and $K_s^0 \omega$ are corrected according to (4.64) and (4.67), respectively.

The systematic errors associated to this measurement arise from the uncertainties in the parameterization of the signal and background ΔE shape and from the evaluation of the particle ID probability. An important contribution is given by the intrinsic charge asymmetry of the detector. One must also take into account possible charge asymmetries in the peaking background that is being subtracted to determine the signal yield. The main systematic uncertainties (in %) on the measurement of the CP asymmetry are reported in Tables 4.43 and 4.44. The details on how such uncertainties are evaluated have been described in Section 4.9.

The resulting asymmetries are

$$A_{CP+}(K^+ K^-) = +0.46 \pm 0.15(\text{stat}) \pm 0.05(\text{syst}) \quad (4.70)$$

$$A_{CP+}(\pi^+ \pi^-) = -0.03 \pm 0.28(\text{stat}) \pm 0.03(\text{syst}) \quad (4.71)$$

$$A_{CP-}(K_s^0 \pi^0) = +0.04 \pm 0.16(\text{stat}) \pm 0.04(\text{syst}) \quad (4.72)$$

$$A_{CP-}(K_s^0 \phi) = -0.10 \pm 0.32(\text{stat}) \pm 0.03(\text{syst}) \quad (4.73)$$

$$A_{CP-}(K_s^0 \omega) = -0.35 \pm 0.30(\text{stat}) \pm 0.08(\text{syst}) \quad (4.74)$$

The combination of the two CP -even measurements gives:

$$A_{CP+} = 0.35 \pm 0.13(\text{stat}) \pm 0.04(\text{syst}) \quad (4.75)$$

The χ^2/ndf is 2.3/1, the corresponding probability is 13%.

The combination of the three CP -odd measurements gives:

$$A_{CP-} = -0.06 \pm 0.13(\text{stat}) \pm 0.04(\text{syst}) \quad (4.76)$$

The χ^2/ndf is 1.2/2, the corresponding probability is 55%.

The systematic error of the combined asymmetry has been evaluated by assuming all the systematic uncertainties on the various asymmetries uncorrelated, with the exception of the contributions due to the detector charge asymmetry and to the Cherenkov angle PDFs, which are 100% correlated between the different channels.

Parameter	Syst. Error on A_{CP+} (%)	
	$D^0 \rightarrow K^+K^-$	$D^0 \rightarrow \pi^+\pi^-$
$q\bar{q}$ bkg ΔE	± 1.3	± 0.6
$B\bar{B}(\pi)$ bkg ΔE	± 0.1	± 0.3
$B\bar{B}(K)$ bkg ΔE	± 0.2	± 0.9
PID	± 0.1	± 0.1
peaking X_1X_2K bkg	± 3.3	± 1.8
Total	± 3.6	± 2.1
Detector charge asymmetry	± 2.7	± 2.7

Table 4.43: Systematic errors on the CP asymmetry of the $B \rightarrow D^0K$, $D^0 \rightarrow K^+K^-$ and $D^0 \rightarrow \pi^+\pi^-$ modes.

Parameter	Syst. Error on A_{CP-} (%)		
	$D^0 \rightarrow K_s^0\pi^0$	$D^0 \rightarrow K_s^0\phi$	$D^0 \rightarrow K_s^0\omega$
$q\bar{q}$ bkg ΔE	± 0.3	± 0.9	± 0.9
$B\bar{B}(\pi)$ bkg ΔE	± 0.1	± 0.2	± 0.2
$B\bar{B}(K)$ bkg ΔE	± 0.4	± 0.2	± 1.0
PID	± 0.2	± 0.1	± 0.3
peaking X_1X_2K bkg	± 3.4	± 0.1	± 2.3
peaking $B \rightarrow D^0K$ bkg	-	± 0.3	± 8.8
Total	± 3.4	± 1.0	± 9.2
Detector charge asymmetry	± 2.7	± 2.7	± 2.7

Table 4.44: Systematic errors on the CP asymmetry of the $B \rightarrow D^0K$, $D^0 \rightarrow K_s^0\pi^0$, $D^0 \rightarrow K_s^0\phi$ and $D^0 \rightarrow K_s^0\omega$ modes.

4.11 Measurement of the ratio R_{\pm}

The double branching fraction ratio

$$R_{\pm} \equiv \frac{\frac{\mathcal{B}(B \rightarrow D_{CP}^0 K)}{\mathcal{B}(B \rightarrow D_{CP}^0 \pi)}}{\frac{\mathcal{B}(B \rightarrow D^0 K)}{\mathcal{B}(B \rightarrow D^0 \pi)}} \quad (4.77)$$

is separately calculated for the five CP D^0 decay channels. The double ratio is computed with the number of $B \rightarrow D_{(CP)}^0 K$ and $B \rightarrow D_{(CP)}^0 \pi$ mesons estimated with the maximum likelihood fit listed in Tables 4.29, 4.31, 4.33, 4.35, 4.37 and 4.39. The resulting double ratios are scaled by a correction factor taking into account small differences in the selection efficiency between $B \rightarrow D^0 K$ and $B \rightarrow D^0 \pi$ in the D_{CP}^0 and in the $K^-\pi^+$ modes. Such correction factors are estimated from the efficiencies evaluated with signal Monte Carlo samples, and are listed in Table 4.45. In these correction factors, which are efficiency double ratios, all systematic uncertainties arising from possible data-Monte Carlo discrepancies of from unknown D^0 branching fractions cancel, and only two contributions survive:

- the uncertainty on selection efficiencies due to the limited statistics of the Monte Carlo, listed in the last two rows of Tables 3.12 and 3.13.
- the uncertainty on fit efficiencies due to the imperfect knowledge of the double-Gaussian ΔE distribution of signal events, in particular of the fraction f_1 of signal events in the main Gaussian. These uncertainties are listed in Tables 4.3 and 4.4.

These two contributions are added in quadrature and reported in Table 4.45.

D_{CP}^0 mode	$\frac{\varepsilon(D_{CP}^0 K)/\varepsilon(D_{CP}^0 \pi)}{\varepsilon(D^0 K)/\varepsilon(D^0 \pi)}$
K^+K^-	99.0 ± 1.3
$\pi^+\pi^-$	99.6 ± 1.3
$K_S^0\pi^0$	98.2 ± 1.8
$K_S^0\phi$	98.6 ± 1.6
$K_S^0\omega$	102.0 ± 3.1

Table 4.45: Ratio of the final efficiencies for true $B^- \rightarrow D^0 K^-$ and $B^- \rightarrow D^0 \pi^-$ candidates, evaluated on Monte Carlo

The errors on the ratio are evaluated by using the statistical and the systematic errors on the signal rates. The correlation between the $B \rightarrow D^0 \pi$ and $B \rightarrow D^0 K$ fit yields, listed in Tables 4.30, 4.32, 4.34, 4.36, 4.38 and 4.40 are taken into account in the statistical error on R_{\pm} .

The main systematic uncertainties on the measurement of these ratios are reported in Tables 4.46 and 4.47. The resulting double ratios are:

$$R_+(K^+K^-) = 0.89 \pm 0.13(\text{stat}) \pm 0.04(\text{syst}) \quad (4.78)$$

$$R_+(\pi^+\pi^-) = 0.94 \pm 0.28(\text{stat}) \pm 0.08(\text{syst}) \quad (4.79)$$

$$R_-(K_S^0\pi^0) = 0.76 \pm 0.13(\text{stat})_{-0.06}^{+0.02}(\text{syst}) \quad (4.80)$$

$$R_-(K_S^0\phi) = 1.06 \pm 0.24(\text{stat}) \pm 0.05(\text{syst}) \quad (4.81)$$

$$R_-(K_S^0\omega) = 1.03 \pm 0.25(\text{stat}) \pm 0.14(\text{syst}) \quad (4.82)$$

The combination of the two CP -even measurements gives:

$$R_+ = 0.90 \pm 0.12(\text{stat}) \pm 0.03(\text{syst}) \quad (4.83)$$

The χ^2/ndf is 0.026/1, the corresponding probability is 87%.

The combination of the three CP -odd measurements gives:

$$R_- = 0.86 \pm 0.11(\text{stat}) \pm 0.03(\text{syst}) \quad (4.84)$$

The χ^2/ndf is 1.78/2, the corresponding probability is 41%.

4.12 Constraints on the CKM angle γ

As stated in the Introduction and in Section 1.7.1, the measurement of the four observables $R_{CP\pm}$, $A_{CP\pm}$ can in principle constrain the CKM angle γ (up to eight discrete ambiguities). We shall see in this Section that the measurements presented here do not allow in practice to pose a constraint on γ , since the sensitivity is too low. However, these measurements can be combined with the results obtained in other analyses (the most powerful of which is the Dalitz analysis of $B \rightarrow D^0 K$, $D^0 \rightarrow K_S^0 \pi^+ \pi^-$ decays described in Section 1.7.3) to improve our knowledge of γ .

Parameter	Syst. Error on R_+ (%)	
	$D^0 \rightarrow K^+K^-$	$D^0 \rightarrow \pi^+\pi^-$
$q\bar{q}$ bkg ΔE	± 1.5	± 2.7
$B\bar{B}(\pi)$ bkg ΔE	± 0.2	± 0.3
$B\bar{B}(K)$ bkg ΔE	± 0.3	± 1.1
PID	± 0.0	± 0.1
peaking X_1X_2K bkg	± 3.3	± 7.9
Efficiency corr. factor	± 1.2	± 1.2
Total	± 3.8	± 8.4

Table 4.46: Systematic errors on R_+ in $B \rightarrow D^0K$, $D^0 \rightarrow K^+K^-$ and $D^0 \rightarrow \pi^+\pi^-$.

Parameter	Syst. Error on R_- (%)		
	$D^0 \rightarrow K_S^0\pi^0$	$D^0 \rightarrow K_S^0\phi$	$D^0 \rightarrow K_S^0\omega$
$q\bar{q}$ bkg ΔE	± 1.3	± 1.4	± 3.2
$B\bar{B}(\pi)$ bkg ΔE	± 0.2	± 0.3	± 0.3
$B\bar{B}(K)$ bkg ΔE	± 0.5	± 0.3	± 0.8
PID	± 0.1	± 0.2	± 0.1
peaking X_1X_2K bkg	$^{+0.0}_{-6.0}$	$^{+0.3}_{-1.5}$	± 10.2
peaking $B \rightarrow D^0h$ bkg	-	± 4.2	± 8.2
Efficiency corr. factor	± 1.4	± 1.8	± 3.2
Total	$^{+1.9}_{-6.3}$	± 5	± 14

Table 4.47: Systematic errors (%) on R_- in $B \rightarrow D^0K$, $D^0 \rightarrow K_S^0\pi^0$, $D^0 \rightarrow K_S^0\phi$ and $D^0 \rightarrow K_S^0\omega$.

The extraction of γ , together with the other two unknowns δ_B and r_B , is in principle allowed by the relations:

$$\frac{R_{CP+} - R_{CP-}}{4} = r_B \cos \delta_B \cos \gamma \quad (4.85)$$

$$\frac{R_{CP+}A_{CP+} - R_{CP-}A_{CP-}}{4} = r_B \sin \delta_B \sin \gamma \quad (4.86)$$

$$\frac{R_{CP+} + R_{CP-} - 2}{2} = r_B^2. \quad (4.87)$$

In theory, one would fix r_B from the third equation and then would solve the first two for the remaining unknowns γ and δ_B : in practice this is not feasible with our measurements, since the uncertainties on $R_{CP\pm}$ are at the level of 12% and therefore we do not have enough sensitivity to the very small values of r_B^2 that are expected ($r_B < 0.2$ implies $r_B^2 < 0.04$). Indeed, from our values of R_{\pm} we can only infer:

$$r_B^2 = -0.12 \pm 0.08 \quad (4.88)$$

However, we can still derive some interesting relations that, combined with the results of the $B \rightarrow D^0K$, $D^0 \rightarrow K_S^0\pi^+\pi^-$ analysis allow to reduce the uncertainty on γ from the

latter. To this purpose, following [2], we introduce the CP -violating parameters:

$$x_{\pm} \equiv r_B \cos(\delta_B \pm \gamma) \quad (4.89)$$

$$y_{\pm} \equiv r_B \sin(\delta_B \pm \gamma) \quad (4.90)$$

and we note that once these four quantities are known, then γ , r_B and δ_B can be extracted: this is essentially the way γ is measured in the *BABAR* $B \rightarrow D^0 K$, $D^0 \rightarrow K_S^0 \pi^+ \pi^-$ analysis in [2], where x_{\pm} and y_{\pm} are determined from the $D^0 \rightarrow K_S^0 \pi^+ \pi^-$ Dalitz distribution. The results of the Dalitz analysis, with the same data sample used here, are:

$$x_+ = -0.129 \pm 0.070 \pm 0.030 \pm 0.032$$

$$y_+ = 0.019 \pm 0.079 \pm 0.023 \pm 0.021$$

$$x_- = 0.077 \pm 0.069 \pm 0.026 \pm 0.019$$

$$y_- = 0.064 \pm 0.092 \pm 0.037 \pm 0.042$$

where the first error is statistical, the second is the experimental systematic uncertainty and the third arises from the choice of the Dalitz model assumed for the $D^0 \rightarrow K_S^0 \pi^+ \pi^-$ amplitude. The measurements presented in this thesis can contribute to improve the accuracy on the two quantities x_{\pm} and thus on γ , once the following relations (which can be deduced from (4.85) and (4.86) using the ordinary trigonometric relations) are exploited:

$$\frac{R_{CP+}(1 - A_{CP+}) - R_{CP-}(1 - A_{CP-})}{4} = x_+ \quad (4.91)$$

$$\frac{R_{CP+}(1 + A_{CP+}) - R_{CP-}(1 + A_{CP-})}{4} = x_- \quad (4.92)$$

From our measured values of $R_{CP\pm}$ and $A_{CP\pm}$ we have in fact

$$x_+ = -0.082 \pm 0.053(\text{stat}) \pm 0.016(\text{syst}) \quad (4.93)$$

$$x_- = +0.102 \pm 0.063(\text{stat}) \pm 0.018(\text{syst}) \quad (4.94)$$

and we see that the errors on x_{\pm} are competitive with those obtained from the Dalitz analysis. On the other hand, the quantities y_{\pm} cannot be measured since the only ‘‘handles’’ we have on them are the relations

$$\frac{R_{CP+} + R_{CP-} - 2}{2} = r_B^2 = x_{\pm}^2 + y_{\pm}^2 \quad (4.95)$$

where y_{\pm} enter in a quadratic way and are affected by the large uncertainties (12%) on $R_{CP\pm}$. The combination of the Dalitz results and those presented in this thesis has not been performed yet, but from initial estimates [90] we expect to improve the sensitivity on γ by 10-15%.

4.13 Conclusions

In this thesis we have reconstructed the Cabibbo-suppressed $B \rightarrow D^0 K$ and the Cabibbo-allowed $B \rightarrow D^0 \pi$ decays, with D^0 decaying to non- CP ($K^- \pi^+$), CP -even ($K^+ K^-$, $\pi^+ \pi^-$) and CP -odd ($K_s^0 \pi^0$, $K_s^0 \phi$, $K_s^0 \omega$) final states. Previously only the Belle experiment had reconstructed the $B \rightarrow D^0 K$ decays, with D^0 decaying to CP -eigenstates, that have been considered here. The measurement is particularly challenging from the experimental side since the branching fractions involved are very low, at the level of $10^{-6} - 10^{-7}$, a large data sample is therefore needed and the analysis must be optimized in order to maintain a high efficiency for the signal while rejecting most of the background. Moreover, excellent kaon/pion separation is needed in order to distinguish $B \rightarrow D^0 K$ decays from the twelve times more abundant $B \rightarrow D^0 \pi$ decays, which are kinematically very similar. The analysis has been performed on a sample of 232×10^6 charged B meson decays collected by the *BABAR* experiment at the SLAC PEP-II B Factory. We have searched for direct CP -violation by measuring the two CP asymmetries:

$$A_{CP\pm}(B \rightarrow D^0 K) \equiv \frac{\mathcal{B}(B^- \rightarrow D_{CP\pm}^0 K^-) - \mathcal{B}(B^+ \rightarrow D_{CP\pm}^0 K^+)}{\mathcal{B}(B^- \rightarrow D_{CP\pm}^0 K^-) + \mathcal{B}(B^+ \rightarrow D_{CP\pm}^0 K^+)}$$

Our results are:

$$\begin{aligned} A_{CP+}(B \rightarrow D^0 K) &= +0.35 \pm 0.13(\text{stat}) \pm 0.04(\text{syst}) \\ A_{CP-}(B \rightarrow D^0 K) &= -0.06 \pm 0.13(\text{stat}) \pm 0.04(\text{syst}) \end{aligned}$$

No evidence for direct CP violation is found within the present data sample: the positive CP asymmetry is 2.5σ far from zero, and the negative one is consistent with zero within one standard deviation. If we extrapolate the current experimental errors, we can expect to reach a sensitivity $\sigma(A_{CP\pm}) \approx 0.06$ with 5 times more data, which *BABAR* should be able to collect by the year 2008, and $\sigma(A_{CP\pm}) \approx 0.04$ in the (unlikely) case that *BABAR* will continue keeping data until 2010. In the former hypothesis, an asymmetry (either A_{CP+} or A_{CP-}) greater than 20% (which is allowed for $r_B \approx 0.15$ for a significant range of possible values of the strong phase δ_B , see the Introduction) can be observed at $> 3\sigma$ level. In the latter case, even smaller asymmetries (of the order of 12%, which should be expected if $r_B \approx 0.1$) could be observed. In this work we have also measured the two double branching fraction ratios:

$$R_{\pm} \equiv \frac{\frac{\mathcal{B}(B^- \rightarrow D_{CP\pm}^0 K^-) + \mathcal{B}(B^+ \rightarrow D_{CP\pm}^0 K^+)}{\mathcal{B}(B^- \rightarrow D_{CP\pm}^0 \pi^-) + \mathcal{B}(B^+ \rightarrow D_{CP\pm}^0 \pi^+)}}{\frac{\mathcal{B}(B^- \rightarrow D^0 K^-) + \mathcal{B}(B^+ \rightarrow \bar{D}^0 K^+)}{\mathcal{B}(B^- \rightarrow D^0 \pi^-) + \mathcal{B}(B^+ \rightarrow \bar{D}^0 \pi^+)}}$$

Our results are:

$$\begin{aligned} R_+ &= 0.90 \pm 0.12(\text{stat}) \pm 0.03(\text{syst}) \\ R_- &= 0.86 \pm 0.11(\text{stat}) \pm 0.03(\text{syst}) \end{aligned}$$

These quantities are expected to be equivalent, up to 1-2%, to the branching fraction ratios:

$$R_{CP\pm} \equiv \frac{\mathcal{B}(B^- \rightarrow D_{CP\pm}^0 K^-) + \mathcal{B}(B^+ \rightarrow D_{CP\pm}^0 K^+)}{\mathcal{B}(B^- \rightarrow D^0 K^-) + \mathcal{B}(B^+ \rightarrow \bar{D}^0 K^+)},$$

which – together with $A_{CP\pm}$ – constitute the four so-called “GLW” observables from which the CKM angle γ can in principle be constrained. At present, however, the statistics is too low to put a significant constraint on γ with these numbers only, as described in the

previous Section: to this purpose we would need to measure R_{\pm} at the % level, which is out of reach. However we can still provide useful information on γ , in the form of two CP -violating parameters x_{\pm} defined in (4.89), which have been measured to be:

$$\begin{aligned} x_+ &= -0.082 \pm 0.053(\text{stat}) \pm 0.016(\text{syst}) \\ x_- &= +0.102 \pm 0.063(\text{stat}) \pm 0.018(\text{syst}). \end{aligned}$$

These can be combined with those measured in the $B \rightarrow D^0 K$, $D^0 \rightarrow K_s^0 \pi^+ \pi^-$ analysis in [2], and are expected to increase the sensitivity on γ by 10-15%: however, this has not been done yet.

We have been working on the field of $B \rightarrow D^0 K$ and $B \rightarrow D^0 \pi$ reconstruction over the years 2001-2005. The measurement of R_+ and A_{CP+} , with the partial data sample collected by *BABAR* in the first 2 runs of data taking ($\approx 89 \times 10^6$ charged B mesons), has already been published in Spring 2004 in the journal “Physics Review Letters” [6], and preliminary results on R_{\pm} and $A_{CP\pm}$ obtained with 92% of the data sample used in this analysis have been approved by the *BABAR* Collaboration and presented at the ICHEP 2004 Conference in Summer 2004 [42]. The results presented here update those results and are going to be submitted to the journal “Physics Review D” for publication. They constitute the world most precise measurements of $A_{CP\pm}$ and R_{\pm} , the other only determination being the ones from Belle, which – although on a larger sample of 274×10^6 charged B mesons – are less accurate than ours, as shown in Table 4.48.

	<i>BABAR</i> (This analysis)	Belle
$N(B^{\pm})$	232×10^6	274×10^6
$A_{CP+}(B \rightarrow D^0 K)$	$+0.35 \pm 0.13(\text{stat}) \pm 0.04(\text{syst})$	$+0.07 \pm 0.14(\text{stat}) \pm 0.06(\text{syst})$
$A_{CP-}(B \rightarrow D^0 K)$	$-0.06 \pm 0.13(\text{stat}) \pm 0.04(\text{syst})$	$-0.11 \pm 0.14(\text{stat}) \pm 0.05(\text{syst})$
R_+	$0.90 \pm 0.12(\text{stat}) \pm 0.03(\text{syst})$	$0.98 \pm 0.18(\text{stat}) \pm 0.10(\text{syst})$
R_-	$0.86 \pm 0.11(\text{stat}) \pm 0.03(\text{syst})$	$1.29 \pm 0.16(\text{stat}) \pm 0.08(\text{syst})$

Table 4.48: Comparison between the data sample used and the results for the four quantities (CP asymmetries and branching fraction ratios) $A_{CP\pm}(B \rightarrow D^0 K)$ and R_{\pm} measured in this analysis and in the only other one previously performed.

Appendix A

γ and charged $B^\pm \xrightarrow{(-)} D^0 K^\pm$ decays

With the diagrams of Figure 1.5 in mind, we can write the following amplitudes for the $B \rightarrow DK$ decay:

$$A(B^- \rightarrow D^0 K^-) = |A|e^{i\delta} \quad (\text{A.1})$$

$$A(B^- \rightarrow \bar{D}^0 K^-) = |\bar{A}|e^{i\bar{\delta}}e^{-i\gamma} \quad (\text{A.2})$$

$$A(B^+ \rightarrow \bar{D}^0 K^+) = |A|e^{i\delta} \quad (\text{A.3})$$

$$A(B^+ \rightarrow D^0 K^+) = |\bar{A}|e^{i\bar{\delta}}e^{+i\gamma} \quad (\text{A.4})$$

We can also write the amplitudes for the $D \rightarrow f_i$ decay:

$$A(D^0 \rightarrow f_i) = |A_i|e^{i\Delta_i} \quad (\text{A.5})$$

$$A(D^0 \rightarrow \bar{f}_i) = |\bar{A}_i|e^{i\bar{\Delta}_i} \quad (\text{A.6})$$

$$A(\bar{D}^0 \rightarrow \bar{f}_i) = |A_i|e^{i\Delta_i} \quad (\text{A.7})$$

$$A(\bar{D}^0 \rightarrow f_i) = |\bar{A}_i|e^{i\bar{\Delta}_i} \quad (\text{A.8})$$

where $\delta, \bar{\delta}, \Delta_i$ and $\bar{\Delta}_i$ are strong (CP -conserving) phases.

When considering $B^- \rightarrow [f_i]_{D^0} K^-$ (the notation $[f_i]_{D^0}$ means that the final state f_i is originated from a D^0 or \bar{D}^0 decay) and its conjugate process, the amplitudes $B^- \rightarrow D^0 K^-, D^0 \rightarrow f_i$ and $B^- \rightarrow \bar{D}^0 K^-, \bar{D}^0 \rightarrow f_i$ interfere, and, neglecting tiny $D^0 - \bar{D}^0$ mixing, the total amplitudes are:

$$\begin{aligned} A(B^- \rightarrow [f_i]_{D^0} K^-) &= A(B^- \rightarrow D^0 K^-)A(D^0 \rightarrow f_i) + \\ &A(B^- \rightarrow \bar{D}^0 K^-)A(\bar{D}^0 \rightarrow f_i) \\ &= |A||A_i|e^{i(\delta+\Delta_i)} + |\bar{A}||\bar{A}_i|e^{i(\bar{\delta}+\bar{\Delta}_i-\gamma)} \end{aligned} \quad (\text{A.9})$$

$$\begin{aligned} A(B^+ \rightarrow [\bar{f}_i]_{D^0} K^+) &= A(B^+ \rightarrow \bar{D}^0 K^+)A(\bar{D}^0 \rightarrow \bar{f}_i) + \\ &A(B^+ \rightarrow D^0 K^+)A(D^0 \rightarrow \bar{f}_i) \\ &= |A||A_i|e^{i(\delta+\Delta_i)} + |\bar{A}||\bar{A}_i|e^{i(\bar{\delta}+\bar{\Delta}_i+\gamma)} \end{aligned} \quad (\text{A.10})$$

The partial widths are:

$$\Gamma(B^- \rightarrow [f_i]_{D^0} K^-) = |A|^2|A_i|^2 + |\bar{A}|^2|\bar{A}_i|^2 + 2|A||\bar{A}||A_i||\bar{A}_i|\cos(\xi_i - \gamma) \quad (\text{A.11})$$

$$\Gamma(B^+ \rightarrow [\bar{f}_i]_{D^0} K^+) = |A|^2|A_i|^2 + |\bar{A}|^2|\bar{A}_i|^2 + 2|A||\bar{A}||A_i||\bar{A}_i|\cos(\xi_i + \gamma) \quad (\text{A.12})$$

where

$$\xi_i \equiv \delta_B + \delta_i \quad (\text{A.13})$$

$$\delta_B \equiv \bar{\delta} - \delta \quad (\text{A.14})$$

$$\delta_i \equiv \bar{\Delta}_i - \Delta_i \quad (\text{A.15})$$

Let us define:

$$r_B \equiv |A(B^- \rightarrow \bar{D}^0 K^-)/A(B^- \rightarrow D^0 K^-)| \quad (\text{A.16})$$

$$r_{f_i}^D \equiv |A(D^0 \rightarrow f_i)/A(D^0 \rightarrow \bar{f}_i)| \quad (\text{A.17})$$

The quantity r_B is expected to be:

$$r_B \approx \left| \frac{V_{ub}V_{cs}}{V_{cb}V_{us}} \right| \times \frac{a_2}{a_1} \quad (\text{A.18})$$

where $a_2/a_1 \approx 0.26 - 0.44$ is a color suppression factor and $\left| \frac{V_{ub}V_{cs}^*}{V_{cb}V_{us}^*} \right| \approx 0.4$, from which r_B is expected to be around $0.1 - 0.2$. $r_{f_i}^D$ depends on the D^0 final state.

Omitting common phase-space factors we have:

$$\mathcal{B}(B^- \rightarrow [f_i]_{D^0} K^-) \propto |A|^2 |\bar{A}_i|^2 \left(r_{f_i}^{D^2} + r_B^2 + 2r_{f_i}^D r_B \cos(\xi_i - \gamma) \right) \quad (\text{A.19})$$

$$\mathcal{B}(B^+ \rightarrow [\bar{f}_i]_{D^0} K^+) \propto |A|^2 |\bar{A}_i|^2 \left(r_{f_i}^{D^2} + r_B^2 + 2r_{f_i}^D r_B \cos(\xi_i + \gamma) \right) \quad (\text{A.20})$$

The direct CP asymmetry is therefore:

$$\begin{aligned} A_{CP} &= \frac{\mathcal{B}(B^- \rightarrow [f_i]_{D^0} K^-) - \mathcal{B}(B^+ \rightarrow [\bar{f}_i]_{D^0} K^+)}{\mathcal{B}(B^- \rightarrow [f_i]_{D^0} K^-) + \mathcal{B}(B^+ \rightarrow [\bar{f}_i]_{D^0} K^+)} \\ &= \frac{\left(r_{f_i}^{D^2} + r^2 + 2r_{f_i}^D r_B \cos(\xi_i - \gamma) \right) - \left(r_{f_i}^{D^2} + r^2 + 2r_{f_i}^D r_B \cos(\xi_i + \gamma) \right)}{\left(r_{f_i}^{D^2} + r_B^2 + 2r_{f_i}^D r_B \cos(\xi_i - \gamma) \right) + \left(r_{f_i}^{D^2} + r_B^2 + 2r_{f_i}^D r_B \cos(\xi_i + \gamma) \right)} \\ &= \frac{2r_{f_i}^D r_B \sin \xi_i \sin \gamma}{r_{f_i}^{D^2} + r_B^2 + 2r_{f_i}^D r_B \cos \xi_i \cos \gamma} \end{aligned} \quad (\text{A.21})$$

and the average (overall) branching fraction is

$$\begin{aligned} \langle \mathcal{B}(B \rightarrow [f_i]_{D^0} K) \rangle &\equiv \frac{\mathcal{B}(B^- \rightarrow [f_i]_{D^0} K^-) + \mathcal{B}(B^+ \rightarrow [\bar{f}_i]_{D^0} K^+)}{2} \\ &= \frac{1}{2} \frac{\left(r_{f_i}^{D^2} + r^2 + 2r_{f_i}^D r_B \cos(\xi_i - \gamma) \right) + \left(r_{f_i}^{D^2} + r^2 + 2r_{f_i}^D r_B \cos(\xi_i + \gamma) \right)}{\left(r_{f_i}^{D^2} + r_B^2 + 2r_{f_i}^D r_B \cos(\xi_i - \gamma) \right) + \left(r_{f_i}^{D^2} + r_B^2 + 2r_{f_i}^D r_B \cos(\xi_i + \gamma) \right)} \\ &\propto |A|^2 |\bar{A}_i|^2 \left(r_{f_i}^{D^2} + r_B^2 + 2r_{f_i}^D r_B \cos \xi_i \cos \gamma \right) \end{aligned} \quad (\text{A.22})$$

Let us consider 3 cases:

- $f_i = f_{CA}$ is a Cabibbo-allowed (CA) D^0 decay final state like for instance $K^- \pi^+$. In that case $r_{f_{CA}}^D \approx \lambda^{-2} \approx 1/0.05$ (indeed, the ratio $|A(D^0 \rightarrow K^+ \pi^-)/(D^0 \rightarrow K^- \pi^+)|$ has been measured to be 0.060 ± 0.003 [38]). Since $r_B \approx 0.1 - 0.2$, the $r_{f_i}^{D^2}$ terms are dominant and the CP asymmetry and average branching fraction are:

$$A_{CP} = 2 \frac{r_B}{r_{f_{CA}}^D} \sin \xi_{CA} \sin \gamma \lesssim 0.3\% \quad (\text{A.23})$$

$$\begin{aligned} \langle \mathcal{B}(B \rightarrow [f_{CA}]_{D^0} K) \rangle &\propto |A|^2 |\bar{A}_{CA}|^2 r_{f_{CA}}^{D^2} = |A|^2 |A_{CA}|^2 \\ &= \langle \mathcal{B}(B \rightarrow D^0 K) \rangle \mathcal{B}(D^0 \rightarrow f_{CA}) \end{aligned} \quad (\text{A.24})$$

- $f_i = f_{CP\pm}$ is a CP -eigenstate, $\bar{f}_{CP\pm} = \pm f_{CP\pm}$. In that case $\bar{A}_i = A_i$ and $\bar{\Delta}_i = \Delta_i$ (if the final state is CP -even, f_{CP+}) or $\bar{\Delta}_i = \Delta_i + \pi$ (if the final state is CP -odd, f_{CP-}), therefore $r_{f_{CP\pm}}^D = 1$, $\delta_{CP+} = 0$ and $\delta_{CP-} = \pi$ and the CP asymmetry and average branching fraction are:

$$A_{CP\pm} = \pm \frac{2r_B \sin \delta_B \sin \gamma}{1 + r_B^2 \pm 2r_B \cos \delta_B \cos \gamma} \quad (\text{A.25})$$

$$\begin{aligned} \langle \mathcal{B}(B \rightarrow [f_{CP\pm}]_{D^0} K) \rangle &\propto |A|^2 |A_i|^2 (1 + r_B^2 \pm 2r_B \cos \delta_B \cos \gamma) \\ &\propto |A|^2 \mathcal{B}(D^0 \rightarrow f_{CP\pm}) (1 + r_B^2 \pm 2r_B \cos \delta_B \cos \gamma) \\ &= \langle \mathcal{B}(B \rightarrow D^0 K) \rangle \mathcal{B}(D^0 \rightarrow f_{CP\pm}) (1 + r_B^2 \pm 2r_B \cos \delta_B \cos \gamma) \end{aligned} \quad (\text{A.26})$$

where the + sign applies to CP -even decays and the – sign applies to CP -odd decays. Dividing by $\mathcal{B}(D^0 \rightarrow f_{CP\pm})$, which is equal to $\mathcal{B}(D_{CP\pm}^0 \rightarrow f_{CP\pm})$:

$$\begin{aligned} \langle \mathcal{B}(B \rightarrow D_{CP\pm}^0 K) \rangle &= \frac{\langle \mathcal{B}(B \rightarrow [f_{CP\pm}]_{D^0} K) \rangle}{\mathcal{B}(D^0 \rightarrow f_{CP\pm})} \\ &= \langle \mathcal{B}(B \rightarrow D^0 K) \rangle (1 + r_B^2 \pm 2r_B \cos \delta_B \cos \gamma) \end{aligned} \quad (\text{A.27})$$

thus

$$\frac{\langle \mathcal{B}(B \rightarrow D_{CP\pm}^0 K) \rangle}{\langle \mathcal{B}(B \rightarrow D^0 K) \rangle} = 1 + r_B^2 \pm 2r_B \cos \delta_B \cos \gamma \quad (\text{A.28})$$

- $f_i = f_{\text{DCS}}$ is a doubly-Cabibbo-suppressed (DCS) D^0 decay final state like for instance $K^+ \pi^-$. In that case $r_{f_{\text{DCS}}}^D \approx \lambda^2 \approx 0.05$ and, since $r_B \approx 0.1 - 0.2$, the r_B^2 , $(r_{f_{\text{DCS}}}^D)^2$ and $r_B r_{f_{\text{DCS}}}^D$ terms are of the same order of magnitude, and the whole expressions for the CP asymmetry and the branching fraction must be retained. In this case the final state \bar{f}_{DCS} is Cabibbo-allowed, therefore $|\bar{A}_{\text{DCS}}|^2 \propto \langle \mathcal{B}(B \rightarrow \bar{f}_{\text{DCS}} K) \rangle / |A|^2$ and we can write:

$$\begin{aligned} \langle \mathcal{B}(B \rightarrow [f_{\text{DCS}}]_{D^0} K) \rangle &= \mathcal{B}(B^- \rightarrow D^0 K^-) \mathcal{B}(D^0 \rightarrow \bar{f}_{\text{DCS}}) \times \\ &\quad \left(r_{f_{\text{DCS}}}^D{}^2 + r_B^2 + 2r_{f_{\text{DCS}}}^D r_B \cos \xi_{f_{\text{DCS}}} \cos \gamma \right) \\ &= \langle \mathcal{B}(B \rightarrow [\bar{f}_{\text{DCS}}]_{D^0} K) \rangle \times \\ &\quad \left(r_{f_{\text{DCS}}}^D{}^2 + r_B^2 + 2r_{f_{\text{DCS}}}^D r_B \cos \xi_{f_{\text{DCS}}} \cos \gamma \right) \end{aligned} \quad (\text{A.29})$$

thus

$$\frac{\langle \mathcal{B}(B \rightarrow [f_{\text{DCS}}]_{D^0} K) \rangle}{\langle \mathcal{B}(B \rightarrow [\bar{f}_{\text{DCS}}]_{D^0} K) \rangle} = r_{f_{\text{DCS}}}^D{}^2 + r_B^2 + 2r_{f_{\text{DCS}}}^D r_B \cos \xi_{f_{\text{DCS}}} \cos \gamma \quad (\text{A.30})$$

Bibliography

- [1] M. Gronau, “Improving bounds on γ in $B^\pm \rightarrow DK^\pm$ and $B^{\pm,0} \rightarrow DX_s^{\pm,0}$ ”, Phys. Lett. B **557**, 198 (2003).
- [2] BABAR Collaboration, B. Aubert *et al.*, “Measurement of γ in $B^\mp \rightarrow D^{(*)}K^\mp$ decays with a Dalitz analysis of $D \rightarrow K_S\pi^-\pi^+$ ”, hep-ex/0504039, submitted to Phys. Rev. Lett.
- [3] Belle Collaboration, K. Abe *et al.*, “Measurement of ϕ_3 with Dalitz Plot Analysis of $B^\pm \rightarrow D^{(*)}K^\pm$ decay at Belle”, hep-ex/0411049, contributed to FPCP2004 (2004).
- [4] CLEO Collaboration, A. Bornheim *et al.*, “Measurements of Charmless Hadronic Two-Body B Meson Decays and the Ratio $\mathcal{B}(B \rightarrow DK)/\mathcal{B}(B \rightarrow D\pi)$ ”, Phys. Rev. D **68**, 052002 (2003).
- [5] Belle Collaboration, S. K. Swain *et al.*, “Measurement of branching fraction ratios and CP asymmetries in $B^\pm \rightarrow D_{CP}K^\pm$ ”, Phys. Rev. D **68**, 051101 (2003).
- [6] BABAR Collaboration, B. Aubert *et al.*, “Measurement of the branching fractions and CP -asymmetry of $B^- \rightarrow D_{(CP)}^0K^-$ decays with the BABAR detector”, Phys. Rev. Lett. **92**, 202002 (2004).
- [7] CKMfitter group, J. Charles *et al.*, “ CP Violation and the CKM Matrix: Assessing the Impact of the Asymmetric B Factories”, hep-ph/0406184 (2005). Accepted for publication by Eur. Phys. Jour. C .
- [8] UTfit Collaboration, M. Bona *et al.*, “The 2004 UTfit Collaboration Report on the Status of the Unitarity Triangle in the Standard Model”, hep-ph/0501199 (2005).
- [9] Belle Collaboration, K. Abe *et al.*, “Study of $B^\pm \rightarrow D_{CP}K^\pm$ and $B^\pm \rightarrow D_{CP}^*K^\pm$ ”, Belle-CONF-0443, submitted to ICHEP’04 (2004).
- [10] S. L. Glashow, “Partial symmetries of weak interactions”, Nucl. Phys. **22**, 579 (1961);
S. Weinberg, “A model of leptons”, Phys. Rev. Lett. **19**, 1264 (1967);
A. Salam, “Gauge unification of fundamental forces”, in *Proceedings of the 8th Nobel Symposium*, ed. N. Swartholm, Almquist and Wiksells, Stockholm (1968).
Gell-Mann, “A Schematic Model of Baryons and Mesons”, Phys. Lett. **8**, 214 (1964).
Zweig, “An SU(3) Model for Strong Interaction Symmetry and Its Breaking”, CERN Preprint 8182/TH401 (1964).
- [11] N. Cabibbo, “Unitary symmetry and leptonic decays”, Phys. Rev. Lett. **10**, 531 (1963);
M. Kobayashi and T. Maskawa, “ CP violation in the renormalizable theory of weak interaction”, Prog. Th. Phys. **49**, 652 (1973).
- [12] BABAR Collaboration, B. Aubert *et al.*, “The BABAR detector”, Nucl. Instr. and Methods A **479**, 1 (2002).

- [13] Belle Collaboration, A. Abashian *et al.*, “The Belle detector”, Nucl. Instr. and Methods A **479**, 117 (2002).
- [14] BABAR Collaboration, *The BABAR Physics Book. Physics at an Asymmetric B Factory*, ed. P. F. Harrison and H. R. Quinn, SLAC-R-504 (1998).
- [15] M. E. Peskin and D. V. Schroeder, *An Introduction to Quantum Field Theory*, Addison-Wesley Publishing Company (1995).
- [16] All experimental data are taken from:
Particle Data Group, S. Eidelman *et al.*, “Review of Particle Physics”, Phys. Lett. B **592**, 1 (2004).
- [17] L. Wolfenstein, “Parametrization of the Kobayashi-Maskawa matrix”, Phys. Rev. Lett. **51**, 1945 (1983).
- [18] The Heavy Flavor Averaging Group, <http://www.slac.stanford.edu/xorg/hfag/> (Winter 2005 averages).
- [19] I. I. Bigi *et al.*, in *CP Violation*, ed. C. Jarlskog, World Scientific, Singapore (1992)
- [20] BABAR Collaboration, B. Aubert *et al.*, “Improved Measurement of CP Asymmetries in $B^0 \rightarrow (c\bar{c})K^{(*)0}$ Decays”, Phys. Rev. Lett. **94**, 161803 (2005).
- [21] Belle Collaboration, K. Abe *et al.*, “Improved Measurement of CP -Violation Parameters $\sin(2\phi_1)$ and $|\lambda|$, B Meson Lifetimes, and $B^0 - \bar{B}^0$ Mixing Parameter Δm_d ”, Phys. Rev. D **71**, 072003 (2005).
- [22] BABAR Collaboration, B. Aubert *et al.*, “Direct CP Asymmetry in $B^0 \rightarrow K^+\pi^-$ Decays”, Phys. Rev. Lett. **93**, 131801 (2004).
- [23] BABAR Collaboration, B. Aubert *et al.*, “Search for T and CP Violation in $B^0 - \bar{B}^0$ Mixing with Inclusive Dilepton Events”, Phys. Rev. Lett. **88**, 231801 (2002).
- [24] Belle Collaboration, K. Abe *et al.*, “ CP violation in $B - \bar{B}$ mixing with dilepton events”, hep-ex/0409012 (2004). Contributed to ICHEP2004, Beijing, China.
- [25] BABAR Collaboration, B. Aubert *et al.*, “Ambiguity-Free Measurement of $\cos 2\beta$: Time-Integrated and Time-Dependent Angular Analyses of $B \rightarrow J/\psi K\pi$ ”, Phys. Rev. D **71**, 023005 (2005).
- [26] M. Gronau and D. Wyler, “Isospin analysis of CP asymmetries in B decays”, Phys. Rev. Lett. **65**, 3381 (1990).
- [27] BABAR Collaboration, B. Aubert *et al.*, “Observation of the Decay $B^0 \rightarrow \pi^0\pi^0$ ”, Phys. Rev. Lett. **91**, 241801 (2003).
- [28] Y. Grossman and H. R. Quinn, “Bounding the effect of penguin diagrams in $a_{CP}(B^0 \rightarrow \pi^+\pi^-)$ ”, Phys. Rev. D **58**, 017504 (1998).
- [29] A. Soffer, Section 3.2 of “The Discovery Potential of a Super B Factory”, SLAC-R-504 (2004).
- [30] M. Gronau and D. Wyler, “On determining a weak phase from charged B decay asymmetries”, Phys. Lett. **B265**, 172 (1991).
- [31] M. Gronau, “Weak phase γ from color-allowed $B \rightarrow DK$ rates”, Phys. Rev. D **58** 037301 (1998).

- [32] D. Atwood, I. Dunietz and A. Soni, “Enhanced CP violation with $B \rightarrow KD^0(\bar{D}^0)$ Modes and Extraction of the CKM Angle γ ”, Phys. Rev. Lett. **78**, 3257 (1997).
- [33] A. Giri, Y. Grossman, A. Soffer and J. Zupan, “Determining γ using $B^\pm \rightarrow DK^\pm$ with multibody D decays”, Phys. Rev. D **68**,054018 (2003).
- [34] B. Kayser and D. London, “Exploring CP Violation with $B_d^0 \rightarrow DK_S$ Decays”, Phys. Rev. D **61**, 116013 (2000).
- [35] R. Aleksan, T. Petersen and A. Soffer, “Measuring the Weak Phase γ in Color Allowed $B \rightarrow DK\pi$ Decays”, Phys. Rev. D **67** 096002 (2003); R. Aleksan and T. Petersen, “Measuring $2\beta + \gamma$ with Color-Allowed $B^0 \rightarrow D^\pm K_S^0 \pi^\pm$ Decays”, hep-ph/0307371 (2003), invited talk at the Workshop on the CKM Unitarity Triangle, IPPP Durham, April 2003.
- [36] I. Dunietz, “Clean CKM Information from $B_d(t) \rightarrow D^{(*)} \mp \pi^\pm$ ”, Phys. Lett. B **427**, 179 (1998).
- [37] D. London, N. Sinha and R. Sinha, “Extracting Weak Phase Information from $B \rightarrow V_1 V_2$ Decays”, in *B physics and CP violation*, Ise-Shima (2001). [hep-ph/0104157]
- [38] BABAR Collaboration, B. Aubert *et al.*, “Search for D^0 - \bar{D}^0 Mixing and a Measurement of the Doubly Cabibbo-suppressed Decay Rate in $D^0 \rightarrow K\pi$ Decays”, Phys. Rev. Lett. **91**, 171801 (2003).
- [39] A. Bondar and T. Gershon, “On ϕ_3 Measurements Using $B^- \rightarrow D^* K^-$ Decays”, Phys. Rev. D **70**, 091503 (2004).
- [40] D. Becirevic, “Heavy Quark Phenomenology from Lattice QCD”, Nucl. Phys. Proc. Suppl. **94**, 337 (2001).
- [41] O. Long, M Baak, R. N. Cahn and D. Kirkby, “Impact of tag-side interference on time-dependent CP asymmetry measurements using coherent $B^0 \bar{B}^0$ pairs”, Phys. Rev. D **68**, 034010 (2003).
- [42] BABAR Collaboration, B. Aubert *et al.*, “Measurement of the Branching Fractions and CP Asymmetries of $B^- \rightarrow D_{(CP)}^0 K^-$ Decays with the BABAR Detector”, hep-ex/0408082, submitted to ICHEP’04 (2004).
BABAR Collaboration, B. Aubert *et al.*, “Measurement of CP -Asymmetries for the Decays $B^\pm \rightarrow D_{CP}^0 K^{*\pm}$ with the BABAR Detector”, hep-ex/0408069, submitted to ICHEP’04 (2004).
BABAR Collaboration, B. Aubert *et al.*, hep-ex/0408060, submitted to ICHEP’04 (2004).
Belle Collaboration, K. Abe *et al.*, “Study of $B^\pm \rightarrow D_{CP} K^\pm$ and $B^\pm \rightarrow D_{CP}^* K^\pm$ ”, Belle-CONF-0443, submitted to ICHEP’04 (2004).
- [43] BABAR Collaboration, B. Aubert *et al.*, “Search for $b \rightarrow u$ Transitions in $B^- \rightarrow D^0 K^-$ and $B^- \rightarrow D^{*0} K^-$ ”, hep-ex/0408028, submitted to ICHEP’04 (2004).
Belle Collaboration, K. Abe *et al.*, “Study of the Suppressed Decays $B^\pm \rightarrow [K^\mp \pi^\pm]_D K^\pm$ at Belle”, hep-ex/0408129, submitted to ICHEP’04 (2004).
- [44] BABAR Collaboration, B. Aubert *et al.*, “Constraints on r_B and γ in $B^\pm \rightarrow D^{(*)0} K^\pm$ decays by a Dalitz analysis of $D^0 \rightarrow K_S \pi^- \pi^+$ ”, hep-ex/0408088, submitted to ICHEP’04 (2004).
Belle Collaboration, K. Abe *et al.*, “Measurement of ϕ_3 with Dalitz Plot Analysis of $B \rightarrow D^{(*)} K$ Decay at Belle”, hep-ex/0411049, contributed to FPCP2004 (2004).

- [45] BABAR Collaboration, B. Aubert *et al.*, “Measurement of Time-Dependent CP Asymmetries and Constraints on $\sin(2\beta + \gamma)$ with Partial Reconstruction of $B^0 \rightarrow D^{*\mp}\pi^\pm$ Decays”, hep-ex/0408038, submitted to ICHEP’04 (2004).
BABAR Collaboration, B. Aubert *et al.*, “Measurement of CP -violating parameters in fully reconstructed $B \rightarrow D^{(*)}\pi$ and $B \rightarrow D\rho$ decays”, hep-ex/0408059, submitted to ICHEP’04 (2004).
Belle Collaboration, K. Abe *et al.*, “Study of CP Violating Effects in Time Dependent $B^0(\bar{B}^0) \rightarrow D^{(*)\mp}\pi^\pm$ Decays”, Phys. Rev. Lett. **93**, 031802 (2004).
Belle Collaboration, K. Abe *et al.*, “Time-Dependent CP Violation Effects in Partially Reconstructed $B^0 \rightarrow D^{*\mp}\pi^\pm$ Decays”, hep-ex/0408106, submitted to ICHEP’04 (2004).
- [46] A. J. Buras, R. Fleischer, S. Recksiegel and F. Schwab, “Anatomy of Prominent B and K Decays and Signatures of CP -Violating New Physics in the Electroweak Penguin Sector”, Nucl. Phys. B **697**, 133 (2004).
- [47] J. Albert, A. Datta and D. London, “A Measurement of γ from the Decays $B_d^0(t) \rightarrow D^{(*)+}D^{(*)-}$ and $B_d^0 \rightarrow D_s^{(*)+}D^{(*)-}$ ”, Phys. Lett. B **605**, 335 (2005).
- [48] BABAR Collaboration, B. Aubert *et al.*, “The BABAR detector”, Nucl. Instr. and Methods **A479** 1 (2002).
- [49] *PEP-II - An Asymmetric B Factory, Conceptual Design Report*, SLAC-418, LBL-5379 (1993).
- [50] J. Seeman *et al.*, “Results and plans of the PEP-II B -Factory”, SLAC-PUB-10547 (2004). Presented at EPAC 2004.
- [51] C. Bozzi *et al.*, “The BABAR Silicon Vertex Tracker”, Nucl. Instr. and Methods A **453**, 78 (2000).
- [52] V. Re *et al.*, “Status and future plans of the BABAR Silicon Vertex Tracker”, Nucl. Instr. and Methods A **A511**, 1 (2003).
- [53] V. Re *et al.*, “Performance of the BABAR Silicon Vertex Tracker”, Nucl. Instr. and Methods A **A501**, 14 (2003).
- [54] G. Sciolla *et al.*, “The BABAR Drift Chamber”, Nucl. Instr. and Methods A **419**, 310 (1998).
- [55] M. H. Kelsey *et al.*, “Performance and aging of the BABAR Drift Chamber”, Nucl. Instr. and Methods A **536**, 206 (2004).
- [56] I. Adam *et al.*, “DIRC, the Internally Reflecting Ring Imaging Cherenkov Detector for BABAR”, IEEE Trans. Nucl. Sci. **45**, 657 (1998).
- [57] I. Adam *et al.*, “Operation of the Cherenkov Detector DIRC of BABAR at High Luminosity”, SLAC-PUB-8783 (2001). Talk given at IEEE NSS-MIC’00.
- [58] B. Lewandowski *et al.*, “The BABAR electromagnetic calorimeter”, Nucl. Instr. and Methods A **494**, 303 (2002).
- [59] F. Anulli *et al.*, “The muon and neutral hadron detector for BABAR”, Nucl. Instr. and Methods A **409**, 542 (1998).
- [60] P. F. Harrison, “Blind analysis”, J. Phys. G: Nucl. Part. Phys. **28**, 2679 (2002). Available online at stacks.iop.org/JPhysG/28/2679

- [61] C. Hearty, “Measurement of the Number of Upsilon(4S) Mesons Produced in Run 1 (B Counting)”, *BABAR Analysis Document #134* (2001).
- [62] The CLEO collaboration (D. Lange *et al.*) and the *BABAR* computing group (A. Ryd *et al.*), “The EvtGen particle decay simulation package”, *Nucl. Instr. and Methods A* **462**, 152 (2001).
- [63] T. Sjostrand, “High-energy physics event generation with PYTHIA 5.7 and JETSET 7.4,” *Comput. Phys. Commun.* **82**, 74 (1994).
- [64] Geant4 Collaboration, S. Agostinelli *et al.*, “Geant4: A Simulation Toolkit”, *Nucl. Instr. and Methods A* **506**, 250 (2003).
- [65] P. Billoir and S. Qian, ‘Simultaneous Pattern Recognition And Track Fitting By The Kalman Filtering Method’, *Nucl. Instr. and Methods A* **294**, 219 (1990).
- [66] A description of the likelihood-based charged particle selectors in *BABAR* is available online at: http://www.slac.stanford.edu/BFROOT/www/Physics/Tools/Pid/Hadrons/Description_of_the_LH_selectors.html
- [67] Updated performance plots of the *BABAR* particle selectors are available online at: <http://www.slac.stanford.edu/BFROOT/www/Physics/Tools/Pid/Selectors/r14b/selectors.html>
- [68] A. Drescher *et al.*, ‘The Argus Electron - Photon Calorimeter. 3. Electron - Hadron Separation’, *Nucl. Instr. and Methods A* **237**, 464
- [69] M. T. Allen *et al.*, “A Measurement of π^0 Efficiency Using $\tau \rightarrow \rho\nu$ and $\tau \rightarrow \pi\nu$ Decays”, *BABAR Analysis Document #870* (2004).
- [70] *BABAR* Electron Identification Analysis Working Group, “Cut-based Electron Identification”, *BABAR Analysis Document #90* (2001).
- [71] *BABAR* Muon Identification Analysis Working Group, “Muon Identification in the *BABAR* Experiment”, *BABAR Analysis Document #60* (2000).
- [72] *BABAR* Vertexing and Composition Tools Group, “The *BABAR* Vertexing”, *BABAR Analysis Document #102* (2005).
- [73] M. T. Ford, “Choice of Kinematic Variables in *B* Meson Reconstruction”, *BABAR Analysis Document #53* (2000)
- [74] S. Brandt *et al.*, “The Principal Axis Of Jets. An Attempt To Analyze High-Energy Collisions As Two-Body Processes”, *Phys. Lett.* **12**, 57 (1964);
E. Fahri, “A QCD Test For Jets”, *Phys. Rev. Lett.* **39**, 1587 (1977).
- [75] J. Ocariz *et al.*, “Background fighting in Charmless Two-Body analyses”, *BABAR Analysis Document #346* (2002).
- [76] G. C. Fox, S. Wolfram, “Event Shapes in e^+e^- Annihilation”, *Nucl. Phys. B* **149**, 413 (1979).
- [77] A description of the Fisher discriminant technique is provided for instance in G. Cowan, *Statistical Data Analysis*, Oxford University Press, New York (1998).
- [78] R. A. Fisher, “The Use Of Multiple Measurements In Taxonomic Problems”, *Annals of Eugenics*, **7**, 179 (1936).

- [79] “Recipes for Correcting MC Tracking Efficiencies and Assigning Systematics”, <http://www.slac.stanford.edu/BFROOT/www/Physics/TrackEfficTaskForce/TrackingTaskForce-2004.html>
- [80] “Neutrals correction”, <http://www.slac.stanford.edu/BFROOT/www/Physics/Analysis/AWG/Neutrals/validation/recipe14.html>
- [81] “Performing Particle ID on Monte Carlo”, <http://www.slac.stanford.edu/BFROOT/www/Physics/Tools/Pid/PidOnMc/pidonmc.html>
- [82] L. Lyons, *Statistics for nuclear and particle physicists*, Cambridge University Press, 1986.
- [83] F. James, “MINUIT: Function Minimization and Error Analysis”, Reference Manual, Version 9.41, CERN Program Library Long Wriepup D506, August 1998.
- [84] T. Ypsilantis and J. Seguinot, “Theory of ring imaging Cherenkov counters”, *Nucl. Instr. and Methods A* **343**, 30 (1994).
- [85] G. Cavoto *et al.*, “Measurement of CP -violating Asymmetries in $B^0 \rightarrow \pi^+\pi^-$, $K^-\pi^+$ Decays”, *BABAR Analysis Document #989* (2004).
- [86] M. Pivk and F. LeDiberder, “sPlot: a statistical tool to unfold data distributions”, *physics/0402083* (2004).
- [87] *BABAR* Collaboration, B. Aubert *et al.*, “Dalitz Plot Analysis of $D^0 \rightarrow \bar{K}^0 K^+ K^-$ ”, *BABAR Analysis Document #10*, 2005. To be submitted to *Phys. Rev. D*.
- [88] J. D. Richman, “An Experimenter’s Guide To The Helicity Formalism,” *CALT-68-1148* (1984).
- [89] A. Palano, private communication.
- [90] M. Rama, “Angle $\gamma(\phi_3)$ from $B \rightarrow DK$ decays in *BABAR* (GLW and ADS methods”, talk presented at the CKM2005 Workshop on the Unitarity Triangle, San Diego, March 15-18 2005. Available online: <http://ckm2005.ucsd.edu/WG/WG5/thu3/Rama-WG5-S4.pdf>
- [91] *BABAR* Collaboration, B. Aubert *et al.*, “Limits on the decay rate difference of neutral B mesons and on CP , T , and CPT violation in B^0 - \bar{B}^0 oscillations”, *Phys. Rev. D* **70**, 012007 (2004).